Design and Analysis of Piezoelectric Transformer Converters

Chih-yi Lin

Dissertation submitted to the Faculty of theVirginia Polytechnic Institute and State University in partial fulfillment of the requirements for the degree of

Doctor of Philosophy
in
Electrical Engineering

Fred C. Lee, Chair

Milan M. Jovanovic

Dan Y. Chen

Dusan Borojevic

David Gao

July 15,1997
Blacksburg, Virginia

Keywords: Piezoelectric, dc/dc converters, Transformers

Design and Analysis of Piezoelectric Transformer Converters

by

Chih-yi Lin

Fred C. Lee, Chairman
Electrical Engineering
(ABSTRACT)

Piezoelectric ceramics are characterized as smart materials and have been widely used in the area of actuators and sensors. The principle operation of a piezoelectric transformer (PT) is a combined function of actuators and sensors so that energy can be transformed from electrical form to electrical form via mechanical vibration.

Since PTs behave as band-pass filters, it is particularly important to control their gains as transformers and to operate them efficiently as power-transferring components. In order to incorporate a PT into amplifier design and to match it to the linear or nonlinear loads, suitable electrical equivalent circuits are required for the frequency range of interest. The study of the accuracy of PT models is carried out and verified from several points of view, including input impedance, voltage gain, and efficiency.

From the characteristics of the PTs, it follows that the efficiency of the PTs is a strong function of load and frequency. Because of the big intrinsic capacitors, adding inductive loads to the PTs is essential to obtain a satisfactory efficiency for the PTs and amplifiers. Power-flow method is studied and modified to obtain the maximum efficiency of the converter. The algorithm for designing a PT converter or inverter is to calculate the optimal load termination, Y_{OPT}, of the PT first so that the efficiency (power gain) of the PT is maximized. And then the efficiency of the dc/ac inverter is optimized according to the input impedance, Z_{IN}, of the PT with an optimal load termination.

Because the PTs are low-power devices, the general requirements for the applications of the PTs include low-power, low cost, and high efficiency. It is important to reduce the number of inductive components and switches in amplifier or dc/ac inverter designs for PT applications. High-voltage piezoelectric transformers have been adopted by power electronic engineers and researchers worldwide. A complete inverter with HVPT for CCFL or neon lamps was built, and the experimental results are presented. However, design issues such as packaging, thermal effects, amplifier circuits, control methods, and matching between amplifiers and loads need to be explored further.

Acknowledgments

I would like to thank my advisor, Dr. Fred C. Lee, for his support and guidance during the course of this research work. Without his constant correction on my research attitude, I would have never accomplish this work.

I would like to express my boundless gratitude to my beloved wife, Kuang-Fen, for her patience over these six years and for taking care of Michael, Serena, and myself in spite of her illness in the past three years. She is the real fighter and hero behind this path of studying abroad. Thanks are also due my parents, brother, and sisters.

I also wish to thank Mr. T. Zaitsu and Y. Sasaki of NEC for their helpful discussions, suggestions, and preparing PT samples.

Special thanks to all VPEC students, secretaries, and staffs for their help during my stay. Finally, I would like to thank Motorola for their support in developing PT converters, and thank NEC, Tokin, and Delta Electronics Inc. for their providing PT samples or HVPT CCFL inverters.

Table of Contents

List of Figures

List of Tables

Nomenclature

Roman Items

A	Area in cm^2
B	Susceptance
C	Capacitance in the mechanical branch of the PT
c	Elastic stiffness constant
Cd1	Input capacitance of the PT
Cd2	Output capacitance of the PT
d	Piezoelectric constant
D (superscript)	At constant electric displacement
D	Electric displacement
E	Electric field
E (superscript)	At constant electric field
e	Piezoelectric constants
F	Force
F_S	Switching frequency in Hz
fn	Normalized switching frequency
f_{+45}	Frequency at $+45^o$ from the origin in admittance plot
f_{-45}	Frequency at -45^o from the origin in admittance plot
fa	Antiresonance frequency, susceptance = 0
fr	Resonant frequency, susceptance = 0

fm	Frequency at maximum admittance
fn	Frequency at minimum admittance
fp	Parallel-resonance frequency
fs	Series-resonance frequency
G	Conductance in 1/Ω
g	Piezoelectric constant
h	Piezoelectric constant
k	Electromechanical coupling coefficient
L	Inductance in the mechanical branch of the PT
l	Length in cm
N	Turns ratio of a transformer; 1:N
n	Normalization of circuit parameters
Qm	Quality factor of the mechanical branch
R	Resistance in the mechanical branch of the PT
S	Strain
s	Elastic compliance constant
S (superscript)	At constant strain
T	Stress
T (superscript)	At constant stress
T_S	Switching period in seconds
t	Time in second
u	Displacement
V	Voltage
v	Velocity
W	Width or energy
X	Electric circuit reactance
x_1, x_2, x_3	Cartesian coordinate axis
Y	Electric circuit admittance

Y	Young's modules
Z	Electric circuit impedance
R_L	load resistance of the rectifier circuit
Rload	load resistance of the PT

Special groups

$\hat{x}$	″x″ in phasor representation
$\hat{X}$	″X″ in phasor representation
x_n	Normalized representation of ″x″
X_n	Normalized representation of ″X″
X_{OPT}	Optimized value for ″X″ to achieve best efficiency of the PT

Greek items

β	Impermittivity component
$\varepsilon 0$	Permittivity of free space
ε	Permittivity component
θ	Angle
ω	Angular frequency ($2\pi f$) in rad/sec
δ	Infinitively small value
ρ	Mass density
η	Efficiency
ψ	Turns ratio of the PT
λ	Wavelength

1. Introduction

1.1 Background

1.1.1 Operational Principles

Piezoelectric ceramics are characterized as smart materials and have been widely used in the area of actuators and sensors. The operation principle of a piezoelectric transformer (PT) is a combined function of actuators and sensors so that energy can be transformed from electrical form to electrical form via mechanical vibration. In the beginning stages of developing the PT, it was used as a high-voltage transformer [1]. Continuous efforts devoted to these subjects have been carried out by many researchers [2-8]; however, the published applications are quite limited [9-23].

The piezoelectric effects are considered to be the result of linear interaction between electrical and mechanical systems. For example, the stress of a PT is linearly dependent on the strain. In this work, only the linear piezoelectric effects of the PTs will be dealt with. The nonlinear effects due to temperature rise, depolarization, and aging are out of the scope of this study and will be discussed only briefly.

1.1.2 Electromechanical Coupling Coefficients

The piezoelectric effect will not be activated until the material is polarized in a specified direction or several directions. The measurement of the coupling between the electrical energy and the mechanical energy is called electromechanical coupling coefficient and is defined as

$$k^2 = \frac{\text{mechanical energy converted from input electrical energy}}{\text{input electrical energy}}, \text{ or}$$

$$k^2 = \frac{\text{electrical energy converted from input mechanical energy}}{\text{input mechanical energy}} \tag{1.1}$$

Therefore, the value of the electromechanical coupling coefficient does not indicate the efficiency of the piezoceramics. The energy, which is not converted from input energy, is simply stored in the intrinsic capacitor or in the mechanical branch of the piezoceramics or the PTs. The best illustration of this constant is described in [7]. For example, one of the linear piezoelectric equations describing a longitudinal vibration PT in the transverse direction is

$$\begin{aligned} S_1 &= s_{11}^{\ E} \cdot T_1 + d_{31} \cdot E_3 \\ D_1 &= d_{31} \cdot T_1 + \varepsilon_{33}^{\ T} \cdot E_3 \end{aligned} \tag{1.2}$$

Figure 1. 1 (a) shows a compressive stress applied along x_1 direction when electric field in x_3 direction is zero; the electrodes are then shorted. When T_1 equals T_m, electrical terminals are opened. At the instant when T_1 is reduced to zero, an electric load is added to the electrodes. Hence, W_1+W_2 represents the input mechanical energy, and W_1 represents the output electrical energy. Therefore, the coupling coefficient is

$$k^2 = \frac{W_1}{W_1 + W_2} = \frac{s_{11}^{\ E} - s_{11}^{\ D}}{s_{11}^{\ E}} \ , \tag{1.3}$$

and

$$s_{11}^{\ D} = s_{11}^{\ E} \cdot (1 - k^2) \ . \tag{1.4}$$

From (1.2), if $D_1 = 0$, $s_{11}^{\ D}$ is

$$s_{11}^{\ D} = s_{11}^{\ E} \cdot \left(1 - \frac{d_{31}^{\ 2}}{\varepsilon_{33}^{\ T} \cdot s_{11}^{\ E}} \right) . \tag{1.5}$$

From (1.4) and (1.5),

$$k^2 = \frac{d_{31}^{\ 2}}{\varepsilon_{33}^{\ T} \cdot s_{11}^{\ E}} \ . \tag{1.6}$$

The coupling coefficient can be obtained by calculating the energy conversion from electrical to mechanical energy in Fig. 1.1 (b). The input energy changes to a voltage source, and the piezoceramic is free of expansion or contraction. During this interval, the electric displacement, D_3, increases by a slope, $\varepsilon_{33}^{\ T}$. When $E_1 = E_m$, the body of the piezoceramic is clamped and voltage source is removed. Meanwhile, the displacement D_3 decreases by a slope, $\varepsilon_{33}^{\ D}$. By a similar derivation,

$$\varepsilon_{33}^{\ S} = \varepsilon_{33}^{\ T} \cdot (1 - k^2) \tag{1.7}$$

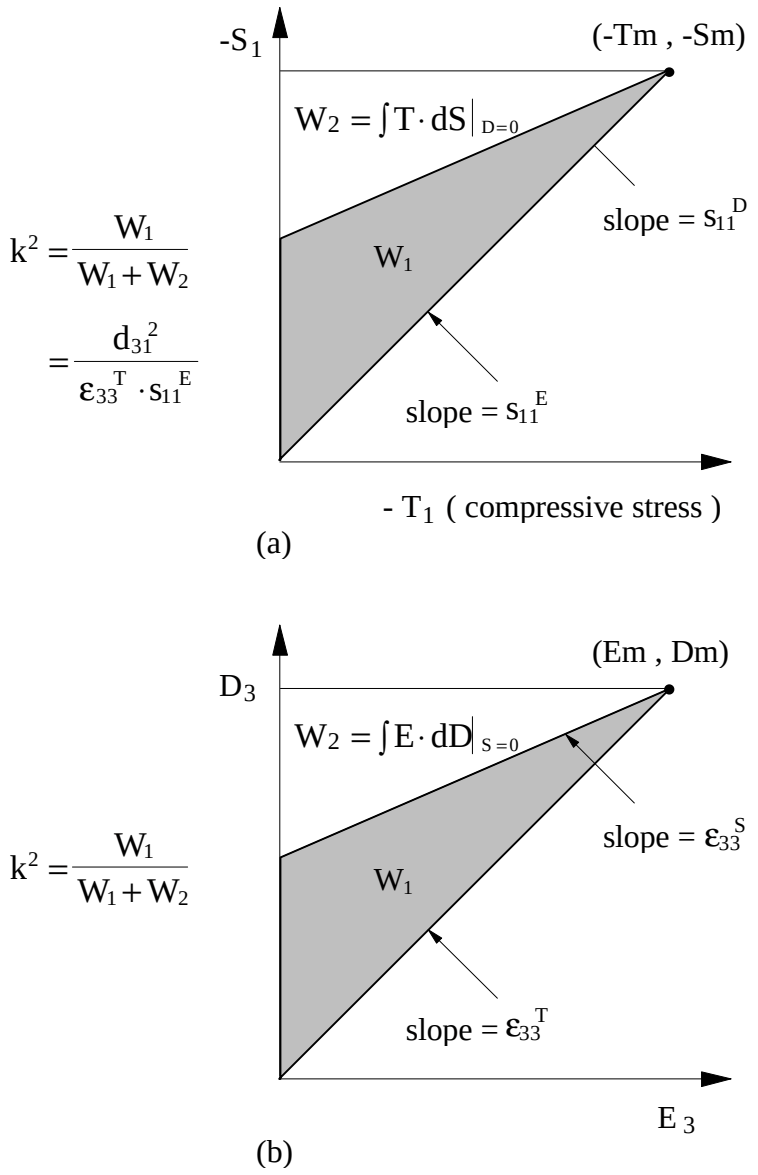

Fig. 1.1. Electromechanical coupling coefficients of piezoelectric ceramics. W1+W2 denotes the input mechanical energy or input electrical energy in (a) and (b) respectively. W_1 represents the output electrical or mechanical energy. The electromechanical coupling coefficient is not necessary a measurement of efficiency of the PT.

1.1.3 Physical Structure of the PTs

PTs can be classified into different categories based on their vibration modes or operating frequencies [5]. It is simpler to classify them from one anther by their vibration modes as the longitudinal vibration mode PT, and the thickness vibration mode PT. For example, for the longitudinal vibration mode PTs, the vibration occurs along the direction shown in Fig. 1.2 (a). Therefore, the longer the PT, the lower the operating frequency. Usually this type of PT is called the rosen-type PT or the high-voltage PT (HVPT) and its main function is to step up the source voltage. Figure 1.2 (b) shows the thickness vibration mode PT, which is suitable for high-frequency and step-down operations and is called the low-voltage PT (LVPT). They are very different in appearance because they operate at distinct frequency bands. The resonant frequency of HVPT is below several hundred kHz because the step-up ratio depends on its physical size [10]. The longer it is, larger the step-up ratio, but the resonant frequency is reduced accordingly. The LVPT, operated in the thickness extensional vibration mode [16,17], has aresonance frequency of several MHz for very thin layers.

1.1.4 Material Properties

The materials used for PTs includes Lead zirconate titanate PZT series, Lead titanate, $PbTiO_3$, and Lithium niobate, $LiNbO_3$. Most of the high-voltage PTs are made of PZT material. The newly developed thickness extensional mode PT is made of $PbTiO_3$ and is very efficient at high frequencies [16, 24-26]. Because of the difficulty in supporting the thickness extensional mode PT, the PT with width-shear vibration was proposed by [27]. It is made from $LiNbO_3$, known as one of the surface-acoustic-wave (SAW) devices.

1.2 Motivation

In the power electronic industry, miniaturization of power supplies has been an important issue during the last decade. The transformers and inductors of the converters are usually tall and bulky compared to transistors and ICs. The low-profile transformers [28] are integrated into the PCB board to reduce the height and size of the converters. The PTs have several inherent advantages over conventional low-profile transformers, such as very low profile, no winding, suitability for automated manufacturing, high degree of insulation, and low cost. Besides the inherent merits of the PTs, they are especially suitable for low-power, high-voltage applications, where making and testing the high-voltage transformers is laborious. Recently, several kinds of PTs, operating at several MHz, have been proposed [16,17]. The output power density is around 20 Watts/cm^3, which is similar to that of the high-frequency ferrite transformers. The PTs are definitely promising components for low-power applications. For higher power operations, it is necessary to reduce the mechanical loss of the PTs. Increasing the number of interdigit fingers in [27] could be one way to reduce the mechanical loss.

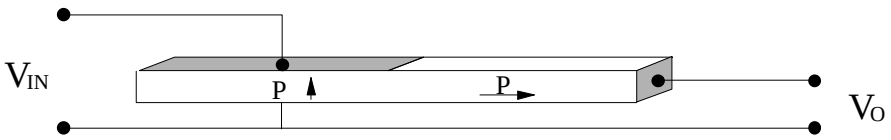

$$\frac{V_O}{V_{IN}} = c \cdot k^2 \cdot Qm \cdot \frac{Length}{Thickness}$$

(a)

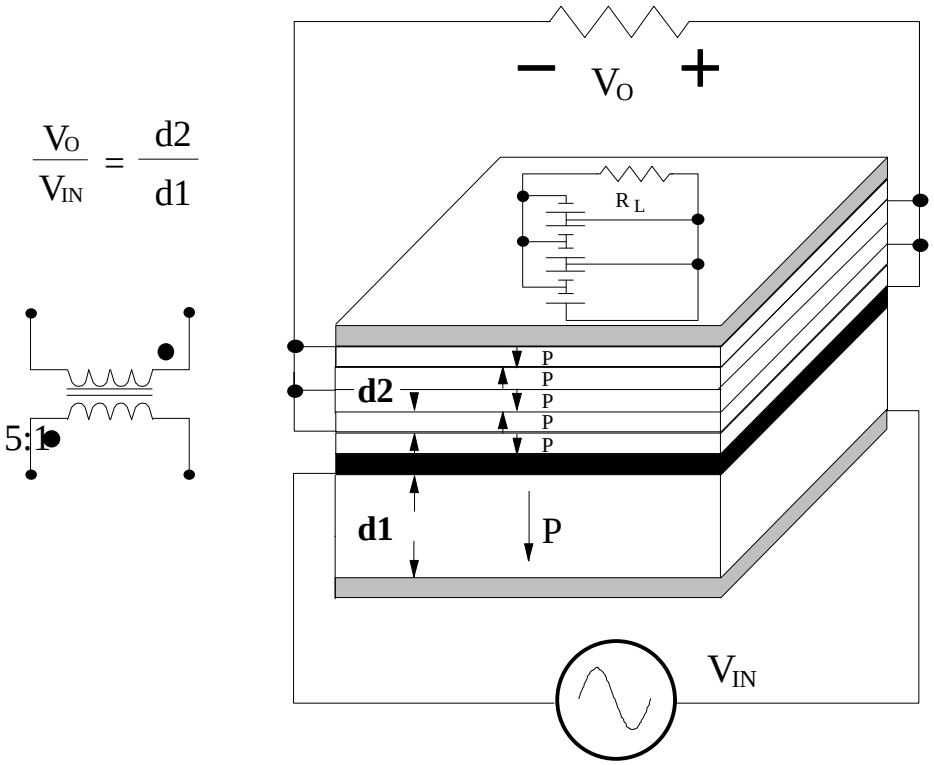

(b)

Fig. 1.2. Construction of different PTs. (a) longitudinal mode PT. (b) multi-layer thickness extensional mode PT provided by NEC.

HVPTs are especially attractive for compact, high-voltage, low-power applications, such as backlit power supplies of notebook computers and neon-light power supplies for warning signs. Presently, the HVPT power supply for cold-fluorescent lamps used in backlighting the screen of notebook computers is already commercialized, and its output voltage is around 1 kV(rms), with 3 to 6-watts output power. LVPTs are developed for on-board power supplies [17,21] with a 48-V input and a 5-V output. The efficiency of the LVPT in an experimental circuit [22] is 92 %. Apparently, the overall efficiency of the PT converter cannot compete with that of the commercial power supplies with the same specifications as above. The PTs are still very attractive because of all the merits mentioned earlier. Another applicable utilization of LVPTs will be the AC adapters whose weight and volume need to be minimized. If a LVPT is designed with a large step-down ratio, 10:1, it would be possible to build an AC adapter. According to the charge pump concept stated in [29], an AC adapter with PFC circuit using LVPT can be implemented by a simple topology [22].

While studying modeling, matching, and applications of the piezoelectric transformer, a good model of the PT can help designers gain better physical insight and to develop the converter circuit with the PTs via simulation. The development of the models of the PTs can be achieved by measurement or theoretical derivation, and they serve different purposes. Measurement results of the PTs from the impedance analyzer can help calculate the parameters of the lumped models according to an ideal resonant band-pass circuitry [30-38] . As far as designing a desired PT is concerned, a physical model [3-5] is essential so that the parameters of the model can be determined from the properties of the material and the physical size of the PT. Operational principles of the PTs are related to electromechanical effects and are explained by the wave motion in a body. A mathematical model can be obtained from the analytical solutions by solving the wave equations.

The efficiencies of the LVPTs and HVPTs are both above 90%, and they can be maximized when the load is optimized. HVPT has a very small output intrinsic capacitor, and its optimal load can be a resistive load that equals the output capacitive impedance [17,21]. On the contrary, the output capacitor of the LVPT is large, and the optimal load, which is optimized by the power-flow algorithm [40,41], is inductive. Once the optimal load of a particular PT is specified, it is necessary to add a matching network between the PT and the rectifier circuits of the converters.

Some sophisticated power-amplifier circuits, demonstrated in [22, 42-45], provide a good way to increase the efficiency of PT converters; however, those circuits are too complicated to use in low-power PT applications. A study of a simple, single-ended quasi-resonant amplifier is conducted by simulation, and then the DC characteristics and design guidelines are presented. Finally, two experimental circuits for LVPT and HVPT applications are built.

1.3 Objective of the Research and Method of Approach

The need to utilize PTs efficiently has motivated the following studies:

1) Study the materials of the PTs to achieve high efficiency in either high or low frequencies, and study the electromagnetic coupling effect as well as wave theory. These are the fundamental tools to establish the mathematical analytical equations for the PTs. Accordingly, the physical models and the nodes, which refer to the support points, can be determined.

2) Derive and verify the electrical equivalent circuits of the PTs. The basic models of the PTs are derived from the measurement results of the impedance analyzer by employing the admittance-circle technique. The dielectric loss of the PTs is incorporated into the basic models by using the curve-fitting method to fit the measurement results obtained from the network analyzer. In order to design the desired PTs, the physical models of the PTs are derived from linear piezoelectric equations and the electromechanical theory. This study will help designers to gain better physical insight and to develop the circuit via simulation.

3) Develop methods to determine the optimal loads for different PTs (LVPT or HVPT). For the PT with very high output impedance, its optimal load is resistive. On the other hand, for the low output-impedance PT, its optimal load needs to be determined by the power-flow method, and the best efficiency of the PT is determined over a certain frequency range. For the given specifications of the PT dc/dc converter, the rectifier circuit and the load can be represented as an equivalent resistive load. As a result, a matching network needs to be added between the output of the PT and the rectifier circuit. In the meantime, it is necessary to study the interaction between the amplifiers and the input impedance of the PT.

4) Analyze and build power amplifiers as the input source of the PTs. Two breadboard circuits employing the LVPT or HVPT respectively were built to demonstrate the feasibility of using the PT as a power-transformation media.

1.4 Dissertation Outline and Major Results

This dissertation includes six chapters, references and appendices.

In Chapter 2, the lumped models for both longitudinal and thickness extension mode PTs are verified with empirical measurements from the impedance analyzer or network analyzers. The resultant lumped models of the PTs can help designers to understand the characteristics of the PTs and to design PT inverters via simulations. Verification of parameters for lumped models of PTs is fulfilled from several aspects, including input admittance, voltage gain, and efficiency, all under various load conditions. The measured performance of the PT agrees with those obtained from lumped model by simulation.

In Chapter 3, the matching networks for the PTs are obtained to maximize the efficiency of the PTs. Output matching network is decided by performing the power flow method, which provides a graphical way to calculate the optimal load of the PTs. The objective of designing the input matching network is to match the input impedance of a matched PT, whose load is optimized to achieve maximum efficiency, to the amplifier circuit. Moreover, matching between the amplifier and the input impedance of the PTs results in reducing the circulation current flowing in PTs and amplifiers.

Chapter 4 provides different power amplifier circuits for low-voltage (or step-down) and high-voltage (or step-up) applications. The design example is a dc/dc converter and it is performed by employing a step-down PT. The performance comparisons between simplicity and efficiency of the converter circuits are summarized.

In Chapter 5, applications for Cold-Cathode-Fluorescent-Lamp (CCFL) are chosen, and the PTs are used as the key components to replace the conventional transformer to demonstrate their values in the real word. Conclusions and future work are presented in Chapter 6.

2. Verifications of Models for Piezoelectric Transformers

2.1 Introduction

Since the PTs behaves as band-pass filters, as shown by their gain vs. voltage gain characteristics, it is particularly important to control their gains as transformers and to operate them efficiently as power-transferring components. In order to incorporate a PT into amplifier design and to match it to the linear or nonlinear loads, suitable electrical equivalent circuits are required for the frequency range of interest. In this chapter, the study of the accuracy of PT models is carried out from several points of view, including input impedance, voltage gain, and efficiency when PTs are connected to the resistive loads directly. Those characteristics will be utilized in designing the converters employing PTs. Intuitively, the PTs should be operated around their resonant frequencies so that both efficiency and voltage gain can be maximized. However, the operating frequencies are selected a little away from their resonant frequencies for control reasons.

2.2 Electrical equivalent circuit of the PTs

The analysis of piezoelectric transformers has been carried out by employing one dimensional wave equations. Accordingly, the mechanical and electrical properties can be derived in a straightforward manner. In order to study their interaction, it is preferable to use the equivalent circuit approach. Meanwhile, mechanical parameters can be replaced by their electric counterparts. Around the 1950s, the piezoelectric transformers had just emerged, and their equivalent circuits had been derived in [3-5] in the forms of different basic model cells. Only the complete model of the longitudinal mode has been described completely [3,4]. Nowadays, the thickness extensional mode multilayer PTs [16] are adopted to enhance the performance of the PTs, for example to increase the gain of the PTs and to improve their power handling. To deal with these multilayer PTs, correct mechanical and electrical boundary conditions have to be created to obtain meaningful equivalent circuits.

Table 2.1. Material constants for HVPT-1.

Constant	Description	Value
ε_{33}^{T}	Relative permittivity	1200
$\tan\delta$	Dielectric tangent (%)	0.5
k_{31}	Electromechanical constant	0.35
k_{33}	Electromechanical constant	0.69
Y_{11}^{E}	Young's modulus (10^{10} N/m)	8.5
Y_{33}^{E}	Young's modulus (10^{10} N/m)	7
d_{31}	Piezoelectric constant (10^{-12} m/N)	-122
d_{33}	Piezoelectric constant (10^{-12} m/N)	273
g_{31}	Piezoelectric constant (10^{-3} Vm/N)	-11.3
g_{33}	Piezoelectric constant (10^{-3} Vm/N)	25.5
Qm	Mechanical quality constant	2000
ρ	Density (kg/m^3)	7800

Table 2.2. Dimensions of HVPT-1.

Variable	Description	Value
2 l	Length of the PT (mm)	33
W	Width of the PT (mm)	5
h	Thickness of the PT (mm)	1
l_S	Length of the side-plated bar	
l_E	Length of the side-plated bar	

Two types of PTs will be studied in this chapter, longitudinal mode PTs and thickness extensional mode PTs. The physical model of the longitudinal PT has been discussed extensively in [3,4] and will be repeated in Appendix A for completion. Applying the one dimensional wave equations, the model with the mechanical for a 1:1 thickness extensional mode PT is also studied in Appendix A. The complete electrical equivalent circuits for both longitudinal and thickness extensional PTs are summarized and the results are given in the following sections.

2.2.1 Longitudinal mode PT

Figure 2.1. shows the construction of a longitudinal PT and its electrical equivalent circuit which is constructed of two basic model cells: the side-plated bar and the end-plated bar. The side-plated bar is the driver part of the PT, where the electrical input is converted to mechanical vibration in x_1 direction due to the strong piezoelectric coupling. In the meantime, the mechanical vibration which appearing at both ends of the end-plated bar is restored to electrical energy, and the detailed derivation of the basic model cells of the longitudinal model PT is presented in Appendix A. Figure 2.2. shows the resultant model for a longitudinal mode PT around its second mode or full-wave mode operation. The parameters of the final model are calculated according to the information tabulated in Table 2.1. This sample is named HVPT-1, and is manufactured by Panasonic in Japan. The equations used to calculate the parameters of the electrical equivalent circuit can be obtained from Appendix A and are summarized below:

$$L = \frac{\rho \cdot Aac \cdot l_s}{4 \cdot \psi'^2} + \frac{\psi^2}{\psi'^2} \cdot L_o \ ; \tag{2.1}$$

$$C = \psi'^2 \cdot \frac{4 \cdot l_S}{\pi^2 \cdot W \cdot h \cdot Y_1^E} \ ; \tag{2.2}$$

$$R = \frac{\pi \, Z_o}{4 \cdot Q_m \, \psi'^2} \ ; \tag{2.3}$$

$$Cd1 = \frac{W \cdot l_s \cdot \varepsilon_{33}^T \cdot \varepsilon_o \cdot (1 - k_{31}^2)}{h} \ ; \tag{2.4}$$

$$Cd2 = \frac{W \cdot h \cdot \varepsilon_{33}^T \cdot \varepsilon_o \cdot (1 - k_{33}^2)}{l_e} \ ; \tag{2.5}$$

$$N = \frac{\psi}{\psi'} \ ; \tag{2.6}$$

$$\psi' = W \cdot d_{31} \cdot Y_{11}^E \ ; \tag{2.7}$$

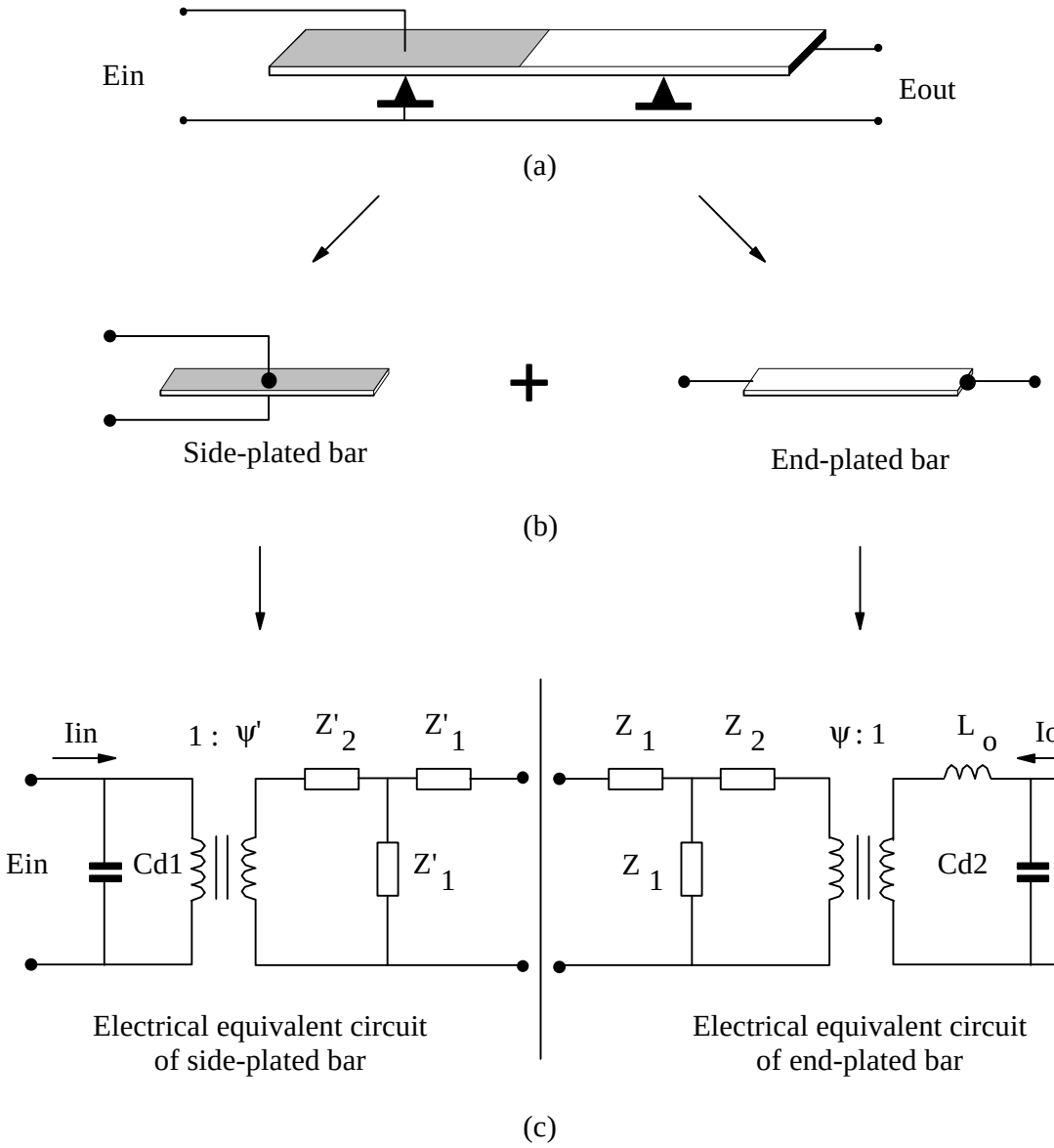

Fig. 2. 1. Construction of longitudinal PTs. (a) nonisolated type. (b) side-plated bar and end-plated bar. (c) their equivalent circuits. The electrode, near the driver portion of the side-plated bar is either shared with one of the electrodes of the driver or appears on the surface of the output part. This arrangement will affect the efficiency of the longitudinal mode PT slightly. The support points at nodes also affect the efficiency of PTs. Co' and Co are the intrinsic capacitors of the bars. The networks composed of Z' and Z represent the mechanical branches in the models. The interaction between electrical and mechanical networks are explained by the transformer ratios: ψ and ψ', which are proportional to the piezoelectric constants.

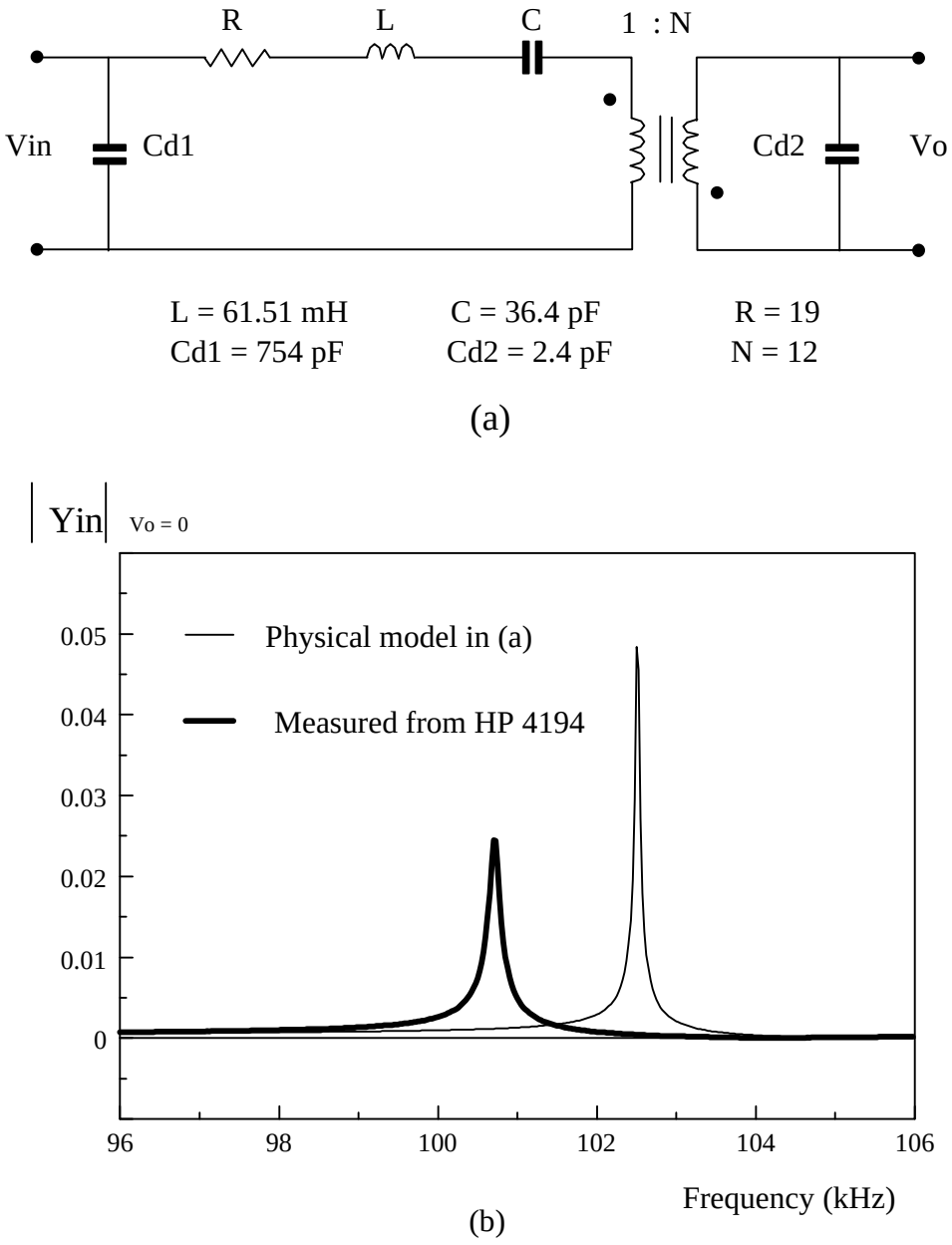

Fig. 2. 2. Physical model of HVPT-1 and its input admittance characteristics. R, L, and C are calculated by using its dimensions and material constants from Table 2.1. The measured input admittance is shown in dark line and the calculated input admittance in thin line. Both curves are drawn when output terminals are shorted. Because there is no spurious vibrations around the resonant frequency from the measurement results. The parameters of the model depicted in (a) can be easily tuned to obtain the same measured characteristics. This model is valid for the PT without any spurious vibration near the resonant frequency.

$$Z_o = \sqrt{\rho \cdot Y_{33}^{\ D}} \cdot h \cdot W \ ; \tag{2.8}$$

$$\psi = \frac{h \cdot W}{l_E} \cdot \frac{g_{33} \cdot Y_{33}^{\ D}}{\beta_{33}^{\ T} + g_{33}^{\ 2} \cdot Y_{331}^{\ D}} \ ; \tag{2.9}$$

$$L_o = \frac{1}{\omega_o^{\ 2} \cdot Cd2} \ ; \tag{2.10}$$

and the dielectric losses can be estimated as

$$Rcd1 = \frac{1}{\omega_o \cdot Cd1 \cdot \tan\delta} \ , \tag{2.11.a}$$

$$Rcd2 = \frac{1}{\omega_o \cdot Cd2 \cdot \tan\delta} \ . \tag{2.11.b}$$

l_S is the length of the side-plated bar and l_E is that of the end-plated bar. The total length of HVPT-1 is equal to $l_S + l_E$. In order to have $\beta' l_S = \beta l_E$ [4], l_S = 15 mm and l_E =18 mm. The other way to simplify the analysis is to let Zo′ = Zo, in which case the cross-sectional areas have the following relationship:

$$\frac{l_S}{l_E} = \frac{A_E}{A_S} = \sqrt{\frac{Y_{11}^{\ E}}{Y_{33}^{\ D}}} \ , \tag{2.12}$$

where A_E is the cross-sectional area of the end-plated bar and is equal to (h W); A_S is the cross-sectional area of the side-plated bar and is equal to (h′ W′). Although the cross-sectional area of HVPT-1 is uniform in shape, the assumption is still made to simplify the analysis of the equivalent circuit. Therefore some mismatch between the measured and calculated characteristics of HVPT-1 is expected. However, as long as the model is correct, the parameters of the electrical equivalent can be tuned by referring to the measurement data.

The input admittance, Yin, of the longitudinal PT, obtained both from the resultant model and measurement data, is shown in Fig. 2.2 (b) when the output terminals of HVPT-1 are shorted. The calculated and measured input admittances of HVPT-1 are similar in shape, without any spurious vibrations, but the resonance frequencies are little different. This predicts that a better measurement technique needs to be developed to describe the characteristics of the PT more accurately. A MCAD program in Appendix B.1 is developed to determine the physical model of HVPT-1 under mismatch conditions.

2.2.2 Thickness extensional mode PT

The sample adopted in this section is a 1:1 thickness extensional mode PT, which is developed in NEC device laboratory and is called LVPT-11. The construction of LVPT-11 is illustrated in Fig. 2.3 (a), and its model is composed of two identical model cells of the broad plate shown in Fig. 2.3 (b). Tables 2.3. and 2.4. show the material, dimensional, and piezoelectric properties of LVPT-11.

Table 2.3. Material constants for LVPT-11.

Constant	Description	Value
ε_{33}^{T}	Relative permittivity	211
ε_{33}^{S}	$\varepsilon_{33}^{S} = \varepsilon_{33}^{T} \cdot (1 - k_t^2)$	156
$\tan\delta$	Dielectric tangent (%)	0.6
k_t	Electromechanical constant	0.52
Y_{33}^{E}	Young's modulus (10^{10} N/m)	11.9
Y_{33}^{D}	$Y_{33}^{D} = Y_{33}^{E} \cdot (1 - k_t^2)^{-1}$ (10^{10} N/m)	16.08
g_{33}	Piezoelectric constant (10^{-3} Vm/N)	25.5
h_{33}	$h_{33} = Y_{33}^{D} \cdot g_{33}$ (x 10^{10})	0.5423
Qm	Mechanical quality constant	1200
ρ	Density (kg/m^3)	6900

Table 2.4. Dimensions of LVPT-11.

Variable	Description	Value
h	Length of the PT (mm)	20
W	Width of the PT (mm)	20
2 l	Thickness of the PT (mm)	3.66
l_S	Length of the insulation layer	0.22

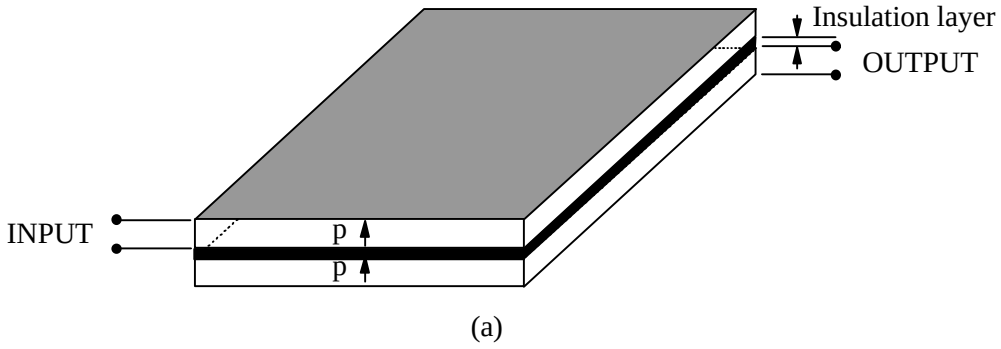

(a)

(a) 1:1 BROAD-PLATE PT

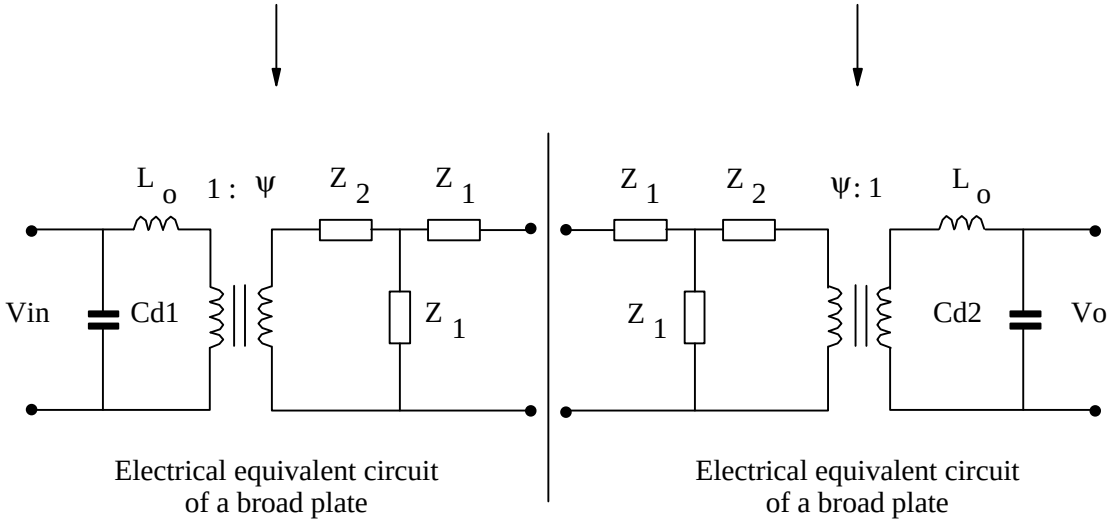

(b)

Fig. 2. 3. Construction of the thickness extensional mode PT (LVPT-11). (a) isolated type 1:1 broad-plated PT. (b) its equivalent circuit. The input and output part of LVPT-11 are identical and the analysis of the PT is focused on input part only. Because it is so broad that the strain is zero around the circumference of the PT where the support points should be located. But technically it is difficult to do so. An alternate way is to support it around four corners on the bottom side with four small elastic material which will not hinder the mechanical vibration.

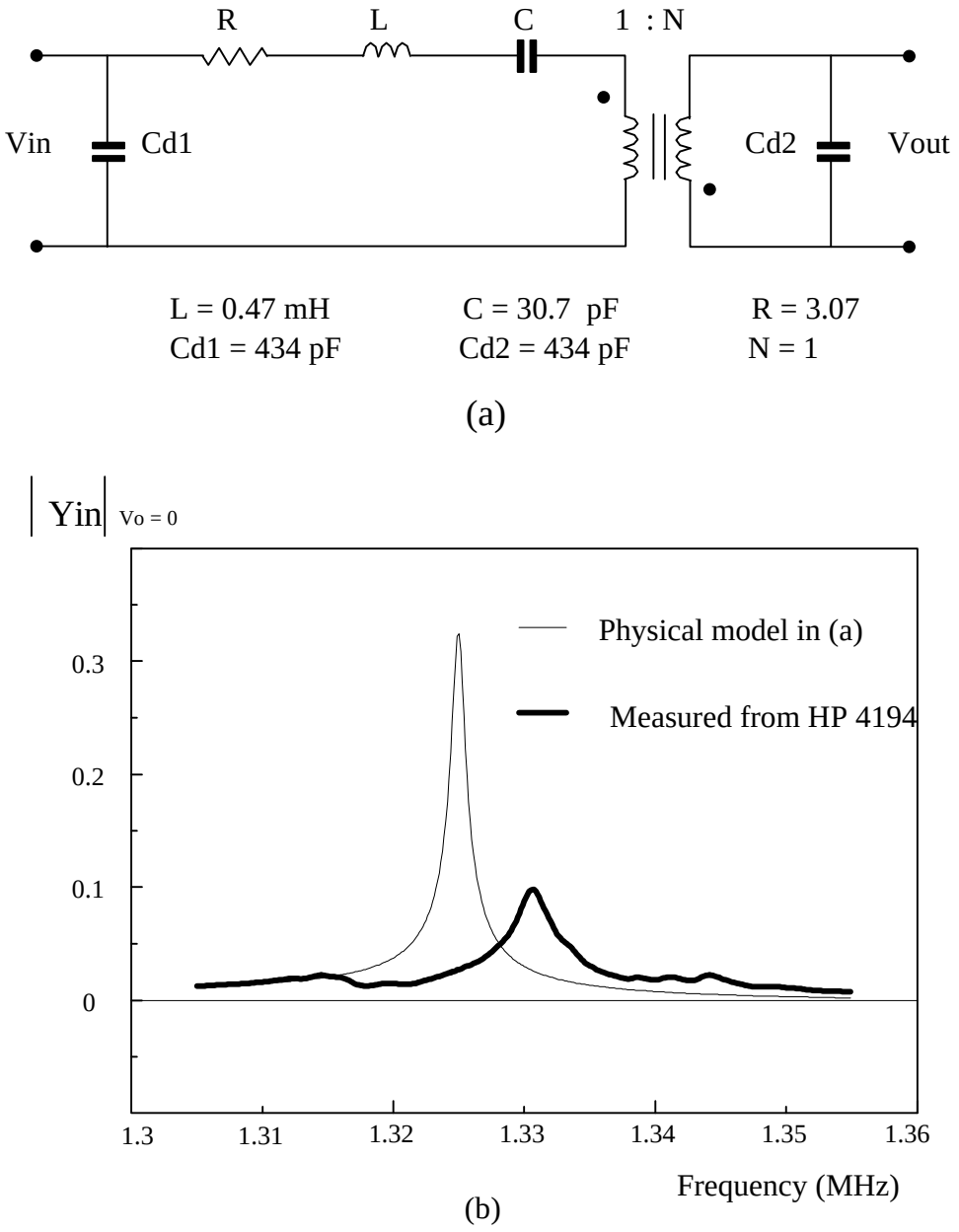

Fig. 2. 4. Physical model of LVPT-11 and its input admittance characteristics. The measured input admittance is shown in dark line. Both input admittance characteristics are obtained when the output terminals are shorted. Because there are a lot spurious vibrations near the resonant frequency from the measurement, the efficiency and voltage gain of the PT will be decreased. The parameters of the model depicted in (a) can no longer duplicate the unwanted spurious vibration. Because there is an insulation layer installed between the input and output parts, the measured mechanical loss is five times higher than the theoretical loss which can be corrected by admittance circle measurement technique.

The complete model of LVPT-11 is shown in Fig. 2.4 (a). The equations to calculate the parameters of LVPT-11 is also summarized from Appendix A and listed below:

$$L = \frac{\rho \cdot \text{Volume of the PT}}{8 \cdot \psi'^2} + 2 \cdot L_o \ ; \tag{2.13}$$

$$C = \psi'^2 \cdot \frac{4 \cdot l}{\pi^2 \cdot W \cdot h \cdot Y_1^{\ D}} \ ; \tag{2.14}$$

$$R = \frac{\pi \, Z_o}{4 \cdot Q_m \, \psi'^2} \ ; \tag{2.15}$$

$$Cd1 = \frac{W \cdot h \cdot \varepsilon_{33}^{\ T} \cdot \varepsilon_o}{l} \ ; \tag{2.16}$$

$$\psi = \frac{h \cdot W}{l} \cdot \frac{c_{33}^{\ D} \cdot g_{33}}{\beta_{33}^{\ D}} \ ; \tag{2.17}$$

$$Z_o = \sqrt{\rho \cdot Y_{33}^{\ D}} \cdot h \cdot W \ ; \tag{2.18}$$

$$L_o = \frac{1}{\omega_o^{\ 2} \cdot Cd1} \ ; \tag{2.19}$$

and the dielectric losses can be estimated as

$$Rcd1 = \frac{1}{\omega_o \cdot Cd1 \cdot \tan\delta} \tag{2.20.a}$$

$$Rcd2 = \frac{1}{\omega_o \cdot Cd2 \cdot \tan\delta} \tag{2.20.b}$$

The turns ratio N = 1 and Cd1 = Cd2. From Fig. 2.4 (b)., the calculated input admittance of the model is verified with the measured model obtained from the impedance analyzer. A lot of spurious vibrations occur around the resonant frequency of the measured input admittance because of the material properties [16]. The efficiency of the PT will decrease around the frequencies of the spurious vibrations. To utilize this type of PTs correctly, the characteristics of the spurious vibrations must be simulated and rebuilt in the model. So the physical model of the PTs is too simplified to employ under those circumstances, and it needs to be modified for the simulation purposes. A MCAD program presented in Appendix B.2 is developed to calculate the electrical equivalent of HVPT-1 from measurement results.

2.3 Measurement of Electric Equivalent Circuit of the PT

Since the physical model mentioned earlier can not duplicate the characteristics of the thickness extensional mode PTs, it is very important to develop a measurement technique to verify the parameters of the improved physical model. To get a closer insight into the PTs, first, a measurement method is proposed to obtain the parameters of the equivalent circuits which is similar to the equivalent circuit of a quartz. A procedure to measure and calculate the equivalent circuit of the PTs is given in detail.

2.3.1 Characteristics of the PT

Besides the admittance characteristics, the information about the voltage gain and efficiency of the PT is essential to its performance as a transformer. Figure 2.5. shows the general gain characteristics of a PT with 1-MΩ load termination, and three peaks are observed. Usually, the left peak shows the fundamental mode or half-wave mode operation. The full-wave mode operation is in the center, and the third-wave mode is on the right. It is not necessary that the maximum voltage gain occur in the full-wave mode operation. However, each peak of the voltage gain for a specified load condition occurs at the mechanical resonant frequency, f_S. Exact modes of operation can be obtained by calculating $v_{sound} = \lambda \cdot f_o$ where v_{sound} represents the velocity of the mechanical vibration in the PTs and λ is the length of the PTs

2.3.2 Admittance Circle Measurements

Generally, the equivalent circuit of the PT is a distributed network rather than a single linear resonant circuit valid only near the fundamental resonance frequency, fs. The impedance characteristics [4,5,8] of the PT with one port shorted are similar to those of a quartz, shown in Fig. 2.6 (a). So it is possible to obtain an empirical model for the PTs by borrowing the model of the quartz. To decide the parameters of the electrical equivalent circuit shown in Fig. 2.2. or 2.4., the measured conductance and susceptance are plotted in G-B axes and result in an admittance circle. Figure 2.6 (b). shows the admittance circle for the electrical equivalent circuit of a PT, when one of the output ports of the PT is shorted, and the critical frequencies are defined as

f_{+45}: frequency at $+45^o$ from the origin, (G,B)=(0,0) ;

fm: frequency at maximum admittance ;

fs: series resonance frequency, $2\pi fs = \omega_s = \frac{1}{\sqrt{LC}}$; (2.21)

fr: resonant frequency, susceptance = 0 ;

f_{-45}: frequency at -45^o from the origin, (G,B)=(0,0) ;

fa: antiresonance frequency, susceptance = 0 ;

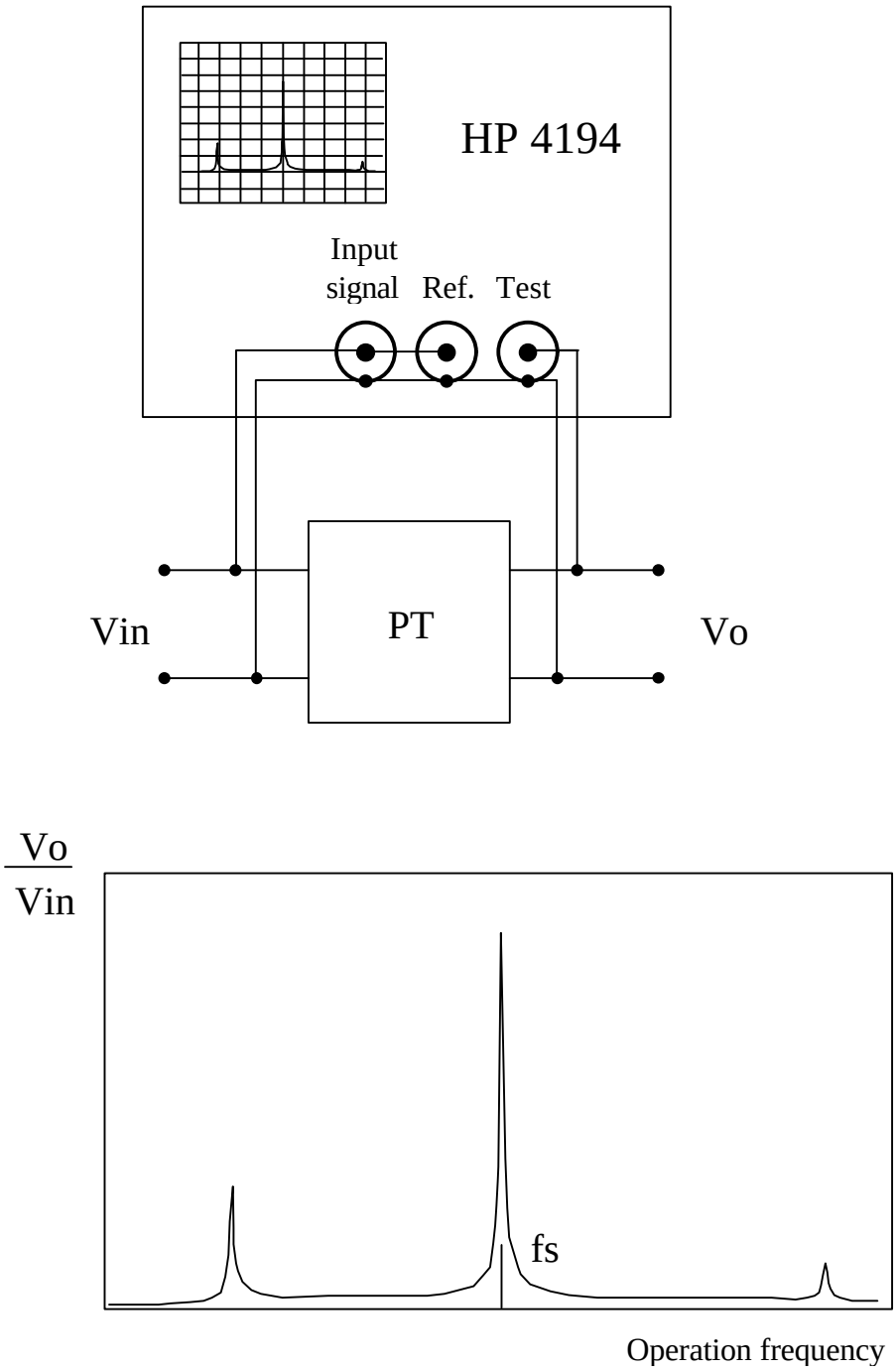

Fig. 2.5. Voltage gain characteristics of the PTs. From the measured fs and velocity of sound Vsound, wave length = Vsound/fs. Accordingly, mode of operation for each peak can be determined. Each mode of operation can be represented by a serial R-L-C branch and decided by the admittance circle measurement.

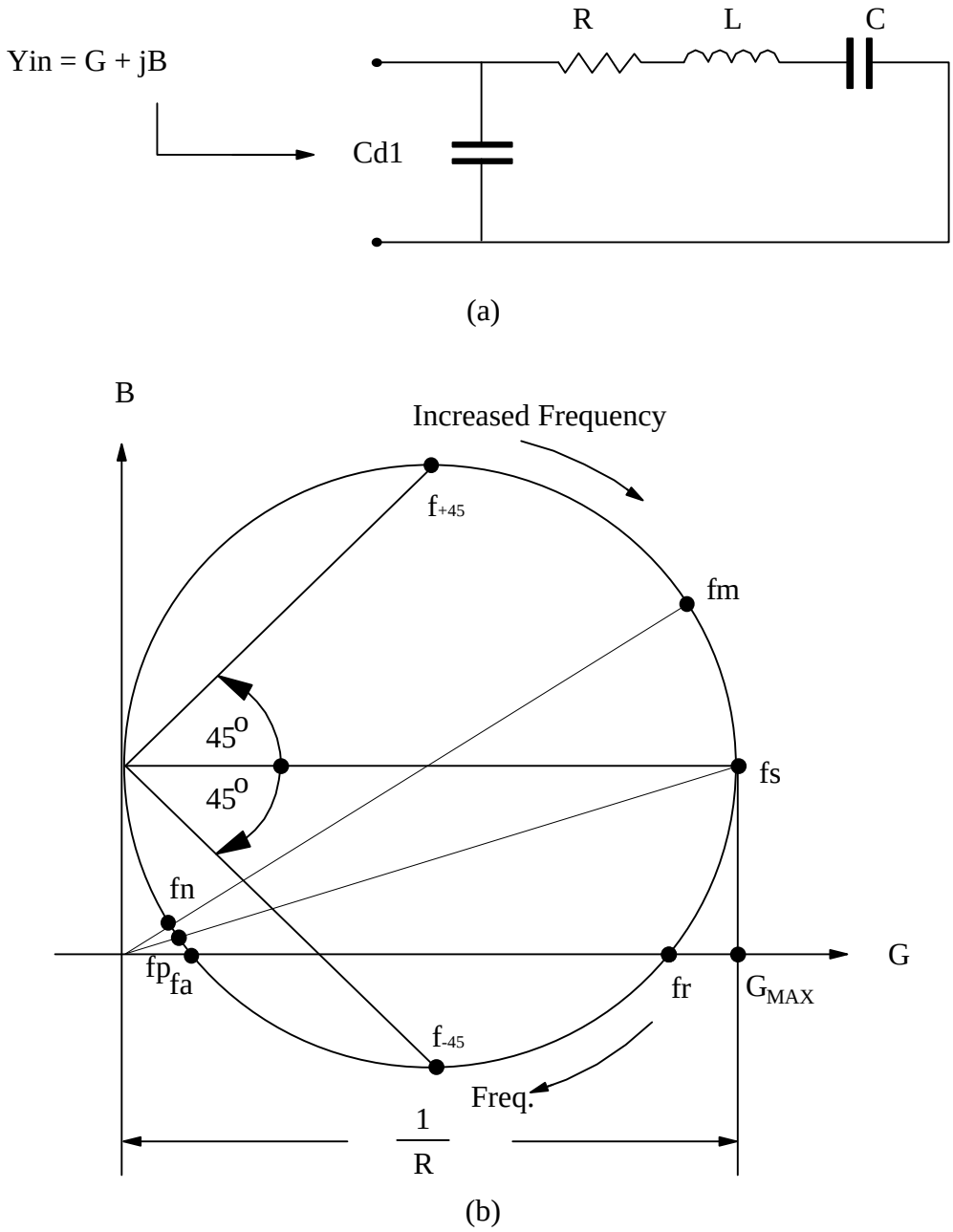

Fig. 2. 6. Admittance circle measurements. The measurement reseults are employed to calculate the parameters of the equivalent circuit: Cd1, R, L, and C when one port of the PT is shorted. In the same manner, when the other port is shorted, another set of parameters are derived. As a result, Cd2 and turns ratio N of the PT are obtained.

fp: parallel resonance frequency, $2\pi fp = \omega_p = \frac{1}{\sqrt{L\left(C \| Cd1\right)}}$; (2.22)

fn: frequency at minimum admittance ;

If the mechanical loss, R, is very small, the critical frequencies, fm, fs, and fr, are merged and so are the frequencies fn, fp, and fa. Except fp, the other five frequencies are easy to obtain from impedance measurement. The only information provided to locate fp in the admittance circle is that the phases of the total admittance of the PTs are identical at fs and fp. To extract the parameters of the PTs, some parameters need to be measured.

At a very low frequency, for example: 1 kHz [8], the impedance of L is almost zero. If admittance of capacitor, C, is larger than the 1/R, only an intrinsic capacitor appears in the input of the PT with a shorted output. The total input capacitance, measured from input port of the PTs, is

$$C_T = Cd1 + C \ , \tag{2.23}$$

and

$$Cd1 = \frac{\omega_s^{\ 2}}{\omega_p^{\ 2}} \cdot C_T \ , \tag{2.24}$$

$$L = \frac{1}{\omega_s^{\ 2} \cdot C} \ , \tag{2.25}$$

$$R = \frac{1}{G_{MAX}} \ . \tag{2.26}$$

Frequencies fs and fp are the key frequencies to calculate the values of L and C in the mechanical branch in the model. It is relatively easy to measure the series-resonance frequency, fs. Unfortunately, parallel resonance frequency, fp, is very difficult to measure in the admittance circle; therefore, an alternative method to decide L and C by using other critical frequencies is developed. Resonance and antiresonance frequencies are calculated in Appendix C to give

$$\omega_r^{\ 2} = \frac{1}{LC} \cdot \left(1 + \frac{R^2}{L} \cdot Cd1\right) = \frac{1}{LC} \cdot \left(1 + \delta\right) \ , \tag{2.27}$$

$$\omega_a^{\ 2} = \frac{1}{LC} \cdot \left(1 + \frac{C}{Cd1} - \frac{R^2}{L} \cdot \left(C + Cd1\right)\right) \cong \frac{1}{LC} \cdot \left(1 + \frac{C}{Cd1} - \delta\right) \ , \tag{2.28}$$

where

$$\delta = \frac{R^2}{L} \cdot Cd1 \ . \tag{2.29}$$

Assume $\delta << 1$, which means

$$\frac{R^2}{LC} << \frac{1}{Cd1 \cdot C} \ , \tag{2.30.a}$$

$$\left(\omega_s R C\right)^2 << \frac{C^2}{Cd1 \cdot C} \ , \tag{2.30.b}$$

$$\frac{Cd1}{C} << Q_m{}^2 \ . \tag{2.30.c}$$

Because the magnitude of Qm usually falls between 300 to several thousands for the piezoceramics, (2.10) holds and δ=0 in (2.7) and (2.8). When dividing (2.7) by (2.8), Cd1 is calculated to be

$$Cd1 \cong \frac{\omega_r{}^2}{\omega_a{}^2} \cdot C_T \tag{2.31}$$

which is identical to (2.4). However, the parallel-resonant frequency fp can be measured by measuring the impedance of the PT instead of admittance of the PT. The parallel-resonant frequency occurs when the real part of Z reaches as its maximum, where the resistive loss represents the mechanical and dielectric losses of the PT. Other than using (fr, fa) and (fs, fp) to calculate Cd1, it is also possible to use fm and fn to do the calculation [5,8]. Figure 2.7 (a). shows equivalent circuit and calculated parameters of the PTs when input port is shorted. In a similar manner, Fig. 2.7 (b). shows the equivalent circuit and its parameters by shorting the input of the PT and transferring the mechanical branch to the secondary side of the PT. As usual, C_{T2} is measured at 1 kHz. Another set of equations to calculate the parameters of the equivalent circuit become

$$C_{T2} = Cd2 + C_N \ ; \tag{2. 32}$$

$$Cd2 = \frac{\omega_{r2}{}^2}{\omega_{a2}{}^2} \cdot C_{T2} \ ; \tag{2.33}$$

$$C_N = C_{T2} - Cd2 \ ; \tag{2.34}$$

$$L_N = \frac{1}{\omega_{s2}{}^2 \cdot C_N} \ ; \tag{2.35}$$

$$N = \sqrt{\frac{L_N}{L}} \ ; \qquad (2.36)$$

(a)

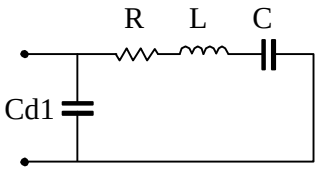

$$C_T = Cd1 + C$$

$$R = \frac{1}{G_{MAX}}$$

$$Cd1 = \frac{\omega_r^2}{\omega_a^2} \cdot C_T$$

$$C = C_T - Cd1$$

$$L = \frac{1}{\omega_s^2 C}$$

(b)

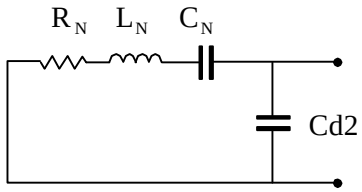

$$C_{T2} = Cd2 + C_N$$

$$R_N = \frac{N^2}{G_{MAX2}}$$

$$Cd2 = \frac{\omega_{r2}^2}{\omega_{a2}^2} \cdot C_{T2}$$

$$C_N = C_{T2} - Cd2$$

$$L_N = \frac{1}{\omega_{s2}^2 C_N}$$

$$N = \sqrt{\frac{L_N}{L}}$$

Fig. 2. 7. Derivation of parameters of PT model by admittance circle measurement techniques. (a) when output port is shorted. (b) when input port is shorted.

where C_N and L_N are capacitor and inductor reflected to the secondary side, and N is the turns ratio. Another method to calculate the parameters of the equivalent circuit was adopted in [35], and the main equations are listed below:

$$R = \frac{1}{B_{MAX}} \; ; \tag{2.37}$$

$$Cd1 = \frac{B_S}{\omega_S} \; ; \tag{2.38}$$

$$C = \frac{1}{2\pi \cdot R} \cdot \frac{f_{-45} - f_{+45}}{f_{-45} \cdot f_{+45}} \; ; \tag{2.39}$$

$$L = \frac{R}{2\pi} \cdot \frac{1}{f_{-45} - f_{+45}} \; . \tag{2.40}$$

This method is still valid when the admittance circle does not intersect G axis in the G-B plot. Again, the disadvantage is that it is very difficult to identify f_{+45} and f_{-45} in an arbitrary admittance circle, which might not be a pure circle at all. Therefore, a curve-fitting method needs to be used to get an ideal circle from the measurement data. Compared to these two admittance circle techniques, the former measurement is easier to perform and has been employed to demonstrate the feasibility later.

2.3.3 Dielectric loss

Due to the high-Q characteristics in the R-L-C branch of the equivalent circuit for the PT, the theoretical efficiency of the PT is relatively insensitive to the load when it is tested near fs and terminated with resistive load. As a matter of fact, the efficiency of the PTs is highly dependent on the load [21]. The disagreement between the model and measurements probably results from the nonlinear effect of the dielectric loss in the input and output intrinsic capacitors of the PTs. To model the PT more accurately, two resistors have been added to the input and output intrinsic capacitors of the PTs, respectively. The dielectric loss can be estimated by the dielectric loss factor tanδ of the input and output intrinsic capacitors Cd.

$$Rd = \frac{1}{2\,\pi\,fr\,Cd} \cdot \frac{1}{\tan\delta} \; , \tag{2.41}$$

where Rd is the parallel resistance representing the dielectric loss of the PT. Taking LVPT-11 as an example, Cd1 = 470 pF, tanδ = 0.006, and fr = 1.33 MHz. The calculated resistance of Rd1 is 42 kΩ. Although a large parallel resistance at the input or output terminals of a two-port network indicates a small loss, it was demonstrated by an empirical experiment that dielectric losses of the PTs are not negligible because of the nonlinearility under high-power operations.

2.4 Complete Model of the Sample PTs

In the following chapters, two PTs are employed in different converter applications. They are different samples from those studied in section 2.2. The first one is a step-up PT HVPT-2, whose step-up ratio is 1:9 when it is terminated with a 200-kΩ resistive load. The other one is a step-down PT LVPT-21 which provides a 2:1 step-down ratio and is manufactured by NEC. In order to proceed to design the converter with the PTs, the voltage conversion ratio and efficiency of the converter employing PTs have to be calculated according to different converter topologies and loads, including linear and nonlinear loads. Therefore, it is very important to develop a method to modify the electrical equivalent circuit of the physical model derived in section 2.2 around resonant frequency. To validate the correctness of the complete PT models, the input admittance characteristics of the PTs are carefully tuned to agree with those of measurement results. Then the calculated voltage gain and efficiency of the PT models are compared with the experimental results for HVPT-2 and LVPT-21, respectively.

2.4.1 Longitudinal mode PT : HVPT-2

2.4.1.1 Complete Model of HVPT-2

The general characteristics of HVPT-2 are listed below:

- Type : Rosen type (single layer, no isolation),
- Power handling : 3 - 6 Watts,
- Series resonant frequency : about 73 kHz (no load),
- Step up ratio : 1:9 when it is terminated with a 200 kΩ resistor, and
- Size : $50 \times 8 \times 1.5 \left(\mathrm{L} \times \mathrm{W} \times \mathrm{T}, \text{ all in mm} \right)$.

Figure 2.8 (a). illustrates the G-B plot of HVPT-2 with output terminals shorted. The electrical equivalent circuit of HVPT-2 is calculated by extracting useful parameters via the measurement data such as fs, fr, fa, and Gmax, and is drawn in Fig. 2.8 (b). Figure 2.8 (c). shows the calculated and measured input admittance of HVPT-2. Because the curves of calculated and measured input admittances coincide with each other, there is no need to improve the model any further. MCAD programs are used to determine the equivalent circuits of HVPT-2 as well as LVPT-21 and are listed in appendix D.

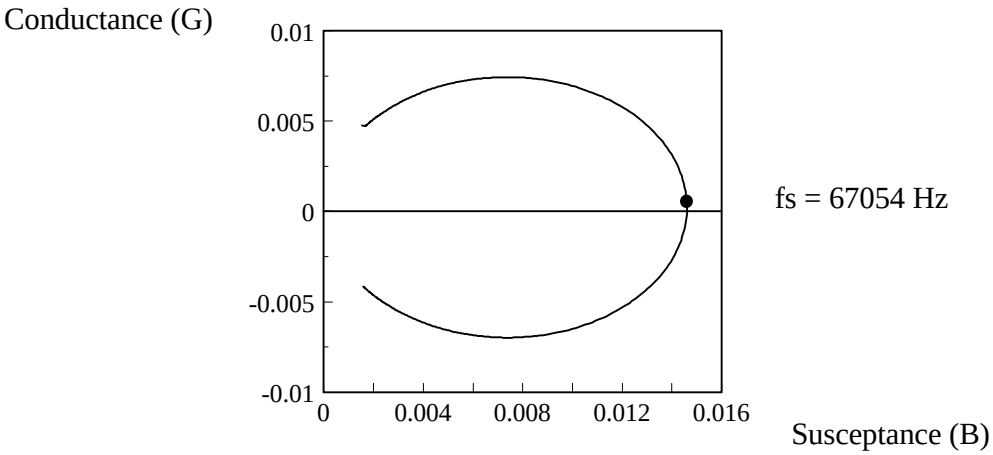

(a)

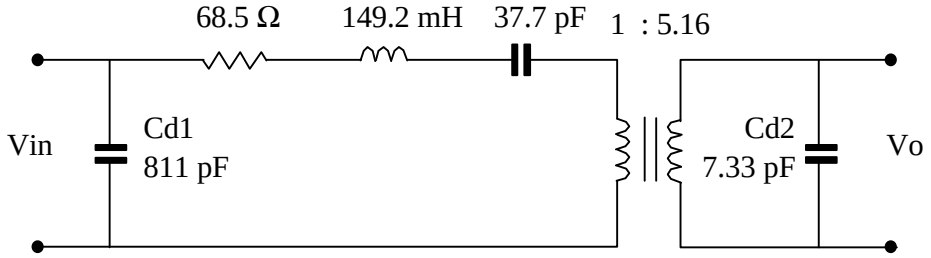

(b)

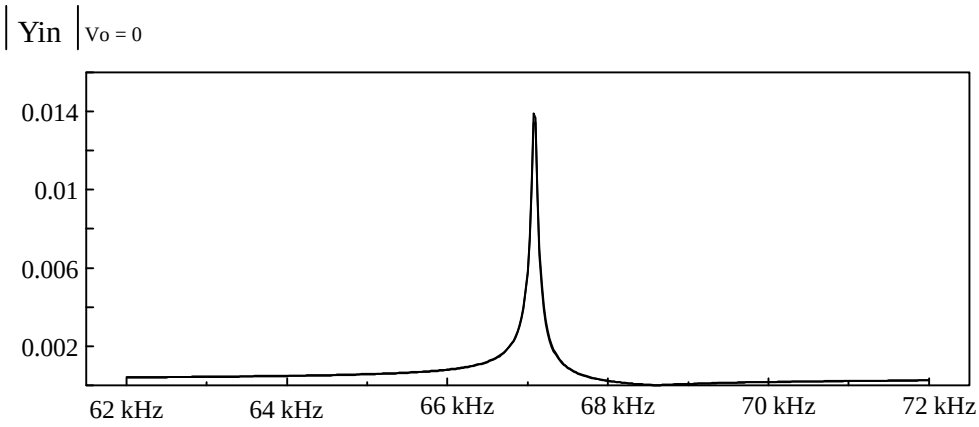

(c)

Fig. 2. 8. Admittance circle measurement and the electrical equivalent circuit of HVPT-2. (a) admittance circle measurement. (b) model of HVPT-2. (c) calculated and measured input admittances. For longitudinal PTs, the model, originated from their physical modeling around fs, can duplicate their characteristics faithfully when admittance circle measurement technique is adopted to calculate parameters of the equivalent circuits.

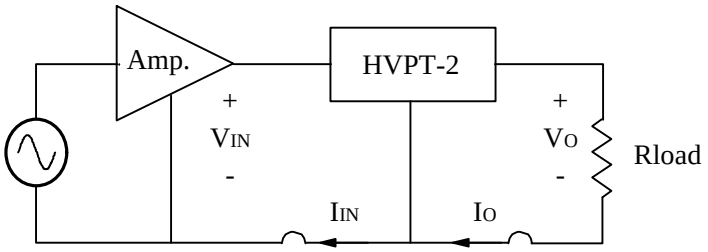

(a)

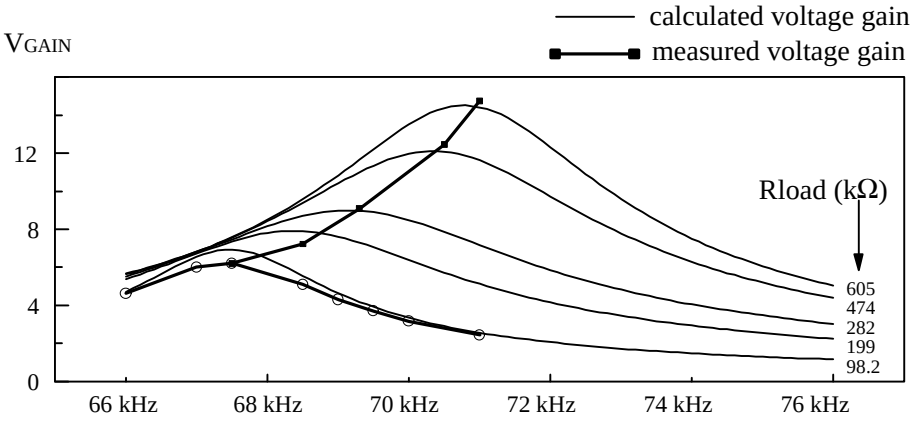

(b)

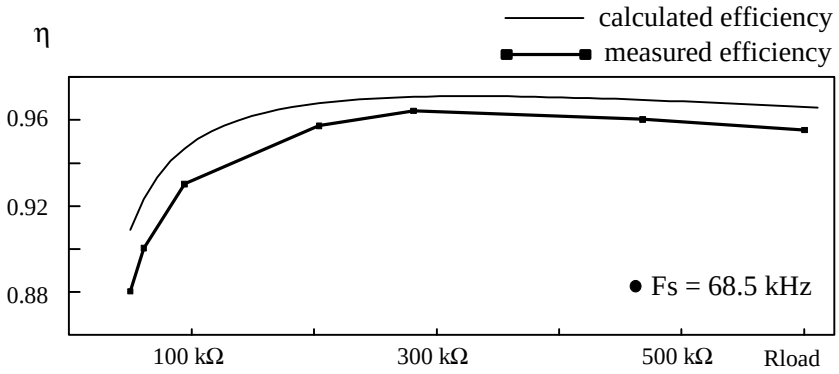

(c)

Fig. 2. 9. Voltage gain and efficiency of HVPT-2. (a) test setup. (b) measured and calculated voltage gain. (c) measured and calculated efficiency. The black solid squares in (b) indicate that the measured peak gains agree with calculated peak gains under different Rload. Moreover, the calculated and measured efficiency curves are similar with 1% ~ 2% difference. It demonstrates the accuracy of the model for HVPT-2.

2.4.1.2 Experimental Verifications

To verify the input admittance and voltage gain of the PT under high-power test, the same test-setup employing impedance analyzer under signal power level is followed. Additionally, the input reference source of the impedance analyzer is first amplified before connecting to the device under test, as shown in Fig. 2.9 (a). Voltage gain and efficiency are defined as

$$\text{Voltage gain} = V_{GAIN} = \frac{V_o(\text{rms})}{V_{IN}(\text{rms})} \; ; \tag{2.42}$$

$$\text{Efficiency} = \eta = \frac{I_o(\text{rms})^2 \cdot \text{Rload}}{V_{IN}(\text{rms}) \cdot I_{IN}(\text{rms}) \cdot \cos\theta} \; ; \tag{2.43}$$

$$V_o(\text{rms}) = I_o(\text{rms}) \cdot \text{Rload} \, , \tag{2.44}$$

where

θ = angle between V_{IN} and I_{IN}.

Figure 2.9 (b). shows the frequency vs. voltage-gain curves measured for several load resistances. It is important to notify that for each load resistance, the maximal voltage gain matches a designated operating frequency.

Figure 2.9 (c). illustrates the calculated and measured load-efficiency curves. Theoretically, the load vs. efficiency curves of the HVPT should not change much when the operating frequency is the running parameter and stays around the series resonance frequency, fs. However, from the measurement data, several interesting results have been observed. The maximal efficiency always occurs when the resistive load equals the output impedance of the HVPT, approximately 330 kΩ. The efficiency of the PT decreases when the operating frequency increases. The lower the load resistance, the lower the efficiency. The last two effects are due to the increased dielectric loss when θ increases or reactive power increases.

The other important factor which will affect the efficiency of an HVPT is its support points. For a full-wave mode operation, when the support points are moved from the nodes where displacement of the HVPT is zero, the efficiency of the HVPT drops at least 5%. Due to high efficiency of the HVPT, the heat generation is insignificant for low-power applications, and it is possible to hold the HVPT in a box and to support it firmly at nodes. In such a way, the HVPT can be treated as a step-up device with input and output electrodes and becomes a promising component for automation.

2.4.2 Thickness Extensional PTs : LVPT-21

2.4.2.1 Two-Port Network Representation of LVPT-21

Two-port network representation of LVPT-21 is certainly the best empirical model. It is easy to convert to any type of linear two-port parameters from S parameters measured by network analyzer, because the operating frequency of thickness extensional PTs is in the MHz range, and their input and output impedances are close to 50 Ω. On the other hand, the output impedance of the longitudinal PT is within hundred kilo Ω. It is inappropriate to measure the two port parameters of the longitudinal PT in the 50-Ω system. Usually, the input admittance of the longitudinal PT is measured by impedance analyzer, and it is also true for the thickness extensional PT. However, with the help of two-port parameters, the efficiency and voltage gain of the PTs can be calculated directly and they provide useful methods to interconnect the peripheral circuits of the PTs, such as power amplifiers and load networks. Accordingly, the performance of the model can be verified with two-port parameters in low-power operation and with direct measurement in high-power operation.

To perform the admittance circle measurement at high-frequency operation, Y parameters are selected. Y_{11} is the input admittance with one end shorted and is the information needed by admittance circle measurement technique. With Y parameters, the voltage gain and efficiency of the two-port network are

$$\text{Voltage gain} = V_{GAIN} = \frac{-Y_{21}}{Y_L + Y_{22}} \text{ and} \tag{2.45}$$

$$\text{Efficiency} = \eta = \frac{Pout}{Pin} = \left|V_{GAIN}\right|^2 \cdot \frac{\text{Re}\left[Y_L\right]}{\text{Re}\left[Y_{IN}\right]}\ , \tag{2.46}$$

where Y_L is the load admittance of the PT and input admittance with arbitrary load is

$$Y_{IN} = Y_{11} + Y_{12} \cdot V_{GAIN}\ , \tag{2.47}$$

where input voltage of the PT is set to unity.

2.4.2.2 Complete Model of LVPT-21

The general characteristics of HVPT-2 are listed below:

- Type : Thickness extensional mode (multilayer layers, isolated input and output),
- Power handling : 10 - 15 Watts,
- Series-resonant frequency : about 1.88 MHz (shorted at one end),
- Step down ratio : 2:1 when it is terminated with an 8-Ω resistor, and
- Size : $20 \times 20 \times 2\ (\text{L} \times \text{W} \times \text{T, all in mm})$.

Figure 2.10 (a). illustrates the G-B plot of LVPT-21 with one end shorted. Besides the fundamental admittance circle whose series-resonant frequency is fs, there are three small circles,

having series-resonance frequencies, f1s, f2s, and f3s. The electrical equivalent circuit of LVPT-21 characterized by the fundamental circle is shown in Fig. 2.10 (b). As a result, the calculated input admittance curve with one end shorted doesn't agree with that of the measurement as shown in Fig. 2.10 (c). The series-resonant frequency of the PT will move to higher operating frequencies, as shown in Fig. 2. 9 (b), when the load resistance increases. Moreover, the unwanted spurious vibrations will affect the efficiency of the PT around their resonance frequencies. To obtain a useful model of LVPT-21, the characteristics of calculated admittance from the electrical equivalent circuit must agree with those from measurement results for a wide frequency range. Therefore, those small admittance circles need to be modeled and can be represented as additional series R-L-C branches in parallel with the fundamental branch.

From the G-B plot in Fig. 2.10 (a), the admittance circles having the resonant frequencies fs1, fs2, and fs3 do not intercept with the G-axis. To calculate the parameters of these spurious vibrations, (2.37) to (2.40) are employed. Although those small admittance circles are not perfect circles[35], f_{-45} and f_{+45} are replaced with the frequencies, where maximum and minimum susceptances occur, respectively. The measured data for constructing three small admittance circles is presented in Fig. 2.11 (a). The final complete model of LVPT-21, shown in Fig. 2.11 (b), is tuned to curve-fit the measured curve of input admittance illustrated in Fig. 2. 11 (c).

2.4.2.3 Experimental Verifications

Employing a similar test setup as the one shown in Fig. 2.9 (a)., Fig. 2.12 (a) shows the calculated voltage-gain curve of the model with the fundamental branch only and the calculated voltage-gain curve according to the measured Y parameters. Apparently, a lot of information is lost in the former curve. When the complete model for LVPT-21 is adopted, both the calculated voltage-gain curves and measured high-power curve are shown in Figs. 2.12 (b) and (c) with 7.5-Ω and 20-Ω load resistors, respectively. The error between the measured high-power V_{GAIN} and calculated V_{GAIN} according to the measured Y parameters is within 2.5 %. This confirms the accuracy of the model and the high-power voltage-gain measurement. At the same time, the calculated voltage-gain curve of the complete model has the similar shape as the measured curve.

Figure 2.13 (a). illustrates the two calculated efficiency curves of LVPT-21 when it is modeled with the fundamental mode only. Three efficiency curves, shown in Fig. 2.13 (b)., for LVPT-21 terminated with a 20 ohm resistor are measured under high-power (2.5 Watts), calculated according to the measured Y parameters, which is drawn in dark black color, and generated from the complete model shown in Fig. 2.11 (a). Figure 2.13 (c) illustrates the other three efficiency curves when the load resistance of LVPT-21 is 7.44 ohm. From Figs. 2.13 (b) and (c), the efficiency of LVPT-21 calculated from the complete model can predict the measured efficiency correctly within a wide frequency range. It can be observed that the efficiency of the PT is load-dependent. How to operate the PT efficiently becomes an important issue. Therefore, in the next chapter, the objective is to use the complete models for HVPT-2 and LVPT-21 as examples to find out the optimal load for the longitudinal and thickness mode PTs.

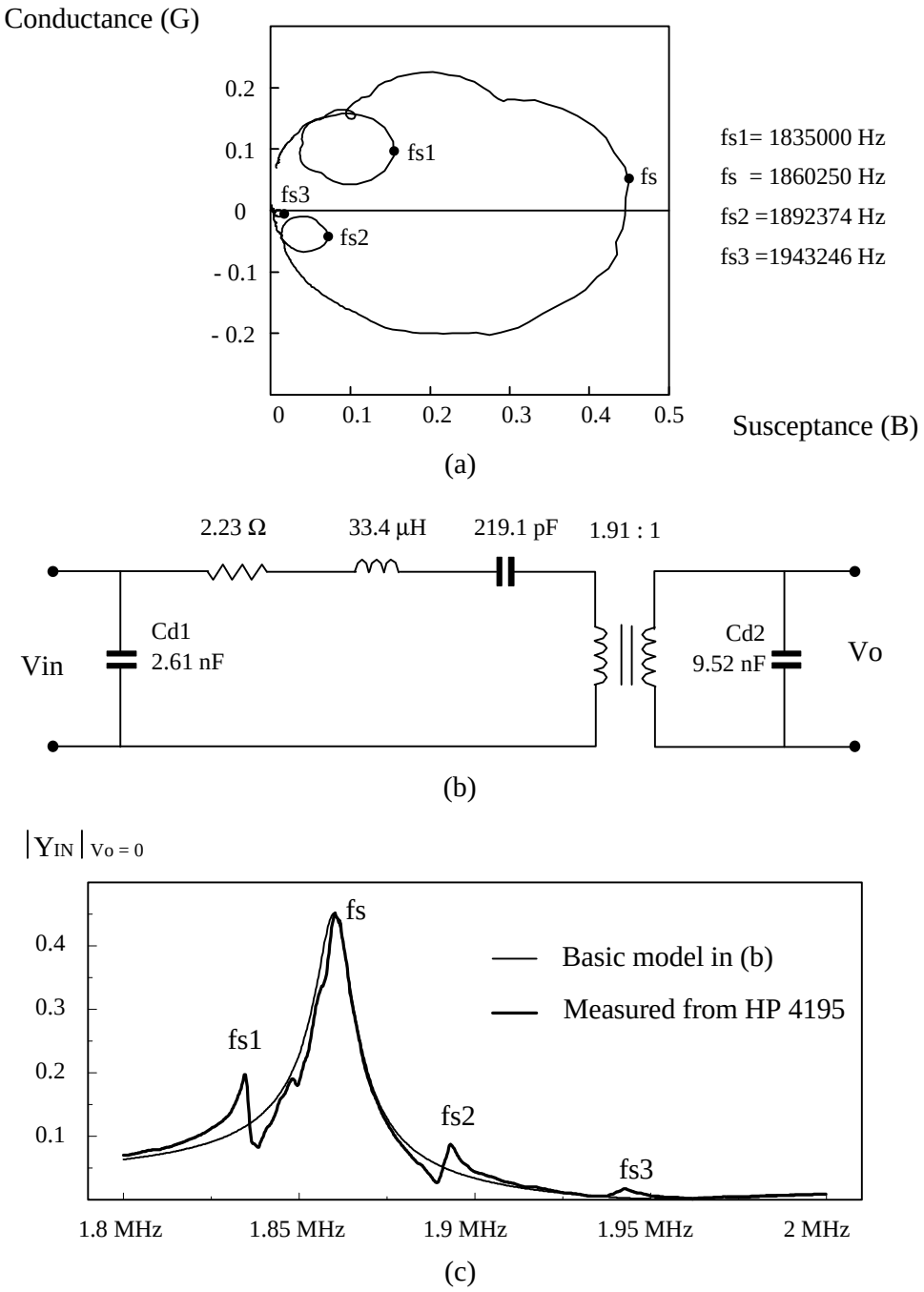

Fig. 2. 10. G-B plot and basic model of LVPT-21. (a) admittance circle measurement when Vo = 0. (b) basic model of LVPT-21. (c) calculated and measured input admittance. The spurious vibration near fs is caused by the electromechanical coupling coefficient k_{31} which results ins unwanted vibration perpendicular to the thickness direction. For thickness mode PTs, the basic model cannot predict the admittance characteristics of LVPT-21.

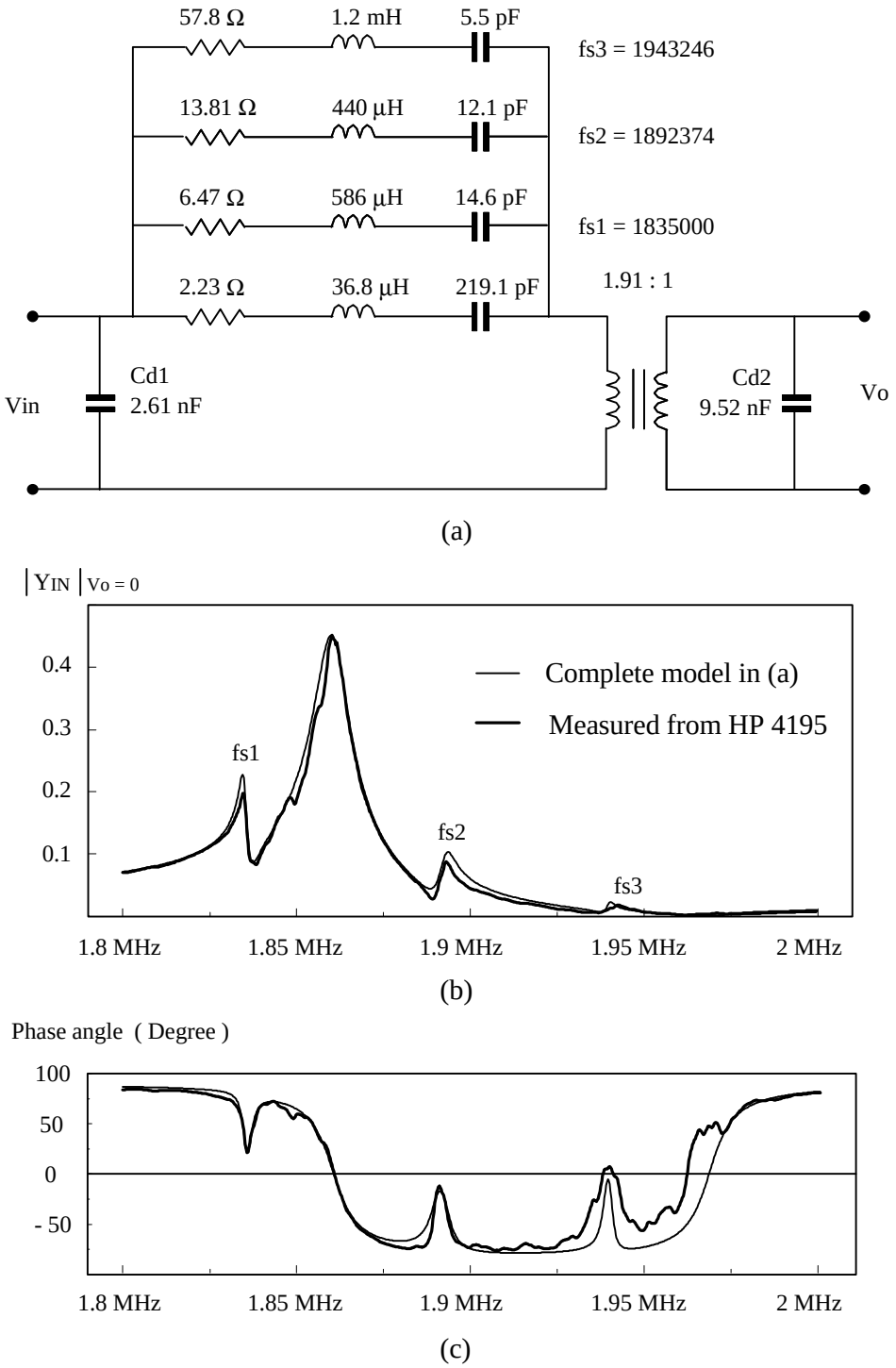

Fig. 2. 11. Complete model of LVPT-21 and its characteristics. (a) complete model of LVPT-21. (b) calculated and measured input admittance. (c) calculated and measured phase angles of input admittance.

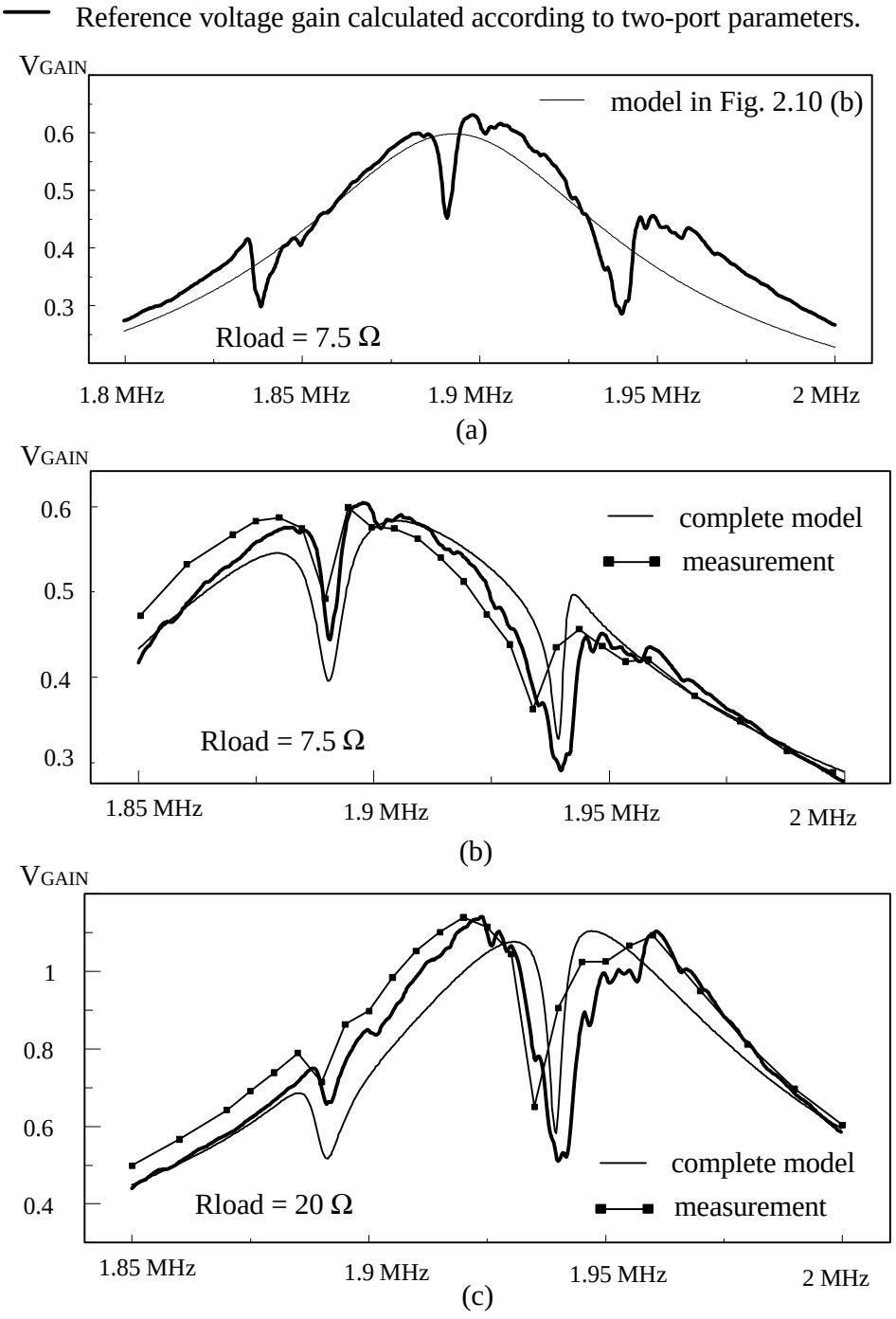

Fig. 2. 12. Experimental and theoretical voltage gain of LVPT-21. (a) fundamental model (b) Rload = 7.5 Ω. (c) Rload = 20 Ω. The higher the load resistance, the higher the voltage gain. Since the voltage-gain curves are monotonous only in several piecewise regions, constant-frequency control is preferred to control voltage gain of LVPT-21.

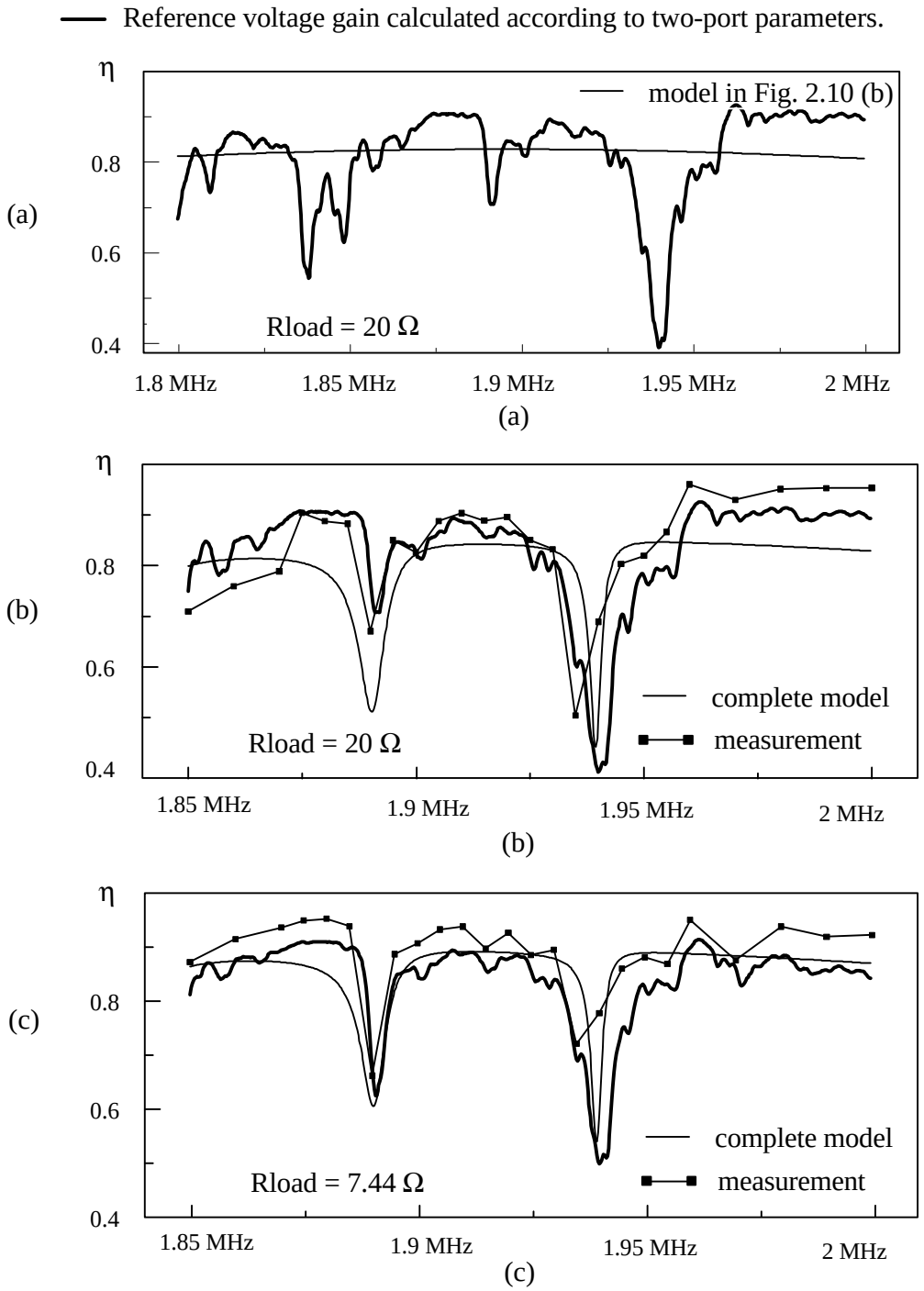

Fig. 2. 13. Experimental and theoretical efficiency of LVPT-21. (a) fundamental model (b) Rload = 20 Ω. (c) Rload = 7.44 Ω. When LVPT-21 is terminated with resistive loads, the efficiency in (b) is lower than that in (c). Therefore, a method is developed to obtain the optimal load where the efficiency of the PT is maximized.

2.5 Summary and Conclusion

The complete models for longitudinal and thickness mode PTs are verified from their input admittance characteristics with one end shorted and performance characteristics including voltage gains and efficiencies. Both complete models have proved their usefulness on component level for simulating their voltage gains and efficiencies via electrical equivalent circuits. The model for the longitudinal PT is simple and can be derived from its fundamental branch because of no additional spurious vibration around fs. However, the complete model for the thickness extensional PT is very complicated due to the unwanted spurious vibrations generated by the electromechanical coupling coefficient k_{31}. Because there is not yet a good method to eliminate all unwanted spurious vibrations in manufacturing, including spurious vibrations in the model is necessary for simulation purposes. As a result, several bands of operating frequencies can be determined, and the efficiency of the PTs can be optimized over one of the frequency bands.

A study of electrical equivalent circuits for the PTs with regard to mechanical vibrations and related mechanical losses gives a better understanding of how the PTs work. The detailed derivation of models for the PTs is shown in Appendix A. This work suggests that it is possible to design a stacked PT with any desired transformer ratio for different applications by using a simulation tool.

3. Design of Matching Networks

3.1 Introduction

From the characteristics of the PTs, it follows that the efficiency of the PTs is a strong function of load and frequency. Due to the large intrinsic capacitors, it is essential to add inductive loads to the PT [5] to obtain a satisfactory efficiency for the PT and amplifiers. It has been established in [40] that the power gain (or efficiency) of a two-port network (or the PT) is determined by its load termination and properties of the two-port network only. And so is the input impedance of the terminated two-port network. Figure 3.1 shows a complete block diagram of a dc/dc converter employing the PT. It is important to choose the design procedure so as to obtain the maximum efficiency of the converter. The algorithm for designing a PT converter or inverter is to calculate the optimal load termination, Y_{OPT}, of the PT first so that the efficiency (power gain) of the PT is maximized. And then the efficiency of the dc/ac inverter is optimized according to the input impedance, Z_{IN}, of the PT with an optimal load termination.

The load resistance, R_L, is decided according to the output specifications of the dc/dc converter. Then the equivalent resistance, R_{EQ} of the nonlinear rectifier load is obtained for different rectifier circuits. For a given PT, an optimal termination, Z_{OPT}, is calculated and decided by the power-flow method. Obviously, R_{EQ} will not equal Z_{OPT} unless the PT is designed for this application. With the help of an output matching network (OMN), the optimal termination of the PT matches the equivalent resistance of the rectifier circuit.

Designing the input matching network (IMN) depends on two parameters. One is the input impedance, Z_{IN}, of the PT with an optimal load, which can be calculated directly. The other parameter is the output impedance, Z_O, of the switching amplifiers, which is different from the usual 50 Ω of regular radio-frequency amplifiers. Because the output impedance of the switching amplifiers is so low, the objective of the IMN is to alleviate the circulating current in the amplifiers and input of the PT. In other words, the IMN could be an inductive network designed to cancel the capacitive impedance seen at the input port of the PT.

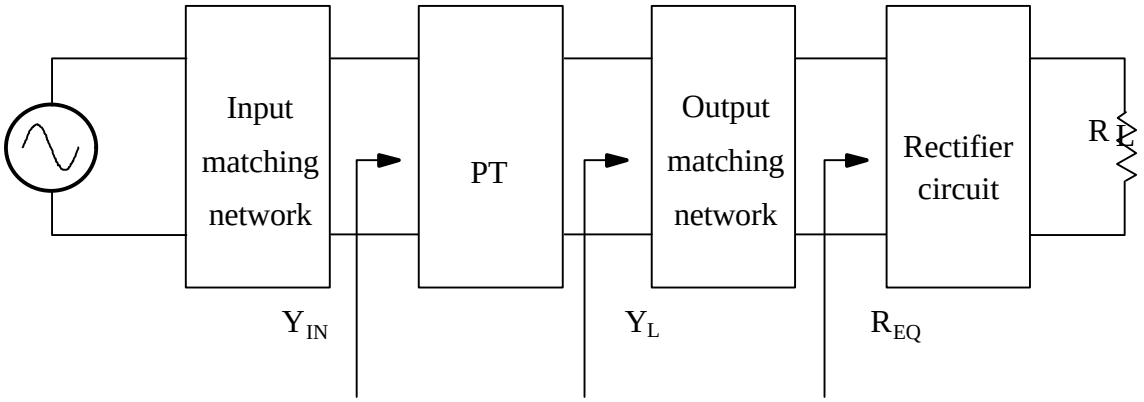

- PT : Piezoelectric Transformer

Fig. 3.1. Complete dc/dc converter with the PT and its matching networks. It is important to operate the PT efficiently and draw as much power as possible from the source amplifier. The design procedure for PT converters is to decide the optimal terminations Y_{LOPT} of the PT and to design the output matching network OMN accordingly. The efficiency of the dc/ac inverter is optimized according to the input admittance Y_{IN} of the PT with an optimal load termination. Therefore, the objective of the input matching network IMN is to reduce the circulating current between the PT and dc/ac inverter so that the efficiencies of both the PT and inverter are optimized and maximum power can be delivered to the load.

In the beginning of this chapter, a unified method, or power-flow method, was discussed to obtain the best efficiency for both the longitudinal mode and the thickness extension mode PTs. Later, the output matching networks, input matching network, and load characteristics for the PTs are calculated.

3.2 Output Matching Networks

The objectives of the output matching networks are to maximize the efficiency of the PTs and to reduce the reactive power flow in both input and output of the PTs.

3.2.1 Power Flow Method

Using the two-port power flow model [40,41], the maximum efficiency of the PT is determined at the specific load condition. The power flow model exploits the relationships between input and output power in a linear two-port network. Instead of using two-port z, y, or h matrices, a 2D Cartesian coordinate system with L and M axes is adopted. The (L,M) coordinate system, or L-M plane, is defined around the neighborhood where the load admittance is a complex conjugate of the output admittance of the PT with an opened input port, Y_{22}. Under

this condition, the input and output power of the PT can be easily calculated in the L-M plane, and show simple geometry in the L-M plane. By using the simple geometry of input and output power in the L-M plane, an intuitive method is developed to calculate the optimal load termination for the PTs.

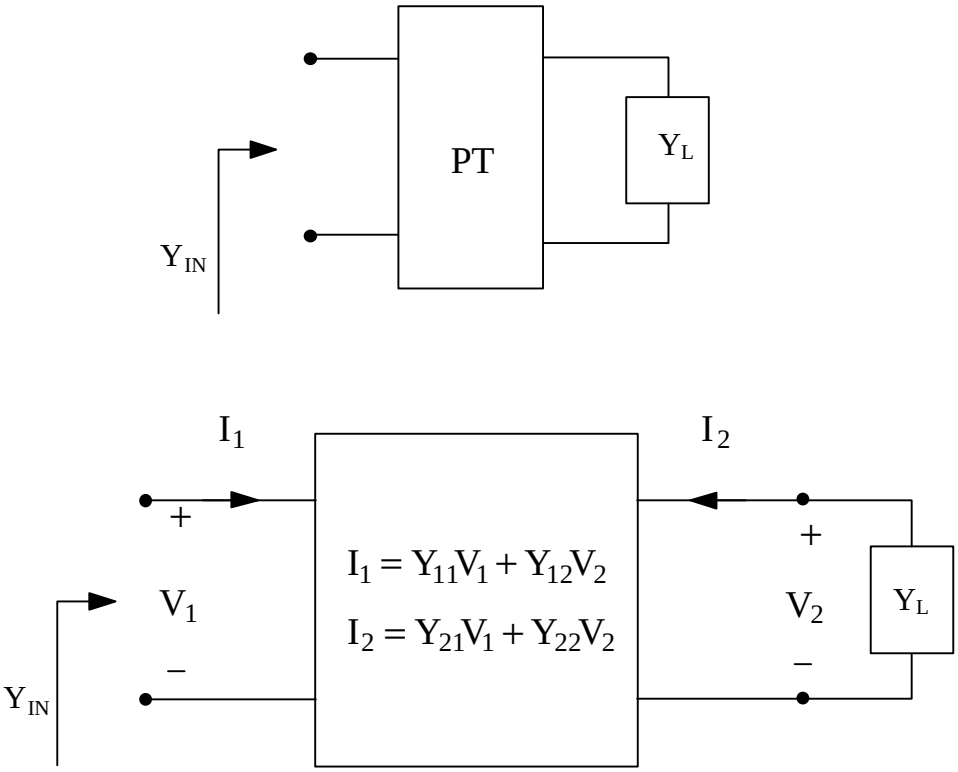

$y_{11} = 0.3641 + j\ 0.3038$

$y_{21} = 0.3602 + j\ 0.1908$

$y_{12} = 0.3602 + j\ 0.1908$

$y_{22} = 0.3588 + j\ 0.3242$

Fig. 3. 2. Two-port network representation of PTs and the sampled Y parameters at fs. The Y parameters of the PT are converted from S parameters measured from the network analyzer and can represent accurate characteristics of the PT. A set of Y parameters is given at fs of a 1:1 acoustic filter transformer for quantitative discussion about the power flow method to decide the optimal Y_L.

3.2.1.1 Input Power Plane

In order to illustrate how the power flow model works, the Y parameters for an 1:1 acoustic filter transformer are given at fs [19]. Usually, this method can calculate the efficiency of a two-port network at one frequency at a time and needs to be repeated at different frequencies to cover the operating frequency range of interest. Figure 3.2. shows the diagram of the two-port network and its notations, as well as the values for the Y parameters at fs. However, the choice of Y-parameter modeling is arbitrary, and the Y-parameters are transformed from the S-parameters of the PT which are measured from a network analyzer. The linear two-port network is represented by Y-parameters in (3.1):

$$\begin{aligned} I_1 &= Y_{11}V_1 + Y_{12}V_2 \ , \\ I_2 &= Y_{21}V_1 + Y_{22}V_2 \ . \end{aligned} \tag{3.1}$$

V_2 is formulated as a function of L and M [40] in (3.1):

$$\frac{V_2}{V_1} = \frac{Y_{21}}{\frac{I_2}{V_2} - Y_{22}} = \frac{-Y_{21}}{2\,\mathrm{Re}\left[Y_{22}\right]} \cdot (L + jM) \ , \tag{3.2}$$

which is derived from (3.1) directly, and

$$Y_L = -\frac{I_2}{V_2} \ . \tag{3.3}$$

When (L,M) = (1,0), Y_L is equal to the complex conjugate of Y_{22}. Due to linearity, let V_1=1 + j0. The normalized input power ,Pin, shown in Fig. 3.3. is expressed as:

$$\frac{V_2}{V_1} = \frac{Y_{21}}{\frac{I_2}{V_2} - Y_{22}} = \frac{-Y_{21}}{2\,\mathrm{Re}\left[Y_{22}\right]} \cdot (L + jM) \ , \tag{3.3}$$

$$\mathrm{Pin}(L,M) = \left| V_1 \right|^2 \mathrm{Re}\left[Y_{IN}\right] = g_{11} - \frac{aL - bM}{2g_{22}} \ , \tag{3.4}$$

where

$$Y_{IN} = \frac{I_1}{V_1} = Y_{11} + Y_{12} \cdot V_2 = Y_{11} + Y_{12} \cdot \frac{-Y_{21}}{2\,\mathrm{Re}\left[Y_{22}\right]} \cdot (L + jM) \ , \tag{3.5}$$

and

$$Y_{12}\,Y_{21} = a + jb \quad \text{and} \quad Y_{ij} = g_{ij} + jb_{ij} . \tag{3.6}$$

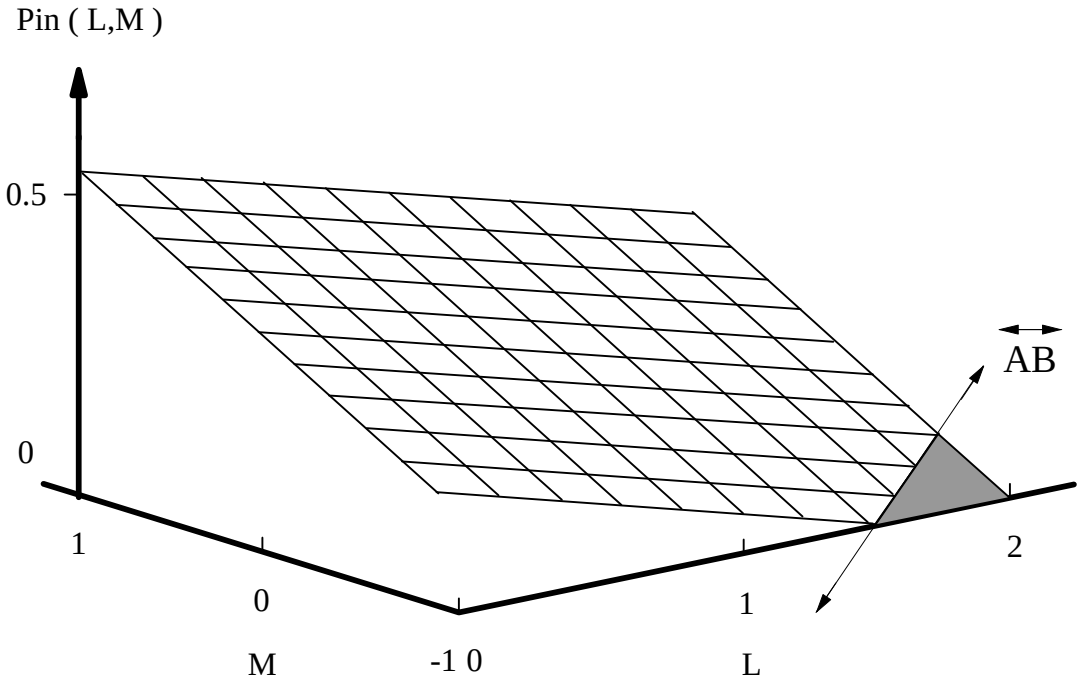

$$\text{Pin}\,(L, M) = |V_1|^2\ \text{Re}\left[Y_{IN}\right] = g_{11} - \frac{aL - bM}{2g_{22}}$$

$$Y_{12}\,Y_{21} = a + jb \quad \text{and} \quad Y_{ij} = g_{ij} + jb_{ij}$$

$$L + jM = \frac{2g_{22}}{Y_L + Y_{22}}$$

Fig. 3. 3. Input power plane in the L-M plane. Line AB is the contour of zero input power in the L-M plane. The line function is aL - bM -2 g11 g22 = 0 and the slope is a/b. The magnitude of the three-dimensional plot is calculated according to y parameters at fs of the 1:1 acoustic filter transformer used as an example.

3.2.1.2 Output Power Plane

The normalized power delivered to the output port of the PT, Pout, can be expressed in the L-M plane as:

$$\text{Pout} = |V_2|^2\ \text{Re}\left[Y_L\right] = |V_2|^2\ \text{Re}\left[\frac{-I_2}{V_2}\right], \tag{3.7}$$

where

$$\frac{-I_2}{V_2} = Y_L = -Y_{22} + \frac{2g_{22}}{L + jM}\ , \tag{3.8}$$

and

$$Y_L = G_L(L,M) + jB_L(L,M) \ . \tag{3.9}$$

Substituting (3.8) into (3.7) yields

$$Pout(L,M) = Poo\left[1-(L-1)^2 - M^2\right] , \tag{3.10}$$

where

$$Poo = Pout(1,0) = \frac{|Y_{21}|^2}{4g_{22}} \ . \tag{3.11}$$

Since the PT is a passive device, the input power, Pin, is always greater than the output power, Pout. The output power surface drawn in Fig. 3.4. forms a paraboloid centered at (L,M) = (1,0), where maximum output power occurs.

3.2.1.3 Maximal Efficiency

Figure 3.5. shows the efficiency in 3D plot. It is very difficult to find an analytical solution for the maximal efficiency in the L-M plane. With the knowledge of the simple geometry for the input and output power surfaces, Fig. 3.6. shows the mapped contours of the output-power surface and the intersection line, $\overline{AB}$, of the input plane in the L-M plane. The function of line $\overline{AB}$ in the L-M plane is

$$aL - bM - 2\cdot g_{11}\, g_{22} = 0 \ , \tag{3.12}$$

which is obtained by substituting Pin(L,M) = 0 into (3.4) and its slope = a/b. The maximal efficiency of the two-port network occurs along one of the lines passing through (L,M) = (1,0) and confined to the unit circle, as shown by the dotted line in Fig. 3.6. Obviously, the maximal efficiency of the two-port network will occur along the line segment from point O to point C, and its slope is defined as tan(180-θ). Because line $\overline{OC}$ is perpendicular to line $\overline{AB}$, it follows that

$$\tan(180-\theta)\cdot\frac{a}{b} = -1 \ , \tag{3.13}$$

or

$$\tan\theta = \frac{b}{a} = \frac{Im[Y_{12}Y_{21}]}{Re[Y_{12}Y_{21}]} \ . \tag{3.14}$$

To simplify the analysis, line $\overline{OC}$ is defined as x axis. The relationships between (L,M) and (x,θ) are :

$$L = 1 + \left(-x\cdot\cos\theta\right) = 1 - x\cdot\cos\theta = 1 - x\frac{Re(Y_{12}Y_{21})}{\sqrt{a^2+b^2}} \tag{3.15}$$

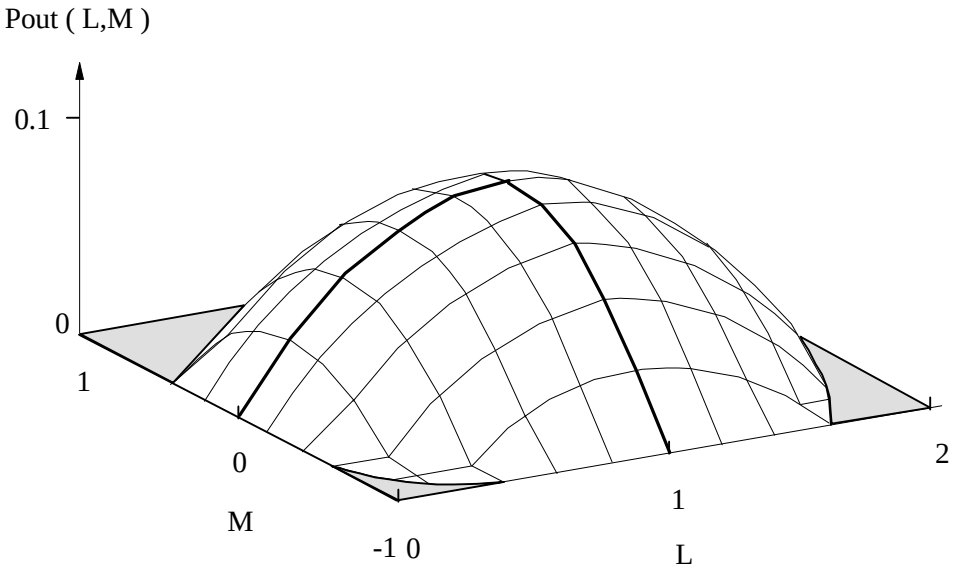

Fig. 3. 4. Output power plane in the L-M plane. The output power surface forms a paraboloid centered at (L,M) = (1,0), where maximum output power occurs and the load admittance $Y_L = y22^*$. The contours of the output power plane are circles with center (L,M) = (1,0) in the L-M plane.

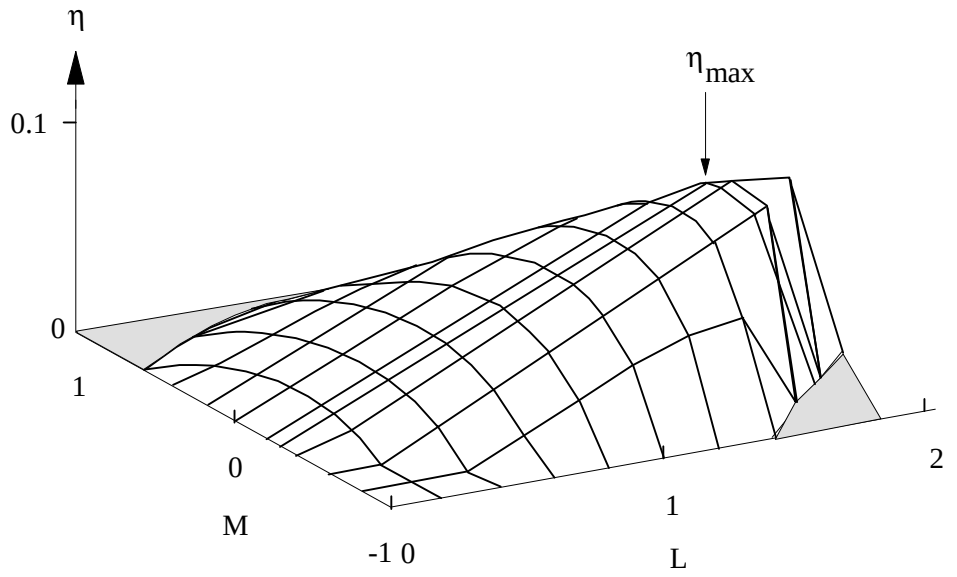

Fig. 3. 5. Efficiency plot in the L-M plane. Although it is very difficult to find an analytical solution for the maximal efficiency in the L-M plane directly, the simple geometry of the input and output planes makes it possible to analyze the efficiency of the two-port network systematically.

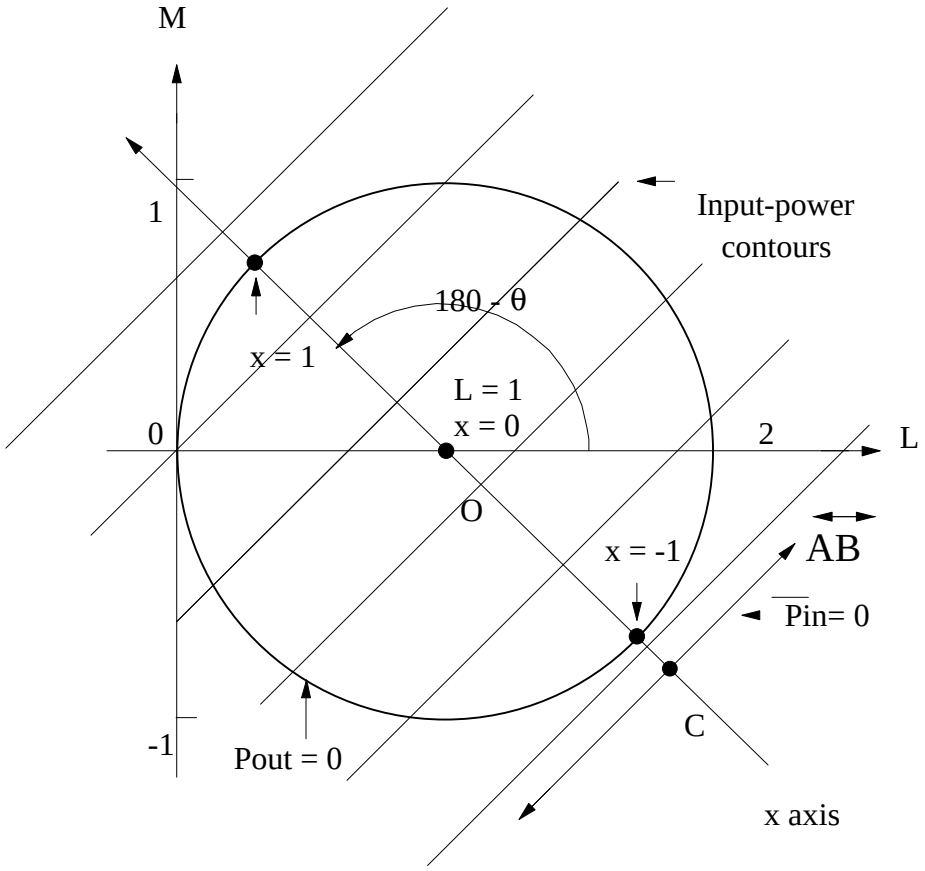

$$L = 1 - x \cdot \cos\theta = 1 - x \frac{\mathrm{Re}\,(Y_{12}Y_{21})}{\sqrt{a^2 + b^2}}$$

$$M = x \cdot \sin\theta = x \frac{\mathrm{Im}(Y_{12}Y_{21})}{\sqrt{a^2 + b^2}}$$

Fig. 3. 6. Mapped contours of the input and output planes. The maximum efficiency of the two-port network will occur along the line segment from point O to point C, and its slope is defined as tan(180-θ). As a result, L and M can be represented by the functions x only, and the analysis is further simplified.

and

$$M = x \cdot \sin\theta = x\frac{\mathrm{Im}(Y_{12}Y_{21})}{\sqrt{a^2+b^2}} \ . \tag{3.16}$$

Figure 3.7. shows the side view of the input and output plane cut by the plane, which is vertical to the L-M plane and contains line $\overline{OC}$. Substituting (3.15) and (3.16) into (3.10), the output power surface in L-M plane is simplified to a parabolic curve along x axis which is shown in Fig. 3.7.

$$\mathrm{Pout}(L,M) = \mathrm{Pout}(x,\theta) = \mathrm{Pout}(x) = \mathrm{Poo}(1-x^2) \tag{3.17}$$

The lengths of $\overline{OC}$ and $\overline{OD}$ are equal to

$$\left|\overline{OC}\right| = \frac{\left|a - 2\cdot g_{11}g_{22}\right|}{\sqrt{a^2+b^2}} \text{ and} \tag{3.18}$$

$$\left|\overline{OD}\right| = \mathrm{Pio} = \mathrm{Pin}(1,0) = g_{11} - \frac{a}{2g_{22}} \ . \tag{3.19}$$

The function of line $\overline{CD}$ is decided by ($\left|\overline{OC}\right|$,0) and (0, $\left|\overline{OD}\right|$).

$$\mathrm{Pin}(x) = \mathrm{Pio}\,(1+\frac{1}{\left|\overline{OC}\right|}x) = \mathrm{Pio}\,(1+cx) \ , \tag{3.20}$$

where

$$c = \frac{1}{\left|\overline{OC}\right|} = \frac{\sqrt{a^2+b^2}}{\left|a-2\cdot g_{11}g_{22}\right|} \ , \tag{3.21}$$

and c is a positive constant. When Pin(x) = 0, x = -1/c. If x fell into the unit circle, the system would be unstable because Pin could be negative, while Pout would still remain than zero. In other words, the system is stable if

$$0 < c < 1 \ . \tag{3.22}$$

The efficiency of the PT is

$$\eta = \frac{\mathrm{Pout}(x)}{\mathrm{pin}(x)} = \frac{\mathrm{Poo}\cdot(1-x^2)}{\mathrm{Pio}\cdot(1+cx)} \ . \tag{3.23}$$

The efficiency of the PT reaches its maximum at x_0, where the first derivative of (3.23) is equal to zero.

$$x_o = \frac{-1+\sqrt{1-c^2}}{c} \quad . \tag{3.24}$$

L_0 and M_0 can be calculated from (3.15) and (3.16), employing $x = x_0$. Once the values of L and M are determined for maximizing the efficiency, the load admittance is calculated by using

$$G_L = -g_{22}\left(1-\frac{2\cdot L}{L^2+M^2}\right) \text{ and} \tag{3.25}$$

$$B_L = -\left(b_{22}+\frac{2\cdot g_{22}}{L^2+M^2}\cdot M\right) . \tag{3.26}$$

3.2.2 Adjustment of the Power-Flow Method for PTs

For longitudinal mode PTs, the dielectric losses for Cd1 and Cd2 are usually insignificant compared to the mechanical loss R in the electrical equivalent circuit. The lumped circuit of the PT shown in Fig. 3. 8 (a)., does not include the parallel resistors at the input and output terminals of the PT. The Y parameters of this lumped circuit can be expressed as:

$$Y_{11} = j\omega Cd1 + \frac{1}{Z_M} \tag{3.27.a}$$

$$Y_{21} = Y_{12} = \frac{-1}{n\cdot Z_M} \tag{3.27.b}$$

$$Y_{22} = j\omega Cd2 + \frac{1}{n^2 Z_M} \ , \tag{3.27.c}$$

where Z_M is the impedance of the mechanical branch and is defined as

$$\frac{1}{Z_M} = \alpha_M + j\cdot\beta_M \quad . \tag{3.28}$$

The Linvill constant c in (3.21) becomes

$$c = \frac{\sqrt{a^2+b^2}}{\left|a-2g_{11}\cdot g_{22}\right|} = \frac{{\alpha_M}^2+{\beta_M}^2}{\left|\left({\alpha_M}^2-{\beta_M}^2\right)-2\,{\alpha_M}^2\right|} = 1 \ , \tag{3.29}$$

where $g_{11} = \alpha_M$, $g_{22} = \alpha_M/n^2$, $a = {\alpha_M}^2 - {\beta_M}^2$, and $b = 2\alpha_M\beta_M$ from (3.6). When c = 1, it indicates that $x_o = -1$ from (3.24). Meanwhile, $L_o = 1+\cos\theta$ and $M_o = \sin\theta$; L_o and M_o are calculated from (3.15) and (3.16), respectively. To calculate optimal load admittance $Y_{LOPT} = G_{LOPT} + j\,B_{LOPT}$, L_o and M_o need to be substituted into (3.25) and (3.26) to obtain

$$G_{LOPT} = -g_{22}\left(1 - \frac{2 \cdot L_o}{L_o^{\,2} + M_o^{\,2}}\right) = 0 \text{ and} \tag{2.29.a}$$

$$B_{LOPT} = -\left(b_{22} + \frac{2 \cdot g_{22}}{L_o^{\,2} + M_o^{\,2}} \cdot M_o\right) = -\omega \cdot Cd2 \ . \tag{3.29.b}$$

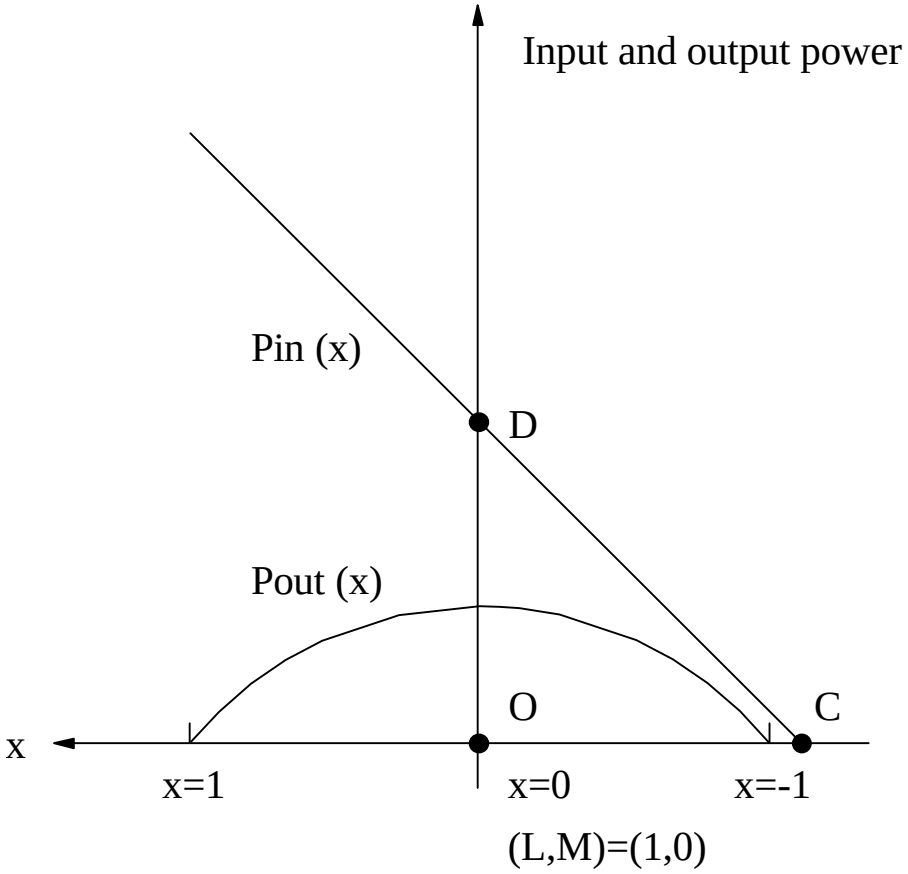

Fig. 3. 7. Side views of the input and output planes on x-axis. The side views are cut by the plane, which is vertical to the L-M plane and contains line segment OC. The input and output power curves are functions of x only. Therefore, the efficiency curve is also a function of x. η_{MAX} is calculated when $\eta'(x) = 0$ and $x = x_o$. Then L_o and M_o are found, and the optimal admittance Y_{LOPT} is obtained from (L_o,M_o). c is called Linvill constant, and it is an index of stability. When c is greater than one, it indicates that the output power is positive while the input power is negative. Therefore, c must be less than one to ensure stability.

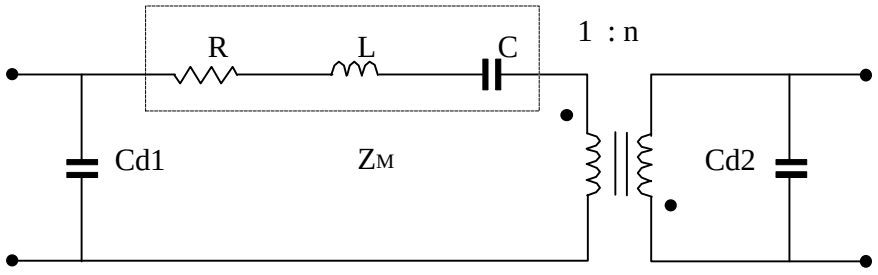

$$Y_{11} = j\omega Cd1 + \frac{1}{Z_M}$$

$$Y_{22} = j\omega Cd2 + \frac{1}{n^2 Z_M} \longrightarrow c = \frac{\sqrt{a^2 + b^2}}{|a - 2g_{11} \cdot g_{22}|} = 1 \longrightarrow \begin{matrix} G_{LOPT} = 0 \\ B_{LOPT} = -\omega \cdot Cd2 \end{matrix}$$

$$Y_{21} = Y_{12} = \frac{-1}{n \cdot Z_M}$$

(a)

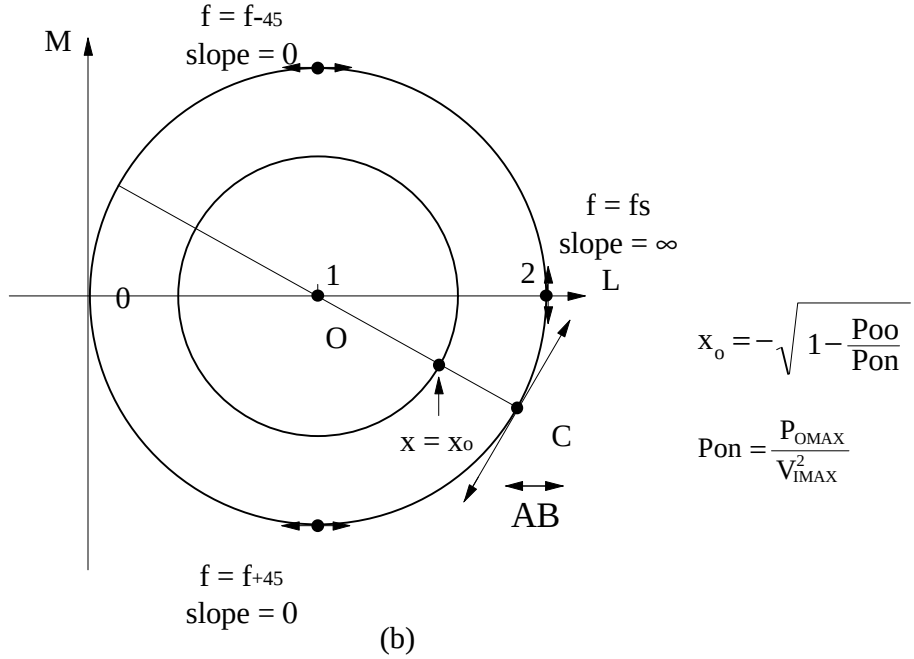

$$x_o = -\sqrt{1 - \frac{Poo}{Pon}}$$

$$Pon = \frac{P_{OMAX}}{V_{IMAX}^2}$$

(b)

Fig. 3.8. Adjustment of the power-flow method for PTs. For longitudinal-mode PTs, the dielectric losses for Cd1 and Cd2 are usually insignificant and result in the Linvill constant approach to unity. An output power limitation is added so that the maximum efficiency of the PT is calculated according to the maximum power handling capability of the PT. Therefore, at any given ω, x = xo is obtained, where line OC and normalized maximum output power contour Pon intercept. From the slopes of the zero input-power contours, the operating frequency increases counterclockwise.

As a result, the maximum efficiency of the PT, whose dielectric losses are very small, approaches unity but there is nearly no output power because of $G_{LOPT} \approx 0$. Theoretically, an inductor will resonate with the output capacitor at any operating frequency ω so that the output reactive power is zero. To prevent this situation, a condition is posed according to the following facts. A maximum input voltage of the PT is provided by the manufacturer to ensure that the ceramic material will not be depolarized or even broken. The power density or power handling capability of the PT can be estimated from its material properties [51]. Therefore, the adjustment for the power-flow method states that a maximal output power P_{OMAX} is generated before its input voltage V_{IMAX} reaches specified upper voltage bound. From this statement, a constant output power contour in the L-M plane is constructed and shown in Fig. 3.8 (b). Accordingly, the normalized constant output power is

$$\text{Pon} = \frac{P_{OMAX}}{V_{IMAX}^{\ 2}} \ . \tag{3.30}$$

Thus, the maximum efficiency of the PT occurs at the intersection of the normalized constant output contour Pon and the x axis. x_o is the intersection point and its value can be obtained from (3.17) to get

$$x_o = -\sqrt{1 - \frac{\text{Poo}}{\text{Pon}}} \ . \tag{3.31}$$

Similarly, the optimal load admittance can be calculated from (3.25) and (3.26).

3.2.3 Optimal Load Characteristics

Generally, longitudinal mode PTs function as step-up transformers and are called the high-voltage PTs (HVPTs). The thickness extensional mode PTs sever as step-down transformers and are named low-voltage PTs (LVPTs). The power-flow technique is a unified method for calculating the optimal load terminations for both HVPTs and LVPTs. However, the output impedance of the HVPT exceeds 200 kΩ and the operating frequency is under 200 kHz. It is unrealistic to use network analyzer, which is a 50-Ω system, to measure the S parameters of the HVPTs. Although the two-port network parameters can be measured by using other methods [47], a conventional method to decide the optimal termination of the HVPTs had been proposed in [4,5,17]. Therefore, the optimal load characteristic of the HVPT could be a resistor only, and its optimal resistance equals the impedance of the output capacitor. Using this method to decide the optimal termination of the HVPT simplifies design procedures for the HVPT applications. On the contrary, the output impedance of the low-voltage PT is relatively closed to the internal resistance, R. To operate the LVPTs efficiently, the two-port flow method must be carried out to calculate the optimal inductive load.

3.2.3.1 Thickness Extensional Mode PT (LVPT-21)

The optimal load characteristics of the LVPT-21 can be obtained by employing the power flow method. The LVPT sample used to demonstrate the load characteristics is a 2:1

piezoelectric transformer [16]. Its complete empirical model has been shown in Fig 2.11 (a) and two resistors Rcd1 and Rcd2 , representing the dielectric losses, are added to the input and output of LVPT-21. In Appendix C, a MATLAB program is presented to calculate the optimal termination at each frequency of interest by using the measured two-port parameters and the complete model of LVPT-21. In the beginning, the Linvill constant c is checked by the program; it is less than unity. Therefore, the adjustment of the power-flow method is bypassed in the program. Figure 3.9 shows several useful design curves calculated from measured two-port parameters and the complete model of LVPT-21 whose efficiency is maximized over the frequencies of interest. These normalized curves describe the characteristics of efficiency, voltage gain, input power, output power, input admittance, and load admittance. According to the simulation results, one of the most desirable operating frequencies is located between 1.91 and 1.92 MHz, because at that frequency band, the efficiency of the PT is maximized and the input power is maximized too under the normalized condition where V_1= 1. For example, (L_o, M_o) = (0.106, 0.158) calculated with two-port parameters at 1.92 MHz. From (3.25) and (3.26), the optimal load admittance and impedance are inductive and are equal to

$$Y_{LOPT}\big|_{f=1.91\,MHz} = 0.0659 - j\cdot 0.0411\ , \tag{3.32.a}$$

$$Z_{LOPT}\big|_{f=1.91\,MHz} = \frac{1}{Y_{LOPT}\big|_{f=1.91\,MHz}} = R_{MS} + j\omega L_{MS} = 10.93 + j\,6.8141\ , \tag{3.32.b}$$

where R_{MS} = 10.93 Ω and L_{MS} = 567 nH at 1.91 MHz. When the operating frequency is 1.92 MHz, R_{MS} = 9.77 Ω and L_{MS} = 450 nH. Since the operating frequency is chosen between 1.91 MHz and 1.92 MHz, the optimal load impedance is selected as

$$Z_{LOPT} = \frac{1}{Y_{LOPT}} = R_{MS} + j\omega L_{MS} = 10 + j\,\omega\cdot(500\,nH)\ . \tag{3.32.c}$$

The efficiency around fs = 1.86 MHz is higher than that in the other region, but the output power around fs is relatively small with V_{IN} = 1. This means a lot of circulating current flowing between the input of the PT and its input sources at fs. As a result, the efficiency of the whole system is going to degrade. From Figs. 3.9 (a) and (d), the calculated results from the lumped model describe the trend of the characteristics, but the results can not faithfully reproduce the characteristics predicted by the two-port network of LVPT-21 when the power-flow method is studied. This is because the measured curves of two-port parameters vs. frequency for LVPT-21 are not smooth curves. This suggests that the parameters of the two-port network are very effective for determining the optimal load of the PTs, but using them in circuit simulations is not feasible. On the other hand, the complete lumped model of LVPT-21 has demonstrated its usefulness by verifying the characteristics such as efficiency, voltage-gain, and input admittance and it is practical to use it in circuit simulation.

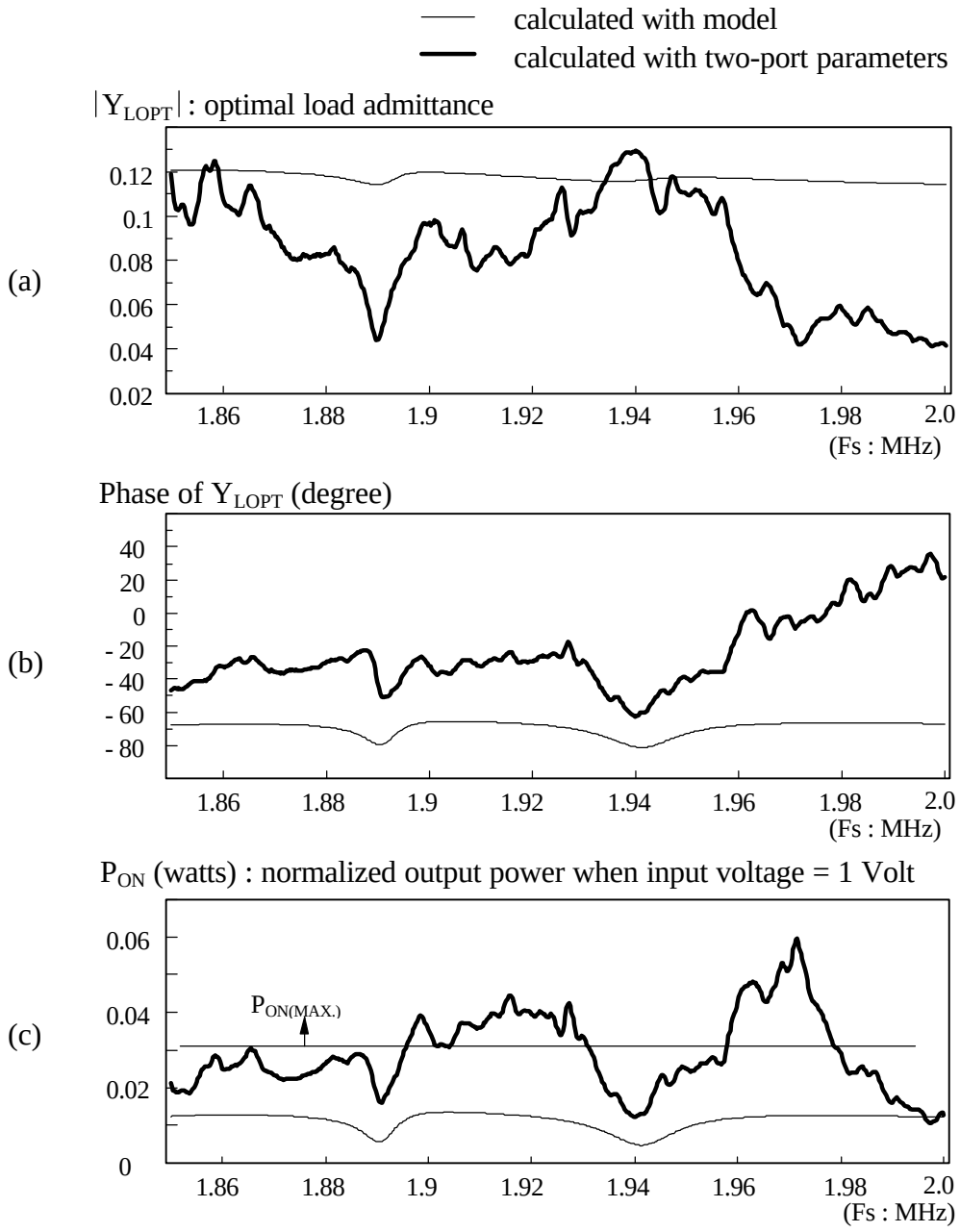

Fig. 3.9. Characteristics of the LVPT-21 matched by using power-flow method. (a) matched load admittance. (b) its phase angle. (c) output power of the LVPT-21 when it is matched and input voltage = 1 Volt. The characteristics of LVPT-21 are calculated when load admittance is optimized and efficiency is maximized at every frequency.

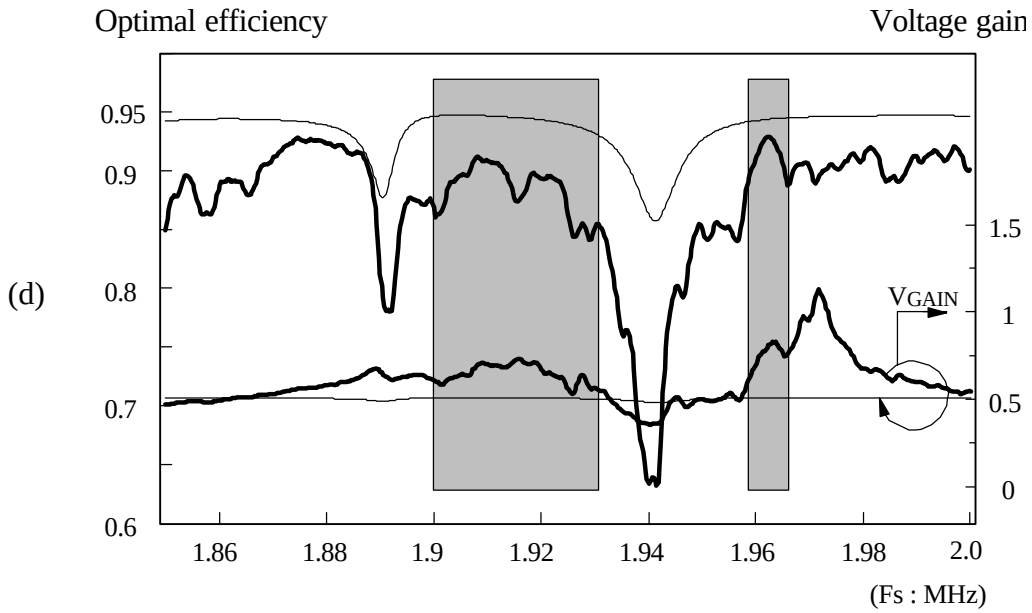

Fig. 3.9. (d) optimal efficiency and voltage gain. The efficiency calculated by the lumped model is higher than that of two-port parameters. However, the output power, determined by the matched load admittance of the LVPT-21, is too small when lumped model is used to calculate the matched load admittance. So, the adjusted power-flow method is employed to find out the optimal load of the PTs under a specified maximum output power.

Although the efficiency, which is calculated by the complete lumped model and shown in Fig. 3.9 (d), is greater than that of the two-port parameters, the output power obtained by the formal is relatively small. It states that the Linvill constant c calculated by the complete lumped model is close to unity, and the adjusted power-flow method needs to be used to obtain specified output power from the PT manufacturer. From Fig. 3.9 (c), the $P_{ON(MAX.)}$ is the normalized maximum output power for LVPT-21, and its corresponding load admittance at each frequency is calculated by adjusted power-flow method shown in the previous section.

From the specifications of LVPT-21, its maximum output power is 15 watts, and the reasonable input voltage should be around 50 Vrms. As a result, the normalized output power P_{ON} is close to 0.03 watts, when input voltage of LVPT-21 is equal to unity. Figure 3.10 shows the simulation results by applying the adjusted power-flow method for both the complete lumped model and two-port parameters. By constraining the output power of the PT, the simulated load characteristics, voltage gain and efficiency of LVPT-21 show much better agreements for both

models than those shown in Fig. 3.9. The notch portions shown in Fig. 3.10 (c) occur at unwanted oscillation frequencies where the output power cannot reach P_{ON}.

Figure 3.11 illustrates simulated and measured efficiency and voltage gain of LVPT-21 with three matched load admittances, and they are found at operating frequencies of 1.91, 1.92, and 1.96 MHz, respectively. From Fig. 3.11., the measured results of voltage gain and efficiencies agree with the theoretical results obtained from the complete model of LVPT-21. Therefore, the lumped model can be very helpful in designing the converter employing PTs.

3.2.3.2 Longitudinal Mode PT (HVPT-2)

The electrical equivalent circuit of HVPT-2 with two resistors added at the input and output ports of HVPT-2 is redrawn in Fig. 3.12 (a). In the beginning, the Linvill constant c is checked and found to be closed to unity. The real part of the optimal load admittance is nearly zero, as shown in Fig 3.12 (b). Therefore, the adjusted power-flow method has to be employed to decide the optimal load of HVPT-2. Taking HVPT-2 as an example, its V_{IMAX} = 100 V_{RMS} and P_{OMAX} = 3 watts. Adding this information into the MATLAB program, the optimal load admittance is decomposed into a parallel combination of resistor and inductor. Figure 3.12 (c). shows that the inductance of the optimal load is approximately 1 H which is difficult and unrealistic to implement. Hence inductive loads are not suitable for the PT with very small dielectric loss and very high output impedance, like most of the longitudinal mode PTs or HVPTs. The conventional method to decide the optimal load terminations for the HVPTs assumes that the termination is resistive [4,5,17]. The derivation of the optimal resistive load for the PT around fs can be found in [17,22] and is obtained by circuit evolution. A new approach is introduced in the L-M plane. So it is possible to visualize the change from an arbitrary optimal load to a specific resistive load, and their relationship in the L-M plane. However, the PT must be operated around fs, which is the same assumption as the one made earlier.

3.2.3.3 Optimal Resistive Load for Longitudinal Mode PT

The conventional method to decide the optimal load terminations for the PTs is to assume that the termination is resistive [5,8]. Figure 3.13 shows the detailed evolution of the model carried out to find the optimal loading of the PTs.

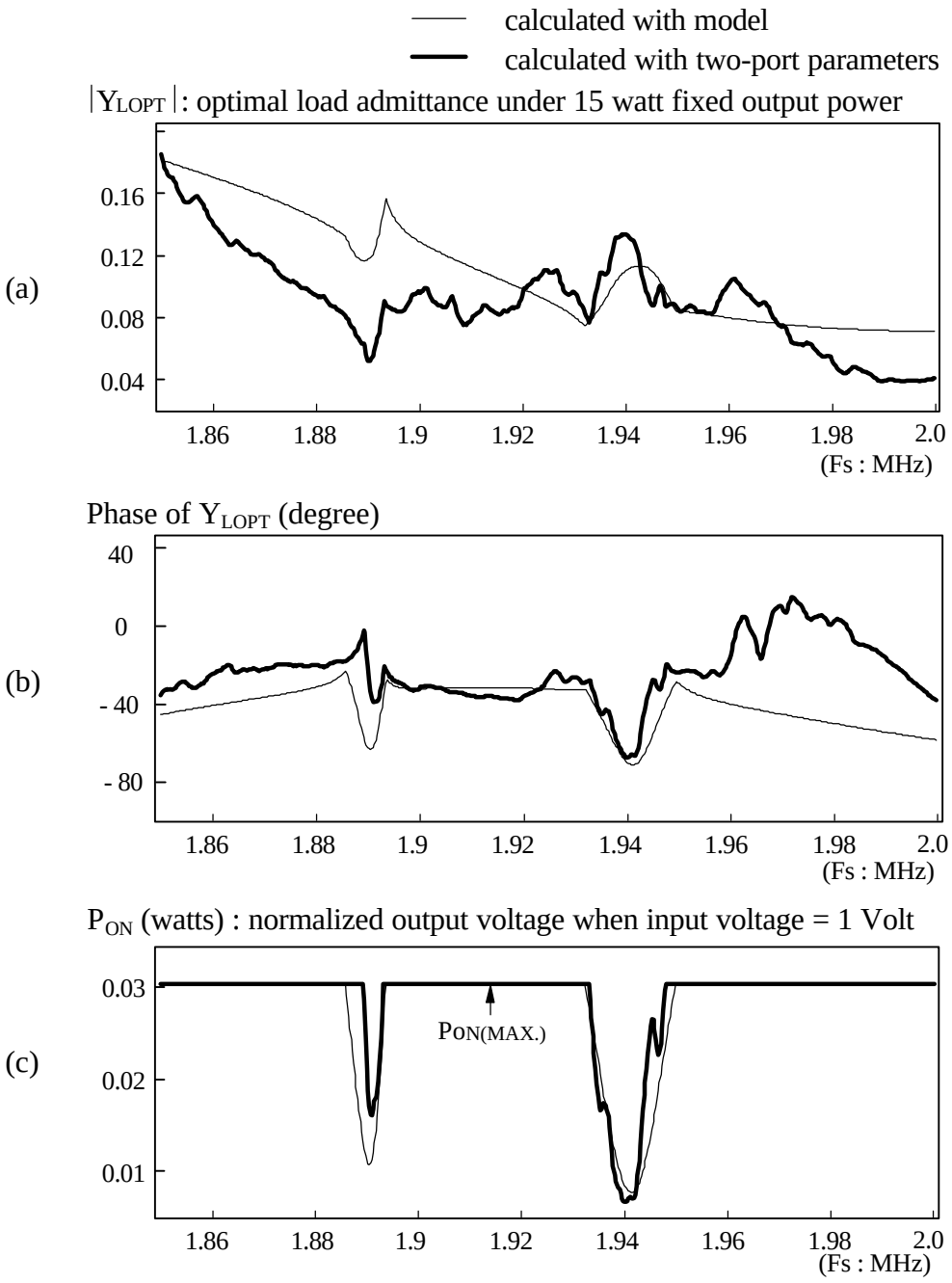

Fig. 3.10. Characteristics of the LVPT-21 matched by using the adjusted power-flow method. (a) load admittance. (b) its phase angle. (c) output power of the LVPT-21 when it is matched and input voltage = 1 Volt.

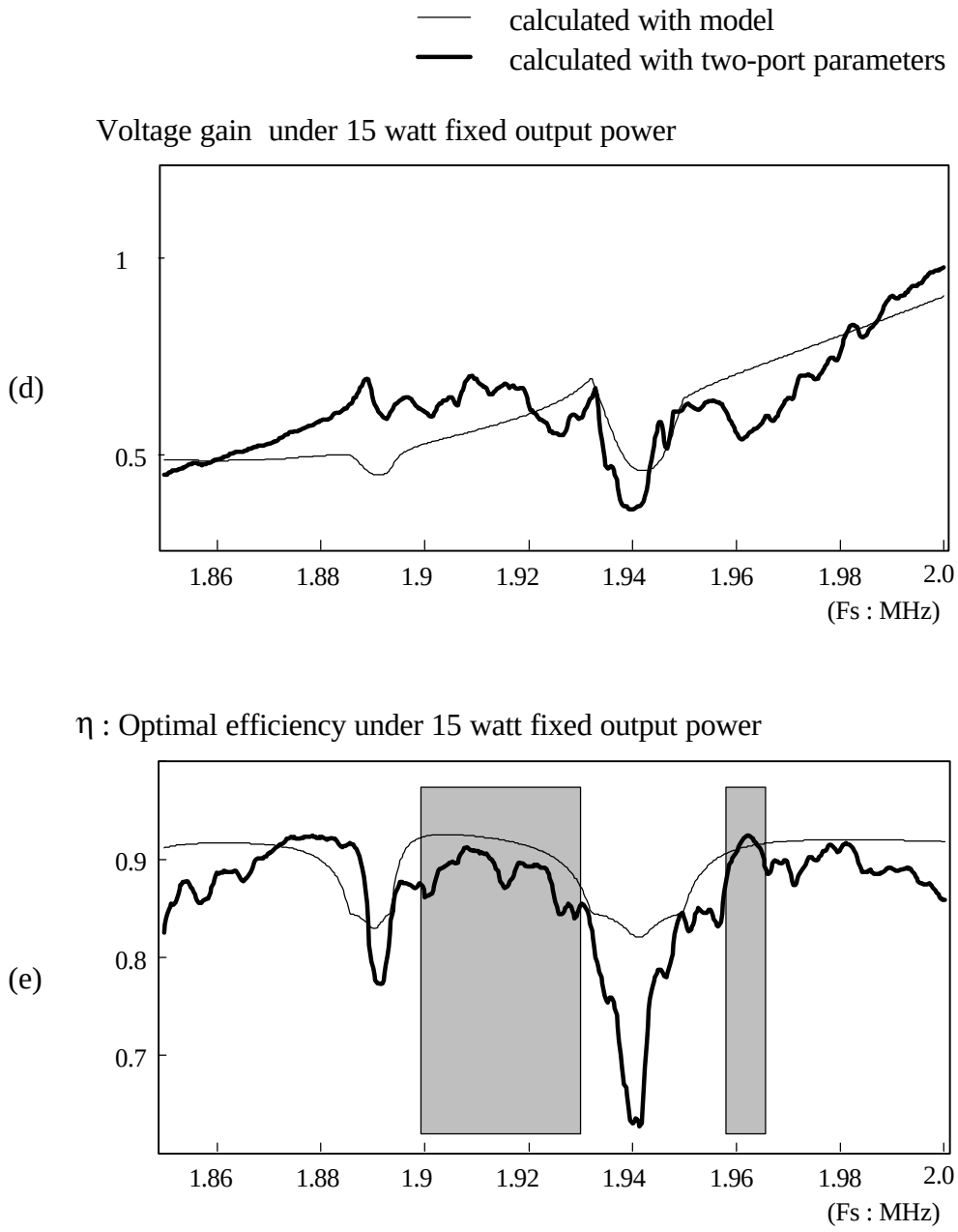

Fig. 3.10. (d) voltage gain. (e) optimal efficiency. To maximize efficiency and input power of LVPT-21 at the same time, two operating frequency zones are chosen and shown in the shaded areas. They are selected according to the requirements of optimized efficiency, reasonable voltage gain, and operation outside of unwanted vibration zones. Therefore, the possible frequency zones are around 1.96 MHz or the frequency zone between 1.91 and 1.925 MHz, to meet all the requirements.

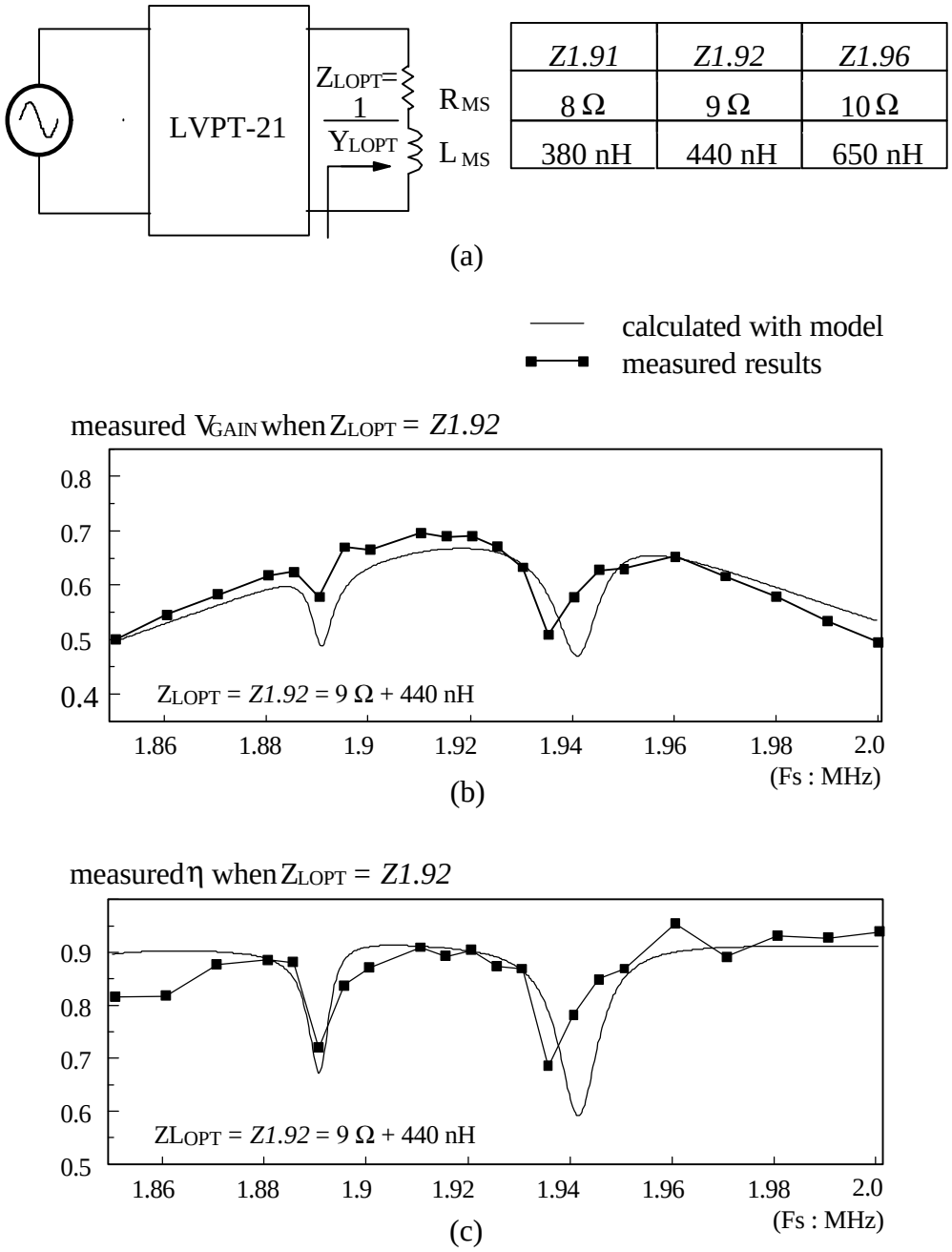

Fig. 3.11. Voltage gains and efficiency of LVPT-21 with matched loads calculated by adjusted power-flow method. (a) simulation setup where the optimal load impedance is composed of R_{MS} and L_{MS}. (b) voltage gain vs. frequency. (c) efficiency η vs. frequency. (b) and (c) are obtained when the load admittance is equal to *Z1.92*.

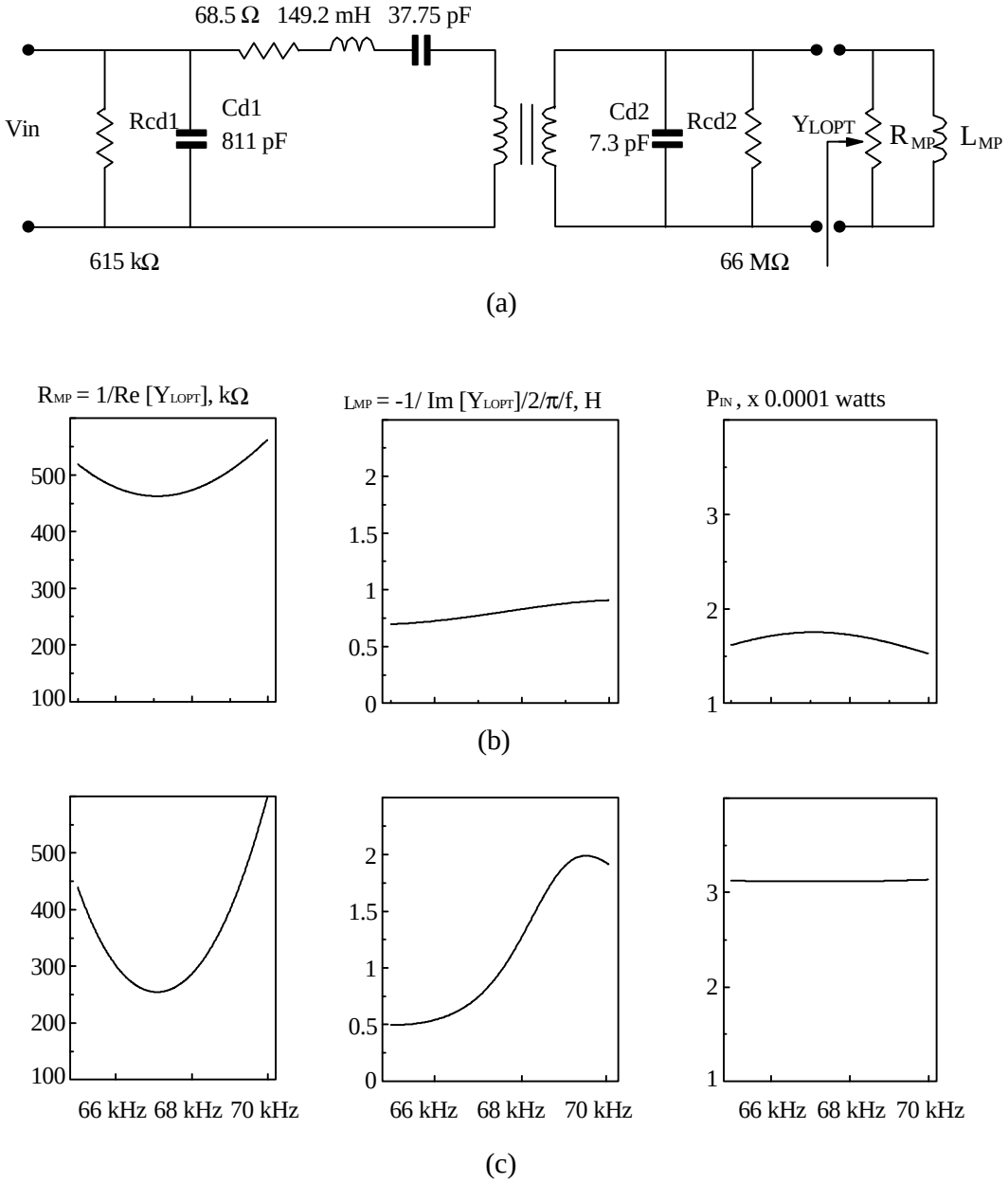

Fig. 3.12. Characteristics of matched HVPT-2. (a) model of HVPT-2 with dielectric loss resistors Rcd1 and Rcd2. (b) characteristics calculated by the power-flow method. (c) characteristics calculated by the adjusted power-flow method. The calculated efficiencies for both methods are close to 96 %. The normalized input power PIN in (c) is two times higher than that in (b). Higher input voltage is needed to accomplish the same output power for (b) because of very high load resistance RMP. However, both methods need to have a big inductance (1H) which is difficult to realize.

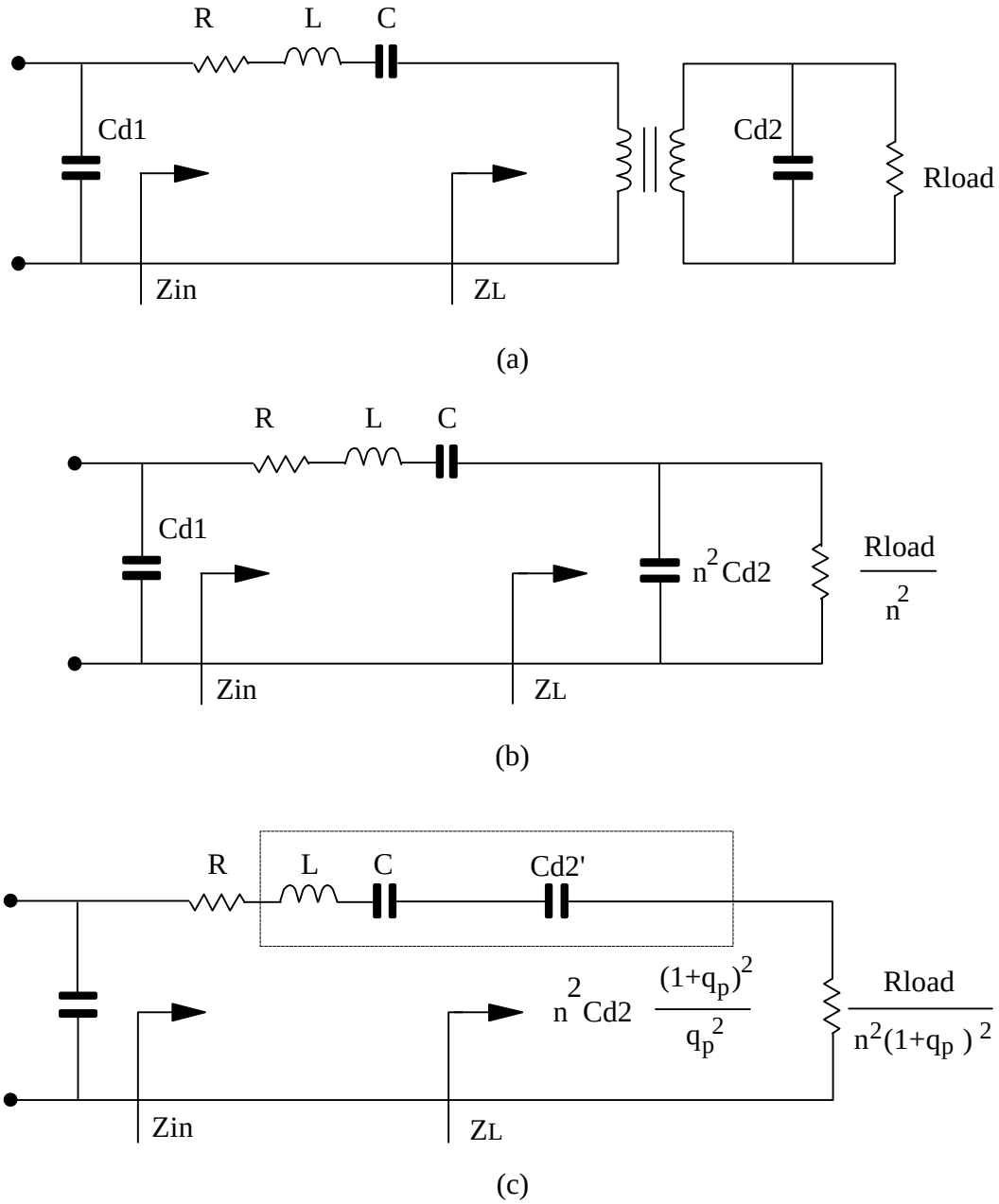

Fig. 3. 13. Optimal termination of the PT under resistive load. (a) PT model with a resistive load. (b) reflecting the load and Cd2 to mechanical branch. (c) changing the parallel to series arrangement for the load. The maximum gain occurs when the reactive components inside the dashed box are resonant with each other.

Equations (3.33) to (3.35) show the voltage gain of the PT, and (3.36) shows the efficiency of the PT. For an arbitrary load resistor Rload, the maximum gain, $V_{GAIN(MAX)}$, occurs when L resonates with C || Cd2' at fo, which is a function of Rload, because the input impedance Z_{IN} is minimized:

$$q_P = \omega \cdot \text{Rload} \cdot \text{Cd2} \ , \tag{3.33}$$

$$Z_{in} = R + j\,\omega L + \frac{1}{j\omega C} + Z_L \ , \tag{3.34}$$

$$V_{GAIN} = \left|\frac{Z_L}{Z_{IN}}\right| = \left|\left(\frac{\text{Rload}}{n^2(1+q_p{}^2)} + \frac{q_p{}^2}{j\omega n^2 \text{Cd2}\,(1+q_p{}^2)}\right)\cdot\frac{1}{Z_{in}}\right| \ , \tag{3.35}$$

$$\eta = \frac{\text{Re}\left[Z_L\right]}{\text{Re}\left[Z_{IN}\right]} = \frac{\text{Rload}}{(1+q_p{}^2)n^2R + R_L} \ , \tag{3.36}$$

$$\eta_{OPT} = \frac{R_{LOPT}}{2n^2R + R_{LOPT}} \ , \tag{3.37}$$

where

$$R_{LOPT} = \frac{1}{\omega s \cdot \text{Cd2}} \ . \tag{3.38}$$

Assuming that fo is close to fs, the maximum efficiency is derived by equating the first derivative of (3.36) with respect to Rload to zero. The maximum efficiency of the PT is obtained when the parallel quality factor $q_p = 1$, and Rload is equal to the matched load, R_{LOPT}, which is the impedance of the output capacitor, Cd2, at ωs.

3.2.3.4 Optimal Resistive Load for Longitudinal Mode PT in L-M plane

Since the load is assumed to be resistive, the imaginary part of the load admittance Y_L is zero and $Y_L = G_L + j\,B_L$:

$$B_L = -b_{22} - 2g_{22} \cdot \frac{M}{L^2 + M^2} = 0 \ . \tag{3.39}$$

The root locus of the above equation for L and M is shown in Fig. 3. 14. and is a much bigger circle than the contour of the output plane with a radius = 1. The function of the circle is

$$L^2 + (M + r)^2 = r^2 \ , \tag{3.40}$$

where r is the radius of the root locus of (3.40) and is defined as

$$r = \frac{g_{22}}{b_{22}} \ . \tag{3.41}$$

Then M can be replaced by L and r from (3.40):

$$M = \sqrt{r^2 - L^2} \tag{3.42}$$

By using the above expression and the Y parameters at fs, it is possible to obtain the input and output functions with respect to the variable L only. $Y_{12} = Y_{21}$ and they are resistive at fs. It means that b = 0 and the Y parameters can be rewritten as

$$Y_{11} = j\omega Cd1 + \frac{1}{R} \ , \tag{3.43.a}$$

$$Y_{21} = Y_{12} = \frac{-1}{n \cdot R} \ , \tag{3.43.b}$$

$$Y_{22} = j\omega Cd2 + \frac{1}{n^2 R} \ . \tag{3.43.c}$$

As a result,

$$g_{11} = \frac{1}{R} \ , \ g_{22} = \frac{1}{n^2 \cdot R} \ , \text{ and} \tag{3.44}$$

$$a + j \cdot b = Y_{12} \cdot Y_{21} = \frac{1}{n^2 \cdot R^2} \tag{3.45}$$

At the same time, the Linvill constant c in (3.21) is equal to 1 because no significant dielectric loss appears in the input and output capacitors, Cd1 and Cd2. From (3.20), the contour of the input plane in the L-M plane is perpendicular to L-axis and can be expressed as L=2 because c=1, and the slope of the contour is decided by $\tan^{-1}(a/b)$ which approaches infinity. When c = 1, the input plane cuts the zero output contour at (L,M) = (2,0) at fs, cuts the zero output contour at (L,M) = (1,1) at f_{+45}, and cuts the zero output contour at (L,M) = (1,-1) at f_{-45}. The distribution of fs, f_{+45}, and f_{-45} in the L-M plane resembles that in the G-B plot of the PT. The input and output power equations, tracking coordinates along curve AB in the L-M plane, can be rewritten as

$$\begin{aligned} Pin(L) &= g_{11} - \frac{a \cdot L}{2g_{22}} = g_{11} - \frac{a \cdot L}{2g_{22}} \\ &= \frac{1}{2 \cdot R}(2 - L) \ . \end{aligned} \tag{3.46}$$

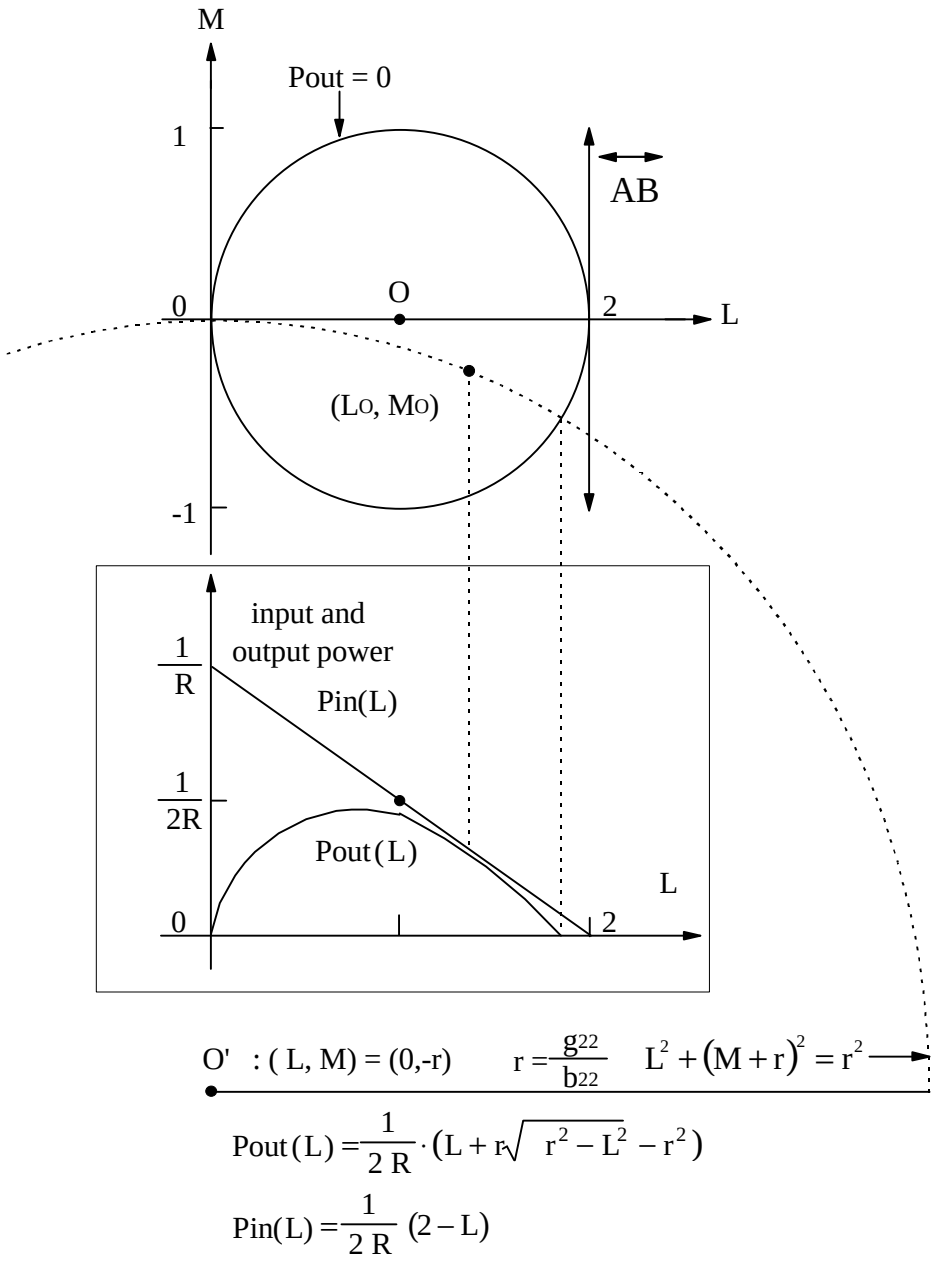

Fig. 3.14. Optimal resistive load for high-output-impedance PTs. For high-output-impedance PTs, the inductance of the matched load by the power-flow method is too large to realize in practical applications. As a result, a pure resistive load is assumed, and the optimal resistance is found in the L-M plane around fs. The part of the big circle with center (L,M) = (0,-r) denotes the root locus of the load admittance whose imaginary part is zero. In the middle of the figure, the input and output powers calculated along the big circle become functions of L only. The optimal resistive load is equal to the reciprocal of b22.

$$\begin{aligned}\mathrm{Pout(L)} &= \mathrm{poo}\cdot(2\,\mathrm{L}-\mathrm{L}^2-\mathrm{M}^2)\\ &= 2\cdot\mathrm{poo}\cdot(2\,\mathrm{L}\cdot\sqrt{\mathrm{r}^2-\mathrm{L}^2}-\mathrm{r}^2)\\ &= 2\cdot\frac{\mathrm{n}^2\,\mathrm{R}}{4}\cdot\left(\frac{1}{\mathrm{n\,R}}\right)^2\cdot(\mathrm{L}+\mathrm{r}\cdot\sqrt{\mathrm{r}^2-\mathrm{L}^2}-\mathrm{r}^2)\\ &= \frac{1}{2\,\mathrm{R}}\cdot(\mathrm{L}+\mathrm{r}\cdot\sqrt{\mathrm{r}^2-\mathrm{L}^2}-\mathrm{r}^2)\,.\end{aligned} \tag{3.47}$$

Pin(L) and Pout(L) are drawn in Fig. 3.14., the efficiency of the PT with resistive load only can be solved and becomes

$$\eta\,(\mathrm{L}) = \frac{(\mathrm{L}+\mathrm{r}\cdot\mathrm{M})}{2-\mathrm{L}} = \frac{(\mathrm{L}+\mathrm{r}\cdot\sqrt{\mathrm{r}^2-\mathrm{L}^2}-\mathrm{r}^2)}{2-\mathrm{L}}\ . \tag{3.48}$$

The procedure used to find out the optimal load resistance where the efficiency of the PT is exactly the same as that stated from(3.20) to (3.24). Equating the first derivative of (3.48) to zero gives

$$\begin{aligned}&(1-\frac{\mathrm{r}\cdot\mathrm{L}}{\sqrt{\mathrm{r}^2-\mathrm{L}^2}})\,(2-\mathrm{L})+\mathrm{L}+\mathrm{r}\cdot\sqrt{\mathrm{r}^2-\mathrm{L}^2}-\mathrm{r}^2=0\\ &(\mathrm{r}^4+4)\cdot\mathrm{L}^2-4\mathrm{r}^4\cdot\mathrm{L}-\mathrm{r}^2\cdot(4-4\mathrm{r}^2)=0\,.\end{aligned} \tag{3.49}$$

Then L is solved as

$$\begin{aligned}\mathrm{L}=\mathrm{L_o} &= 2\cdot\frac{\mathrm{r}^4-\sqrt{\mathrm{r}^8+\mathrm{r}^2\cdot(1-\mathrm{r}^2)\cdot\left(\mathrm{r}^4+4\right)}}{\mathrm{r}^4+4}\\ &= 2\,\mathrm{r}\cdot\frac{\mathrm{r}^3-\mathrm{r}^2+2}{\mathrm{r}^4+4}\,.\end{aligned} \tag{3.50}$$

At the same time, M can be solved as

$$\begin{aligned}\mathrm{M}=\mathrm{M_o} &= \sqrt{\mathrm{r}^2-\mathrm{L_o}^2}-\mathrm{r}\\ &= \frac{\mathrm{r}}{\mathrm{r}^4+4}\cdot\left(\sqrt{(\mathrm{r}^4+4)^2-4\cdot(\mathrm{r}^3-\mathrm{r}^2+2)^2}-(\mathrm{r}^4+4)\right)\\ &= \frac{\mathrm{r}}{\mathrm{r}^4+4}\cdot\left(\mathrm{r}\cdot(\mathrm{r}^2-2\,\mathrm{r}+2)\cdot(\mathrm{r}+2)-(\mathrm{r}^4+4)\right)\\ &= \frac{-2\,\mathrm{r}}{\mathrm{r}^4+4}\cdot(\mathrm{r}^2-2\,\mathrm{r}+2)\,.\end{aligned} \tag{3.51}$$

Substituting (3.50) and (3.51) to (3.25), the optimal conductance G_{OPT} is found to be

$$
\begin{aligned}
G = G_{OPT} &= -g_{22} \cdot \left(1 - \frac{2\,L_o}{L_o^{\,2} + M_o^{\,2}}\right) \\
&= -g_{22} \cdot \left(1 + \frac{2\,L_o}{M_o \cdot 2r}\right) \\
&= -g_{22} \cdot \left(1 - \frac{r^3 - r^2 + 2}{r \cdot (r^2 - 2\,r + 2)}\right) \\
&= -g_{22} \cdot \left(1 - \frac{r+1}{r}\right) \\
&= b_{22}\ .
\end{aligned}
\tag{3.52}
$$

Equivalently, the optimal load resistance $Rload_{OPT}$ is given as

$$
Rload_{OPT} = \frac{1}{G_{OPT}} = \frac{1}{\omega_S \cdot Cd2}\ . \tag{3.53}
$$

Meanwhile, the maximum efficiency of the PT η_{MAX} with $Rload_{OPT}$ from (3.48) is

$$
\begin{aligned}
\eta_{MAX} &= \frac{L_o + r \cdot M_o}{2 - L_o} = \frac{r}{r+2} \\
&= \frac{g_{22}}{g_{22} + 2\,b_{22}} \\
&= \frac{Rload_{OPT}}{Rload_{OPT} + 2\,n^2 \cdot R}\ .
\end{aligned}
\tag{3.54}
$$

The theoretical and measured efficiency curves for different load resistance and optimal load resistance $Rload_{OPT}$ = 330 kΩ are shown in Figs. 3.15 (a) and (b). Although the calculated and measured efficiencies have a 2% error, the maximum efficiency occurs when the load resistance approaches 330 kΩ and the operating frequency is around fs. The curve of the measured efficiency is like a convex which is different from the simulated curve because of losing the nonlinear information of dielectric loss in the simulation model. This again [21] suggests that the dielectric loss is critical to determining the efficiency of the PTs.

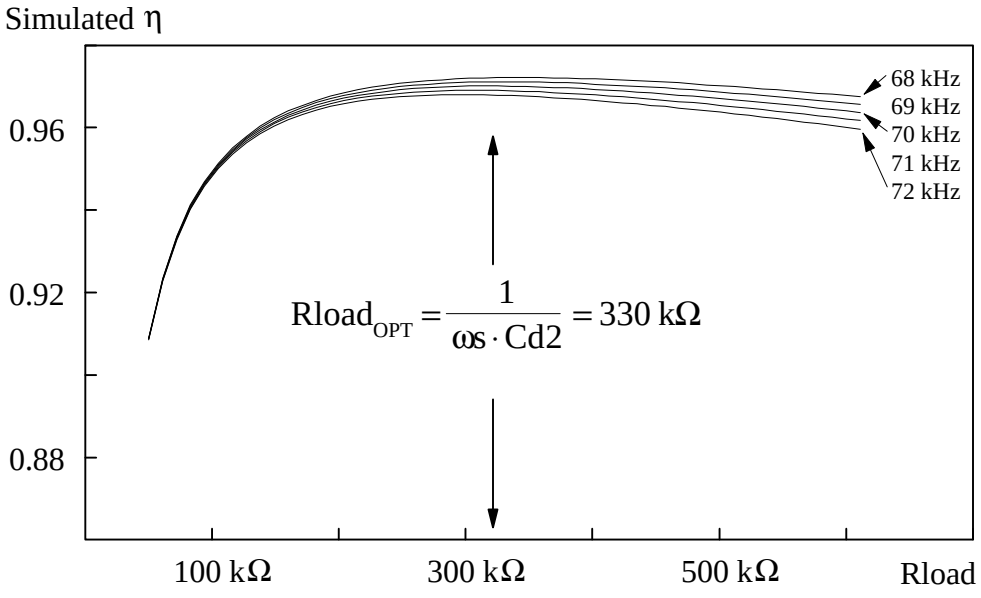

(a)

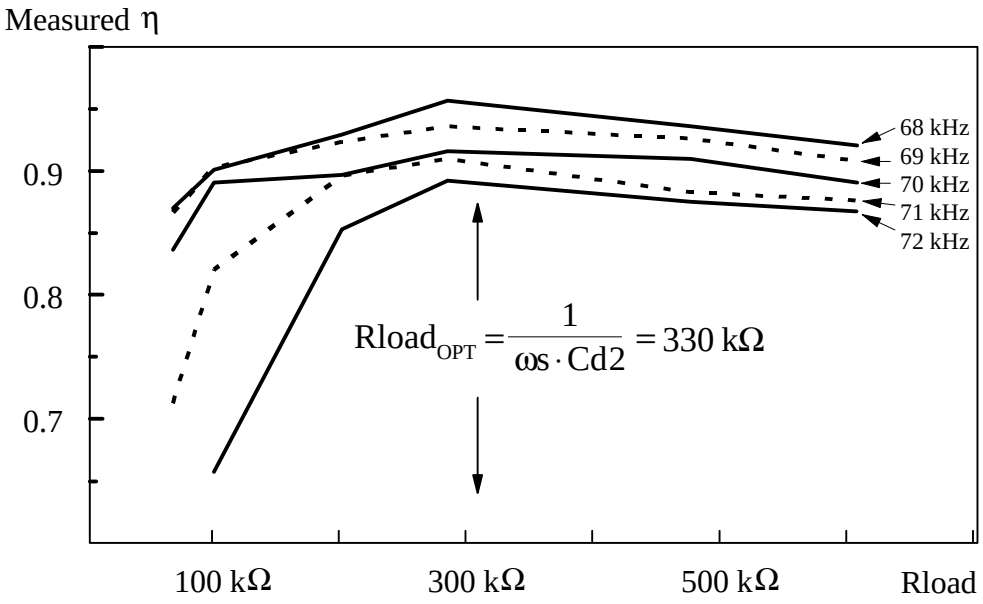

(b)

Fig. 3.15. Efficiencies of HVPT-2 with various resistive loads. (a) theoretical results. (b) measurement results. The maximum efficiency of HVPT-2 always occurs when the load resistance $\mathrm{Rload}_{\mathrm{OPT}}$ is equal to 330 kΩ for a particular operating frequency. The other information is that η of HVPT-2 decreases when the operating frequency increases.

If the adjusted power-flow method is applied to HVPT-2, the maximal efficiency is 97 %. However, a 1H inductor is needed because of the high output impedance of the HVPT. Because the calculated maximum efficiency of HVPT-2 is 95.7 %, it demonstrates that employing a matched resistive load can provide a highly efficient operation of the longitudinal PTs. The same analysis is carried out for the 1:1 acoustic filter transformer[19]. The calculated results are $Rload_{OPT}$ = 7.53 Ω and η_{MAX} = 63.6 % because the term $2n^2R$ = 2.15 Ω which is close to the value of $Rload_{OPT}$. If a resistive load is added to the output of the low-voltage PT, the highest efficiency is only 63.6 %. Comparing this result to the efficiency calculated from the power-flow technique in 3.2.3.1 shows that the efficiency calculated from power-flow methods is 24 % better than that obtained with the use of the conventional method [21].

3.2.4 Equivalent Circuit of Output Rectifier Circuits and Loads

When a nonlinear load is applied to the output of the PTs, there are several rectifier circuits interfacing with the output matching network. The objective is to derive the equivalent resistance, R_{EQ}, for the rectifier circuit and load, R_L so that the OMNs are built to match the R_{EQ} to the optimal load admittance, Y_{LOPT}, of the PTs. Functioning as a filter, the PT will screen out most harmonics. Therefore, the output voltage of a PT almost prefers a sinusoidal voltage source. Figure 3.16. illustrates the operating waveforms of the rectifier stage and the function of the OMN. To provide a dc current path through the half-wave rectifier, an inductor, L_{DC}, is placed adjacent to the rectifier and serves as part of the OMN. Employing the first-order Fourier series approximation , the current of D_1 can be decomposed to

$$i_{D1} = \frac{I_L}{2} + \frac{2}{\pi} \cdot I_L \cdot \sin \omega t \ . \tag{3.55}$$

The dc output power is

$$P_O = {I_L}^2 \cdot R_L \ . \tag{3.56}$$

For ideal component, $P_{Oi} = P_O$

$$\frac{1}{2} \cdot \left(\frac{2}{\pi} \cdot I_L \right)^2 \cdot R_{EQ} = {I_L}^2 \cdot R_L \ . \tag{3.57}$$

It follows that

$$R_{EQ} = \frac{\pi^2}{2} \cdot R_L \ . \tag{3.58}$$

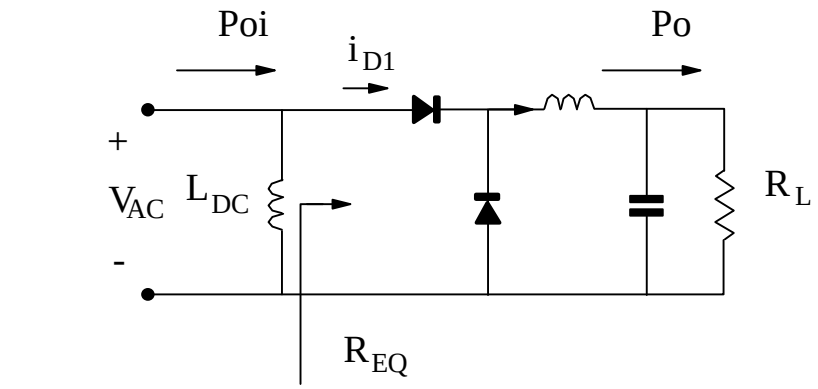

(a)

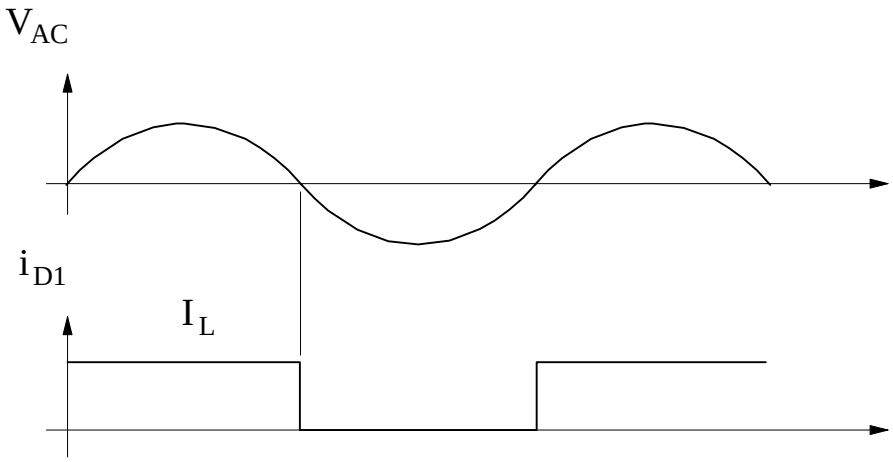

(b)

$$i_{D1} = \frac{I_L}{2} + \frac{2}{\pi} \cdot I_L \cdot \sin \omega t$$

Let Poi = Po $\longrightarrow$ $R_{EQ} = \frac{\pi^2}{2} R_L$

Fig. 3.16. Operating waveforms of the half-bridge rectifier stage. (a) half-bridge rectifier and load resistor RL. (b) theoretical waveforms. From power balance, the equivalent resistance of REQ is found from the operation waveforms for the half bridge rectifier. Similar results can be obtained for the other type of rectifier circuits and are listed in Table 3.1. LDC is added to provide a dc current path and a part of the output matching network of PTs.

Table 3.1. Output rectifier stage.

Full- bridge with Voltage Load	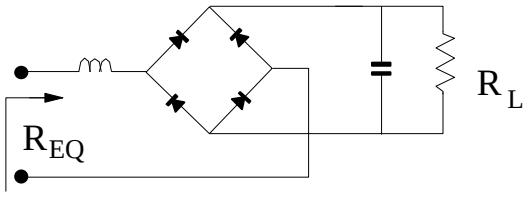	$R_{EQ} = \frac{8}{\pi^2} R_L$
Full- bridge with Current Load	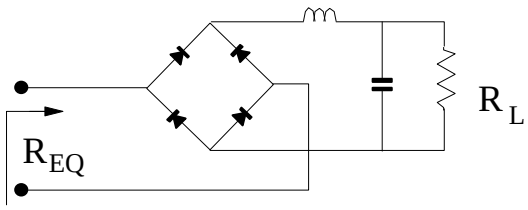	$R_{EQ} = \frac{\pi^2}{8} R_L$
Current Doubler	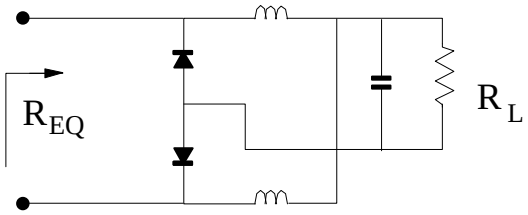	$R_{EQ} = \frac{\pi^2}{2} R_L$
Half bridge	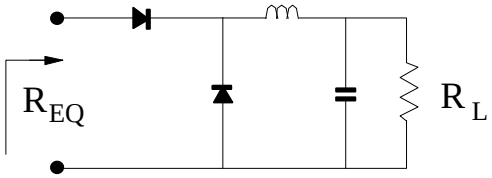	$R_{EQ} = \frac{\pi^2}{2} R_L$
Voltage multiplier	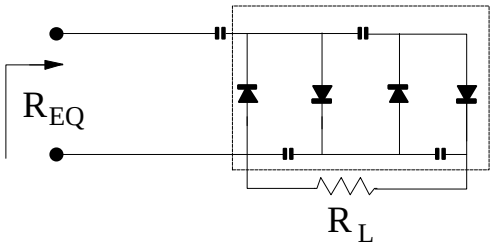	$R_{EQ} = \frac{1}{32} R_L$

By using the same derivation, the equivalent resistances of other five different rectifier circuits are tabulated in Table 3.1. To determine the form factor of the output rectifier stage, two effects need to be discussed. One is the ratio of R_{EQ}/R_L. The other effect is caused by adding an inductor between the PT and the rectifier stage. For the LVPTs, the optimal inductive load could be a series or a parallel connection of the resistor and inductor. Using a parallel connection results in undesirable noise and ringing due to the stray capacitance among the winding of parallel inductor and the surface of the PT. So the series connection is more desirable. However, adding an inductor decreases the amplitude of the input voltage for the output rectifier stage. Therefore, the form factor of the full-wave rectifier with an inductor was set to 0.5 approximately.

The reason why the full-bridge type rectifiers are employed is that the ratio R_{EQ}/R_L is higher than those of half-bridge and current doubler rectifiers. The higher the R_{EQ}/R_L, the lower the required voltage ratio M; accordingly, the voltage stress on the main switch is reduced. The half-wave and current doubler rectifiers have the same R_{EQ}/R_L ratio, but an extra inductor is required to provide a dc path for the former. From the ratios of R_{EQ}/R_L, the full bridge rectifier and voltage multiplier offer step-up voltage ratios, which are very useful for the high-voltage PT applications.

3.2.5 Design of Output Matching Networks

Similarly, the half-bridge rectifier circuit is used to illustrate how to design the OMNs. The matching network could be a π-type or an L-type as long as it contains the required inductor, L_{DC}. The difference between the π-type and L-type impedance matching networks is that the π-type ones have another degree of freedom to decide the bandwidth of the matching networks. To explain the design of the OMN, an L-type OMN is introduced in Fig. 3.17. where $Z_L=1/Y_L$. Assuming Re $[Z_L]$ is smaller than R_{EQ} and q_P is the parallel quality factor, q_P is resolved from (3.59):

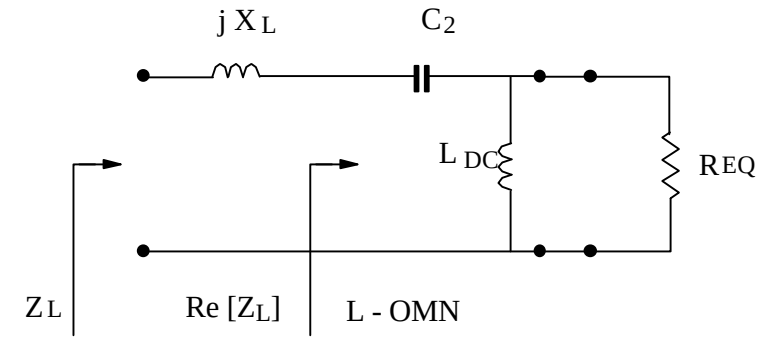

(a)

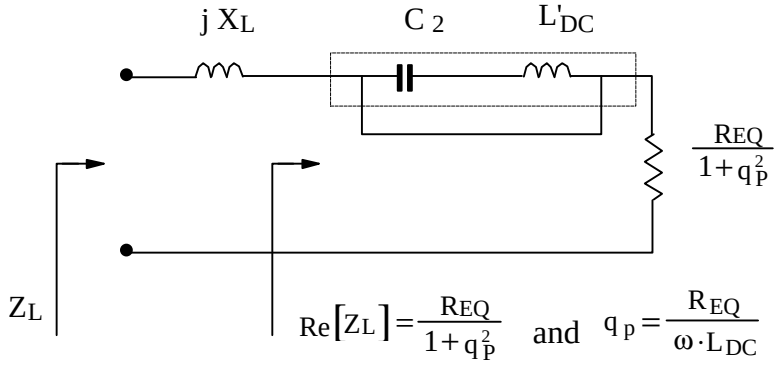

(b)

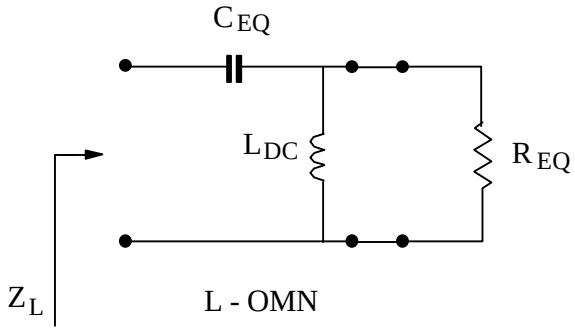

(c)

Fig. 3.17. L-type matching network. (a) objectives of the OMN; (b) and (c) derivation of OMN. Z_L is the optimal load where the efficiency of the PT is maximized, and REQ is the equivalent resistance of the rectifier circuit and load. These impedances are obviously different, and hence, a matching network is necessary. The L-type matching network is simple, but can not cover a wide range of operating frequencies. It is suitable to be adopted in a constant-frequency controlled converter.

$$\mathrm{Re}\left[Z_L\right] = \frac{1}{1+q_P{}^2} \cdot R_{EQ} \ , \tag{3.59}$$

$$q_p = \frac{R_{EQ}}{\omega \cdot L_{DC}} \ . \tag{3.60}$$

L_{DC} is obtained from (3.60). Then the parallel of L_{DC} and R_{EQ} is rearranged to the series of the real part of Z_L and an inductor, L_{DC}'. Because L_{DC}' resonates with C_2 at the switching frequency, C_2 can be derived easily. The imaginary part of Z_L can be combined with C_2 at the switching frequency. Finally, the resultant OMN is composed of L_{DC} and C_{EQ}.

Based on the optimal load admittance for the 1:1 acoustic filter transformer, Y_{LOPT}, at 3.325 MHz and the equivalent impedance of the half-bridge rectifier stage in this section, both π-type and L-type OMNs have been designed to maximize the efficiency of the PT. To obtain a monotonic curve for voltage conversion ratio versus frequencies, the selected matching networks are checked with the lumped model circuit of the PT by using the Pspice simulation program. The simulation results employing π-type and L-type OMNs, respectively shown in [19] explain that the monotonic curve for voltage gain of the PT is obtained by using π-type OMN.

3.3 Input Matching Networks

The input matching networks (IMNs) form an interface circuit between the dc/ac inverter and input impedance of the PT with a certain load termination. The PTs are passive devices and are connected in series with the dc/ac inverters, which are switching amplifiers . For a conventional radio-frequency (RF) amplifier, the input of the amplifier is usually a signal-level periodical source. The function of IMNs for RF circuits is to match the source impedance to the input impedance of two-port networks with optimal terminations so that the transducer gains [40] of the two port networks are maximized. From the aspect of efficiency for the input signal source, the efficiency under matched condition is no more than 50 %. But the power dissipation in the source is much smaller than the loss in the RF amplifier circuit whose efficiency is maximized by the power-flow technique. Unlike the function of IMNs in the RF circuits, the function of IMN in a PT converter is not to ensure the maximum power transfer from dc/ac inverters to the input of the PTs. Instead, IMNs are used to decrease the reactive flow in the PTs and dc/ac inverters, or to make sure the zero-voltage switching is achieved to reduce the switching loss and noises in dc/ac inverters.

3.3.1 Input Impedance Characteristics for the PT

3.3.1.1 Thickness Extensional Mode PT (LVPT-21)

Figure 3.18 (a). shows the input block diagram of the PT converter, including a dc/ac inverter, IMN, PT and its load. Based on the optimal load admittance, Y_{LOPT}, for LVPT-21, at 1.91 MHz, the input admittance of LVPT-21 is drawn in Fig. 3.18 (b).

$$\begin{aligned} Y_{IN} &= \frac{1}{Z_{IN}} = 0.0397 + j \cdot 0.0266 \\ &= \frac{1}{R_{IN}} + j \cdot \omega \cdot C_{IN} = \frac{1}{25.21} + j \cdot \omega \cdot 2.2n \,. \end{aligned} \tag{3.61}$$

This is an example which demonstrates that the characteristics of the input impedance for the PTs are capacitive around the desired operating frequencies. The input admittances of LVPT-21 with the matched load at 1.92 MHz are shown in Fig. 3.18 (b) and (c), and they are always capacitive. These three matched input admittance curves are obtained from the calculation results employing the complete lumped model, measurement results directly from the impedance analyzer, and the calculation results with the two-port parameters measured form the network analyzer. They are similar in shape and values and this again verifies the usefulness of the lumped model. Figures 3.18 (d). and (e). illustrate the input admittances of LVPT-21 when series load resistance R_{MS} changes from 5 Ω to 150 Ω at 1.91 and 1.92 MHz, respectively. Although the input admittance is still capacitive, the input admittances are not only load-dependent but also frequency-dependent. To further illustrate the relationship among Y_{IN}, the load of the PT, and the operating frequency, 3-D plots are shown in Figs. 3.18 (f). and (g). Figure 3.18 (g) is an important plot which shows that Y_{IN} may become inductive when series load resistance R_{MS} is large. Besides, the phase falls into negative values abruptly around 1.97 MHz, and it indicates that operating frequency of the PT converter beyond 1.97 MHz should be avoided. As a result, the PT and its load cannot simply be replaced by a combination of resistor and capacitor unless the operating frequency and load of the PT are fixed.

The objective of the IMN is not to match the source impedance of the switching amplifier. Firstly, it is important to maintain high efficiency of the switching amplifier in power electronics applications. The second reason is that the source impedance of the switching amplifier is nearly zero, and it is impossible to deliver infinite available input power under matched condition. Therefore, the IMN is added to maximize the efficiency of the dc/ac inverter and to minimize the circulating current in the input branch of the PT. Normally, IMNs consist of inductive components to compensate for the large input capacitance of the PT, Cd1. Moreover, the IMNs can be built into the dc/ac inverters so that the output impedances of the dc/ac inverters are inductive over the operation frequency range. If the efficiency of the dc/ac inverters had been assumed to be maximized to the resistive loads [43], in such conditions, the IMN could be an inductor or a simple L-matching network.

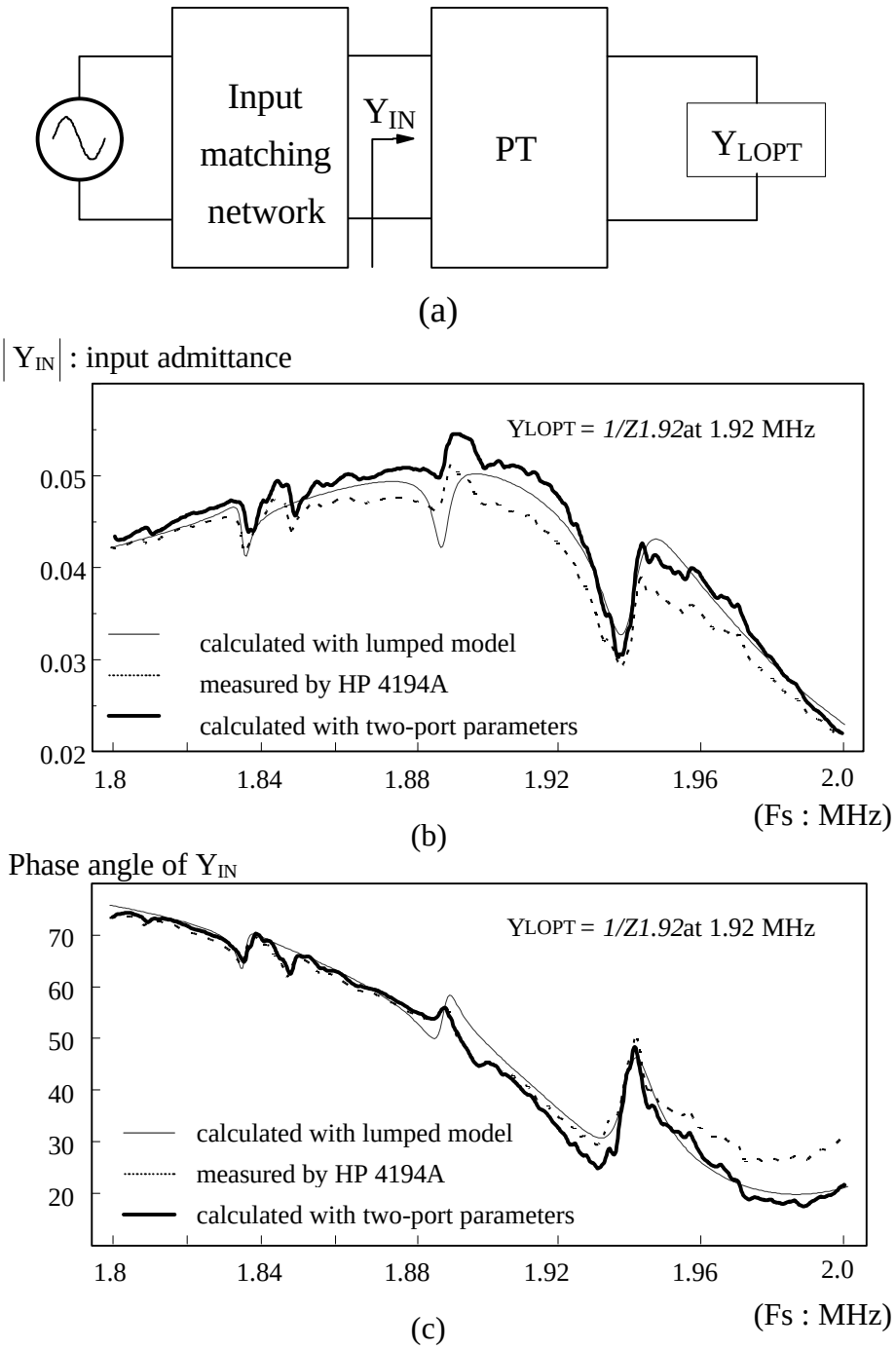

Fig. 3.18. Input characteristics of LVPT-21. (a) input network. (b) input admittance. (c) phase angle of the input admittance. The input admittance is capacitive over a wide range of operating frequencies when the load is optimized at 1.92 MHz. The capacitive characteristics might be cooperated into amplifier circuit design as a part of resonant or filtering circuits.

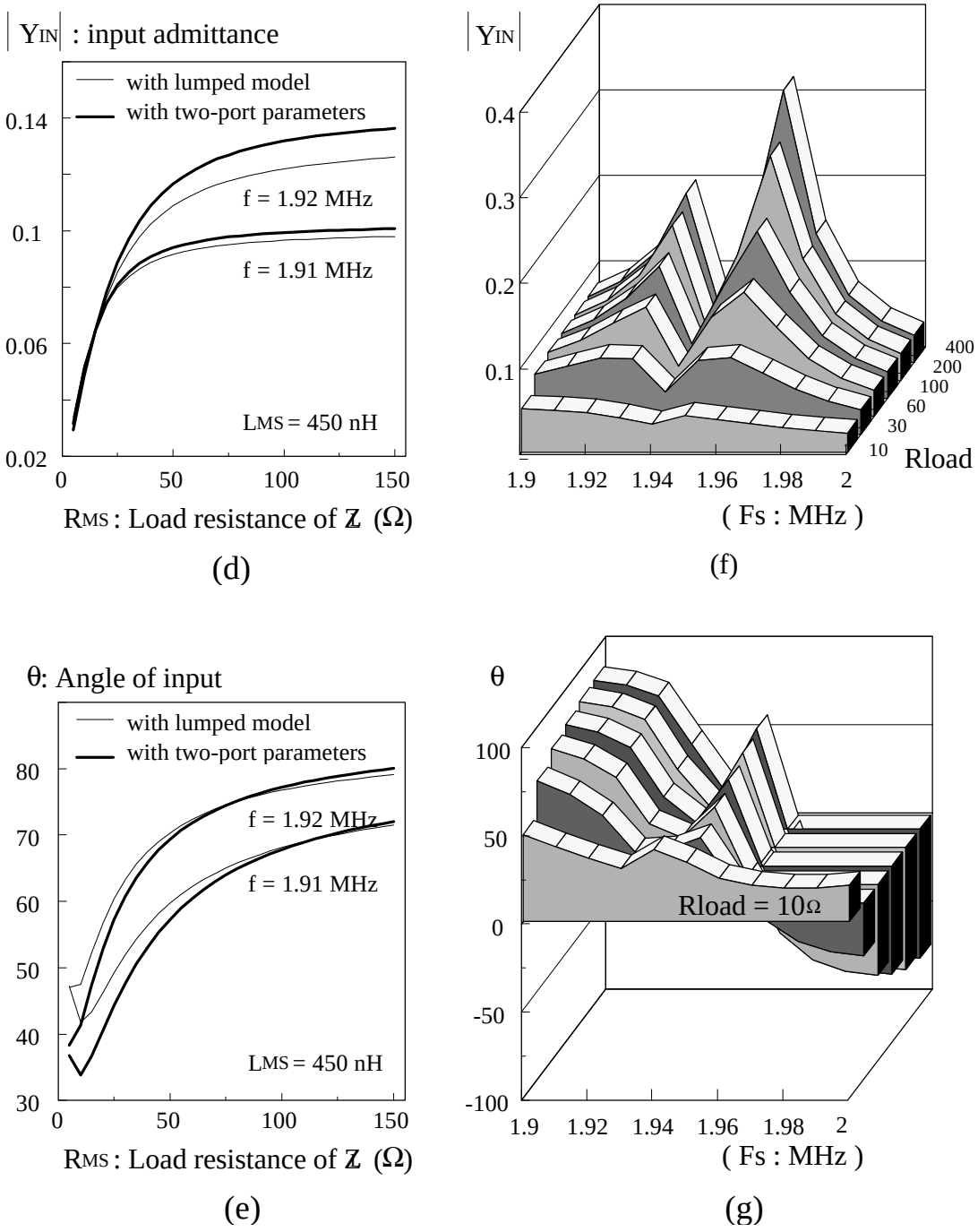

Fig. 3.18. (d) input admittance vs. RMS with operating frequencies as running parameter. (e) its phase angle. (f) 3-D plot of the input admittance. (g) 3-D plot of its phase angle. When load resistance is very high, the input admittance is almost like a pure capacitor. However, the phase of the input admittance becomes negative when RMS increases and frequency is beyond 1.96 MHz. This will change the performance of the power amplifier dramatically.

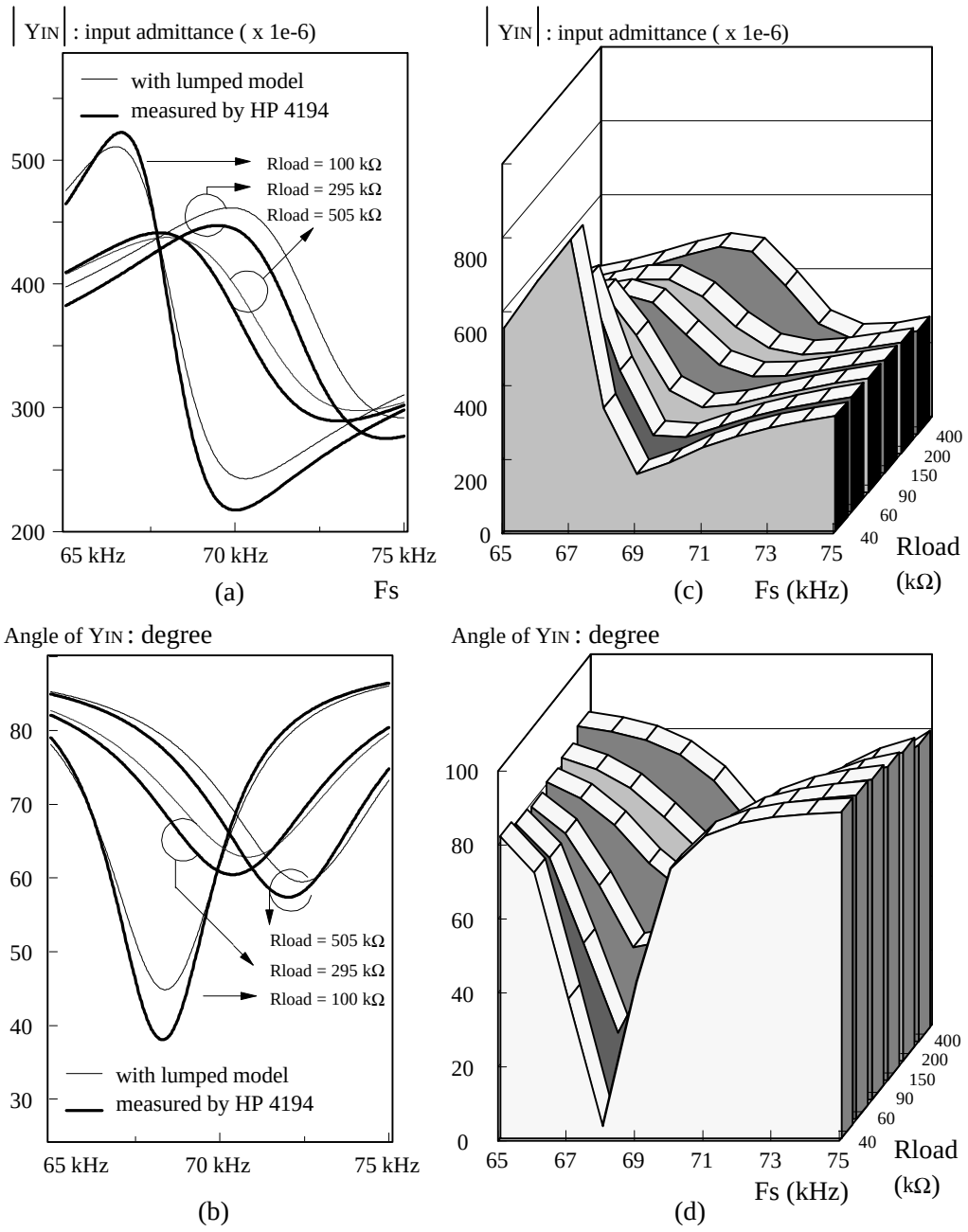

Fig. 3.19. Input characteristics of HVPT-2. (a) input admittance vs. operating frequencies with load resistance as running parameter. (b) its phase angle. (c) 3-D plot of YIN. (d) 3-D plot of its phase angle. The measured and simulated results of YIN agree with each other. This validates the characteristics of the model again. From (c) and (d), the phase of YIN is always positive, and hence, YIN is capacitive under the normal operating conditions. As a result, the amplifier design is easier and the soft-switching technique can be applied.

3.3.1.2 Longitudinal Mode PT (HVPT-2)

Figure 3.19 (a) and (b). illustrate the input admittance vs. frequency characteristics of HVPT-2 with resistive load as running parameters. The thin lines represent curves of Y_{IN} calculated by the lumped model of LVPT-2 and show agreement with those measured directly with impedance analyzer. In Fig. 3.19 (c) and (d), the 3-D plot in (d) illustrates the phase angle of the input admittance, and it is always positive as long as the load resistance Rload is greater than 40 kΩ for HVPT-2. Therefore, Y_{IN} of HVPT-2 is capacitive over a wide range of operating frequencies and load resistances. Besides, there is no abrupt phase drop as shown for LVPT-21; this makes it possible to use either constant-frequency or variable-frequency control to control the voltage gain of the converter with HVPTs.

3.3.2 Study of Output Impedance for Amplifiers

Previewing the topologies for switching dc/ac inverters or amplifiers in Chapter 4 indicates that they can be divided into two categories. The first category can be simplified to a square-wave or quasi-square-wave source accompanied with a resonant tank or a low-pass filter. So the output of the resonant tank is sinusoidal which is most desirable for the PT. The source impedance is very small for the switching amplifier. The output impedance of the amplifier is reactive and dependent on the operating frequency. The other topology consists of a switch and resonant inductor only. When the switch is turned on, the output impedance is zero. When the switch is turned off, the output impedance is essentially inductive. From the study above, the characteristics of the output impedance of switching amplifiers in the next chapter depict that the design of IMNs can be incorporated into the design of dc/ac inverters.

3.4 Summary

The power-flow method can be applied to both HVPTs and LVPTs. In order to obtain the two-port parameters to perform this method, a network analyzer or impedance analyzer is needed. Nevertheless, both analyzers are very expensive. A conventional method was proposed to decide the optimal load by knowing the output capacitance of the PT, Cd2, and its mechanical resonance frequency, fs. This method is especially useful for the HVPTs for its high output impedance and lower frequency operation. On the contrary, the power-flow method must be adopted in finding the optimal load of the LVPTs. Based on the optimal load, decided by power flow model, the matching networks for the PT were designed and implemented to obtain an optimal power gain of the PT. However, the total efficiency for the PT and matching networks turned out to be lower than expected, because the inductances of matching inductors were relatively low and could not be tuned continuously for the thickness vibration PTs. Besides the optimal termination of the PT, the other parameters that will affect the efficiency of the PT converters include support points of the PT, input matching network designs, and power amplifier or dc/ac inverter designs for PT converters. The first three issues were discussed in Chapters 2 and 3. The amplifier design will be introduced in the next chapter.

4. Design Tradeoffs and Performance Evaluations of Power Amplifier Topologies

4.1 Introduction

The function of a typical power amplifier is to increase the amplitude of the signal to a larger value for higher power applications. The power amplifiers specified in this chapter are actually dc/ac switching inverters having sinusoidal waveforms at outputs, and the frequency of the sinusoidal waveforms is equal to the switching frequency of the switches. It is possible to use conventional power amplifiers to drive the PTs, but apparently the efficiency of the power amplifiers is lower than that of switching amplifiers. Because PTs are low-power devices, the general requirements for the applications of PTs include low-power, low cost, and high efficiency. It is important to reduce the number of inductive components and switches in amplifier or dc/ac inverter designs for PT applications.

In order to study all possible interactions between PTs and amplifier circuits, LVPT-21 is chosen in this chapter as the example PT. Constant-frequency control is adopted to prevent operating LVPT-21 between spurious vibration frequencies where variable frequency control of the LVPT-21 is impossible to achieve. Therefore, the performance of the amplifier circuits is evaluated with the load, including LVPT-21 and its output rectifier circuit, under two possible operating frequencies of 1.92 and 1.96 MHz, as concluded in Chapter 3. At the same time, the optimal loads of LVPT-21 are calculated by the power flow method with two-port parameters at two different frequencies. As a result, the loads for the amplifier circuits are known, and it is feasible to design the amplifier circuits or desired output matching networks. Because of no spurious vibration for most of HVPTs, either constant and variable frequency control can be applied to HVPT-2, and it will be introduced in Chapter 5.

It seems feasible to utilize resonant circuits or low-pass filters to generate sine waveforms to the input of PTs. They are half-bridge parallel-resonant amplifiers, single-ended multi-resonant (SE-MR) amplifiers [45], and a family of single-ended quasi-resonant (SE-QR) amplifiers [17,23]. The design curves and their associated design examples by using LVPT-21 as a step-down

transformer are given for half-bridge and single-ended amplifier circuits. The load of amplifier circuits includes LVPT-21 and its output rectifier circuit. Finally, the performances of different amplifier circuits are compared for efficiency, component counts, and suitability.

4.2 Half-Bridge PT Converter

4.2.1 Operational Principles of Half-Bridge Amplifier

The half-bridge amplifier can be decomposed to a square wave source, generated by two complementary switches, and a parallel resonant circuit. Figure 4.1 shows the circuit diagram of a half-bridge amplifier and its theoretical waveforms. C_B is the blocking capacitor. L_R and C_{IN} form the low-pass filter, and C_{IN} might be replaced by the input intrinsic capacitor of the PTs. The low-pass filter is needed to prevent the harmonic contents from entering into the PTs and is regarded as an input matching network. From the theoretical waveforms shown in Fig. 4.1 (b), the ZVS operation can be achieved naturally when the switching frequency Fs is greater than the tank resonant frequency Fo, where

$$Fo = \frac{1}{2 \cdot \pi \cdot \sqrt{L_R \cdot C_{IN}}} \ , \tag{4.1}$$

and the load characteristic is inductive. However, when R_{IN} becomes small, the resonant inductor current will decrease accordingly. Thus, the ZVS operation will be lost, as shown by the dotted line in Fig. 4.1 (b). Therefore, La is used to assure zero-voltage switching on S_1 and S_2. This type of amplifier was introduced to drive PT converter circuit in [20]. More detailed design considerations are presented in the following sections.

4.2.2 Equivalent Circuit of the Half-Bridge PT Converter

Because the nature of the half-bridge amplifier is similar to that of the buck converter, it is suitable for step-down applications, and it can be operated either by constant- or by variable-frequency control. Figure 4.2 shows a complete LVPT dc/dc converter powered by a half-bridge inverter or amplifier. Because the input voltage and current waveforms of the LVPT-21 are sinusoidal, the input impedance Y_{IN} can be calculated directly from the model derived in Chapter 2 and is represented by a parallel combination of R_{IN} and C_{IN}. R_{IN} and C_{IN} are functions of R_L and Fs, and are shown in Fig. 4.2 (b). For example, R_{IN} = 35 Ω and C_{IN} = 1350 pF when R_L = 10 Ω and Fs = 1.96 MHz from Fig. 4.2 (b). The square-wave source shown across La can be approximated by its first order harmonics and

$$\left|V_S\right| = \frac{\sqrt{2}}{\pi} \cdot V_{IN} \cdot \sqrt{1 - \cos(2 \cdot \pi \cdot D)} \ , \tag{4.2}$$

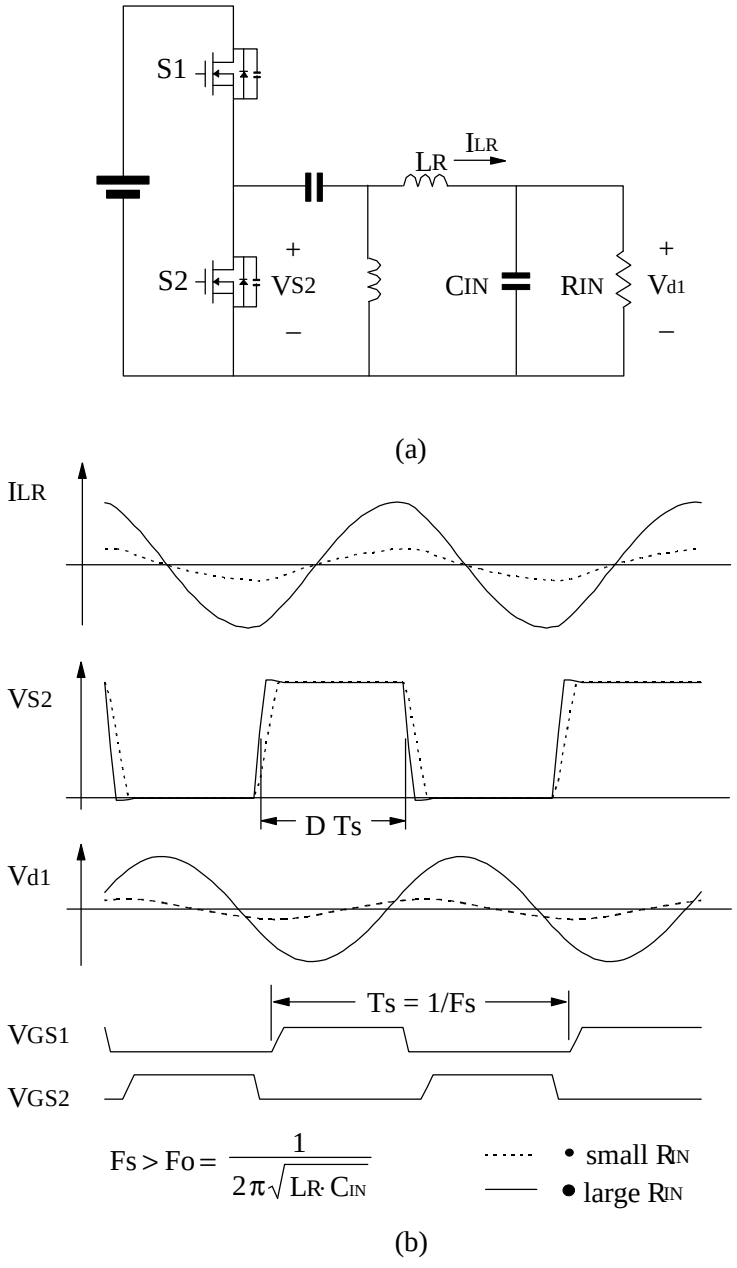

Fig. 4. 1. Half-bridge amplifier and its theoretical waveforms. (a) half-bridge amplifier. (b) theoretical waveforms. When R_{IN} becomes smaller, the resonant frequency will move to a smaller value for the typical operation of a parallel resonant circuit. Therefore , ZVS will be lost if no external inductor is added to help discharge the capacitors of the switches.

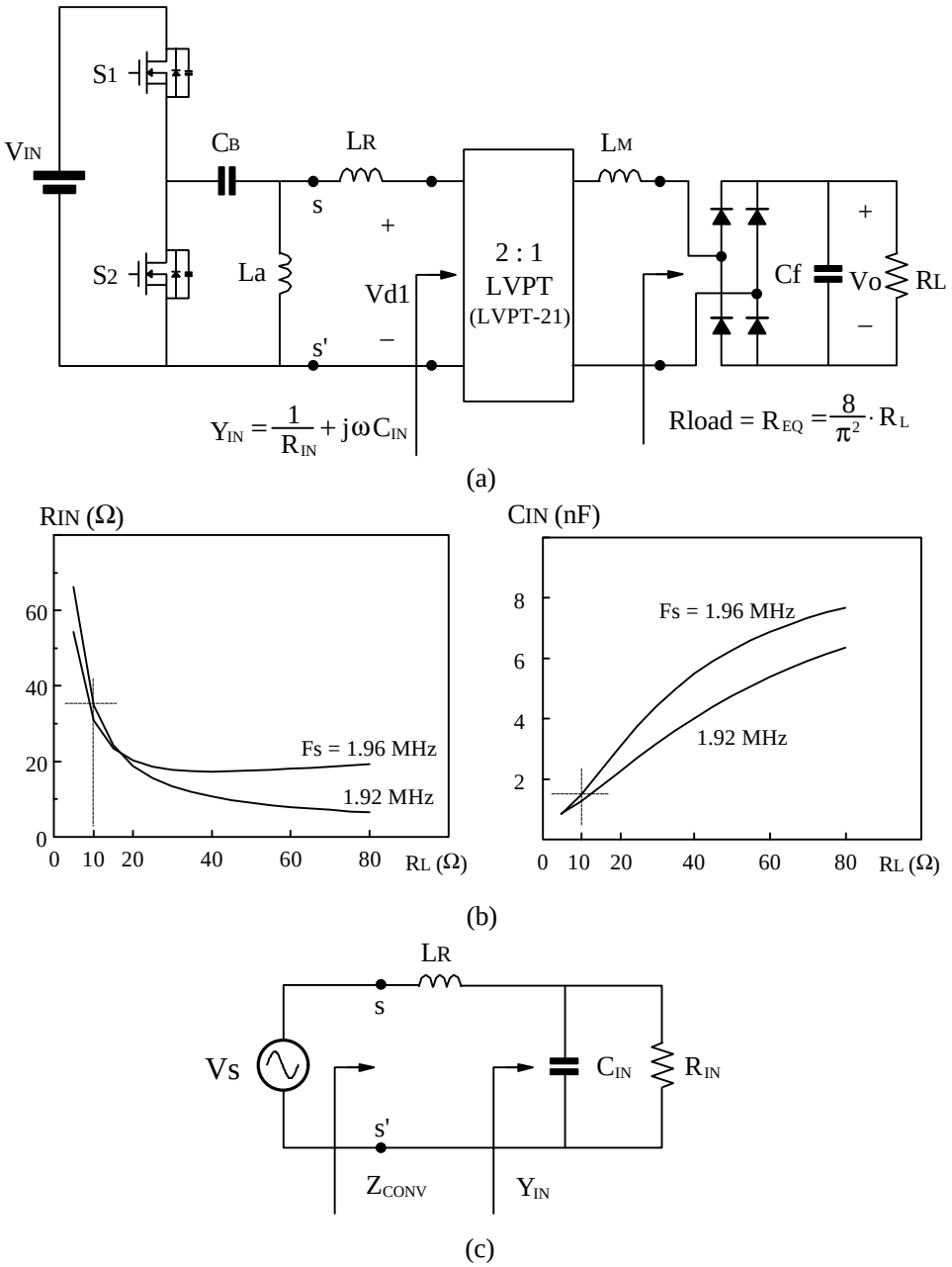

Fig. 4. 2. Complete half-bridge PT converter and its equivalent circuit. (a) half-bridge PT converter. (b) R_{IN} and C_{IN} of the LVPT-21. (c) equivalent circuit. R_{IN} and C_{IN} are the parallel combination of Y_{IN} which is a function of R_L and Fs. The higher the R_L, the smaller the R_{IN}. Therefore, La is added to help achieving ZVS operation while q_p becomes small.

where D is the duty cycle of the half-bridge amplifier and is less than 0.5. In order to provide enough dead time between two gate drives and enhance transient response performance, the maximum duty cycle is chosen between 0.35 to 0.4. Figure 4.2 (c) shows the equivalent circuit of a half-bridge PT converter; the input power stage of the half-bridge amplifier is equivalent to a sinusoidal source Vs, and the PT and its load Z_L are represented by R_{IN} and C_{IN}. As a result, the equivalent circuit does not include any active switch, and it can be analyzed by employing a software program in MATLAB.

4.2.3 DC Characteristics and Experimental Verifications

In Chapter 3, the possible operating frequencies for LVPT-21 to obtain satisfactory efficiencies and voltage gains are 1.92 MHz and 1.96 MHz. Since the operating frequencies and optimal load Rload and matching inductance L_M of LVPT-21 are all predetermined in section 3.3.3.1, the only design parameter left is L_R. Figure 4.3 (a) depicts the phase angle of the input impedance of the converter Zconv. vs. the load resistance R_L with L_R as the running parameters at 1.92 MHz and 1.96 MHz, respectively. When R_L is less than 10 Ω, the phase angles of Z_{CONV} become negative for L_R = 1μH and 1.5μH. This indicates that the ZVS operation of the half-bridge amplifier is lost if there is no extra La added. By adding an inductor La = 6 μH, the phase angles of Z_{CONV} shown in Fig, 4.3 (b) are positive. Therefore, the impedance characteristic of the half-bridge converter is inductive and ZVS on the switches are maintained. The voltage gains of the converter are shown in Fig. 4.3 (c) when D = 0.36. It can be seen that the higher L_R is, the more easily the switches can achieve the ZVS operation. However, the gain of the converter decreases when L_R becomes large.

To verify the previous results for the equivalent circuit, a half-bridge LVPT converter was built with the following parameters and input-voltage values:

- Vin = 25 Vdc,
- D = 0.36,
- L_R = 1.6 μH, and
- L_M = 420 nH.

Figure 4.4 shows output voltages vs. load resistance R_L at 1.92 and 1.96 MHz. The waveform with solid line is simulated by MATLAB for the equivalent circuit of the half-bridge LVPT converter. The waveform with square symbols is generated by the SIMPLIS software program for circuit simulation. The last curve shows the experimental results. These three curves are close to each other and well explain the usefulness of the lumped model of LVPT-21 and its associated equivalent circuit for the half-bridge PT converter.

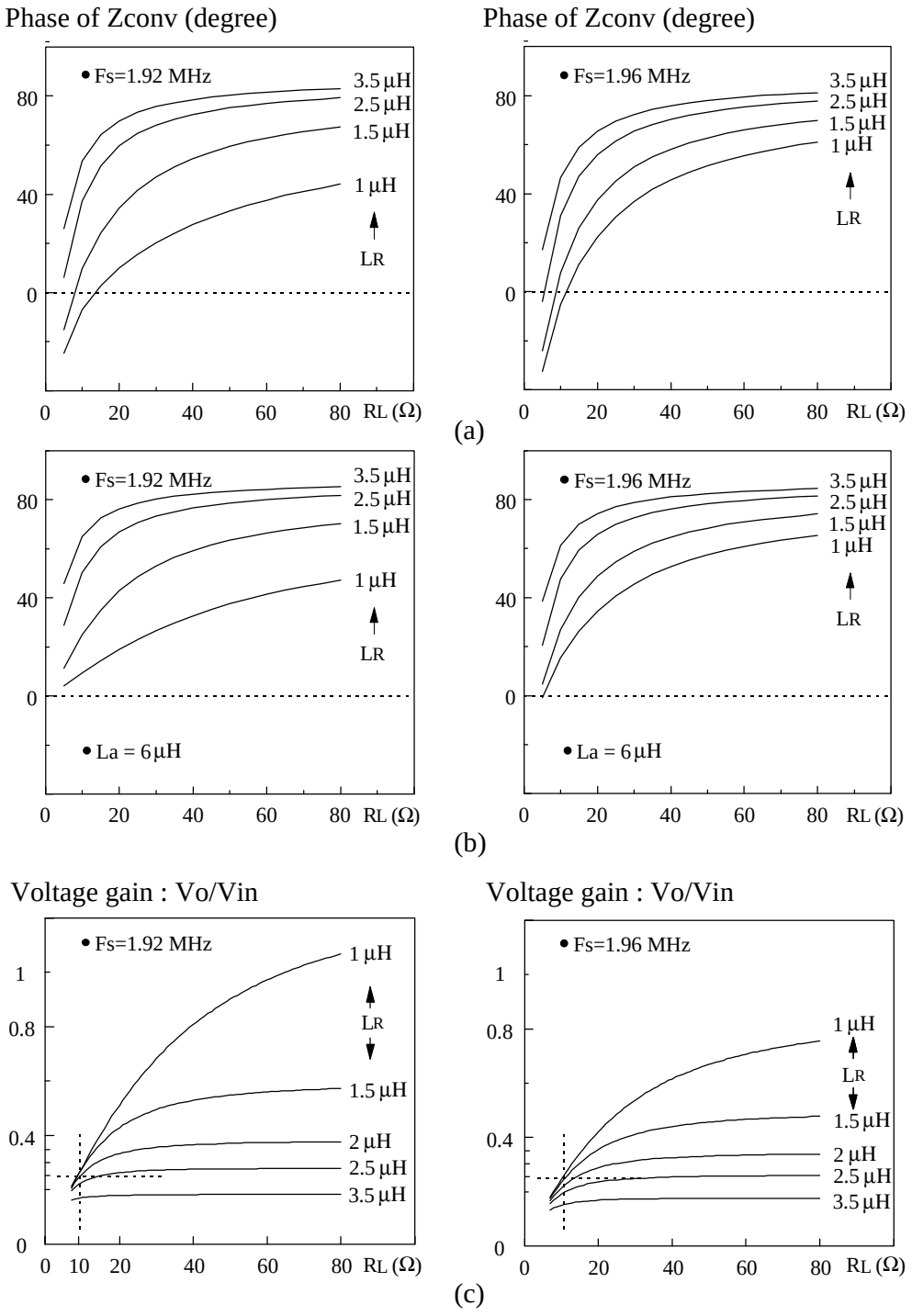

Fig. 4.3. DC characteristics of the half-bridge LVPT converter. (a) phase angle of the input impedance Z_{CONV}. (b) phase angle of the input impedance in parallel with La. (c) voltage gain of the converter. Both results have been calculated by MATLAB.

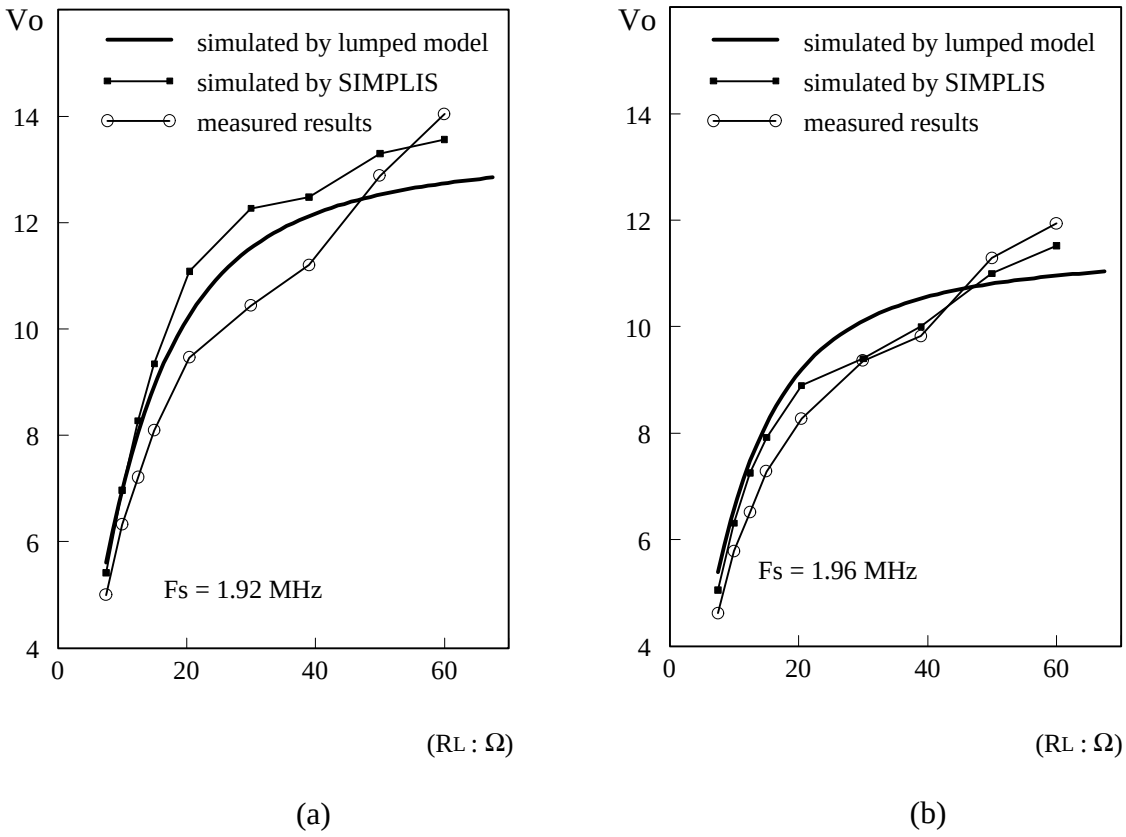

Fig. 4. 4. Output voltage of the half-bridge PT converter. (a) Fs = 1.92 MHz. (b) 1.96 MHz. The voltage curves with solid line are calculated by MATLAB with the lumped model of the converter. The curves with square makers are simulated by SIMPLIS, and the curves with circle maker are measured results. Measurements are taken when Vin = 25 Vdc, D = 0.36, and L_R = 1.6 uH.

Another experimental result for verification purposes is shown in Fig. 4.5 which illustrates output voltage Vo vs. Fs, and again the solid line is calculated by MATLAB with the equivalent circuit for the LVPT converter. The curve with square symbols is also calculated by MATLAB, except that the model of the LVPT-21 is based on the measured two-port parameters and the third curve shows the experimental results. The last two curves are almost identical in shape; however, a frequency shift is observed. Figure 4.5 (b) shows the output-voltage curves measured at different power levels. This tells that the mechanical resonant frequency of LVPT-21 is changed by the amount of power processed by the PT. When the power level is low, the input impedance of the PT is similar to that measured by impedance analyzer. Figure 4.5 (c) suggests that the efficiency at 1.96 MHz for LVPT-21 is better than that at 1.92 MHz. So Fs is chosen as 1.96 MHz in the final design example. Besides, the constant-frequency control is adopted because the voltage gain characteristic shown in Fig. 4.5 (a) is not monotonous.

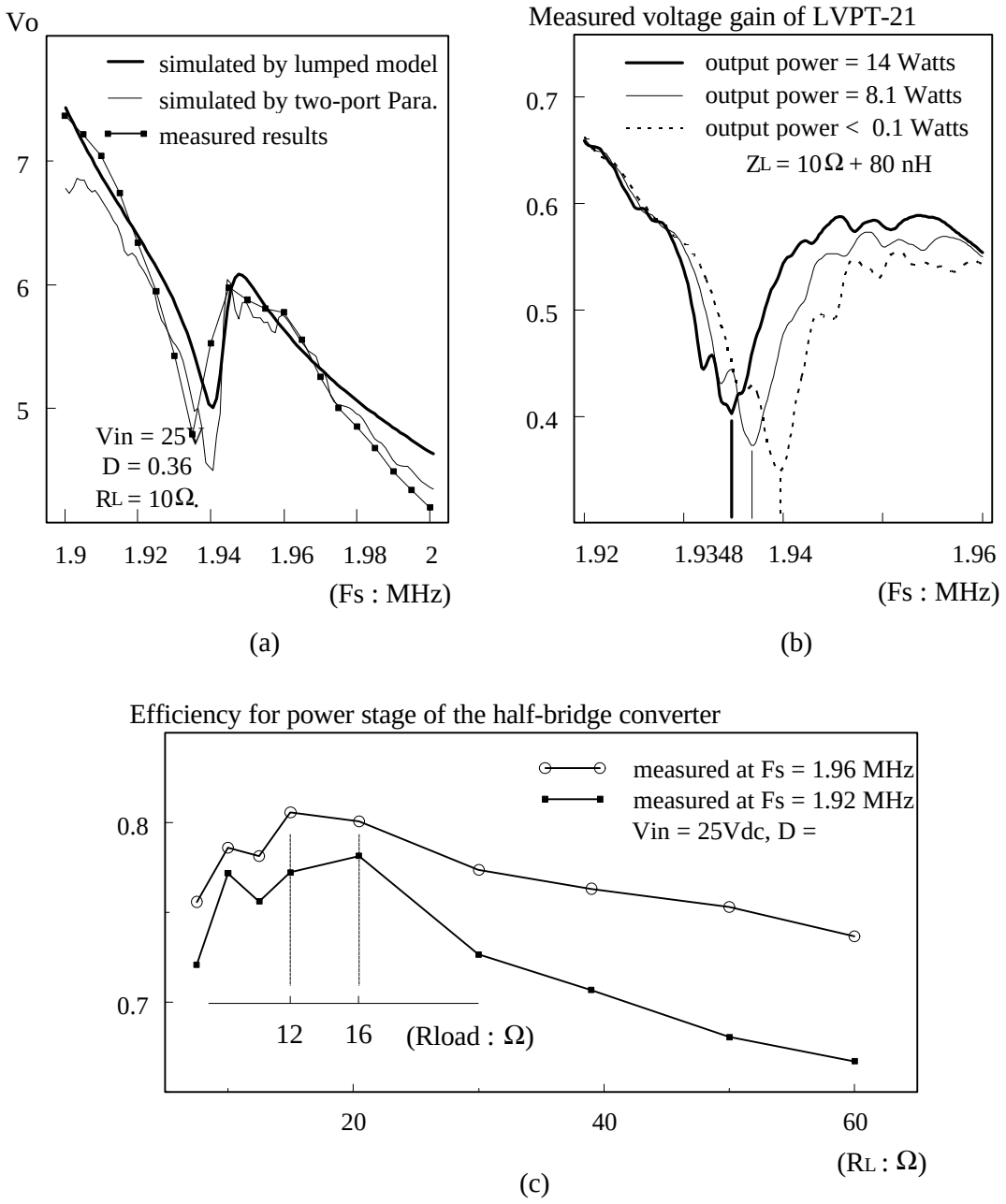

Fig. 4. 5. Efficiencies and output voltage of the half-bridge PT converter. (a) output voltage vs. switching frequency Fs. (b) shift on resonant frequency. (c) efficiencies of the PT converter. Measurements in (a) and (b) are taken when Vin = 25 Vdc, D = 0.36, and L_R = 1.6 uH. From (a), it can be observed that the experimental voltage curves shift about 50 kHz from the calculated curves, because the voltage-gain curves for LVPT-21 shift with the output power level, as shown in (b).

4.2.4 Design Guidelines and Experimental Results

The specifications of the LVPT converters are given below:

Input voltage = 44 - 52 Vdc,
Output voltage = 12 Vdc, and
Output Power = 14.4 watts (maximum)

The voltage gain of the converter is around 0.25 and the R_L = 10 Ω under maximum output power. From Fig. 4.3 (c) for Fs = 1.96 MHz, L_R falls between 1.5 μH and 2 μH. L_R = 1.6 μH is chosen. La is calculated so that the peak stored inductor energy is greater than the total energy required to discharge the combined capacitor of S_1 and S_2. To simplify the derivation, assuming that D = 0.5, the objective equation to decide La is

$$\frac{1}{2}\cdot La\cdot i_{pk}^{\ 2} \geq \frac{1}{2}\cdot C_T\cdot V_{IN}^{\ 2}\ , \tag{4.3}$$

where C_T is the total capacitance of a shorted and a full charged parasitic capacitance of the switches and can be found separately from the data sheet of the switch. The peak current of La, i_{pk}, is one half of the current charged by Vin/2 when S_1 is turned on.

$$i_{pk} = \frac{V_{IN}}{8\cdot La\cdot Fs} \tag{4.4}$$

Substituting (4.4) to (4.3), La is solved as

$$La \leq \frac{1}{64\cdot C_T\cdot Fs^2}\ . \tag{4.5}$$

La needs to be chosen carefully so that the magnitude of the circulating current is minimized and ZVS operation is kept. Figure 4.6 (a) illustrates the complete power stage of the PT converter and its component values. La is calculated as 6.56 μH when Fs = 1.96 MHz and C_T = 620 pF for the MOSFET IRF 520. The salient waveforms are shown at the bottom in Fig. 4.6. The waveform of Vd2 is almost sinusoidal compared to the input voltage waveform Vd1 of the PT. This illustrates the band-pass and high-Q characteristics of LVPT-21. Figure 4.7 shows the efficiencies of the PT converter when L_R = 1.6 and 0.8 μH. The efficiency for L_R = 1.6 μH is better than that for L_R = 0.8 μH because of higher duty-cycle operation for the former L_R. The best efficiency is 84 % when output power is 10 Watts.

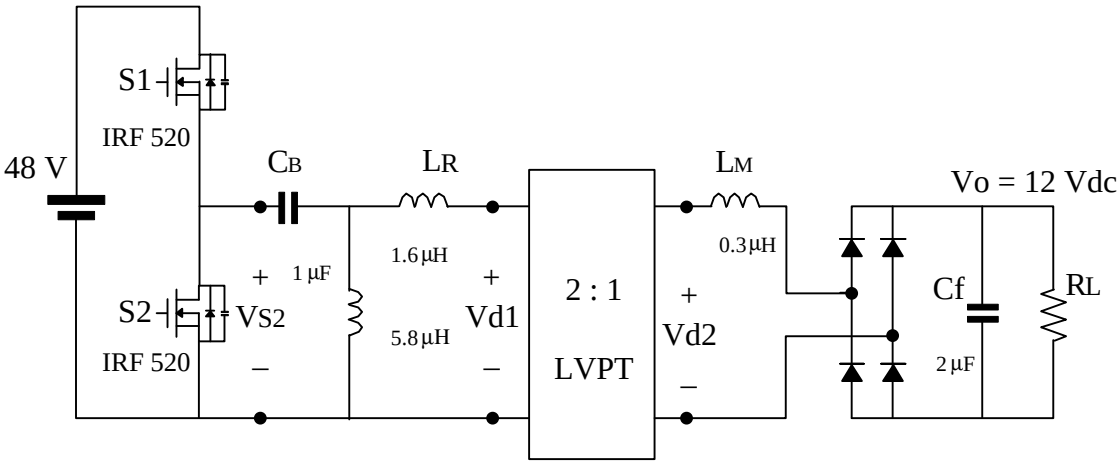

(a)

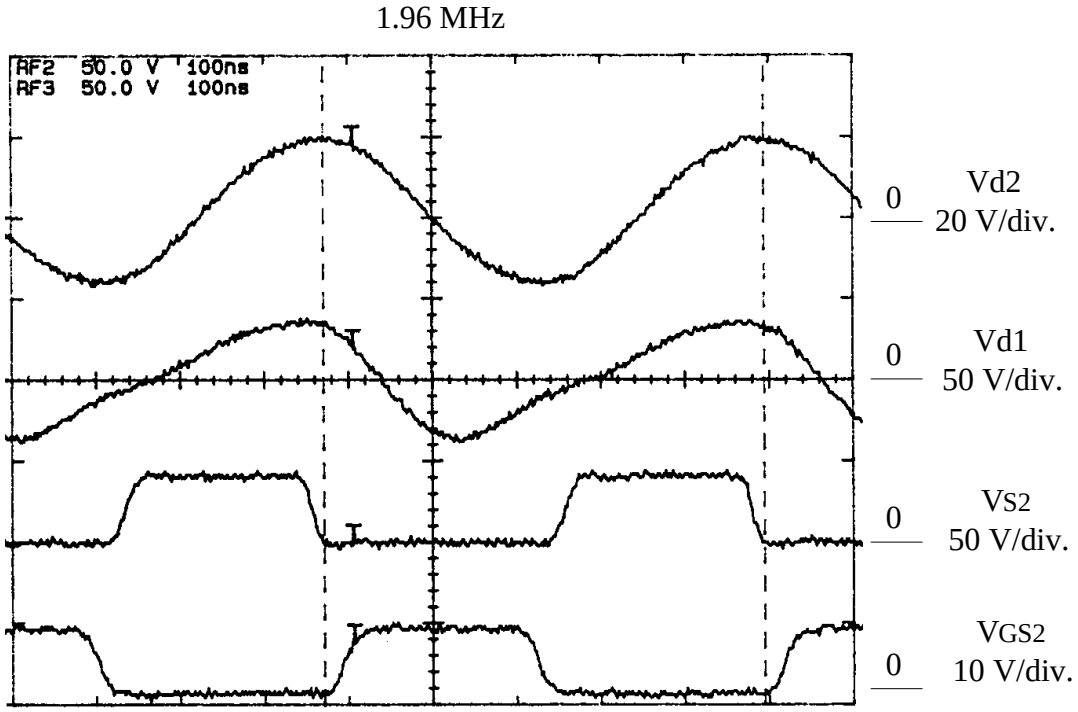

(b)

Fig. 4. 6. Design example of the half-bridge PT converter. (a) power stage. (b) experimental waveforms.

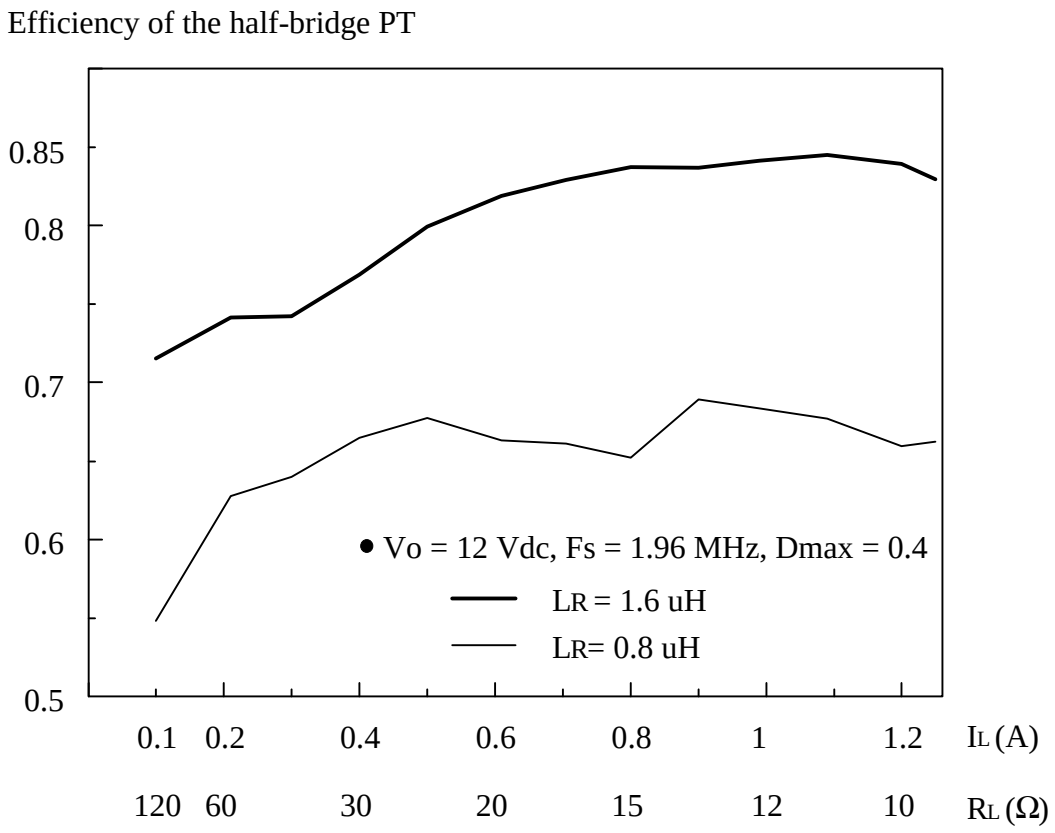

Fig. 4. 7. Efficiencies of the half-bridge PT converter. When LR = 1.6 μH, the maximum efficiency occurs around RL = 12 Ω which is close to the optimal load resistance calculated by the power flow method in Chapter 3. When L_R = 0.8 μH, the characteristic impedance decreases and voltage gain increases, and so does the current stress in the switches. Therefore, the conduction loss of the converter increases, and efficiency reduces by 10%.

4.3 Single-Ended Multi-Resonant PT Converter

4.3.1 Operational Principles of SE-MR Amplifier

A single-ended multi-resonant (SE-MR) amplifier [45], shown in Fig. 4.8 (a)., is capable of delivering a sinusoidal voltage to the load R_{IN} and achieving zero-voltage switching for the main switch. C_B is the blocking capacitor, and the DC bias is equal to V_{IN}. This is a multi-resonant converter. When S_1 or its anti-parallel diode conducts, the resonant frequency is determined by LR and C_{IN}. While S_1 is turned off, the resonant frequency is decided by L_R and the parallel

combination of C_{IN} and C_S. Compared to the SE-MR amplifier, the class E amplifier [43-44] does not utilize the input capacitor of the PT as a resonant component. But the class E amplifier does not need the blocking capacitor; however, the size of the blocking capacitor is small due to the high-frequency operation. So the SE-MR amplifier was chosen as a design example in the multi-resonant converter family. Figure 4.8 (b). illustrates the theoretical waveforms of the SE-MR amplifier.

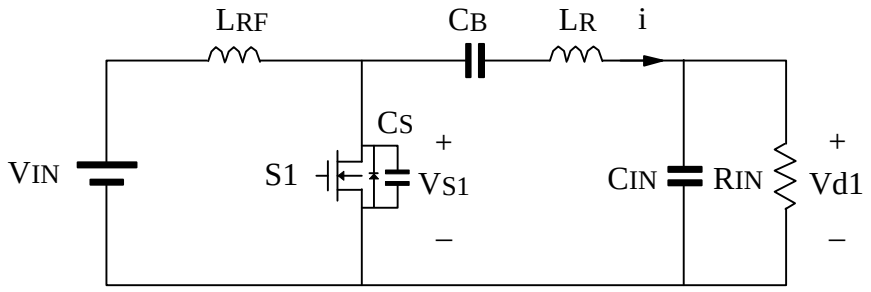

(a)

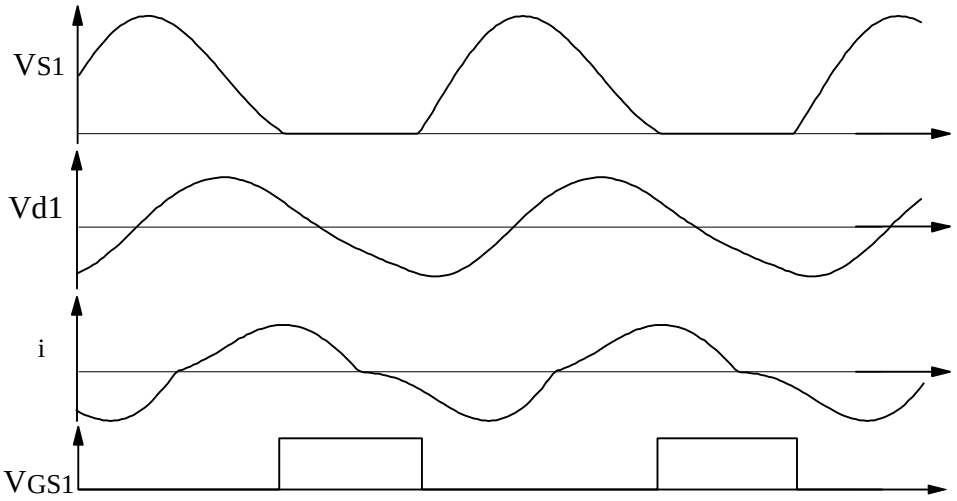

(b)

Fig. 4. 8. Single-ended multi-resonant (SE-MR) amplifiers. (a) Power stage. (b) theoretical waveforms.

4.3.2 Equivalent Circuit of the SE-MR PT Converter

Figure 4.9 (a) shows the block diagram of a SE-MR PT converter. Because the model of the PT has been derived earlier, it is possible to incorporate the PT model and other components of the converter into circuit simulation program directly. This is probably the best way to analyze any multi-resonant related converter. However , the PT and its load can be represented by a frequency and load dependent impedance which is mentioned in the section discussing the half-bridge PT converter. Using the fact that the waveform of Vd1 is nearly sinusoidal makes it possible to simplify the PT and its load as a parallel connection of R_{IN} and C_{IN} in Fig. 4.9 (b).

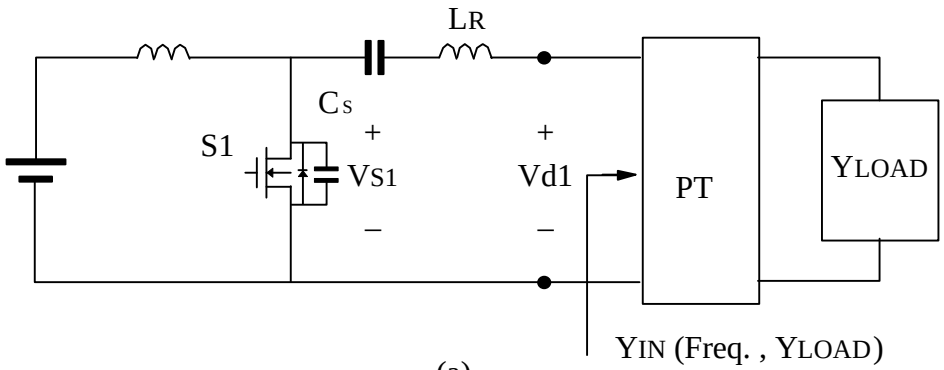

(a)

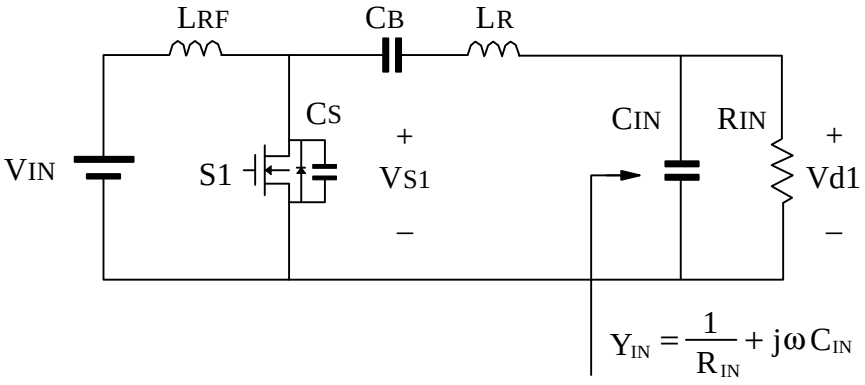

(b)

Fig. 4. 9. SE-MR PT converter and its equivalent circuit. (a) block diagram of power stage. (b) equivalent circuit of SE-MR PT converters.

4.3.3 DC Characteristics

The equivalent circuit of the SE-MR PT converter consists of the SE-MR amplifier and the PT model. Because the active switch exists in the equivalent circuit, it is very tedious to find an analytical solution for the state variables such as inductor current and capacitor voltages for multi-resonant circuits. Therefore, the DC analysis of the multi-resonant converter can only be studied via software circuit simulation programs where the steady-state or the periodic solutions of the state variables can be resolved. The DC analysis of the SE-MR PT converter is carried out by employing a software program SIMPLIS. For the purpose of designing the power stage of the SE-MR amplifier, the voltage ratio M is equal to

$$M = \frac{Vd1_{(RMS)}}{V_{IN}} , \tag{4.6}$$

where $Vd1_{(RMS)}$ is defined as the RMS voltage at the output of the amplifier. Vs_max is the maximum voltage stress of S_1, and C_n is C_{IN}/C_S. The characteristic impedance and the resonant frequency can be defined as:

$$Z_o = \sqrt{\frac{L_s}{C_s}} \tag{4.7}$$

$$F_o = \frac{1}{2\pi\sqrt{L_S C_S}} . \tag{4.8}$$

All the voltages and switching frequencies are normalized as follows:

$$v_n = \frac{v}{V_{IN}} , \tag{4.9}$$

$$F_n = \frac{F_S}{F_o} , \tag{4.10}$$

$$q_P = \frac{R_{IN}}{Z_o} . \tag{4.11}$$

4.3.4 Design Guidelines and Experimental Results

Figure 4.10 shows M and Vs_max vs. normalized frequency Fn employing q_p as running parameters for C_N = 2, 3, and 4. The optimal frequency is chosen between 0.7 and 0.9. The upper limit is obtained to ensure the ZVS operation on S_1, and the lower limit is set for minimizing the voltage stress of S_1. From Fig. 4.10, the design steps are:

Step 1: Pick a C_N

Step 2: Choose the voltage conversion ratio. $Vd1_{(RMS)}$ is calculated according to the output power and efficiency η_{PT} of the PT and the rectifier circuit.

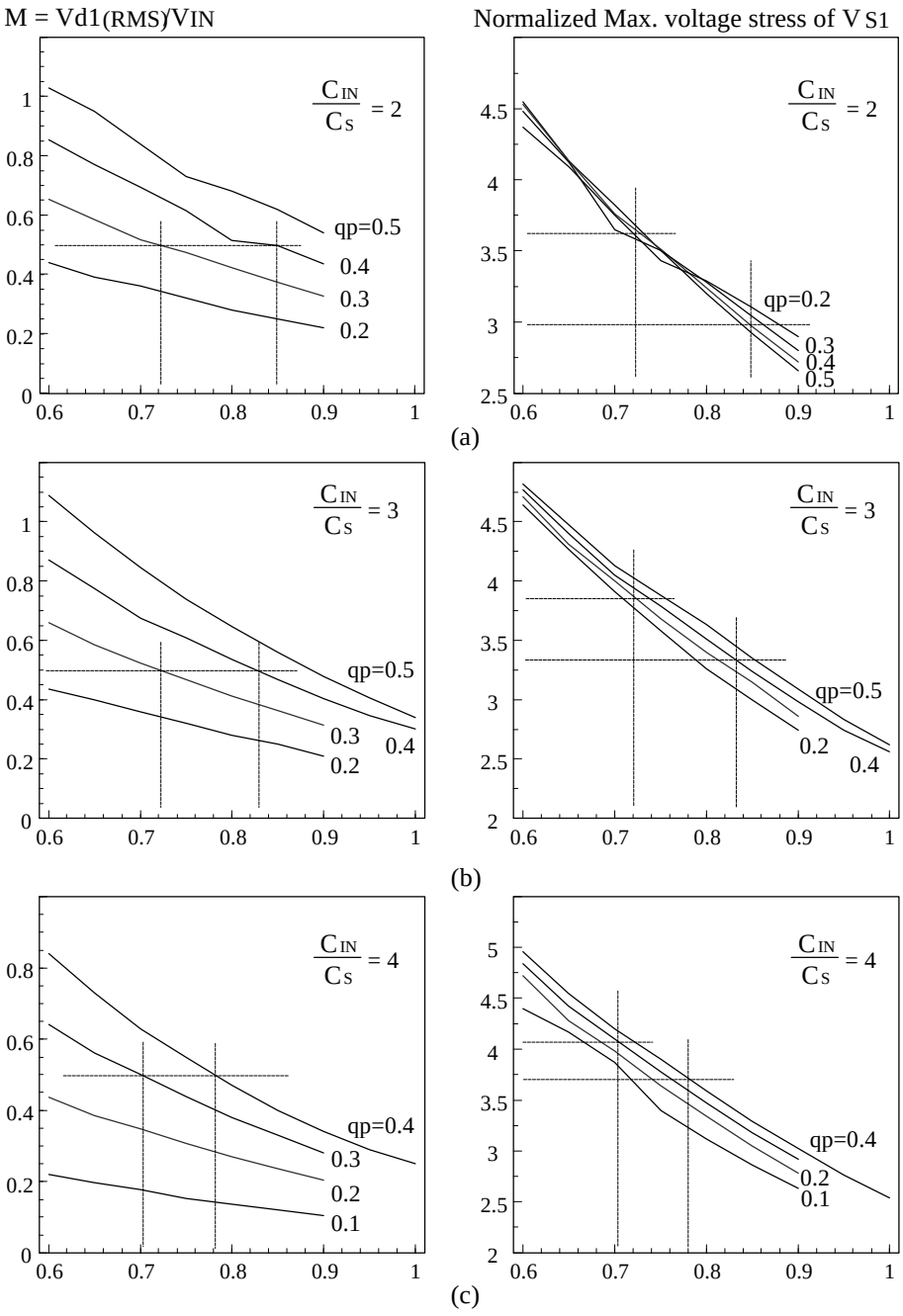

Fig. 4. 10. Normalized voltage gain and voltage stress of SE-MR amplifiers. (a) Cn = 2. (b) Cn = 3. (c) Cn = 4. The break points indicate where the ZVS is lost. Since the optimal load of the PT and operating frequencies are predetermined, L_R is the only design parameter left. The calculated results are simulated by the SIMPLIS software program.

$$Vd1_{(RMS)} = \sqrt{\frac{Pout \cdot R_{IN}}{\eta_{PT}}} \tag{4.12}$$

$$M = \frac{Vd1_{(RMS)}}{V_{IN}} \tag{4.13}$$

Step 3: Choose q_p and F_n. From a calculated M, the lower and upper limits of qp are determined from Fig. 4.10. The lower limit of qp is set to determine the minimum Fn, and the upper limit of qp is used to determine the maximum Fn. Fn should be located between 0.7 and 0.9.

Step 4: Find L_R , Cs, and C_{IN}. Once Fn and qp are known, Cs is calculated by

$$Cs = \frac{Fn}{2\pi \cdot Fs \cdot Zo} = \frac{Fn \cdot q_p}{2\pi \cdot Fs \cdot R_{IN}} \ , \tag{4.14}$$

where Fs is the switching frequency of the converter and R_{IN} is shown in Fig. 4.2 (b).

The specifications for the design example are identical to those for the half-bridge converter in 4.2.4. LVPT-21 is used as a step-down transformer. Since maximum output power is equal to 14.4 Watts and η_{PT} = 0.9, $Vd1_{(RMS)}$ is calculated to be 23.66 Volts when Fs = 1.96 MHz, R_{IN}=35 Ω, and C_{IN}=1.35 nF shown in Fig 4.2 (b). The voltage ratio M = 23.66/48 = 0.49. Table 4.1 tabulates the values for Fn, Vs_max, Cs, and L_R for different values of C_N when qp = 0.3 and 0.4, respectively. When C_N = 4, the highest Vs_max is obtained. It is appropriate to adopt the results calculated when C_N = 2 or 3. The final design selects C_N = 3 because the parasitic capacitance of the MOSFET and the input capacitance of LVPT-21 are fully utilized under the full load condition. From Table 4.1, Cs = 500, L_R = 6.8 μF and three times of Cs is 1500 pF. The normalized maximum voltage stress is 3.85.

Table 4.1. Calculated parameters for the SE-MR LVPT converter at Fs = 1.96 MHz.

• qp = 0.3

Cn	Fn	Vs_max	Cs	Cs x Cn	L_R
2	0.72	3.65	500 pF	1 nF	6.8 μ
3	0.72	3.85	500 pF	1.5 nF	6.8 μ
4	0.7	4.15	487 pF	1.9 nF	6.6 μ

• qp = 0.4

Cn	Fn	Vs_max	Cs	Cs x Cn	L_R
2	0.85	3	789 pF	1.6 nF	6 μ
3	0.83	3.3	770 pF	2.3 nF	5.9 μ
4	0.78	3.7	724 pF	2.9 nF	5.5 μ

When Cn = 4, the highest normalized voltage stress is obtained and extra capacitor is needed to add on the input of the PT for C_{IN} = 1.35 nF. The calculated parameters for both Cn = 2 and 3 can meet the design requirements. When Cn = 2 and qp = 0.4, Fn = 0.86. S1 will lose the ZVS operation when R_L is increased and R_{IN} decreased in Fig. 4.2 (b). When Cn = 3 and qp = 0.3, Cs and 3 x Cs are close to output capacitances of S_1 and C_{IN} respectively; they are chosen in the experimental circuit.

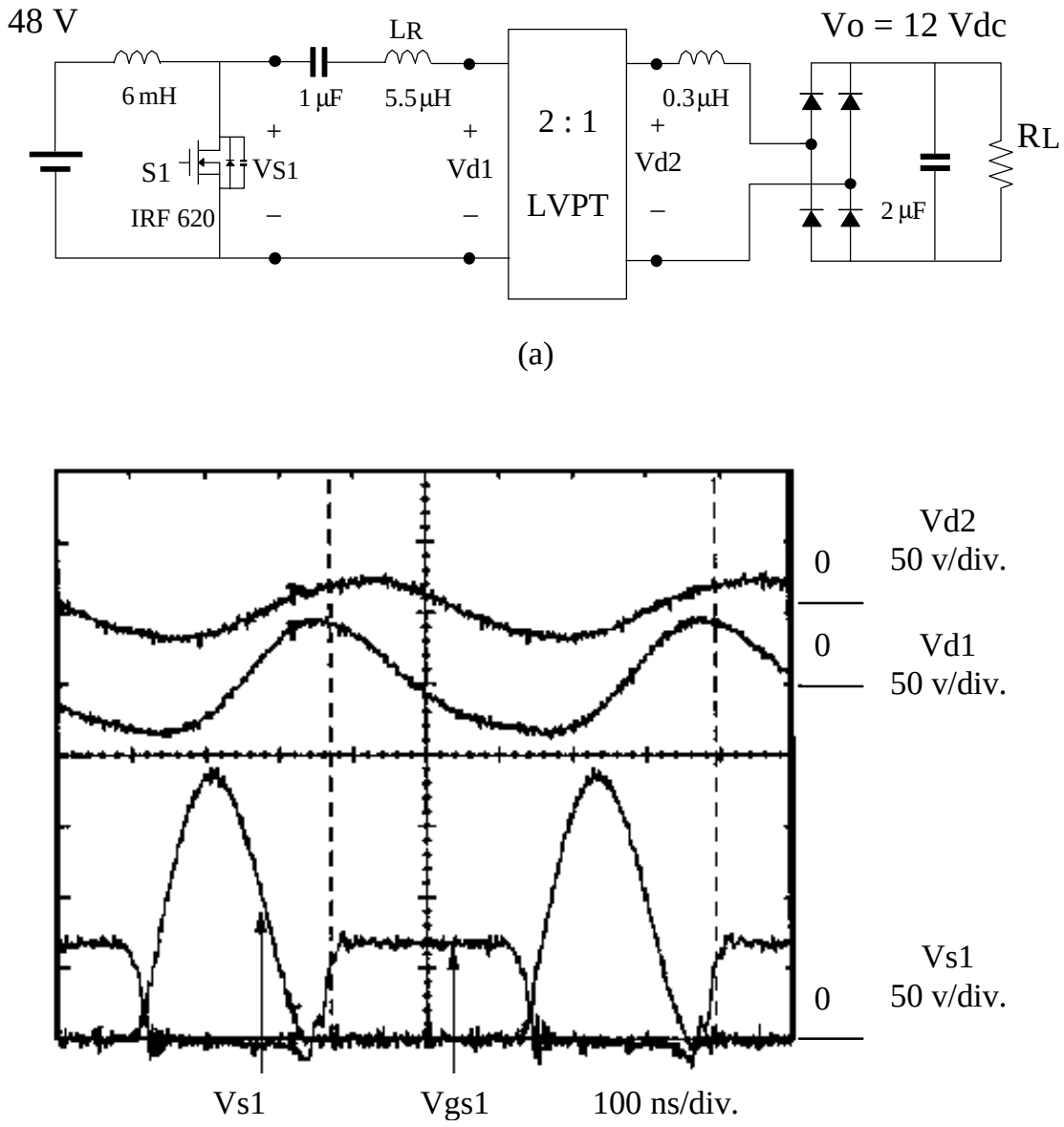

Fig. 4. 11. Design example of the SE-MR PT converter. (a) power stage. (b) experimental waveforms.

The experimental circuit is shown in Fig. 4.11 (a), the inductance for L_R changes slightly so that no extra capacitances are required to add to Cs and C_{IN} while the same voltage gain is kept. From the experimental waveforms in Fig. 4.11 (b), the maximum voltage stress of S_1 is 180 Vdc

which is similar to the simulation results. The best efficiency of this converter for the power stage is 81 %.

4.4 Single-Ended Quasi-Resonant (SE-QR) PT Converter

4.4.1 Operational Principles of the SE-QR Amplifier

4.4.1.1 SE-QR Amplifiers

This family of this type of amplifier circuit had been found in [10,17]. Figure 4.12 (a). shows the SE-QR amplifier with a load R_{IN} and the resonant capacitor C_{IN}. The amplifier includes only a resonant inductor L_R and a switch S_1. Compared to the SE-MR amplifier, the resonant tank is composed of L_R and C_{IN} and is only activated when the switch is turned off as shown in Fig. 4.12 (b). When the switch is on, the resonant inductor is charged linearly by the input voltage. Figure 4.12 (c). illustrates the theoretical waveforms of a SE-QR amplifier. The DC level of the resonant inductor current I_{LR} is determined by the load resistance R_{IN} as well as the characteristics impedance of the resonant tank Z_o, where

$$Z_o = \sqrt{\frac{L_R}{C_{IN}}} . \tag{4.15}$$

Therefore, the efficiency of this amplifier decreases when load current or Z_o decreases.

4.4.1.2 Flyback SE-QR Amplifiers

For the purpose of providing isolation and controlling the voltage gain, a flyback version of the SE-QR amplifier is introduced in Fig. 4.13 (a) and its theoretical waveforms are shown in Fig. 4.13 (b). Inductor L_P with a secondary winding L_R is used as both a resonant inductor and a step-up or step down transformer depending on the applications. Adding the secondary winding in L_P can be avoided if a designated step-up or step-down ratio of the PT can be designed in the beginning phase for a particular application. During the first stage, either S_1 or its anti-parallel diode is on, and the current in L_P is charging up while part of the energy is transferred to the load resistance. This is the major difference between the basic and flyback SE-QR amplifiers. At t0, S_1 is turned off and the primary current approaches zero because the capacitance, C_{IN}, of the PT to the primary side is much larger than the stray capacitance of the S_1. The voltage waveform of S_1 is actually shaped by the resonant circuit in the secondary side. Not until the voltage of S_1 reaches zero will the current flow in the secondary side. At t1, the anti-parallel diode conducts and current begins to flow in the primary side in the opposite direction. Before the primary current charges to the positive direction, S_1 is turned on with ZVS, and stage 1 resumes.

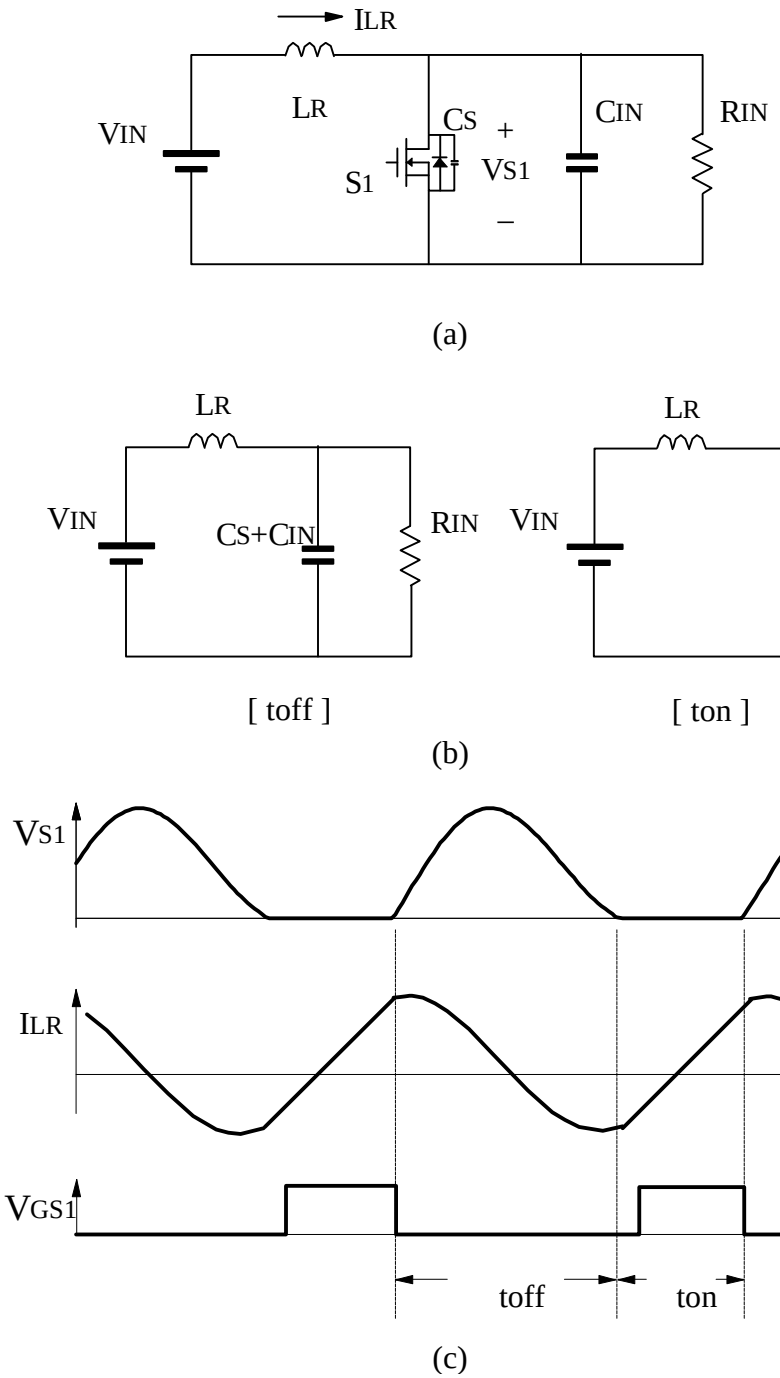

Fig. 4. 12. Single-ended quasi-resonant (SE-QR) amplifier. (a) power stage. (b) topological stages. (c) theoretical waveforms.

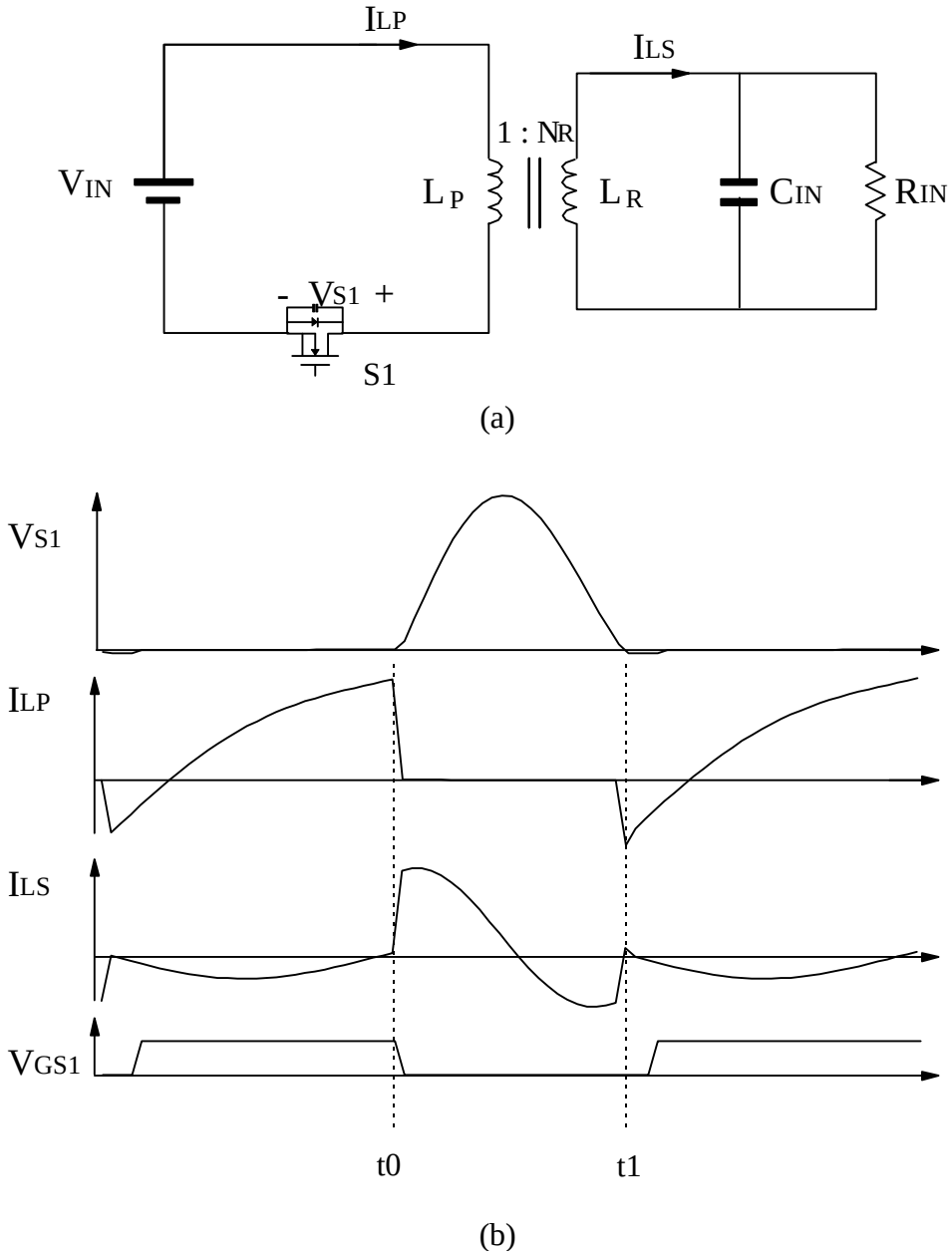

Fig. 4. 13. Flyback SE-QR amplifier. (a) power stage. (b) theoretical waveforms. This topology provides isolation and design of voltage conversion ratio by adjusting the turns ratio of the transformer.

4.4.2 Equivalent Circuit of the SE-QR PT Converter

This amplifier is connected to the input side of the PT. Although the current flowing inside of the PT is sinusoidal due to the very high Q from the characteristics of the PT, the input voltage waveform of the PT ,V_{S1} , is a quasi-square one. The concept of the driving point impedance is no longer valid under these voltage and current waveforms. In other words, the excitation force V_{S1} at Fs is not sinusoidal and contains strong second, third, and other high harmonic components. It can not be modified to a sinusoidal waveform with fundamental component only. Figure 4.14 (a) shows the block diagram of a SE-QR PT converter. Because the characteristics of the input impedance of the PT are capacitive under normal operation, as shown in Chapter 3 for LVPT-2, it is possible to find a parallel combination of capacitor C_{IN} and resistor R_{IN} shown in Fig. 4.12. to simulate the effect of PT and its load Y_{LOAD}. To find the resistance R_{IN}, the power balance between the power delivered to load Pout and the equivalent power consumed in R_{IN} is assumed. The output power of the PT Pout is equal to

$$\text{Pout} = \text{Vd1}_{(\text{RMS})}{}^{2} \cdot \text{Re}\left(Y_{\text{LOAD}}\right) , \tag{4.16}$$

and Vd1 is

$$\text{Vd1} = V_{\text{GAIN\_PT}}(\text{Freq.}, Y_{\text{LOAD}}) \cdot V_{\text{S1\_1st}} , \tag{4.17}$$

where V_{GAIN_PT} is the voltage gain of the PT calculated by its lumped model, and V_{S1_1st} is the fundamental harmonic of V_{S1}, as shown in Fig. 4.14 (b). Due to the high Q characteristics for the mechanical branch of the PT, the output voltage of the PT Vd2 is sinusoidal at Fs which is the fundamental component of V_{S1}. As a result, the voltage gain of the PT can be calculated by its lumped model as written in (4.17). The normalized vcn_1st is independent of load as long as qp is large, because it is a parallel resonant circuit whose voltage gain is load-insensitive. Since vcn_1st and V_{GAIN_PT} are known, the output power of the PT is determined for the given V_{IN} and Y_{LOAD}. In a similar manner, the normalized vcn with its root-mean-square value can be calculated, and R_{ACP} is used to replace R_{IN} and to represent the power delivered to PT:

$$R_{\text{ACP}} = \frac{\left(V_{\text{S1(RMS)}}\right)^{2} \cdot \eta_{\text{PT}}}{\text{Pout}} , \tag{4.18}$$

where η_{PT} is the efficiency of LVPT-21. As far as C_{IN} is concerned, the capacitance of C_{IN} is used to resonate with L_R and to shape the voltage waveform V_{S1}. In Fig. 4.14 (a), when S_1 is turned off, the amount of current flowing into Cd1 is much larger than that flowing in the mechanical branch of the PT. As a result, it is reasonable to assume that the voltage across S_1 is shaped by L_R and the input capacitance Cd1 of the PT under the condition that the characteristic impedance of the mechanical branch of the PT is very high. The complete equivalent circuit for the SE-QR PT converter is shown in Fig. 4.14 (c). Although an active switch is included in the equivalent circuit, the analytical solutions for the inductor current and the capacitor voltage are derived. Therefore, the DC characteristics of the equivalent circuit can be calculated by employing a software program in MATLAB.

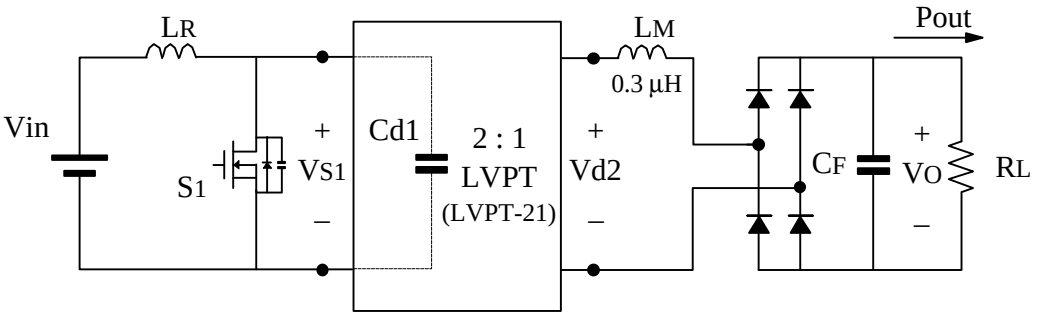

SE-QR Amplifier (a)

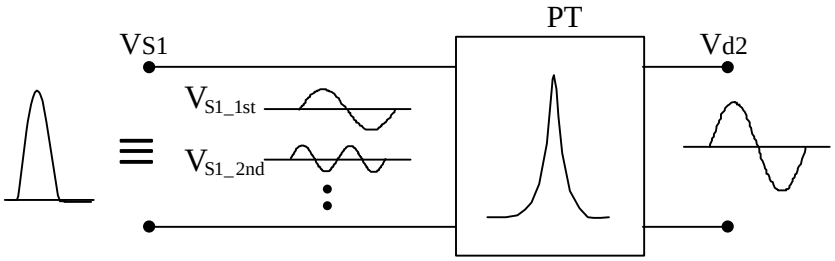

- $Vd2 = V_{GAIN\_PT}(Freq., Y_{LOAD}) \cdot V_{S1\_1st}$

(b)

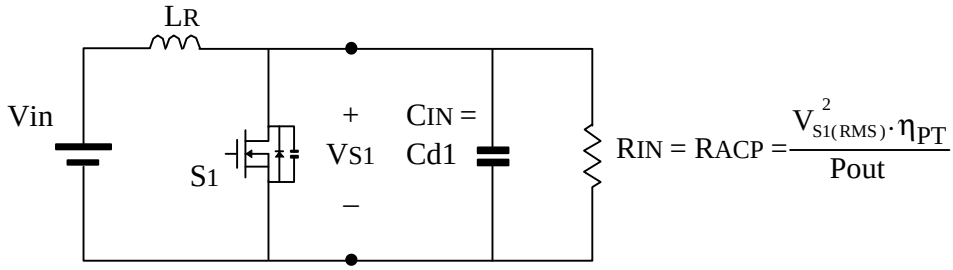

(c)

Fig. 4. 14. SE-QR PT converter and its equivalent circuit. (a) block diagram of the power stage. (b) band-pass characteristics of the PT. (c) equivalent circuit. During the turn-off stage of S_1, the input capacitance Cd1 provides a low impedance path compared to the mechanical branch of the PT. Accordingly, the major resonant component is Cd1 for the SE-QR inverter. The DC analysis of the equivalent circuit is done by a software program in MATLAB.

4.4.3 DC Analysis of SE-QR Amplifiers

4.4.3.1 SE-QR Amplifiers

From the topological stages shown in Fig. 4.12 (b), the normalized steady-state capacitor voltage vcn and inductor current iln during toff are derived as:

$$vcn(t) = 1 - \cos\omega t \cdot e^{-\alpha t} - \frac{\alpha}{\omega} \cdot \sin\omega t \cdot e^{-\alpha t} + Io \cdot \frac{\omega_o}{\omega} \cdot \sin\omega t \cdot e^{-\alpha t} \tag{4.19}$$

$$i\ln(t) = e^{-\alpha t} \cdot \left(\frac{\omega_o}{\omega} \cdot \sin\omega t + Io \cdot \left(\cos\omega t + \frac{\alpha}{\omega} \cdot \sin\omega t \right) \right) + \frac{1}{q_p} \cdot \left(1 - \cos\omega t \cdot e^{-\alpha t} - \frac{\alpha}{\omega} \cdot \sin\omega t \cdot e^{-\alpha t} \right) , \tag{4.20}$$

where

$$\omega^2 = \frac{1}{L_R \cdot C_{IN}} - \frac{1}{4 R_{IN}^{\ 2} \cdot C_{IN}^{\ 2}} , \tag{4.21}$$

$$\alpha = \frac{1}{2 R_{IN} \cdot C_{IN}} \text{ , and} \tag{4.22}$$

$$\omega_o^{\ 2} = \frac{1}{L_R \cdot C_{IN}} . \tag{4.23}$$

All the voltages and switching frequency are normalized as follows:

$$vn = \frac{v}{V_{IN}} , \tag{4.24}$$

$$in = \frac{i}{\frac{V_{IN}}{Z_o}} , \tag{4.25}$$

$$F_n = \frac{F_S}{F} = \frac{F_S}{\omega} \cdot 2\pi , \tag{4.26}$$

$$q_P = \frac{R_{IN}}{Z_o} . \tag{4.27}$$

Assuming that the ZVS operation needs to be maintained from load and line changes, then Fn is less than unity and is solved numerically by using MATLAB software program. Figure 4.15 illustrates the normalized vcn by using q_p as running parameters for several Fn within a switching cycle. It can be observed that the smaller the Fn, the larger the voltage stress across the switch and the larger the circulating current appearing in the circuit. However, a large Fn indicates the negative portion of the resonant inductor current becomes less and the ZVS operation on S_1 is lost. Figure 4.16 reconstructs the previous figure with a 3D plot, and q_p is the running parameter. vcn_1st is the normalized first order harmonic voltage of vcn with RMS value and it is particular

by important for the PT load. iln_max is the normalized peak-to-peak inductor current. The discontinuous region indicates that there is no ZVS operation for the switch.

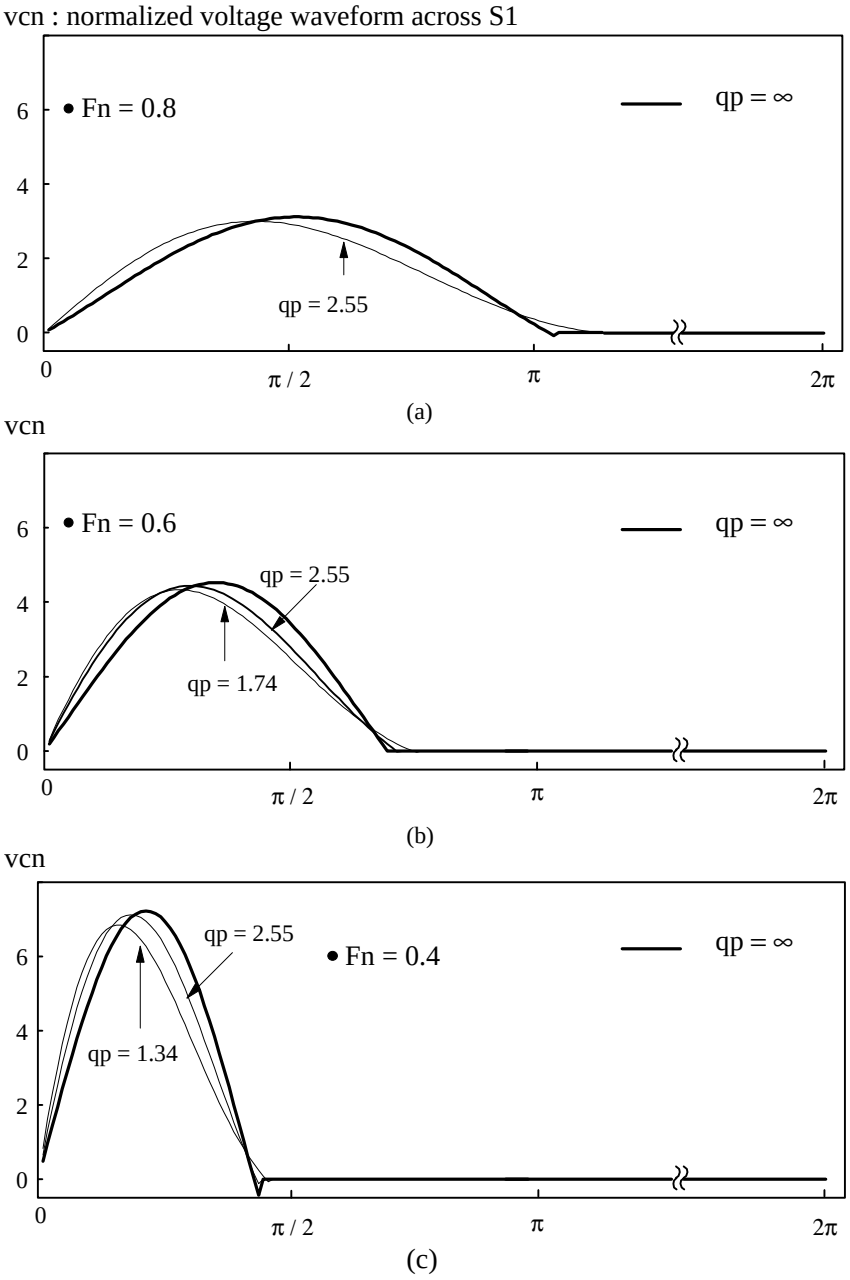

Fig. 4. 15. Normalized switch voltage waveforms of the SE-QR amplifier. (a) Fn = 0.8. (b) Fn = 0.6. (a) Fn = 0.4. These voltage waveforms are drawn with different Fn under the ZVS operation on the switch during a switching cycle. In (a), (b), or (c), the RMS values of vcn with different qp are almost identical. In other words, the RMS value of vcn is close to that when RIN or RACP approaches infinity.

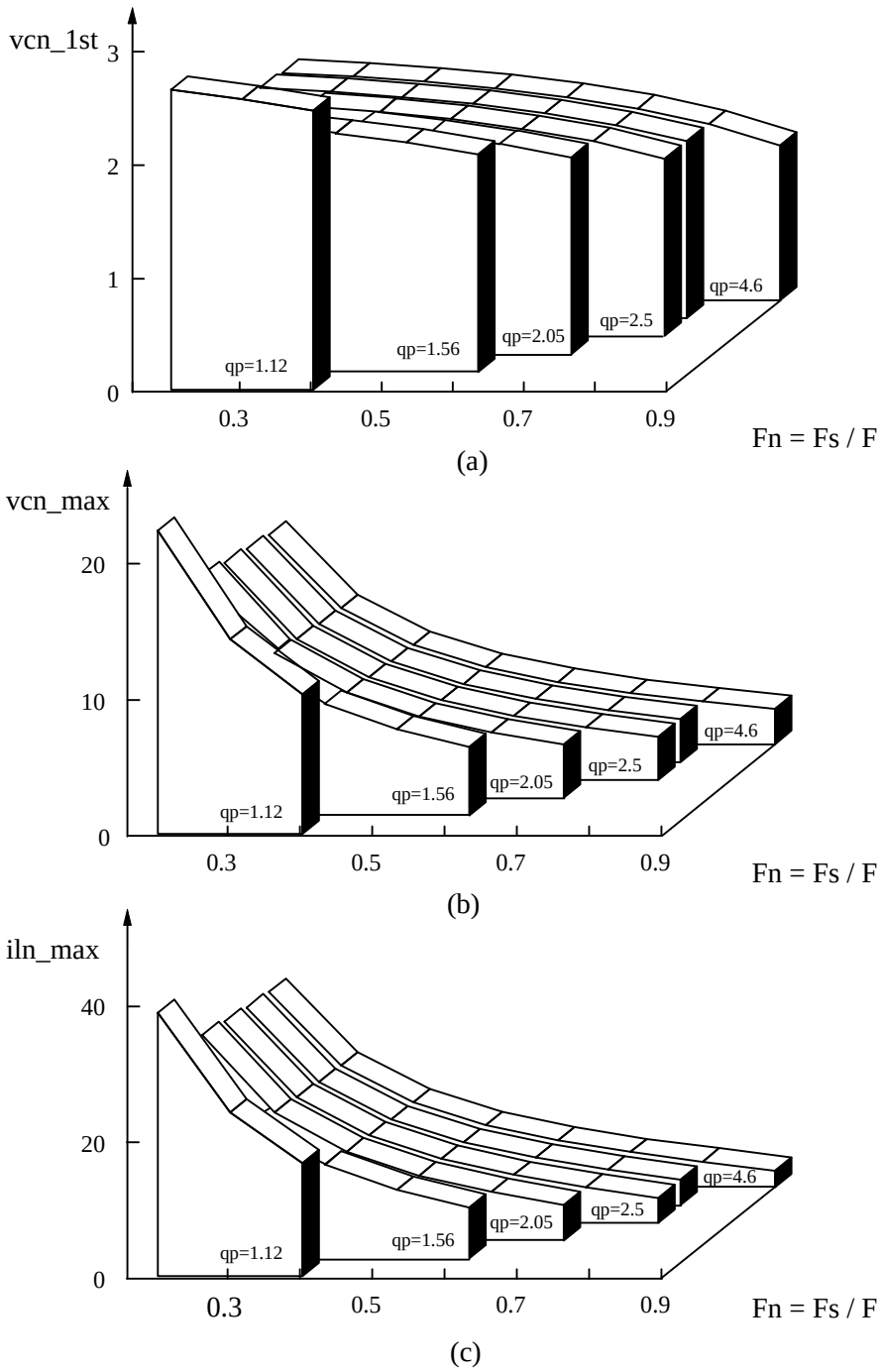

Fig. 4. 16. Normalized switch voltage and current stress of the flyback SE-QR amplifier. (a) peak fundamental voltage of V_{S1}. (b) maximum voltage of V_{S1}. (c) peak-to-peak current of V_{S1}. Fn is greater than 0.7 so that the normalized voltage stress is less than 4. qp is chosen to be greater than 2.05 to maintain the ZVS operation when the load changes.

4.4.3.2 Flyback SE-QR Amplifiers

From Fig. 4.13 (b), the normalized capacitor voltage vcn and inductor current iln during turn-off interval are similar to those in (4.19) and (4.20). They are:

$$vcn(t) = 1 - \cos\omega t \cdot e^{-\alpha t} + \frac{\alpha}{\omega} \cdot \sin\omega t \cdot e^{-\alpha t} + Io \cdot \frac{\omega_o}{\omega} \cdot \sin\omega t \cdot e^{-\alpha t} \tag{4.28}$$

$$i\,ln(t) = e^{-\alpha t} \cdot \left(\frac{\omega_o}{\omega} \cdot \sin\omega t + Io \cdot \left(\cos\omega t + \frac{\alpha}{\omega} \cdot \sin\omega t \right) \right) . \tag{4.29}$$

Although (4.28) and (4.29) are different from (4.19) and (4.20), their calculated steady-state current waveforms are almost identical. Using the same MATLAB program, the normalized voltage and current characteristics can be obtained and will not be repeated.

4.4.4 DC Characteristics and Experimental Verifications

4.4.4.1 DC Characteristics

From Fig. 4.15 and 4.16, vcn_1st, vcn_max, and iln_max are functions of Fn only under the condition that q_p is greater than 2.05. In other words, the voltage gain of the amplifier, for example vcn_1st, is a constant value when Fn is fixed and q_p is no less than 2.05. By using this characteristic, the design of the SE-QR PT converter is achieved without considering the load effect in the beginning. The flow chart used to calculate the current and voltage waveforms of the equivalent circuit for the SE-QR PT converter is listed in Fig. 4.17. Figure 4.18 illustrates the voltage gain and maximum voltage stress of the SE-QR PT converter with LVPT-21. In Fig. 4.18, Fn is the running parameter and the DC characteristics are calculated for different values of R_L at Fs = 1.92 and 1.96 MHz. The broken lines indicate where the ZVS operation on S_1 is lost.

4.4.4.2 Experimental Verifications

Figure 4. 19 (a) shows the experimental SE-QR LVPT converter, and its equivalent circuit is shown in 4.14 (c) at Fs = 1.96 MHz. The measured and experimental waveforms for voltage gain are shown in Fig. 4.19 (b), and they are similar in shape and value. The ZVS operation is maintained only when R_L is less than 20 Ω shown in Fig. 4.19 (c). When R_L increases, q_p decreases and Fn increases. Those factors are counterproductive to achieving the ZVS operation because the inductor current i_{LR} only flows in the positive direction shown in the right upper corner of Fig. 4.19 (c). The voltage waveforms of V_{S1} for different load conditions have been measured from the experimental circuit, simulated by SIMPLIS software program, and also simulated by the developed software program in MATLAB. These three sets of waveforms are shown in Fig. 4.20. The waveforms with circular marks are measured or simulated under R_L = 10 Ω and Fs = 1.96 MHz. They are similar in shape and their peak voltage stresses are close to 35 V.

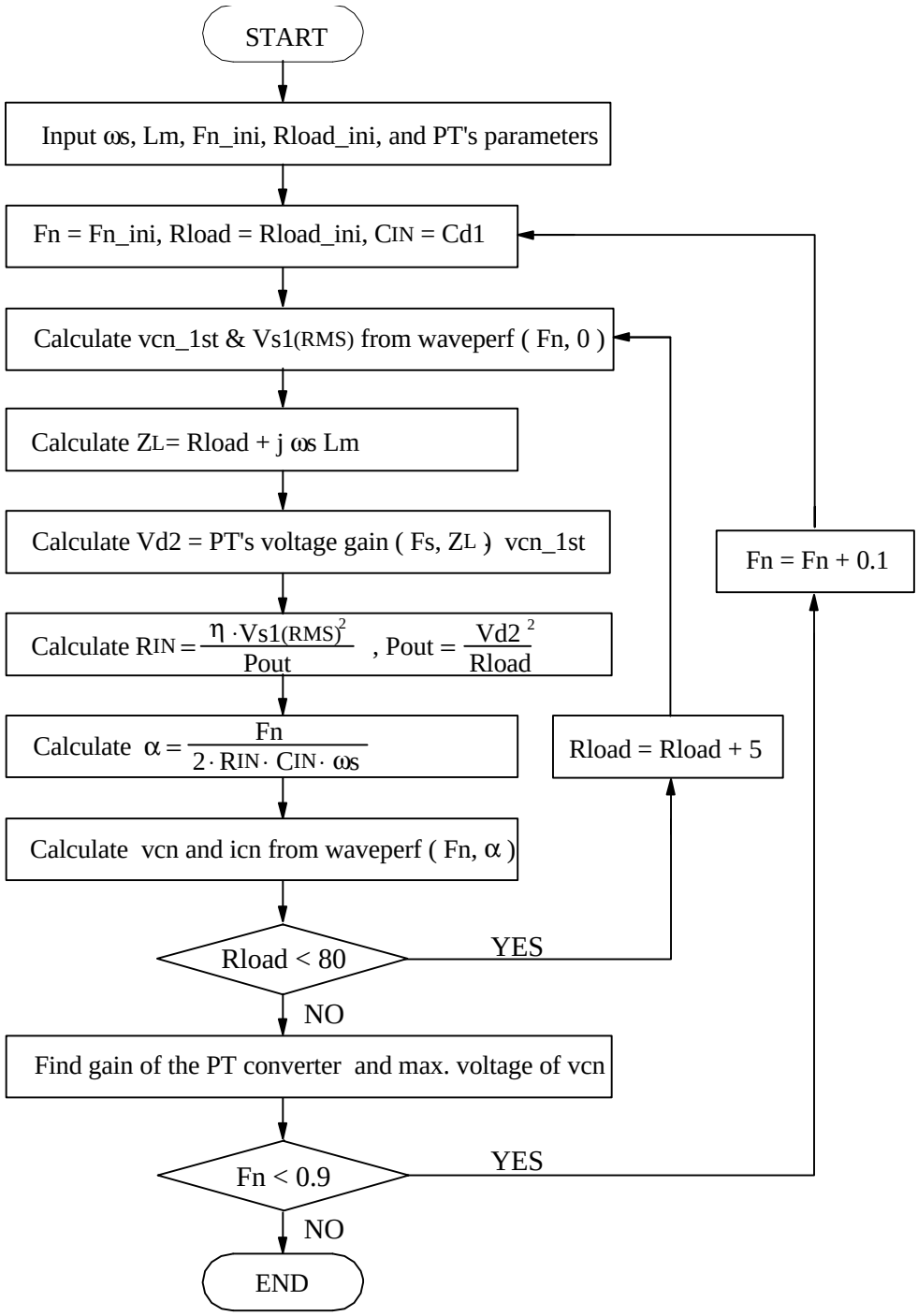

Fig. 4.17. Flow chart used to calculate the normalized voltage and current waveforms of the SE-QR amplifier. The subroutine waveperf (Fn, α) is employed to calculate the normalized vcn and iln when the Fn and α are specified. This program is coded in MATLAB.

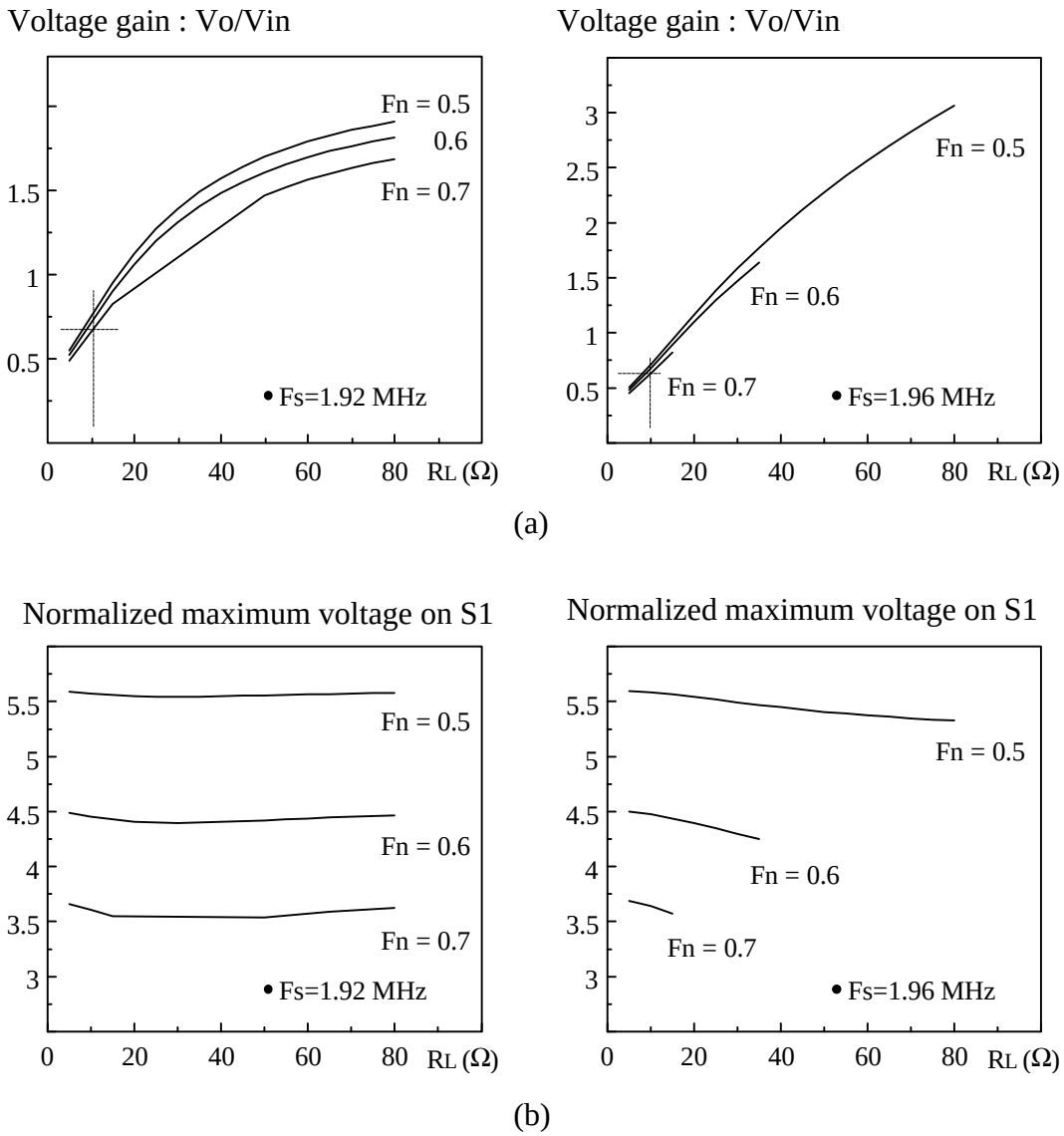

Fig. 4.18. Voltage gain and maximum voltage stress of the SE-QR LVPT converter. (a) voltage gain. (b) maximum voltage on S_1. The power stage of the converter is shown in Fig. 4.14 (a). The broken lines indicate where the ZVS operation is lost. Voltage gain is normalized to input voltage and is greater than 0.5. This means that the gain of the SE-QR amplifier is greater than unity and it is not suitable for step-down applications.

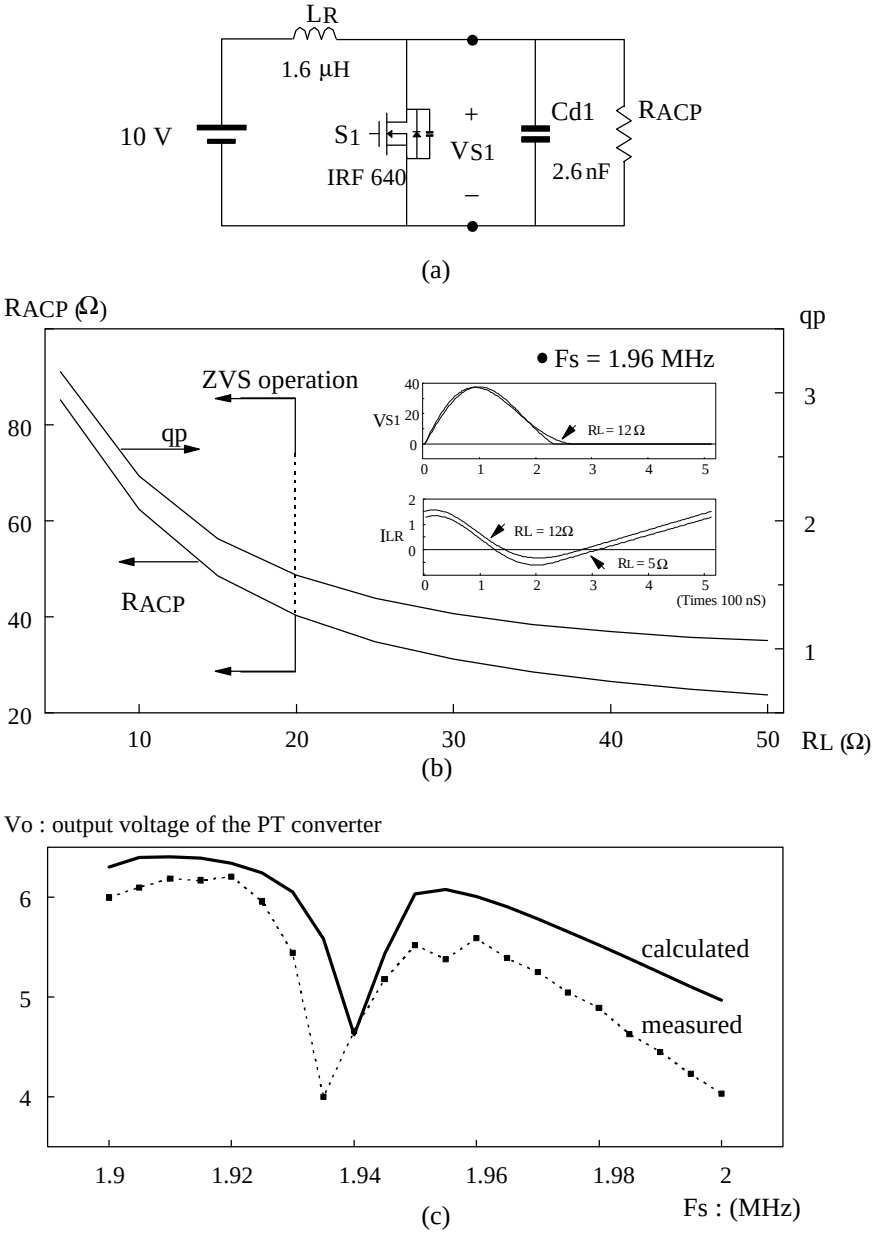

Fig. 4. 19. Experimental verification of the SE-QR LVPT converter. (a) simplified equivalent circuit. (b) R_{ACP} of LVPT-21. (c) calculated and measured voltage gain. Comparing R_{ACP} in (c) with R_{IN} in Fig. 4.2 (b), they are totally different. To maximize the efficiency of LVPT-21, the operating frequency is set to 1.96 MHz determined by the power flow method.

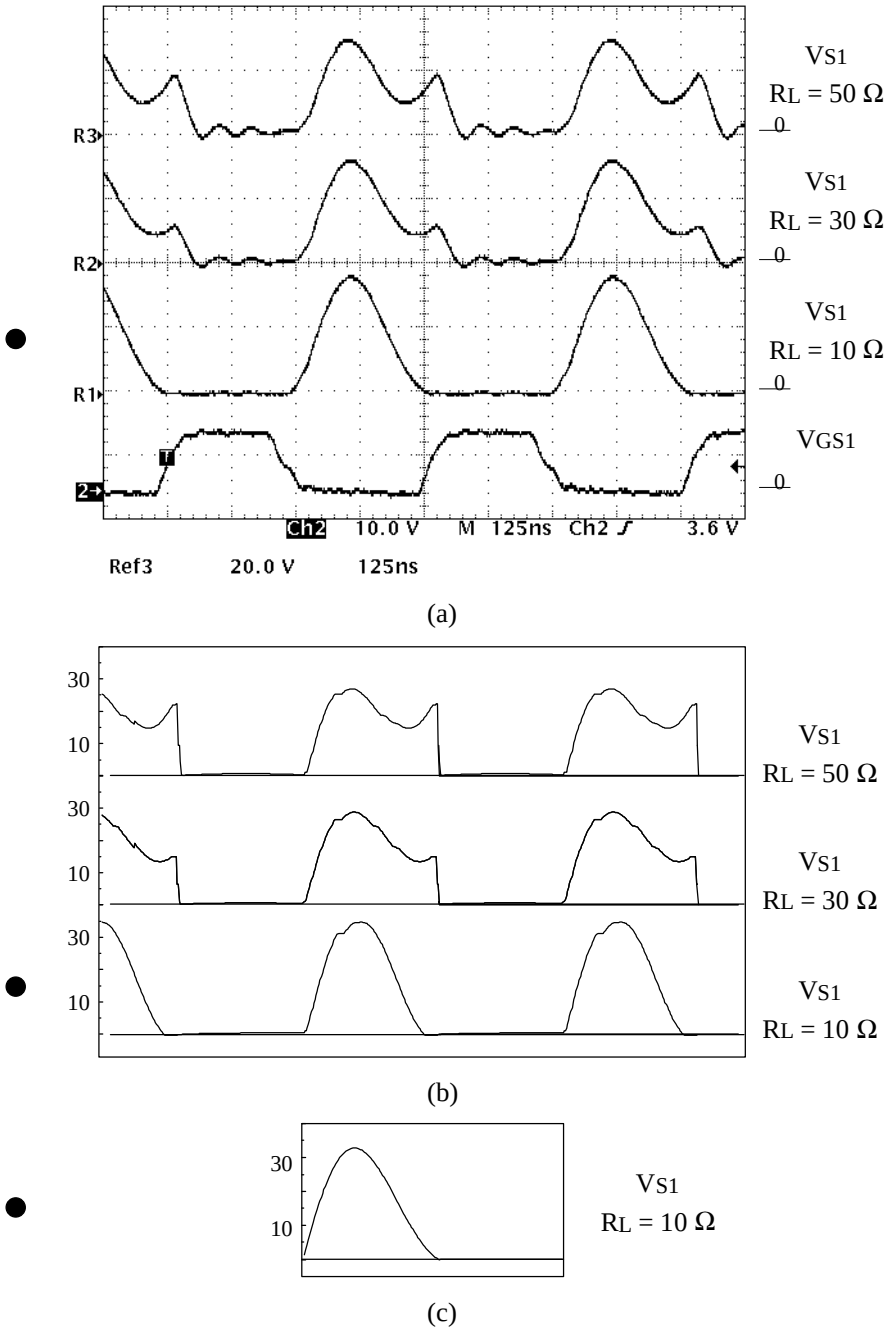

Fig. 4. 20. Experimental waveforms of the SE-QR LVPT converter with different values of RL. (a) experimental results. (b) simulation results obtained from SIMPLIS. (c) simulation results employed analytical expression of vcn and the host simulation program is MATLAB.

4.4.5 Design Guidelines

To operate the PT efficiently, the optimal load and operating frequencies of the PT are predetermined as mentioned in section 3.2.3. From the DC characteristics of the SE-QR LVPT converters shown in Fig. 4.18, the major design parameter is Fn which is defined in (4.26). To maintain the ZVS operation and to minimize the voltage and current stresses on S_1 when R_L changes, Fn is chosen to be 0.7. It is always desirable to choose the minimum capacitance of C_{IN} to minimize the current and voltage stress. Therefore, C_{IN} is equal to input capacitance of the LVPT-21, Cd1, in Fig. 4.14.(c). Since C_{IN}, Fs, and Fn are known for the constant-frequency-controlled SE-QR LVPT converter, L_R can be calculated by substituting (4.26) to (4.21) and is

$$L_R = \frac{1}{C_{IN} \cdot \left(\frac{\omega_S^{\,2}}{F_n^{\,2}} + \frac{1}{4 \cdot R_{IN}^{\,2} \cdot C_{IN}^{\,2}} \right)} \quad . \tag{4.30}$$

For example, L_R = 1.4 μH when Fs = 1.96 MHz, Fn = 0.7, $R_{IN} = R_{ACP}$ = 62 Ω and C_{IN} = Cd1 = 2200 pF. Another important simulation result observed from the DC characteristics of the amplifier is the fact that the voltage gain of the amplifier is always greater than unity. Therefore, it is preferable to adopt this topology in step-up applications.

4.4.6 Conclusions

The equivalent circuit of the SE-QR PT converters is verified with LVPT converters, and it has been confirmed that the calculated results are similar to the experimental results. Because of the step-up characteristics of the voltage gain, this amplifier is not suitable for step-down or LVPT applications. Thus, the design example will be concentrated on step-up or high-voltage applications, and this will be discussed in Chapter 5. However, an SE-QR PT converter with LVPT-21 is built and tested for the purpose of evaluating three amplifier circuits in LVPT applications.

4.5 Performance Comparison of LVPT Converters

Figure 4.21 summarizes the efficiency of the three converters under different loads at a fixed switching frequency of 1.96 MHz, where the efficiency of LVPT-21 is maximized under the optimal load. These three LVPT converters are the half-bridge converter shown in Fig. 4.6 (a) with V_{IN} = 48 Vdc, the SE-MR converter shown in Fig. 4.11 (a) with V_{IN} = 48 Vdc, and the SE-QR LVPT converter shown in Fig. 4.19 (a) with V_{IN} = 20 Vdc. It can be seen that the best efficiency occurs around R_L = 9.6 Ω, which is equal to the calculated optimal value in Chapter 3. Table 4.2. shows the component counts and the performance indices for the three converters.

The advantages of the SE-MR PT converter include simple structure, fewer components, and utilization of circuit parasitics. Also, the control method is variable-frequency, which can be modified to track the optimal operating frequency which varies with load and temperature. The advantages of the half-bridge PT converter are greater efficiency and less generated noise than the

SE-MR PT converters. But two inductors are required to act as buffers for the transition from square wave to sinusoidal wave or vice versa. They both are suitable to step-down applications employing LVPT. The SE-QR amplifier is the simplest circuit among three amplifier topologies, and it is ideal for high-voltage applications.

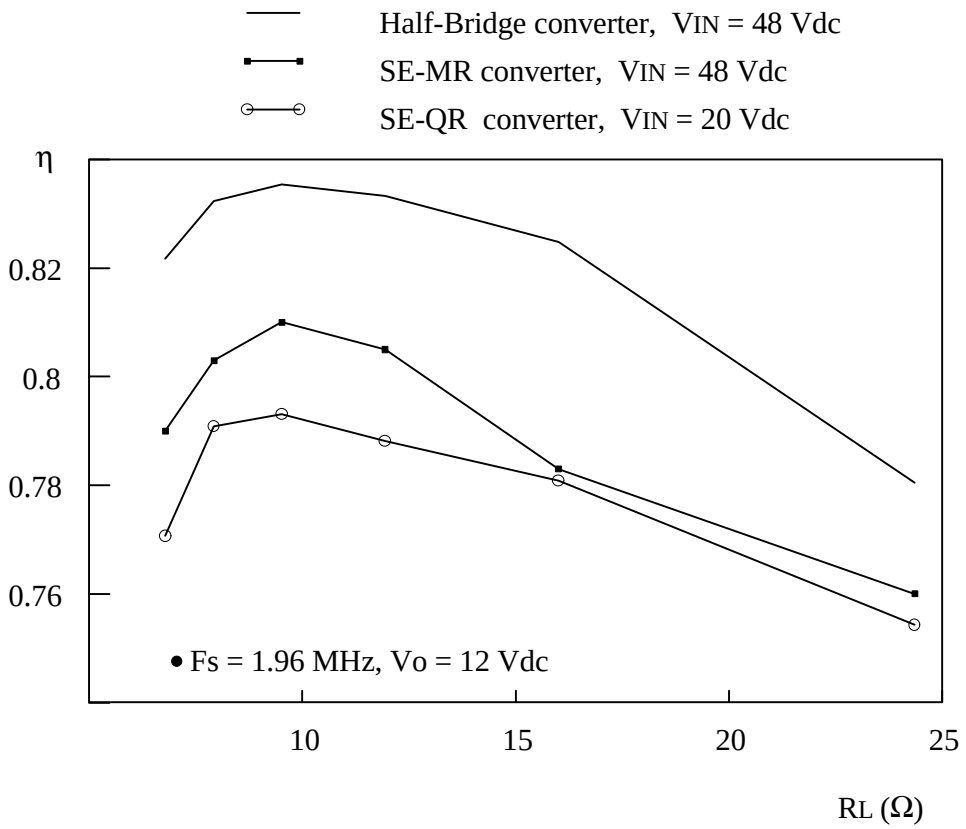

Fig. 4.21. Efficiency comparison of three LVPT converters.

Table 4.2. Comparison of three LVPT converters employing the half-bridge, SE-MR, and SE-QR amplifier topologies.

Topologies / Items	HB 2:1 LVPT dc/dc Con.	SE-MR 2:1 LVPT dc/dc Con.	SE-QR 2:1 LVPT dc/dc Con.
no. of inductors	3	3	2
no. of capacitors	2	2	1
no. of switches	2	1	1
input voltage	48 Vdc	48 Vdc	20 Vdc
η @ output = 12 V, 14.4 Watts	83.6 %	81 %	79.3 %
switching Freq.	1.96 MHz	1.96 MHz	1.96 MHz
no. of high-side drivers	1	0	0
voltage gain of the converter	< 1	< 1	> 1

4.6 Summary

The design guidelines are given for these three amplifiers according to the DC analysis from carried out while employing the respective lumped equivalent circuits. Comparative studies on efficiency, cost, and complexity for different amplifier topologies have been performed. Although the performance comparison is made on LVPT applications, it is also applied to the applications using HVPTs. Because the current applications suitable for HVPTs are usually lower than 10 watts and require very tight packaging, cost, simplicity, and efficiency of the circuit are all major concerns. Among those three types of amplifiers, it seems that only the SE-QR amplifier can meet those requirements by sacrificing the efficiency factor slightly.

The dc/ac voltage gain of the half-bridge and SE-MR amplifiers can be feasibly below unity. It suggests that these two amplifiers are useful for step down applications, like on-board power supplies or AC adapters. On the other hand, the dc/ac voltage gain of the SE-QR amplifier is naturally larger than unity. Besides, it consists of only one switch and a resonant inductor, and so it is the most cost-effective circuit and suitable for step-up applications. Therefore, this type of amplifier topologies is chosen for the application circuits in the next chapter, entitled High-Voltage Applications for Piezoelectric Transformers.

5. High-Voltage Applications of Piezoelectric Transformers

5.1 Introduction

Different kinds of applications for high-voltage piezoelectric transformers (HVPTs) can be found in several publications [1,14,15,18,48,49]. HVPTs have been adopted by power electronic engineers and researchers worldwide. However, design issues such as packaging, thermal effects, amplifier circuits, control methods, and matching [21] between amplifiers and loads need to be explored further. This chapter contains an extensive discussion of the last three design issues. Packaging and thermal effects of PTs are still under research.

The HVPTs are definitely better high-voltage sources for devices which need low-power high-voltage sources, such as cold-cathode fluorescent lamps (CCFLs), neon lamps, and miniature cathode-ray tubes (CRTs). The HVPT's low profile and low cost make it especially attractive for backlighting the LCD in a notebook computer. The CCFL HVPT inverters are divided into two groups, depending on the applied control methods. Two sets of comparison studies are established, and the constant-frequency-controlled HVPT CCFL inverter is used as the basis. The first set of inverters includes the constant-frequency-controlled and the conventional inverters; meanwhile, the comparison is made according to the specifications of the conventional CCFL inverter provided by Delta Electronics Inc. The second set of inverters includes both constant- and variable-frequency-controlled inverters. Similarly, the comparison is achieved according to the specifications of the variable-frequency-controlled HVPT CCFL inverter from Tokin Corp.

The flyback single-ended quasi-resonant (SE-QR) amplifier was adopted to incorporate the input capacitance of the PT into the amplifier design. Because the step-up ratio for a Rosen-type HVPT with a CCFL load is too low, and the output voltage of the HVPT is low for the input source from a battery, it is necessary to modify the resonant inductor in the SE-QR amplifier to a step-up transformer. Accordingly, a large capacitance is presented on the primary side of the amplifier due to the reflected input capacitance of the PT on the secondary side. This large reflected capacitance needs to be considered in the amplifier design. In this amplifier, the circulating current is moved to the secondary side of the transformer, and there is no current flowing in the primary circuit when the main switch is turned off. By adding an extra switch to

regulate the output current of the lamps, dimming control and line regulation are achieved through constant-frequency control. A complete inverter with HVPT for CCFL or neon lamps was built, and the experimental results are presented.

Choosing a suitable HVPT for a CCFL is very important for matching the source and the load. The output impedance for a general CCFL is around 100 kΩ, but the matched output impedance for a typical HVPT is above 200 kΩ. A multilayer (stacked) structure HVPT was proposed in [48] and could be built according to the load requirements. The multilayer HVPT makes it possible to achieve matching between load and output of HVPT and also increases the step-up ratio under heavy load conditions. A large input capacitance was found due to the stacked structure and needs to be incorporated into the amplifier design. A commercial prototype variable-frequency-controlled CCFL inverter with HVPT was investigated. The major interest of the comparison focuses on the control methods and their corresponding performances.

5.2 Characteristics of the HVPT

The purpose of this section is to present the characteristics of the HVPTs and to demonstrate the usefulness of the model of the HVPT in circuit simulation. The general characteristics of the experimental HVPT, which is HVPT-02, are listed below:

- Type : Rosen type (single layer, no isolation),
- Power handling : 3 - 6 Watts,
- Series resonant frequency : about 73 kHz (no load) , and
- Size : $50 \times 8 \times 1.5 \left(\mathrm{L} \times \mathrm{W} \times \mathrm{T} \text{ all in mm} \right)$.

Figure 5.1. shows the equivalent circuit and voltage gain of HVPT-02. The parameters of the equivalent circuit can be obtained by measurements [5,8] described in Chapter 2, or by direct calculation [3-5] employing the physical size and material properties of the HVPTs.

To maximize the efficiency of the HVPT, it is essential to decide its full load and corresponding operating frequency. The simulation results in [17] show that the maximal efficiency of the HVPT with a resistive load occurs when HVPT voltage gain reaches maximum at a specified operating frequency. Voltage gain of the HVPT is defined as

$$\text{Voltage gain} = \frac{V_o(\text{rms})}{V_{IN}(\text{rms})} \tag{5.1}$$

Figure 5.1 (b) shows the frequency vs. voltage-gain curves calculated for several load resistances. It is important to notice that for each load resistance, the maximal voltage gain matches a designated operating frequency. Figure 5.1 (c) illustrates that the optimal resistive load of HVPT-2 is 330 kΩ, which is the impedance of the output capacitance around fs. Besides, the efficiency of the PT decreases when the switching frequency increases. Because of the increased dielectric loss, this phenomenon will become more prominent while the output power increases.

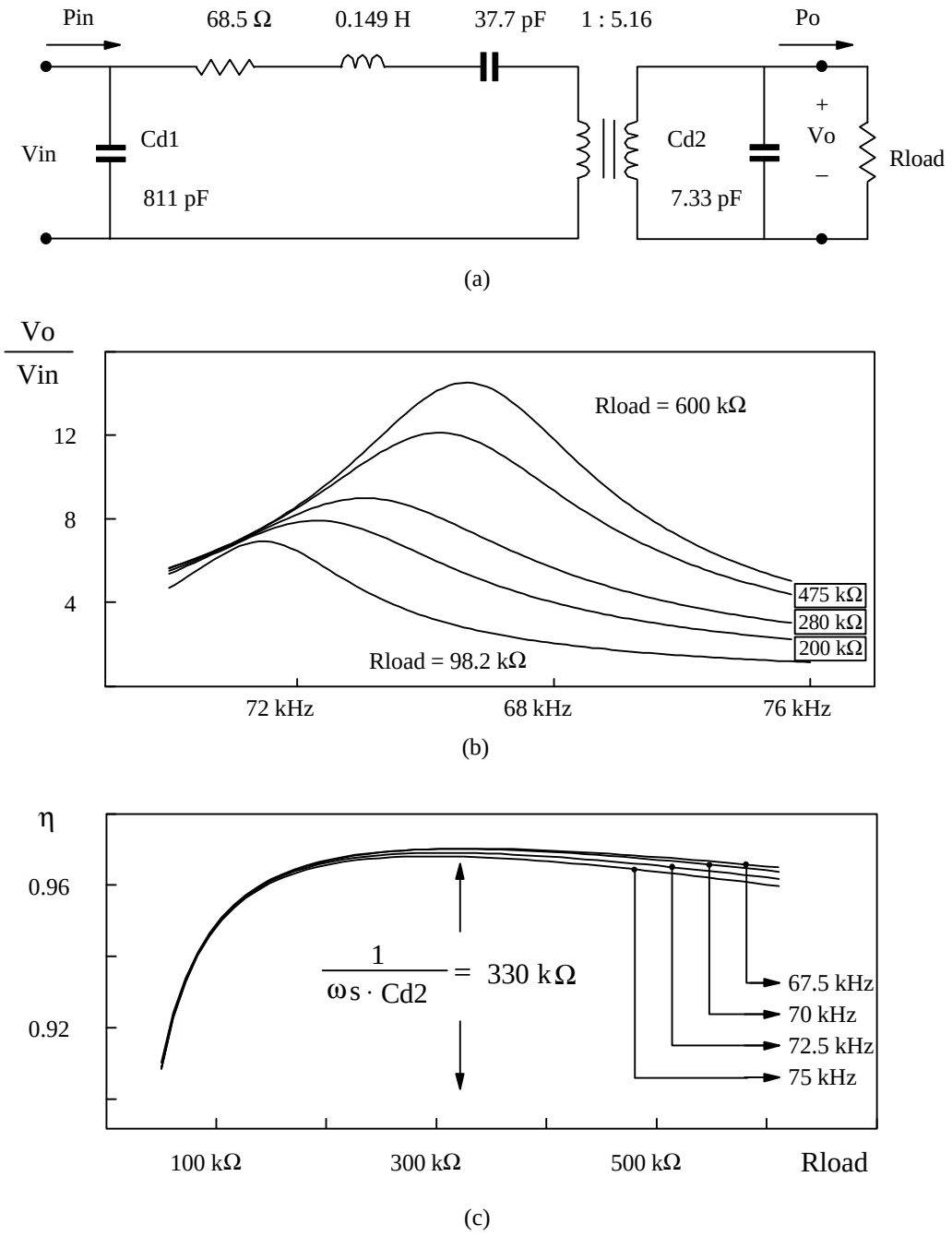

Fig. 5.1. Theoretical voltage gain and efficiency of HVPT-2. (a) model of HVPT-2. (b) gain characteristics of the HVPT-2. (c) calculated efficiency of HVPT-2 employing the PT model shown in (a) under different resistive loads. The maximum gain for each resistive load is different and occurs at different frequency, fo. As long as the switching frequency stays close to fs, the efficiency of the HVPT does not change much with different loads.

To control the power processed by the PTs is actually to control the voltage gain of the PT. The methods for controlling the PTs could be either constant-frequency control or variable-frequency control. The voltage gain of the PTs increases when the load resistance increases. This characteristic will help to ignite the high-pressure lamps such as CCFLs and neon lamps. For constant-frequency control, the voltage gain cannot track the peak of the curves, and the advantage of using PTs is lost. Figure 5.2 further illustrates the trajectories for constant-frequency and variable-frequency controls during start-up of the CCFL.

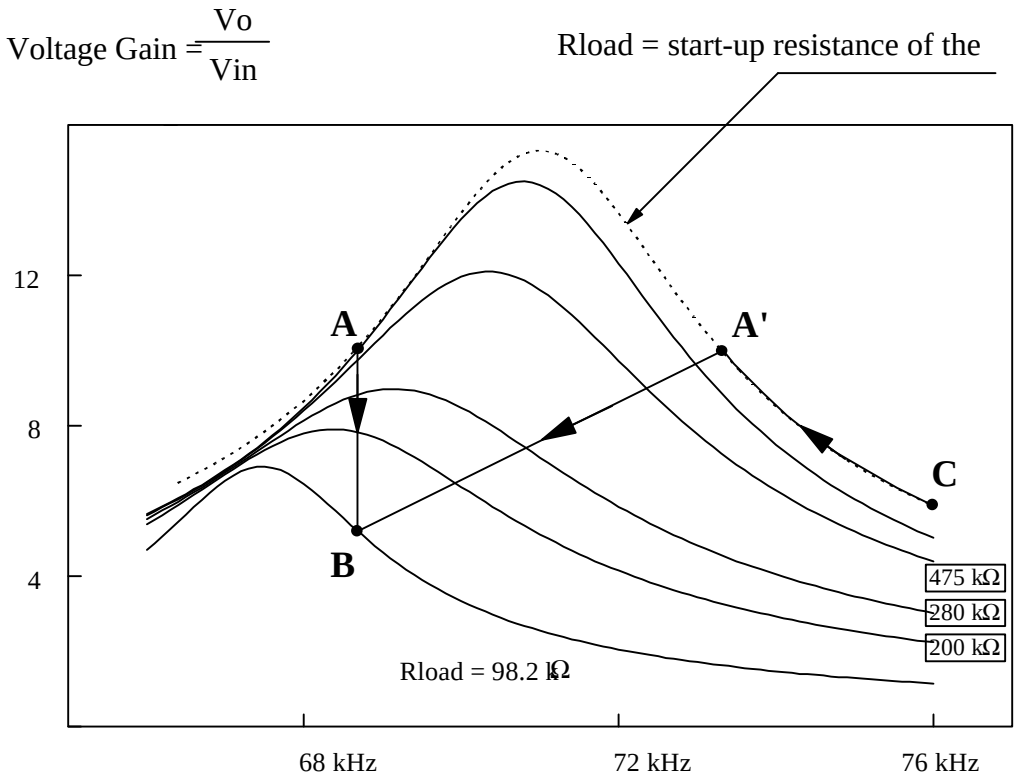

Fig. 5.2. Gain characteristics and control methods of HVPT-2. For constant-frequency control, the trajectory for starting up the lamp is from A to B. On the other hand, the variable-frequency control follows the curve C A' to B. The voltage gains at A and A' are identical, and the lamp ignites at this voltage. At B, the lamp is operating under the nominal condition and behaves like a resistor.

For constant-frequency control, the maximum gain at a particular frequency is fixed. Once the lamp is ignited, the operating point moves from A to B, and the nominal operating condition is set at point B. On the other hand, the operating frequency is swept from high frequency (point C) to point A′, where the lamp ignites and operation point will move to point B later. Therefore, the highest voltage gain is fully explored for variable-frequency control, and start-up of the lamp is achieved easily. However, the lamp might fail to ignite if the operating frequency weres not chosen carefully.

From section 2.4.1, the efficiency of the PT decreases when the operating frequency increases. The lower the load resistance, the lower the efficiency. The last two effects result from the increased dielectric loss when the reactive power increases. Therefore, the efficiency of the PT can not be maximized when variable-frequency control is used. The pros and cons for these two control methods will be discussed further in the examples.

5.3 Characteristics of the CCFL and Neon Lamps

The lamps used in this report are CCFLs and neon lamps. Dynamically, these two lamps work like negative resistors. Therefore, a ballast is required to be added to each of these lamps to limit the negative current. While in steady state, these lamps show the characteristics similar to resistors [49].

5.3.1 Characteristics of the CCFL

The specifications for the experimental CCFL are listed below:

- Model No.: FC2EX50 / 250T4,
- Strike voltage: 1050 Vrms @ 0^{o} C,
- Maintaining voltage : 490 Vrms,
- Nominal lamp current: 5 mArms, and
- Physical size : 20 cm long and 5mm in radius.

Basically, there are four parameters important in lighting up the CCFL: strike voltage, maintaining voltage, frequency, and lamp current [50]. The brightness does not change much with the operating frequency of the lamp and is mostly determined by the lamp current. Under a specified lamp current, when the output voltage of the inverter reaches the maintaining voltage, the impedance of the CCFL is resistive and changes with the lamp current. The impedance vs. lamp current curve of CCFL is shown in Fig. 5.3 (a). This curve illustrates that the CCFL behaves like a resistor in steady state, but dynamically the CCFL shows the negative resistance characteristic. Therefore, a ballast is required between a CCFL inverter and its lamp. Nevertheless, the HVPT is a perfect source for the CCFL because it generates a very high strike voltage at light load and behaves like a ballast for its positive impedance characteristics.

5.3.2 Characteristics of Neon Lamps

Similarly, the neon lamps, which need very high strike voltage to ignite and are very high-impedance components, could be the desirable loads for the HVPTs. Standard B2A high-brightness lamps have the following specifications:

- Strike voltage: 90 Vrms,
- Maintaining voltage : 70 Vrms, and
- Nominal lamp current: 1 mArms.

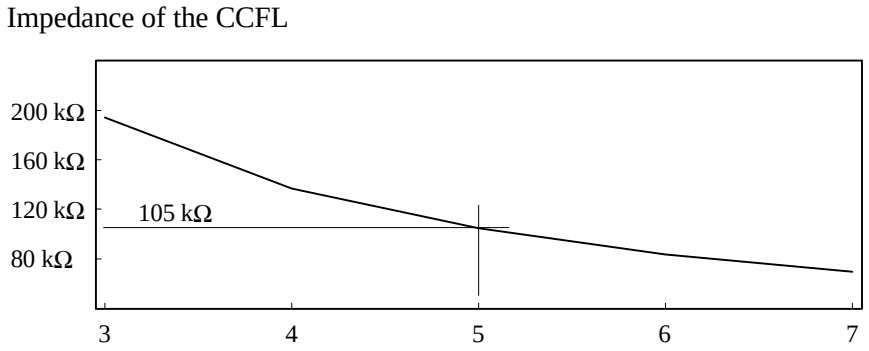

(a)

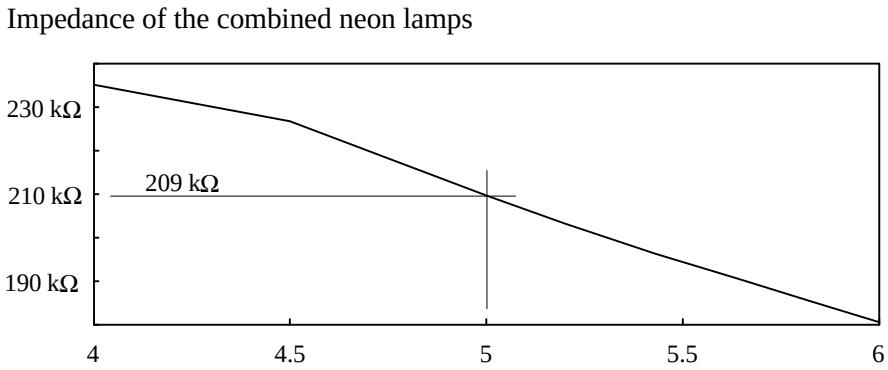

(b)

Fig. 5.3. Characteristics of the experimental CCFL and neon lamps. (a) CCFL. (b) neon lamps. Dynamically, the V-I curve for CCFL indicates the nature of the negative resistance of CCFL. Nevertheless, the lamp voltage and lamp current are in phase, and this indicates they are resistors at certain operating points.

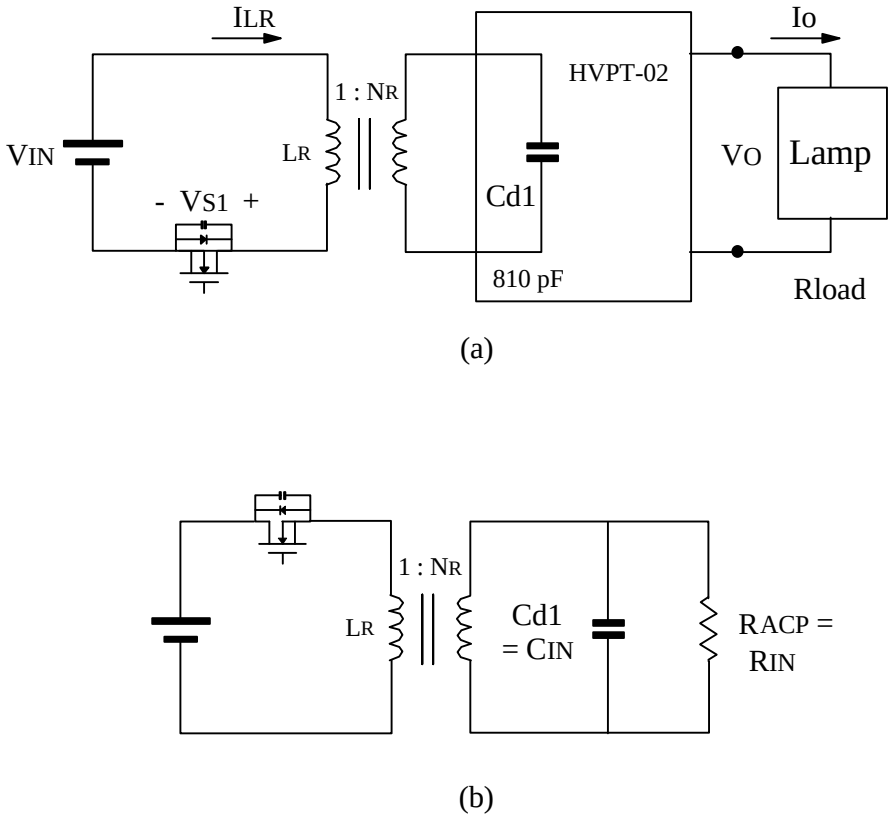

Fig. 5.4. Experimental flyback SE-QR CCFL inverter and its DC characteristics. (a) power stage. (b) equivalent circuit.

The four factors necessary to light up the CCFL are also applicable to neon lamps. Employing the same test setup, the lamp current-impedance characteristic is shown in Fig 5.3 (b). These data verify that the neon lamp acts like a resistive load in steady state [49]. In order to obtain the optimal impedance for the HVPT, fifteen B2A lamps are connected in series, and two of them are arranged in parallel to achieve the desirable impedance for HVPT-02.

5.4 Design Examples of Flyback SE-QR HVPT Inverters

5.4.1 Flyback SE-QR HVPT Inverters

Block diagram of the flyback SE-QR inverter is shown in Fig. 5.4 (a), and its equivalent circuit developed in the previous chapter is illustrated in Fig. 5.4 (b). The operating principles of this inverter were described in Fig. 4.13. In Fig. 5.4 (b), $R_{IN} = R_{ACP}$ and $C_{IN} = Cd1$, where R_{IN} and C_{IN} are the load of the flyback SE-QR amplifier shown in Fig. 4.13 (a). The lamps used as the

load of HVPT-02 are CCFLs and neon lamps. The analytical forms for the voltage across Cd1 and inductor current I_{LR} had been derived in (4.28) and (4.29). Using the flow-chart shown in Fig. 4.17, the DC characteristics of the flyback SE-QR HVPT inverter can be obtained and employed to design the inverters.

5.4.2 DC Characteristics

Figures 5.5 and 5.6 shows the DC characteristics of the flyback SE-QR inverter when Rload = 105 kΩ and 209 kΩ, respectively. Under the normal operating condition, the lamp current = 5 mA, the load resistance of the CCFL is 105 kΩ, and that of the neon lamps is 209 kΩ. R_{ACP} vs. switching frequency curve is shown in Fig. 5.5 (a). The maximum voltage stress on S_1 is shown in Fig. 5.5 (b), where the voltage is a function of Fn only as predicted in the last chapter. Figure 5.5 (c) shows the normalized voltage-gain curves with Fn as the running parameter and N_R = 1. Here, q_p is decoupled from the voltage-gain design, because the first-order harmonic contents shown in Fig. 4.14 (a) do not change much when q_p is greater than 2.05 with a fixed Fn.

5.4.3 Design of the Power Stage

The design example is a CCFL inverter employing HVPT-02. The specifications of the experimental CCFL inverter are:

- input voltage : 9 - 16 volts,
- maximum lamp current : 5 mA (rms).

The design issue is to find the inductance L_R and the turns ratio of the transformer so that the desirable output voltage can be obtained under low-line and heavy-load conditions. To maintain a constant output voltage across Rload, either constant- or variable- frequency control may be adopted for different line and load conditions. The following example is designed for constant-frequency controlled inverters. From Fig. 5.3 (a), Rload = 105 kΩ and $Vo_{(RMS)}$ = 525 volts when Io = 5 mA. Figure 5.5 (c) shows the major design curve representing the voltage-conversion ratio between $Vo_{(RMS)}$ and the input voltage with N_R =1. From the specifications, the necessary voltage gain M from V_{IN} = 9 volts is

$$M = \frac{Vo_{(RMS)}}{V_{IN}} = \frac{525}{9} = 58.3 \tag{5.2}$$

From the maximum voltage stress shown in Figs. 5.5 (b) and 5.6 (b), Fn is chosen to be greater than 0.7. To maximize both efficiency and voltage gain of HVPT-02, the operating frequencies of the inverter are 68.2 and 68.7 kHz, for Rload = 100 kΩ and 200 kΩ, respectively. Therefore, the normalized voltage-gain conversion ratio is equal to 6.3 obtained from Fig. 5.5 (c) when Fn = 0.7, Fs = 68.2 kHz, and Rload =105 kΩ. The turns ratio of the transformer is calculated as

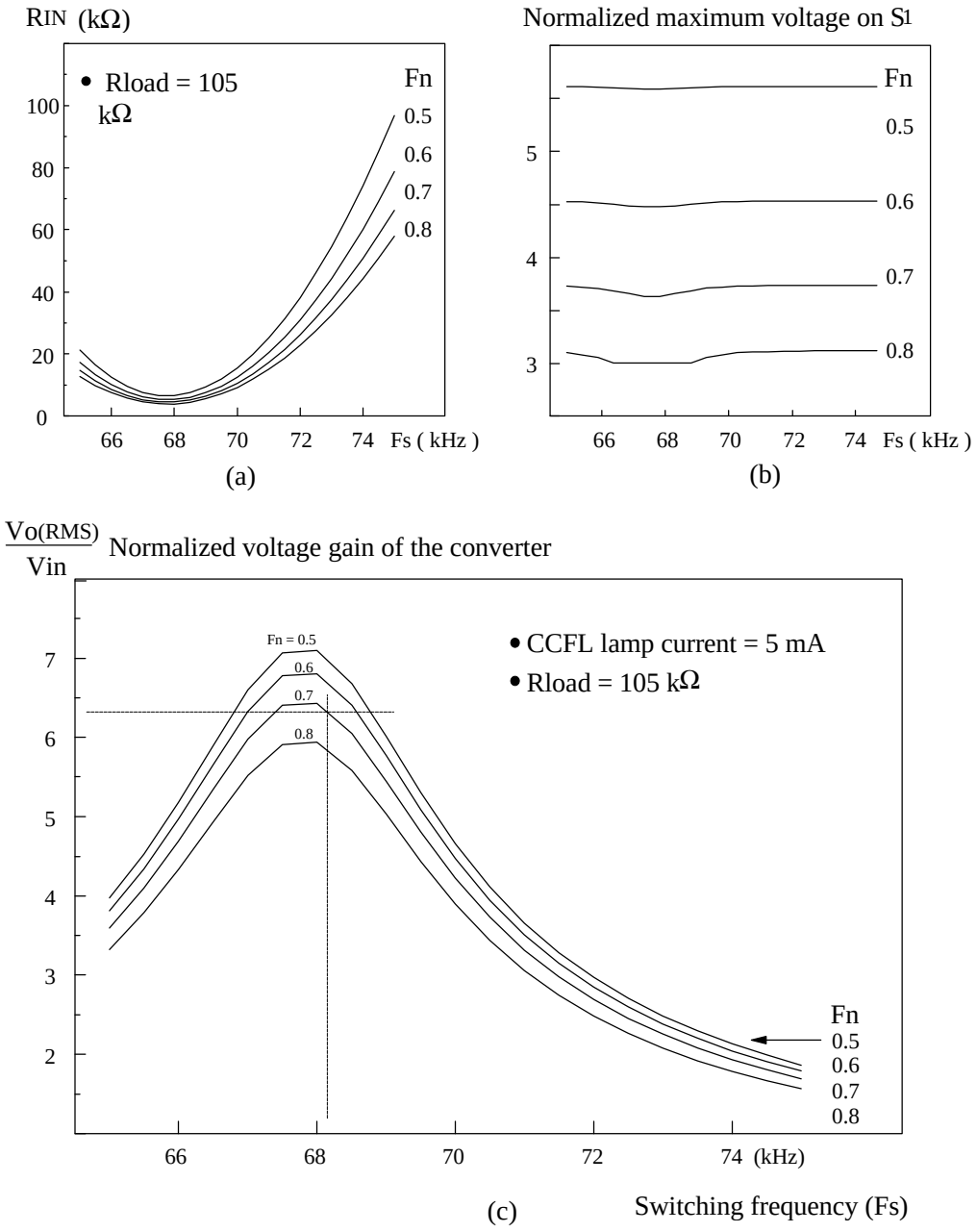

Fig. 5.5. DC characteristics of flyback SE-QR HVPT inverters when Rload = 105 kΩ. (a) calculated RACP (b) normalized maximum voltage. (c) normalized voltage gain. For example, the voltage gain is equal to 6.3 when Fs = 68.2 kHz, Fn = 0.7, and NR = 1. RACP is calculated according to the power balance in the equivalent circuit. These curves are calculated when Rload = 105 kΩ = the impedance of the CCFL with 5-mA lamp current.

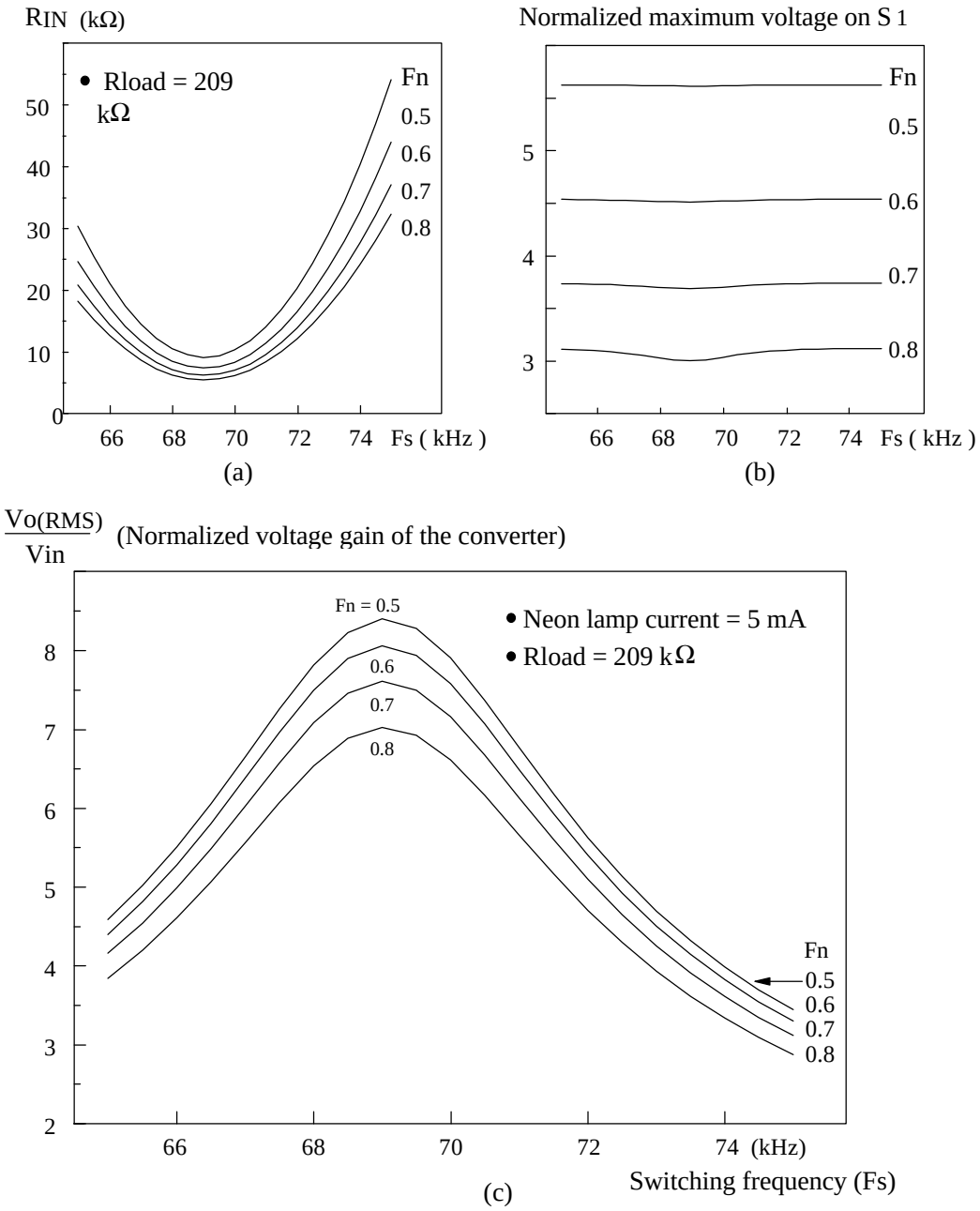

Fig. 5.6. DC characteristics of flyback SE-QR HVPT inverters when Rload = 209 kΩ. (a) calculated R_{ACP} (b) normalized maximum voltage. (c) normalized voltage gain. These curves are calculated when Rload = 209 kΩ = the impedance of the neon lamps with 5-mA lamp current.

$$N_R = \frac{58.3}{6.3} = 9.26 \tag{5.3}$$

N_R is chosen as 9.5. In Fig. 5.5 (a), R_{ACP} is equal to 4900. R_{IN} is the reflected resistance of R_{ACP} from the secondary side and R_{IN} = 54.3 Ω. The resultant capacitance of the reflected Cd1 and the winding capacitor C_W is

$$N_R{}^2 \cdot Cd1 + C_W = (9.25)^2 \cdot 810\ \text{pF} + 1\ \text{nF} = 70.3\ \text{nF}\ . \tag{5.4}$$

With C_{IN} = 70.3 nF and Fs = 68.2 kHz, L_R is found:

$$L_R = \frac{1}{C_{IN}} \cdot \left(\frac{Fn}{2\pi Fs} \right)^2 = \frac{1}{70.3n} \cdot \left(\frac{0.7}{2\pi \cdot 68200} \right)^2 = 38\ \mu\text{H}\ . \tag{5.5}$$

5.4.4 Experimental Results

In this section, a flyback SE-QR inverter is built and CCFL and neon lamps are connected to the same inverter designed for the CCFL inverter. The purpose of this arrangement is to verify the influence of the inverters on different loading conditions. The output impedances of the experimental CCFL and neon lamps are 100 kΩ and 200 kΩ, respectively, when both lamp currents are 5 mA (rms). So the switching frequency of the experimental circuit needs to be changed with the different lamps to maximize the gain of the inverter. Figure 5.7 (a) shows the experimental flyback SE-QR converter whose parameters are calculated in section 5.4.1. The comparison between experimental and theoretical results is illustrated in Fig. 5.7 (b), and the results are close to each other.

5.4.4.1 CCFL Inverters

The load resistance of the CCFL equals 100 kΩ. The experimental waveforms for the CCFL inverter are shown in Fig. 5.8 (a).

5.4.4.2 Neon-Lamp Inverters

The load resistance of the neon lamp is 200 kΩ. The experimental waveforms for the neon-lamp inverter are shown in Fig. 5.8 (b). From Fig. 5.8, the output current and voltage waveforms are not quite sinusoidal, but they are almost in phase. In order to verify the efficiency of the inverter with different loads, two power resistors are used to replace the CCFL and neon lamps. The measurement results for the inverter with different loads are summarized in Fig. 5.8 (c). For lower load impedance, like that of the CCFL, the operating frequency is lower than that of a neon-lamp inverter. However, the efficiency of the inverter with different loads is almost identical. These facts verify the characteristics of this HVPT with different loads.

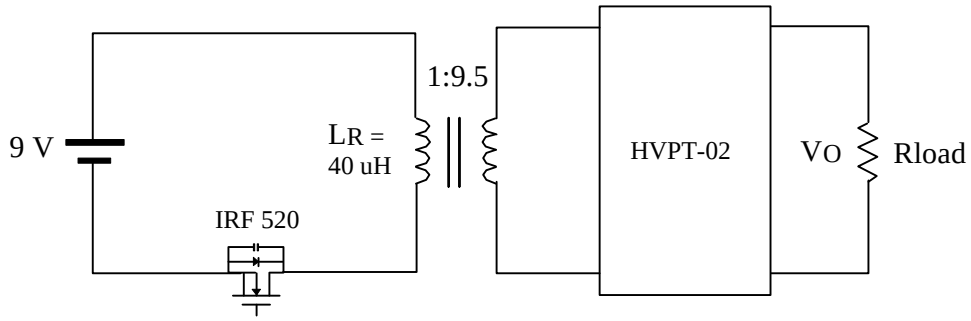

(a)

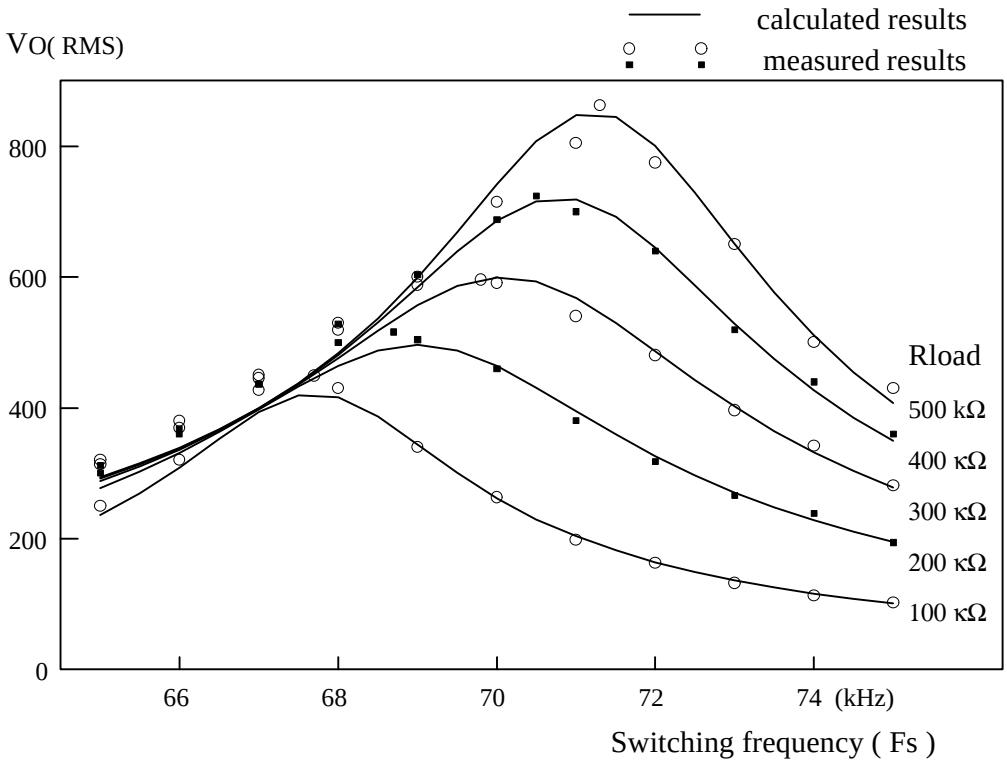

(b)

Fig. 5.7. Experimental flyback SE-QR HVPT inverter and its experimental verifications. (a) flyback SE-QR HVPT inverter. (b) voltage gain vs. frequency.

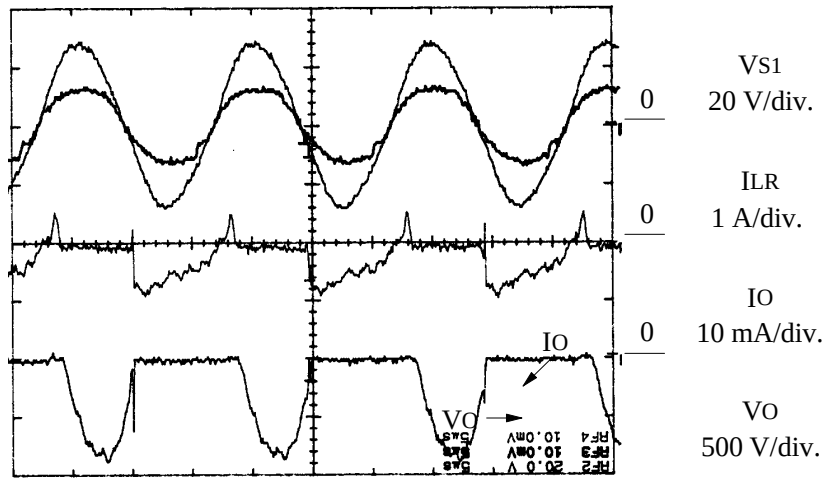

(a)

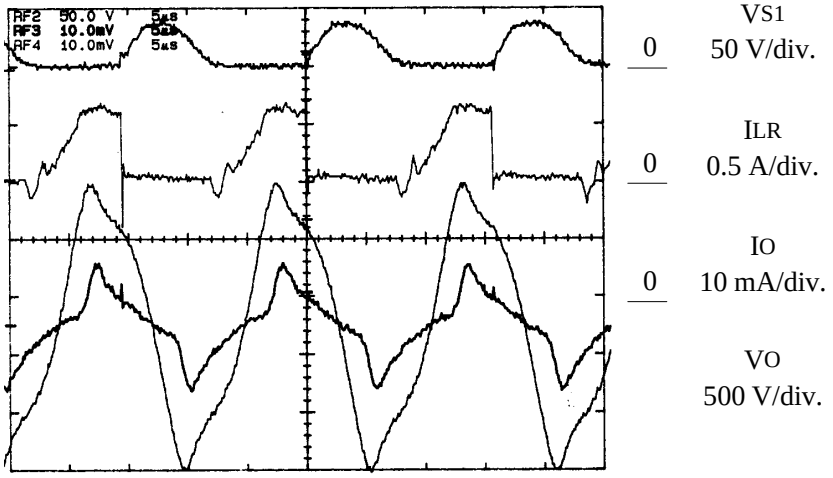

(b)

Rload	FS (kHz)	VIN (V)	IIN (mA)	IO(rms)	η (%)
100 kΩ	68.2	8.7	0.35	5	81
200 kΩ	68.7	11.5	0.54	5	80

(c)

Fig. 5.8. Experimental waveforms of flyback SE-MR HVPT inverters. (a) CCFL. (b) neon lamps. (c) comparisons of efficiency. The VO and IO are almost in phase for both lamps. This verifies that these lamps are resistors under nominal operating points. All notations are referred to Fig. 5.4 (a).

5.5 Buck + Flyback SE-QR HVPT Inverters (The Reference Circuits)

The performance of this inverter is compared with that of a commercial product from Delta Electronics Inc. in section 5.6. Its performance is also compared with that of a prototype HVPT CCFL inverter from Tokin Corp. in section 5.7.

5.5.1 Operation Principles

In order to maintain the same output current delivered to the load in spite of line variations, two control methods can be applied to this inverter. One is the variable-frequency control or fixed-off time control; however, the efficiency of the PTs decreases when the switching frequency is changed under fixed load. The other method is the PWM control, but an additional switch is added. The power stage and theoretical waveforms of the complete amplifier are shown in Fig. 5.9. The idea is to turn off S_2 before turning off S_1 so that the primary current is maintained at the same value at t0, and the output current can be regulated. The shaded area shows that the current circulating through S_1 and D_1 results in extra conduction loss in the switches. The operation principle of the complete inverter is described below.

During time interval [t0,t1], its operation principle is identical to that of the flyback SE-QR inverter. Both S_1 and S_2 can achieve the ZVS operation. At t_2, S_2 is turned off, and voltage across L_R is not clamped by V_{IN} or D_1 any more. In the meantime, the reflected capacitance of CIN in the primary side is much larger than the output capacitance of S_2. As a result, the current flows in the secondary side entirely, and V_{S2} is shaped by the input capacitor of the PT and L_R. At t_3, D_1 conducts, and the primary current, I_{LP}, is circulating through D_1 and S_1. At t_0, S_1 is turned off and another cycle of the operation repeats.

5.5.2 Design of Power Stage

The power stage and its control circuit of a complete CCFL inverter with the HVPT are shown in Fig. 5.10. The power stage consists of a buck converter and a flyback SE-QR inverter which was designed in section 5.4. The control chip of the inverter is UC 3871, which is a fluorescent lamp driver from Unitrode and constant-frequency control is adopted. Instead of using another extra switch to perform the buck operation, it is possible to use variable-frequency control for the flyback SE-QR inverter. However, the efficiency of this variable-frequency-controlled inverter is less than that of the basis circuit by 4 % under high-line operation, where the switching frequency is away from the series resonance frequency fs of the HVPT. The final breadboard CCFL inverters can deliver up to 6 watts, and the range of line regulation is from 8 Vdc to 16 Vdc. Its physical size is $127 \times 16.5 \times 5.5 \left(\mathrm{L} \times \mathrm{W} \times \mathrm{T} \text{ all in mm}\right)$.

In order to demonstrate the uniformity of both HVPTs and their usefulness for inverter applications, four HVPT CCFL inverters have been built and tested under a 2.5-watt output power. Figure 5.11. illustrates the efficiencies of the four experimental inverters from 8 Vdc to 16 Vdc. The measured efficiencies of all HVPT inverters agree with one another.

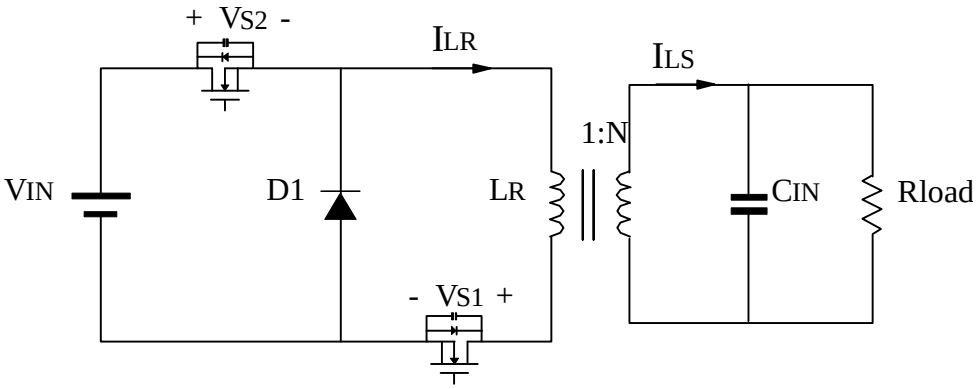

(a)

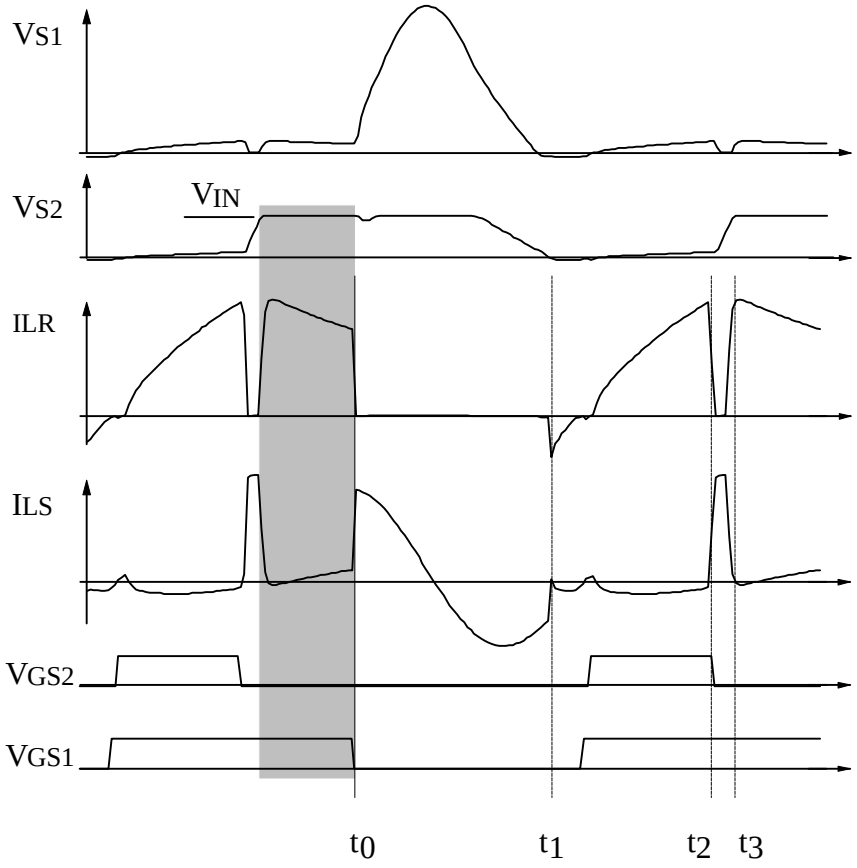

(b)

Fig. 5. 9. Buck + flyback single-ended quasi-resonant (SE-QR) amplifiers. (a) power stage. (b) theoretical waveforms.

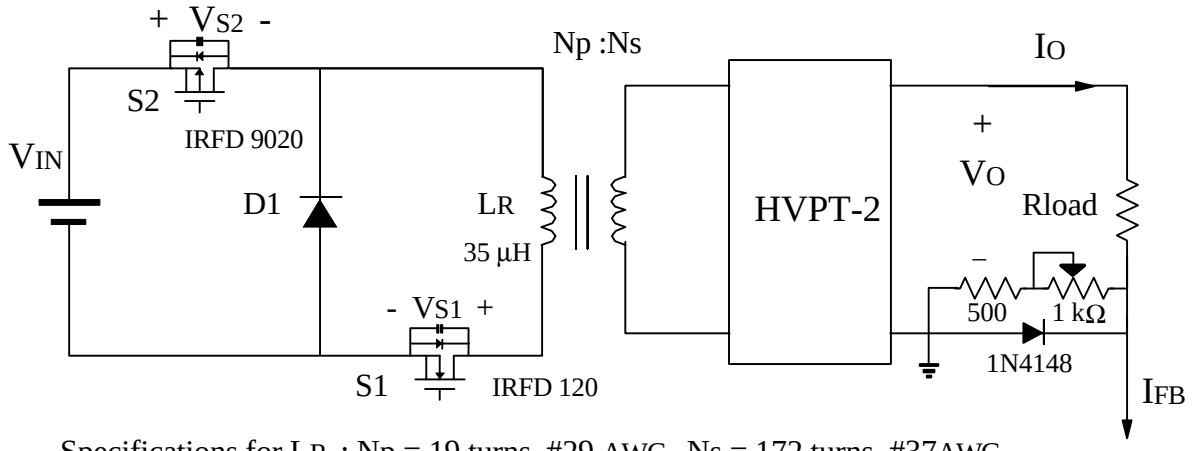

Specifications for L_R : Np = 19 turns, #29 AWG, Ns = 172 turns, #37AWG
Core : PC44EEM12.7 /13.7-Z, Gap : 6 mil

(a) the reference circuit

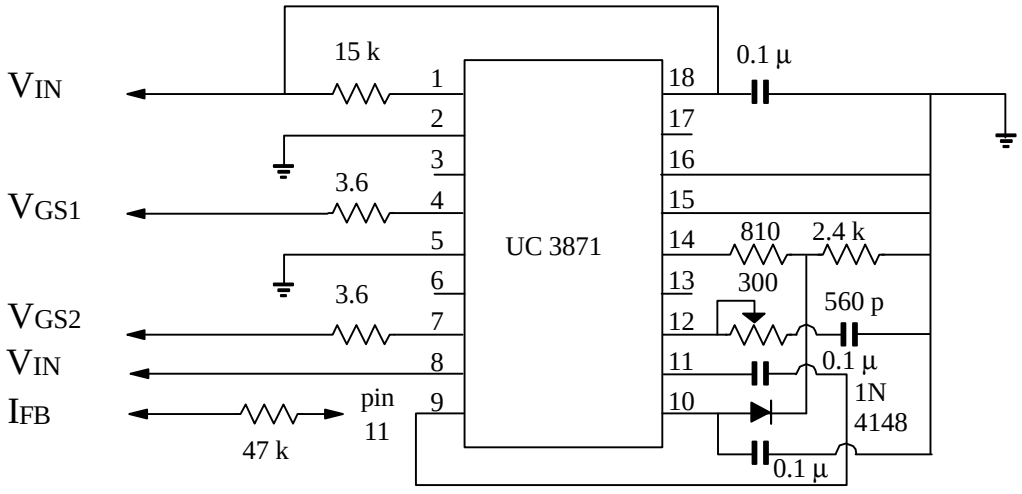

(b)

Fig. 5.10. Complete flyback SE-QR HVPT inverters : the reference circuit. (a) power stage. (b) control circuit. This circuit is used as a reference circuit for efficiency comparison with different HVPT inverters.

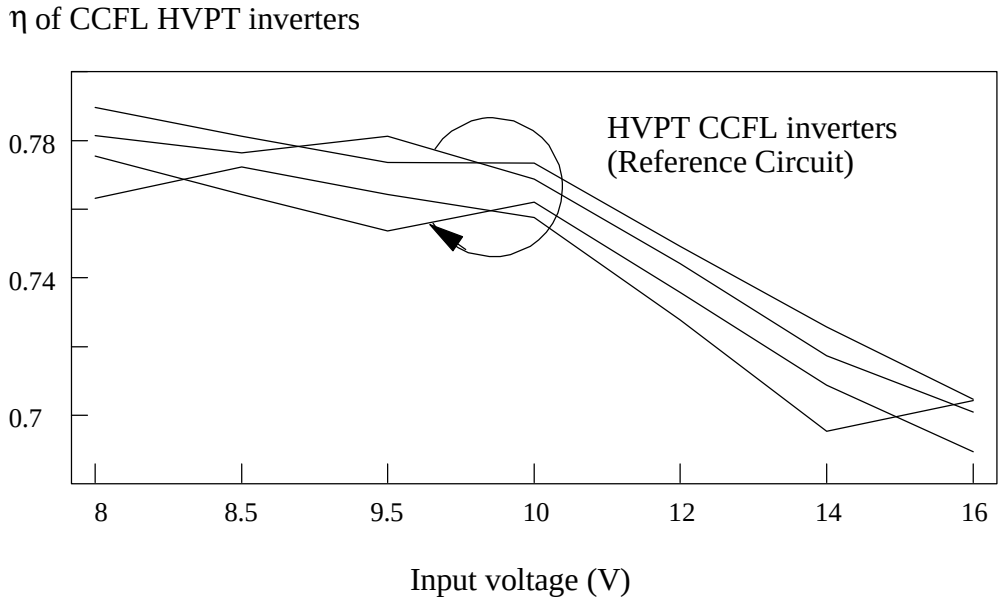

- LAMP is replaced with a 98.2-kΩ resistor

Fig. 5.11. Efficiency of experimental CCFL HVPT inverters (reference circuits). Four experimental CCFL HVPT inverters show almost identical efficiency characteristics. This indicates the uniformity of HVPT and the feasibility to use HVPT in high-voltage applications.

5.6 Comparison Between Conventional HV Transformer with HVPT

Conventionally, the number of turns for the secondary of an HV transformer exceeds a thousand turns for CCFL applications. The immediate advantages of using HVPTs over using conventional HV transformers include no winding and automation. The following experimental circuits show the performance comparison of HVPTs and HV transformers for CCFL applications. At first, a complete HVPT CCFL inverter and a commercial self-oscillated CCFL inverter were employed to examine their performance. Both inverters are operated in the constant-frequency control mode, and the comparison is made via the specification of the conventional CCFL inverter provided by Delta Electronics Inc.

5.6.1 Specifications

The first specifications for the CCFL inverters are recorded below:

- input voltage : 8 volt - 16 volt,
- output current : 5 mA (rms), and
- output power : 2.5 watts.

5.6.2 Conventional CCFL Inverter

Figure 5.12 (a) shows the power stage of a conventional CCFL inverter, which follows a two-stage approach. The first stage is a buck converter followed by a self-oscillated sine wave oscillator. In the oscillator, a parallel resonant tank is formed by T_1 and C_P, and L_{RF} is a choke to realize a current source for the tank. C_B performs the function of a ballast to limit the lamp current, and it needs to withstand high voltage. Generally, C_B is a high-frequency and high-voltage capacitor, and choosing the right capacitor is critical to limiting the variations of the inverter efficiency to the range of 5% to 10% [50].

5.6.3 Experimental Results

It is very difficult to prevent the loading effect of the capacitance of the high-voltage probe when a commercial CCFL inverter, having a capacitor in series with CCFL as its ballast, is tested. Therefore, an illumination meter is required to measure the output power of CCFL. For the CCFL inverter with the HVPT, the efficiency of the CCFL could be measured and calculated by measurement waveforms, but those experimental results include the effect of the capacitance of the high-voltage probe. To verify the performance of both HVPTs and commercial inverters, resistors are used to represent the CCFLs.

Four complete inverters with HVPT and two commercial CCFL inverters were built and tested for better agreement with measurement results shown in Fig 5.11. Figure 5.12 (b) shows that the efficiency of the HVPT inverter is better than that of the conventional inverter under the low-line condition and worse than that of the conventional inverter under the high-line condition. However, the circuit is greatly simplified by employing HVPTs instead of HV transformers, and no ballast is required. If an HVPT with very high step-up ratio can be built by using the stacked structure, it is not necessary to have a second stage step-up. The profile of this HVPT inverter can be further reduced from 5.5 mm.

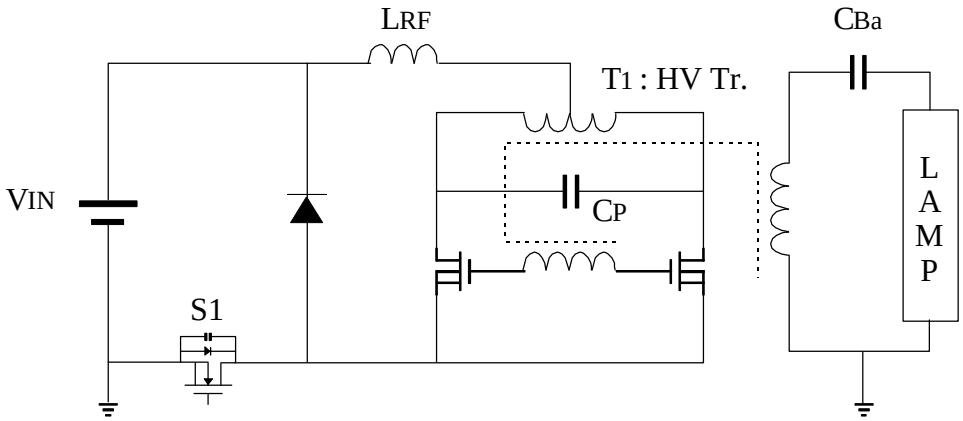

· input voltage : 8 volts - 16
· output current : 5 mA (rms),
· output power : 2.5 watts.

(a)

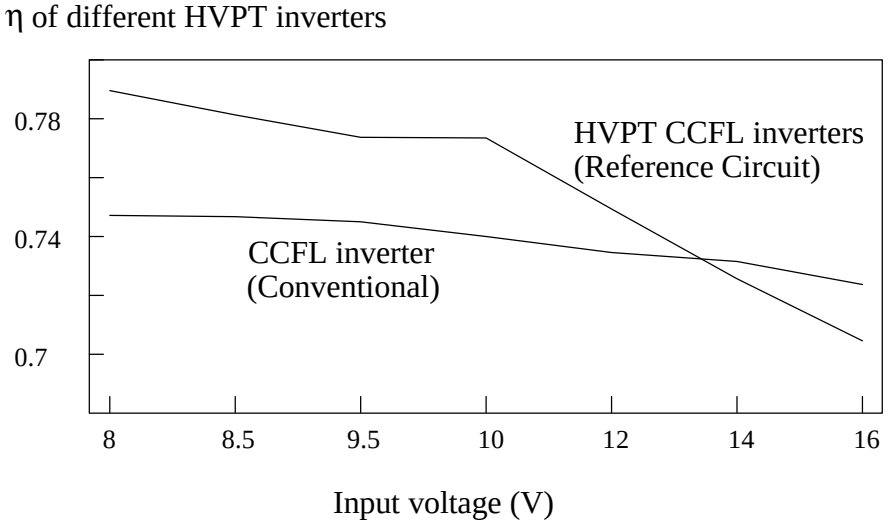

(b)

- LAMP is replaced with a 98.2- kΩ resistor

Fig. 5.12. Efficiency comparison between conventional CCFL inverter and the reference circuit. (a) power stage of conventional CCFL inverters. (b) efficiency of these two different types of inverters.

5.7 Comparison Between Constant- and Variable-Frequency HVPT CCFL Inverters

The objective of this comparison study is to discuss the merits and demerits of two different control methods applied to HVPTs. This set of inverters includes both constant and variable frequency controlled complete HVPT inverters. The comparison has been made via the specification of a prototype variable-frequency-controlled HVPT CCFL inverter from Tokin Corp.

5.7.1 Specifications

- input voltage : 12 volts - 17 volts,
- output current : 7 mA (rms), and
- output power : 5 - 6 watts.

5.7.2 Two-Leg SE-QR HVPT CCFL Inverters

Figure 5.13 (a) shows the power stage of these modified inverters [48]. The HVPT with a very high step-up ratio, approximately 1:32 @ matched CCFL load, has been installed. This HVPT inverter is composed of two SE-QR dc/ac inverters, and control signals of the switches are arranged complementarily. Instead of producing half of the sine wave in the SE-QR amplifier, a nearly sinusoidal waveform is obtained in the input of the HVPT. Therefore, this topology allows to double the voltage gain of the inverter. As a result, the voltage gain , measured from the RMS output voltage to dc input voltage, is at least 64 under the nominal operation of the CCFL. In this circuit, two switches and two inductors are required. The variable-frequency control is used in order to ignite the CCFL easily and to prevent adding any more components.

5.7.3 Experimental Results

At the startup of the CCFL, the impedance of the CCFL increases, and the striking voltage of the CCFL is very high. It can be seen from Fig. 5.2 that the voltage gain of the HVPT increases with the load resistance under matched conditions. If constant-frequency control is used, the voltage gain will not increase dramatically upon startup. In this regard, the variable-frequency control is a better choice for striking the lamp and compensating for temperature effects of the CCFL inverter with the HVPT. However, from the experimental results shown in Fig. 5.13 (b), the efficiency of constant-frequency-controlled HVPT inverters was higher than that of their counterparts at high input line when the controlled frequencies of the counterparts were pushed away from fs.

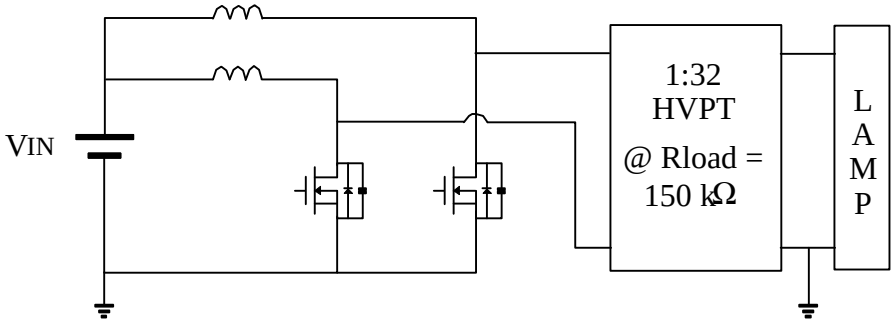

· input voltage : 12 volts- 17
· output current : 7 mA (rms)
· output power : 5 - 6 watts

(a)

η of different HVPT inverters

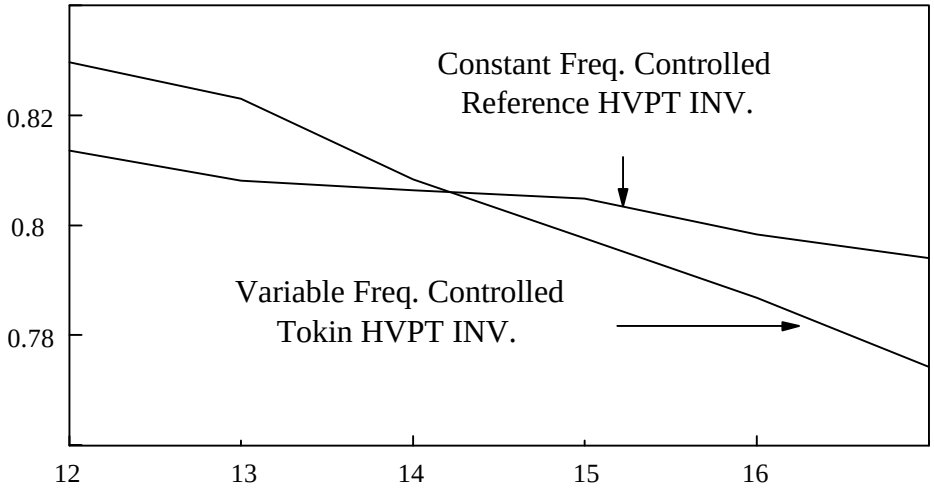

(b)

- LAMP is replaced with a 125- kΩ resistor

Fig. 5.13. Two-leg SE-QR HVPT CCFL inverter and its experimental results. (a) power stage. (b) efficiency comparison with the reference circuit in Fig. 5.8 (a).

5.8 Conclusions

While reviewing all the lamp inverters with HVPT presented in the published papers, one can see that it is necessary to use at least one magnetic component. Usually, this inductor has the highest profile among all components of the circuits employing HVPTs, and it introduces EMI. How to avoid the use of the magnetic core in HVPT circuits seems to be the most challenging issue in developing HVPT circuits. The other design issues, such as temperature effects, possibility of self oscillation, and lifetime test, are still under development. However, the merits of the HVPT make it very attractive to industry and worthy of further exploration.

6. Conclusions and Future Works

A systematic approach towards the design and analysis of PT converters has been conducted in this dissertation. It is developed by introducing lumped models of the PT, optimizing the efficiency of the PT, designing the power amplifiers and matching networks, and building CCFL inverters for HVPT applications which are already commercialized.

Because of the spurious vibrations existing in LVPT-21, its lumped model includes more than three satellite overtones and becomes very complex. However, the developed lumped model for LVPT-21 can actually predict the efficiency drop at unwanted spurious vibration frequencies. A design strategy to control the voltage gain of LVPT-21 is then limited to constant-frequency control for nonmonotonous voltage-gain curve.

As far as the efficiency of LVPT-21 is concerned, the power-flow method is developed to find out the optimal load admittance so that the efficiency of the PT is maximized. The maximal efficiency is calculated where the Linvill constant "c" is close to unity. This results in the calculated efficiencies being very sensitive to the parameters used. Because the two-port parameter vs. frequency curves of LVPT-21 are not smooth curves, the calculated efficiency vs. frequency curve of LVPT-21 is very irregular. However, the calculated efficiency curves are smooth functions with respect to frequencies when the lumped model of LVPT-21 is used. In other words, the optimal load admittance Y_L can be theoretically determined by measured two-port parameters only. Nevertheless, the power-flow method can still be applied to the lumped model, and a similar efficiency curve shows where the efficiency drops significantly at spurious vibration frequencies. At the same time, the voltage-gain curves, obtained from either two-port parameters or the lumped model, have good agreement in shape and magnitude. This verifies the usefulness of the lumped model of LVPT-21. This modeling technique can be extended to other LVPTs for spurious vibration frequencies or overtones of PTs.

In Chapter 3, the optimal load of the high-voltage PT has been proved to be resistive load only. Because of the high-impedance characteristics at the output of the PT, the matching inductance is too large to realize if the power-flow method is applied to HVPTs. The derivation of the optimal resistive load of the HVPT is obtained both from a systematic procedure of circuit rearrangements and from a theoretical derivation in the L-M plane directly.

A design-oriented analysis for various PT converters is presented. This analysis uses the fundamental of the voltage in the amplifier circuits, the lumped model of the PT, and equivalent impedance for the matched rectifier and load. As a result, the PT converters can be represented by very simple equivalent circuits. The theoretical results obtained from the equivalent circuits have been verified and compared with those of experimental waveforms, measured for LVPT and HVPT applications.

The analysis by equivalent circuits makes it possible that all the currents, voltages, and the switching frequency can be normalized easily. This normalization provides a simple method for the design of the parameters of the power amplifier circuits. Also, the peak voltage and current stress can be calculated using this simplified analysis.

To compare the performances of different power amplifier topologies, a design example is given for the application of LVPT converters for on-board power supplies. The half-bridge PT converter gives the best efficiency, but it has the highest component count. The topology of the single-ended quasi-resonant converter is the simplest one, but it is not ideal for LVPT converters because of the high step-up ratio , which is usually greater than unity. The SE-MR LVPT converter needs a resonant tank compared to the SE-QR converter, and variable-frequency control is also needed. To control the voltage gain of LVPT-21, variable-frequency control is not suitable because of the existence of spurious vibration frequencies. The designs show that half-bridge amplifiers are suitable for step-down applications employing LVPTs. On the other hand, SE-QR PT converters are good for step-up applications with HVPTs.

A practical example is presented, and the design procedure is verified with a breadboard implementation of the CCFL HVPT inverter. In the example, a secondary winding needs to be added to the resonant inductor to increase the gain of the converter, and the constant-frequency control is used in the complete inverter. A comparison of constant-frequency and variable-frequency control is based on the efficiencies of the experimental inverters and a commercial HVPT inverter by Tokin. The latter gives a better efficiency than the former at low-line, where the switching frequency Fs is optimized to full-load conditions. With variable-frequency control, Fs is far away from the resonant frequency fs of the PT for high-line operation. Hence, the efficiency of the PT decreases, and so does that of the inverter.

Piezoelectric transformers are new and promising components in power electronics. They are inexpensive, low-profile, and suitable for automation. With these merits, the applications of various types of the PT emerge quickly. Future research goals include the following:

- Future work would include using this systematic approach to characterize the PT so that the requirement of matching networks could be eliminated, and the PT can be incorporated into the amplifier design. As a result, the number of magnetic components is minimized and the advantages of adopting PT into power electronics become significant.

- To maximize the benefit of using the HVPTs, the step-up ratio of the HVPT under nominal load needs to be increased.

- The nonlinear properties of the PTs, such as aging, temperature effect, and packaging, have to be studied to assure the reliability of the PT products.

- In addition, for mass production of PT converters, tuning each PT amplifier circuit to an optimal index is unavoidable because the resonant frequencies of PTs are different from each other. Therefore, to design a reliable self-oscillated or peak-power-tracked PT converter is very important from a manufacturing perspective.

References

[1] C. A. Rosen, "Ceramic Transformers and Filters," Proc. Electronic Comp. Symp., pp. 205-211, 1956.

[2] W. G. Cady, Piezoelectricity. NY: McGraw, 1946.

[3] W. P. Mason, Electromagnetic Transducers and Wave filters. NY: 2nd ed., D. Van Nostrand Company Inc., pp. 399-404, 1948.

[4] H.W. Katz, Solid State Magnetic and Dielectric Devices. NY:, Wiely, pp.94-126, 1959.

[5] D.A. Beringcourt, D.R. Curran and H. Jaffe, ”Piezoelectric and Piezomagentic materials and their function in transducers,” In: W.P. Mason, ed., Physical Acoustics, vol. 1A, Academic Press, New York, pp. 233-249, 1964.

[6] H.F. Tiersten, Linear Piezoelectric Plate Vibrations, Plenum Press, New York, 1969.

[7] D.A. Beringcourt, ”Piezoelectric Crystals and Ceramics,” In: O.E. Mattiat, ed., Ultrasonic Transducer Materials, Plenum Press, New York, pp. 63-124, 1970.

[8] B. Jaffe, W.R. Cook Jr. and H. Jaffe, Piezoelectric Ceramics. NY: Academic Press, pp. 7-47, 1971.

[9] I. Keizi, “Self-exciting type high voltage generation apparatus utilizing piezoelectric voltage transforming elements,” US Patent, No. 3679918, 1969.

[10] Y. Kodama, O. Kumon and N. Saito, “Study of Piezoelectric Ceramic Transducer for High Voltage Generation,” Sumitomo Electric Technical Review, No. 14, pp. 78-87, 1970.

[11] D. A. Berlingcourt, C. Falls, L. S. Sliker, and S. Heights, “Piezoelectric transformer,” US Patent, No. 3736446, 1973.

[12] S. Takahashi, Y. Ebata and K. Kishi, “Applications of acoustic surface wave to power electronics, ” Power Electronic Specialists Conf. Record, pp. 187-196, 1974.

[13] E. Dieulesaint, D. Royer, D. Mazerolle, and P. Nowak, “Piezoelectric transformers,” Electronics Letters, Vol. 24, No. 1, pp. 444-445, Mar. 1988.

[14] S. G. Bochkarev, D. G. Voronin, G. A. Danov, V. V. Drozhzhev, and V. N. Frolov, “Use of integrated circuits of series 1114 in control system for high-voltage piezoelectric-semiconductor converters,” Moscow Institute of Radio Engineering, Electronics, and Automation, pp. 868-870, 1991.

[15] A.X. Kuang, T.S. Zhou, C.X. He, L.Y. Chai, and J.F. Xie, "Piezoelectric ceramic material with large power output ability," US Patent, No. 5173460, 1992.

[16] O. Ohnishi, H. Kishie, A. Iwamoto,T. Zaitsu, and T. Inoue, "Piezoelectric ceramic transformer operating in thickness extentional mode for power supply," Ultrasonics Symposium, pp. 483-488, 1992.

[17] T. Zaitsu, T. Inoue, O. Ohnishi, and A. Iwamoto, "2 MHz power converter with piezoelectric ceramic transformer," IEEE. Intelec Proc., pp. 430-437, 1992.

[18] T. Tanaka, "Piezoelectric Devices in Japan," In: C. Z. Rosen, ed., Piezoelectricity. NY: American Institute of Physics, pp. 289-309, 1992.

[19] C.Y. Lin and F.C. Lee, "Development of a Piezoelectric Transformer Converter," VPEC Power Electron. Sem. Proc., pp. 79-85, 1993.

[20] T. Zaitsu, O. Ohnishi, T. Inoue, M. Shoyama, T. Ninomiya, F.C. Lee, and G.C. Hua, "Piezoelectric transformer operating in thickness extensional vibration and its application to switching converter," IEEE. PESC'94 Record, June, 1994.

[21] C.Y. Lin and F.C. Lee "Design of a Piezoelectric Transformer Converter and Its Matching Networks," Power Electronic Specialists Conf. Record, pp. 607-612, 1994.

[22] C.Y. Lin and F.C. Lee, " Design Of Piezoelectric Transformer Converters Using Single-Ended Topologies," VPEC Power Electron. Sem. Proc., 1994.

[23] C.Y. Lin and F.C. Lee, " Piezoelectric Transformer and its applications," VPEC Power Electron. Sem. Proc., 1995.

[24] I. Ueda and S. Ikegami, “Piezoelectric properties of modified $PbTiO_3$ Ceramics,” Jpn. J. Appl. Phys., Vol. 7, pp. 236-242, 1968.

[25] S. Takahashi, “Longitudinal mode multilayer piezoelectric actuators,” Ceramic Bulletin, Vol. 65, pp. 1156-1157, 1986.

[26] H. Tsuchiya and T. Fukami, “Design principles for multilayer piezoelectric transformers,” Ferroelectrics, Vol. 68, pp. 225-234, 1986.

[27] M. Ueda, M. Satoh, S. Ohtsu, and N. Wakatsuki, "Piezoelectric transformer using energy trapping of width-shear vibration in $LinbO_3$ plate," Ultrasonics Symposium, pp. 977-980, 1992.

[28] N. Dai, A. W. Lofti, G. Skutt, W. Tabisz and F. C. Lee, “ A comparison study of high-frequency, low-profile planar transformer technologies,” Proc. of IEEE App. Power Elec. Conf, 1994.

[29] W. Chen and F.C. Lee, “An Improvement of a Nondimming Electronic Ballast for the Fluorescent Lamp,” , VPEC Power Electron. Sem. Proc., 1995.

[30] E. A. Gerber, “A review of methods for measuring the constants of piezoelectric vibrators,” Proc. of the IRE, pp. 1103-1112, Sep. 1953.

[31] E. Hanfner, “The piezoelectric crystal unit -- definition and methods of measurement,” Proc. of IEEE, Vol. 57, No. 2, pp. 179-201, Feb. 1969.

[32] R. Holland and E. P. Eernisse, “Accurate measurement of coefficients in a ferroelectric ceramic,” IEEE Trans. Sonic and Ultrasonics, Vol. SU-14, No. 4, pp. 173-181, Oct. 1969.

[33] Y. Tsuzuki and M. Toki, “Precise determination of equivalent circuit parameters of quartz crystal resonators,” Proc. of IEEE, pp. 1249-1250, Aug. 1976.

[34] M. Toki, Y. Tsuzuki, and O. Kawano, “A new equivalent circuit for piezoelectric disk resonators,” Proc. of IEEE, Vol. 68, No. 8, pp. 1032-`033, Aug. 1980.

[35] J.-P. Rivera and H. Schmid, "Piezoelectric measurements of Ni-I boracite by the technique of admittance circle and motional capacitance," In: G. W. Taylor, ed., Piezoelectricity. NY: Gordon and Breach Science Publishers, 1985.

[36] P. Gonnard and R. Briot, “Studies on dielectric and mechanical properties of PZT doped ceramics, using a model of losses,” Ferroelectrics, vol. 93, pp. 117-126, 1989.

[37] S. Hirose, Y. Yamayoshi, M. Taga, and H. Shimizu, “A method of measuring the vibration level dependance of impedance-type equivalent circuit constants,” Japanese Journal of Applied Physics, Vol. 30, pp. 117-119, 1991.

[38] R. Briot, P. Gonnard and, M. Troccaz, “Modelization of the Dielectric and Mechanical Losses in Ferroelectric Ceramics,” pp. 580-583, 1991.

[39] S. Hirose, M. Aoyagi, Y. Tomikawa, “Dielectric loss in a piezoelectric ceramic transducer under high-power operation; Increase of dielectric loss and its influence on transducer efficiency,” Jpn. J. Appl. Phys., Vol. 32, pp. 2418-2421, 1993.

[40] J. G. Linvill and J. F. Gibbsons, Transistor and active circuit. NY: McGraw, Chap. 11 and 14, 1961.

[41] J. Choma,Jr., Electrical networks theory and analysis. NY: John Wiley & Sons, pp. 178-197, 1985.

[42] N. O. Sokal and A. D. Sokal, "Class E-A new class of high-efficiency tuned single-ended switching power amplifiers," IEEE Jl. Solid-State Circuits, Vol. SC-10, no. 3, pp. 168-176, 1975.

[43] M. K. Kazimierczuk and K. Puczko, "Exact analysis of class E tuned power amplifier at any Q and switch cycle," IEEE Trans. Circuits and Systems, Vol. CAS-34, no. 2, pp. 149-158, 1987.

[44] M. K. Kazimierczuk and X. T. Bui, "Class-E dc/dc converters with a capacitive impedance inverter," IEEE Trans. Industrial Electron., Vol 36, no. 3, pp. 425-433, 1989.

[45] E.X. Yang, Qiong Li and F.C. Lee, "Analysis and Design of Single-Ended-Parallel Multi-Resonant Converter," Power Electronic Specialists Conf. Record, pp. 1405-1412, 1994.

[46] D. Frederick and T.S. Chang, Continuum mechanics. Cambridge, Scientific Publishers, Inc., 1972.

[47] Dong-Bing Zhang, "Switching mode power source impedance measurement and EMI filter characterization", Thesis, VPI&SU, September 1996.

[48] S. Kawashima, O. Ohnishi, H. Hakamata, A. Fukuoka, T. Inoue, and S. Hirose, "Third order longitudinal mode piezoelectric ceramic transformer and its application to high-voltage inverter," Ultrasonics Symposium, pp. 525-530, 1994.

[49] PJM Smidt and JL Duarte, "Powering neon lamp through piezoelectric transformers," Power Electronic Specialists Conf. Record, pp. 310-315, 1996.

[50] Dan Ward " Matching inverters to CCFL backlights," Information Display, " pp. 15-17, Feb. 1992.

[51] T. Zaitsu, T. Shigehisa, M. Shoyama, T. Ninomiya, "Piezoelectric transformer converter with PWM control," IEEE APEC Proc., pp. 279-283, 1996.

APPENDIX A : Physical Modeling of the PT

A.1 Introduction

Around 1950s, the piezoelectric transformers just emerged and their equivalent circuits had been derived in [3-5] in the forms of different basic model cells. Only the complete model for the longitudinal mode had been described completely [3,4]. Nowadays, the thickness extensional mode multilayer PTs [16] are adopted to enhance the performance of the PTs, for example to increase the gain of the PTs and to improve their power handling. To deal with these multilayer PTs, correct mechanical and electrical boundary conditions have to be created to obtain meaningful equivalent circuits

A.2 Model of the Longitudinal Mode PT

The longitudinal PT is composed of two parts which are the side-plated bar and the end-plated bar. The side-plated bar functions as an actuator, where mechanical vibration is generated due to electrical excitation on their electrodes, as shown in Fig. A.1 (a). On the other hand, the side-plate bar works like a sensor, where the mechanical vibration is transferred to electrical energy, as shown in Fig. A.1 (b). To describe the coupling between electrical and mechanical properties, the linear piezoelectric equations are:

$$\begin{aligned} S &= s^{E} \cdot T + d \cdot E \\ D &= d \cdot T + \varepsilon^{T} \cdot E \,. \end{aligned} \tag{A.1}$$

Instead of using [T, E] as independent variables, it is possible to use [T, D] [S, D], and [S,E] to be independent ones. If (A.1) is solved for [T, D] and [S, D] to give

$$\begin{aligned} S &= s^{D} \cdot T + g \cdot D \\ E &= -g \cdot T + \beta^{T} \cdot D \,, \end{aligned} \tag{A.2}$$

$$\begin{aligned} T &= c^{D} \cdot S - h \cdot D \\ E &= -h \cdot S + \beta^{S} \cdot D \,. \end{aligned} \tag{A.3}$$

In a similar way, other linear piezoelectric equations include

$$T = c^E \cdot S - e \cdot E$$
$$D = e \cdot S + \varepsilon^S \cdot E\,, \tag{A.4}$$

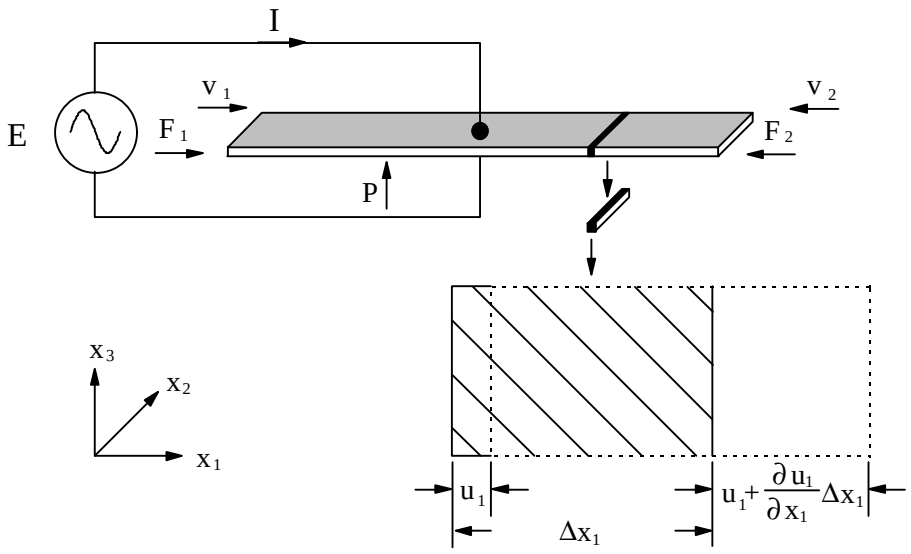

(a)

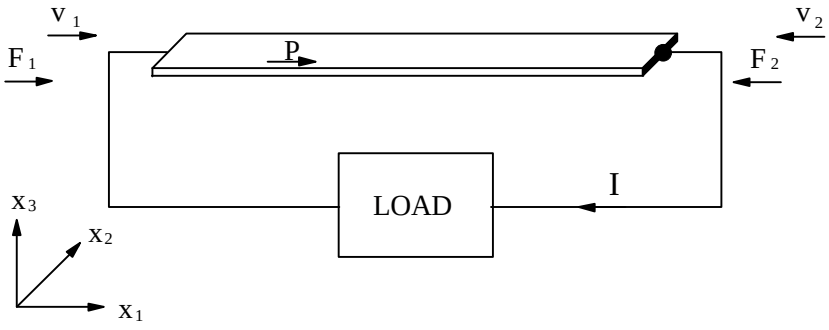

(b)

Fig. A.1. Components of the longitudinal PT. (a) the side-plated bar. (b) the end-plated bar. When a electrical excitation is stimulated on electrodes of the side-plated bar, a longitudinal wave will be generated along x1-direction. The mechanical vibration will generate electric charges in the end-plated bar. Thus, input electrical energy applied to the side-plated bar is transformed to load via the end-plated bar.

where

T: stress,

S: strain,

D: electric displacement,

E: electric field,

s: Elastic compliance constant,

c: Elastic stiffness constant,

ε: Permittivity component,

β: Impermittivity component,

d, h, g, e : Piezoelectric constants,

S (superscript) : At constant strain,

T (superscript) : At constant stress,

D (superscript) : At constant electric displacement,

E (superscript) : At constant electric field,

and

$$h = c^{D} \cdot g \ . \tag{A.5}$$

For the following analysis, all strains and stresses are assumed to occur in only one direction. In other words, the shear stress and shear strain are neglected.

A.2.1 Side-Plated Bar

A.2.1.1 Derivation of One-Dimensional Wave Equation

From Fig. A.1 (a)., the electrical excitation, E, is applied to top and bottom electrodes of the piezoceramic side-plated bar in x_3 or thickness direction. Stresses along x_2 and x_3 are zero, $T_2 = T_3$, and this means the piezoceramics are free to vibrate along the x_2 and x_3 directions. At the same time, the electrical field is distributed uniformly only along x_3 direction, and it indicates that $E_1 = E_2 = 0$. Therefore, electrical field, E_3, and mechanical stress, T_1, are chosen as independent variables of the linear piezoelectric equations. This is a one-dimensional problem, and the electromechanical equations can be expressed in the following equation:

$$\begin{aligned} S_1 &= s_{11}^{E} \cdot T_1 + d_{31} \cdot E_3 \\ D_3 &= d_{31} \cdot T_1 + \varepsilon_{33}^{T} \cdot E_3 \ . \end{aligned} \tag{A.6}$$

For this one-dimensional vibration, Fig. A.1 (a). shows the basic component before applying electrical field with a solid line, and a strained component with a dashed line. Then the total strain equals $\frac{\partial u_1}{\partial x_1} \cdot \Delta x_1$. Because the linear relationship between stress and strain, the total stress applied to the basic component is

$$\sum T = T_1 - T_2 = \frac{dT_1}{dx_1} \cdot \Delta x_1 \ . \tag{A.7}$$

According to Newton's first law, F = m a, and F = T · Area. The net force can be expressed as a function of stress:

$$F_1 = \rho \cdot A \cdot \Delta x_1 \cdot \frac{\partial^2 u_1}{\partial t^2} = \frac{\partial T_1}{\partial x_1} \cdot \Delta x_1 \cdot A \ . \tag{A.8}$$

Stress, T_1, can be replaced by Strain, S_1, in (A.6), and the previous equation becomes

$$\rho \cdot A \cdot \Delta x_1 \cdot \frac{\partial^2 u_1}{\partial t^2} = \frac{\partial}{\partial x_1}\left(\frac{1}{s_{11}^{E}} S_1 - \frac{d_{31}}{s_{11}^{E}} E_3\right) \cdot \Delta x_1 \cdot A \ . \tag{A.9}$$

Since $\frac{d}{dx_1} E_3 = 0$, the one dimensional wave equation is

$$\rho \cdot \frac{\partial^2 u_1}{\partial t^2} = \frac{1}{s_{11}^{E}} \cdot \frac{\partial^2 u_1}{\partial x_1^2} \ . \tag{A.10}$$

If the excitation electric field, E, is sinusoidal , $E_3 = E_0 e^{j\omega t}$, a separate method is used to solve this wave equation. Let $u_1 = X_1 \cdot \tilde{T}$, the previous equation is then arranged as

$$\rho \cdot \frac{\partial^2 (X_1 \cdot \tilde{T})}{\partial t^2} = \frac{1}{s_{11}^{E}} \cdot \frac{\partial^2 (X_1 \cdot \tilde{T})}{\partial x_1^2} \tag{A.11}$$

$$\frac{1}{\rho \cdot s_{11}^{E}} \frac{X_1''}{X_1} = \frac{\tilde{T}''}{\tilde{T}'} = -\omega^2 \ . \tag{A.12}$$

The solution for the wave equation (A.12) is

$$u_1 = X_1(x_1) \cdot \tilde{T}(t) = (B_1 \sin \beta x_1 + B_2 \cos \beta x_2) \cdot e^{j\omega t} \ , \tag{A.13}$$

where

$$\beta = \frac{\omega}{c} \quad \text{and} \quad c = \sqrt{\frac{1}{\rho \cdot s_{33}^{E}}} \ .$$

The electrical and mechanical boundary conditions can be inserted into (A.6) and (A.7). As a result, B_1 and B_2 are calculated directly, and the impedance or admittance of the PT can be derived [5]. However, it is preferable to obtain the general PT's equivalent circuit first and apply the network theory to derive impedance or admittance of the PT by adding suitable electrical and

mechanical boundaries. Therefore, analytical expressions between electric properties (voltage and current) and mechanical properties (force and velocity) have to be derived first. From Fig. A.1 (a)., the analytical equations for forces and velocities at the boundary of the material along the x_1 axis are shown in the following:

$$\begin{aligned} F_1 &= -T_1\big|_{x_1=0} \cdot A = -\left(\frac{1}{s_{11}^E} S_1 - \frac{d_{31}}{s_{11}^E} E_3\right)\Bigg|_{x_1=0} \cdot A \cdot e^{j\omega t} \\ &= \frac{-1}{s_{11}^E}\frac{\partial^2 u_1}{\partial x_1} + \frac{d_{31}}{s_{11}^E} E_3\Bigg|_{x_1=0} \cdot A \cdot e^{j\omega t} \\ &= \frac{-\beta \cdot A}{s_{11}^E}(B_1 \cos\beta x_1 - B_2 \sin\beta x_1)\Bigg|_{x_1=0} \cdot e^{j\omega t} + \frac{d_{31} \cdot A}{s_{11}^E} E_3 \cdot e^{j\omega t} . \end{aligned} \tag{A.14}$$

To simplify the analysis, phasor representation is used and the previous equation becomes:

$$\hat{F}_1 = \frac{-\beta \cdot A}{s_{11}^E} B_1 + \frac{d_{31} \cdot A}{s_{11}^E} \hat{E}_3 \tag{A.15}$$

$$\begin{aligned} \hat{F}_2 &= -\hat{T}_1\big|_{x_1=l} \cdot A \\ &= \frac{-\beta \cdot A}{s_{11}^E}(B_1 \cos\beta l - B_2 \sin\beta l) + \frac{d_{31} \cdot A}{s_{11}^E} \hat{E}_3 \end{aligned} \tag{A.16}$$

$$v_1 = \frac{\partial u_1}{\partial t}\Bigg|_{x_1=0} \tag{A.17}$$

$$\hat{v}_1 = j\omega B_2$$

$$v_2 = -\frac{\partial u_1}{\partial t}\Bigg|_{x_1=l} \tag{A.18}$$

$$\hat{v}_2 = -j\omega((B_1 \sin\beta l + B_2 \cos\beta l) .$$

From (A.17)-(A.18), B_2 and B_1 are

$$B_2 = \frac{1}{j\omega} \cdot \hat{v}_1 , \tag{A.19}$$

$$\begin{aligned} B_1 &= \frac{1}{-j\omega \cdot \sin\beta l}(\hat{v}_2 + j\omega \cdot \hat{v}_1 \cdot \frac{\cos\beta l}{j\omega}) \\ &= \frac{-1}{j\omega}(\frac{\hat{v}_1}{\tan\beta l} + \frac{\hat{v}_2}{\sin\beta l}) . \end{aligned} \tag{A.20}$$

2.2.1.2 Basic Model Cell

The electrical properties, voltage and current, are derived according to the following equations:

$$V = -\int E \cdot dx\,,$$
$$I = \frac{d}{dt}\oint D \cdot ds\,. \tag{A.21}$$

Therefore,

$$\hat{V} = -\int_h^0 \hat{E}_3 \cdot dx_3 = \hat{E}_3 \cdot h \text{ , and} \tag{A.22}$$

$$\begin{aligned} I &= \frac{d}{dt}\int_0^l D_3 \cdot W \cdot dx_1 \\ &= W \cdot \frac{d}{dt}\int_0^l \left(d_{31} \cdot T_1 + \varepsilon^T \cdot E_3\right) \cdot dx_1 \\ \hat{I} &= j\omega \cdot W \cdot \int_0^l \left(d_{31} \cdot \hat{T}_1 + \varepsilon^T \cdot \hat{E}_3\right) \cdot dx_1 \\ &= \frac{j\omega \cdot W \cdot d_{31}}{s^E} \cdot \int_0^l \left(\hat{S}_1 - d_{31} \cdot \hat{E}_3\right) \cdot dx_1 + j\omega \cdot W \cdot \varepsilon^T \cdot \hat{E}_3 \cdot l \\ &= \frac{j\omega \cdot W \cdot d_{31}}{s^E} \cdot \left(\hat{u}_1\big|_{x_1=l} - \hat{u}_1\big|_{x_1=0}\right) + j\omega \cdot W \cdot \varepsilon^T \cdot l \cdot \left(1 - \frac{d^2{}_{31} \cdot Y^E}{\varepsilon^T}\right) \cdot \hat{E}_3 \\ &= -W \cdot d_{31} \cdot Y^E \cdot \left(\hat{v}_1 + \hat{v}_2\right) + \frac{j\omega \cdot W \cdot \varepsilon^T \cdot l}{h} \cdot \left(1 - \frac{d^2{}_{31} \cdot Y^E}{\varepsilon^T}\right) \cdot \hat{V} \end{aligned} \tag{A.23}$$

The electrical clamped impedance, $Z_E{}^{LC}$, is defined when the piezoceramics are clamped at both ends , $\hat{v}_1 = \hat{v}_2 = 0$, and can be expressed as:

$$Z_E{}^{LC} = \frac{h}{j\omega \cdot W \cdot \varepsilon^T \cdot l \cdot \left(1 - k_{31}{}^2\right)}\ . \tag{A.24}$$

With $Z_E{}^{LC}$, (A.23) can be rearranged to give

$$\begin{aligned} \hat{I} &= -W \cdot d_{31} \cdot Y^E \cdot \left(\hat{v}_1 + \hat{v}_2\right) + \frac{1}{Z_E{}^{LC}} \cdot \hat{V} \\ &= -\psi \cdot \left(\hat{v}_1 + \hat{v}_2\right) + \frac{1}{Z_E{}^{LC}} \cdot \hat{V}\,. \end{aligned} \tag{A.25}$$

where

$$\psi = W \cdot d_{31} \cdot Y^E\ . \tag{A.26}$$

Substituting (A.19) and (A.20) to (A.15) and (A.16), F_1 and F_2 in phasor representation become

$$\begin{aligned}\hat{F}_1 &= \frac{-\beta \cdot A}{s_{11}^{E}} \cdot \frac{-1}{j\omega}\left(\frac{\hat{v}_1}{\tan\beta l} + \frac{\hat{v}_2}{\sin\beta l}\right) + \frac{d_{31} \cdot A}{s_{11}^{E}} \frac{\hat{V}}{h} \\ &= \frac{Z_o}{j \cdot \tan\beta l} \cdot \hat{v}_1 + \frac{Z_o}{j \cdot \sin\beta l} \cdot \hat{v}_2 + \psi \cdot \hat{V}\,;\end{aligned} \tag{A.27}$$

$$\begin{aligned}\hat{F}_2 &= \frac{-\beta \cdot A}{s_{11}^{E}}\left(\left(\frac{-1}{j\omega}\left(\frac{\hat{v}_1}{\tan\beta l} + \frac{\hat{v}_2}{\sin\beta l}\right)\right)\cos\beta l - \frac{\hat{v}_1}{j\omega} \cdot \sin\beta l\right) + \frac{d_{31} \cdot A}{s_{11}^{E}} \hat{E}_3 \\ &= \frac{Z_o}{j \cdot \sin\beta l} \cdot \hat{v}_1 + \frac{Z_o}{j \cdot \tan\beta l} \cdot \hat{v}_2 + \psi \cdot \hat{V}\,,\end{aligned} \tag{A.28}$$

where

$$\begin{aligned}Z_o &= \frac{\beta \cdot A}{s_{11}^{E} \cdot \omega} = \frac{\frac{\omega}{\sqrt{\frac{1}{\rho \cdot s_{11}^{E}}}} \cdot (h \cdot W)}{s_{11}^{E} \cdot \omega}\,. \\ &= \sqrt{\rho \cdot Y_{11}^{E}} \cdot h \cdot W\end{aligned} \tag{A.29}$$

Instead of using (A.25), (A.27), and (A.28) to represent the electromechanical system, a different notation is used to constitute the electrical network more easily as shown below

$$\begin{bmatrix}\hat{F}_1 \\ \hat{F}_2 \\ \hat{V}\end{bmatrix} = \begin{bmatrix}a_{11} & a_{12} & a_{13} \\ a_{21} & a_{22} & a_{23} \\ a_{31} & a_{32} & a_{33}\end{bmatrix} \cdot \begin{bmatrix}\hat{v}_1 \\ \hat{v}_2 \\ \hat{I}\end{bmatrix}; \tag{A.30}$$

$$\hat{V} = \psi \cdot \hat{v}_1 + \psi \cdot \hat{v}_2 + Z_E^{LC} \cdot \hat{I}\,; \tag{A.31}$$

$$\begin{aligned}\hat{F}_1 &= \frac{Z_o}{j \cdot \tan\beta l} \cdot \hat{v}_1 + \frac{Z_o}{j \cdot \sin\beta l} \cdot \hat{v}_2 + \psi \cdot \hat{V} \\ &= \left(\frac{Z_o}{j \cdot \tan\beta l} + \psi^2\right) \cdot \hat{v}_1 + \left(\frac{Z_o}{j \cdot \sin\beta l} + \psi^2\right) \cdot \hat{v}_2 + \psi \cdot Z_E^{LC} \cdot \hat{I}\,;\end{aligned} \tag{A.32}$$

$$\begin{aligned}\hat{F}_2 &= \frac{Z_o}{j \cdot \sin\beta l} \cdot \hat{v}_1 + \frac{Z_o}{j \cdot \tan\beta l} \cdot \hat{v}_2 + \psi \cdot \hat{V} \\ &= \left(\frac{Z_o}{j \cdot \sin\beta l} + \psi^2\right) \cdot \hat{v}_1 + \left(\frac{Z_o}{j \cdot \tan\beta l} + \psi^2\right) \cdot \hat{v}_2 + \psi \cdot Z_E^{LC} \cdot \hat{I}\,.\end{aligned} \tag{A.33}$$

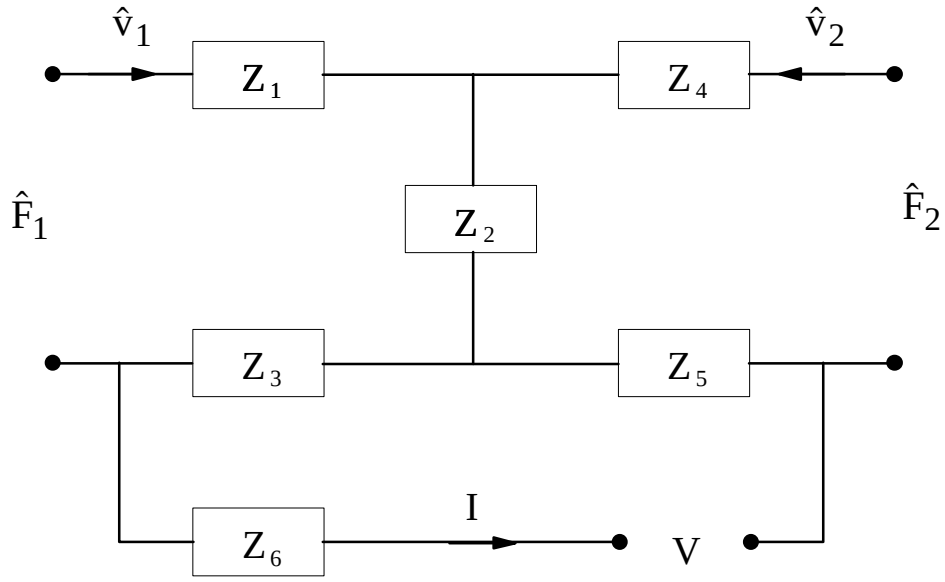

Fig. A.2. The three-port network for the side-plated bar. v, F1, and F2 are derived from one-dimensional wave equation. The three-port network can not separate the electrical and mechanical systems clearly. However, $\psi^2 \cdot Z_E^{LC}$ term in Z_2 offers a solution by introducing an ideal transformer whose turns ratio is equal to ψ.

If the velocity in the mechanical system is analogous to the current in the electrical system, it is possible to build a three-port network [3], as shown in Fig. A.2, and the impedances Z_1 to Z_6 are equal to

$$
\begin{aligned}
Z_1 &= \frac{Z_o}{j \cdot \tan \beta l} - \frac{Z_o}{j \cdot \sin \beta l} - \psi \cdot Z_E^{LC}; \\
Z_2 &= \frac{Z_o}{j \cdot \sin \beta l} + \psi^2 \cdot Z_E^{LC}; \\
Z_3 &= \psi \cdot Z_E^{LC}; \\
Z_4 &= \frac{Z_o}{j \cdot \tan \beta l} - \frac{Z_o}{j \cdot \sin \beta l} + \psi \cdot Z_E^{LC}; \\
Z_5 &= -\psi \cdot Z_E^{LC}; \\
Z_6 &= Z_E^{LC}.
\end{aligned}
\tag{A.34}
$$

These mathematical expressions do not clearly represent the coupling between the electrical and mechanical systems. By introducing a transformer, (A.31) to (A.33) can be rearranged to give

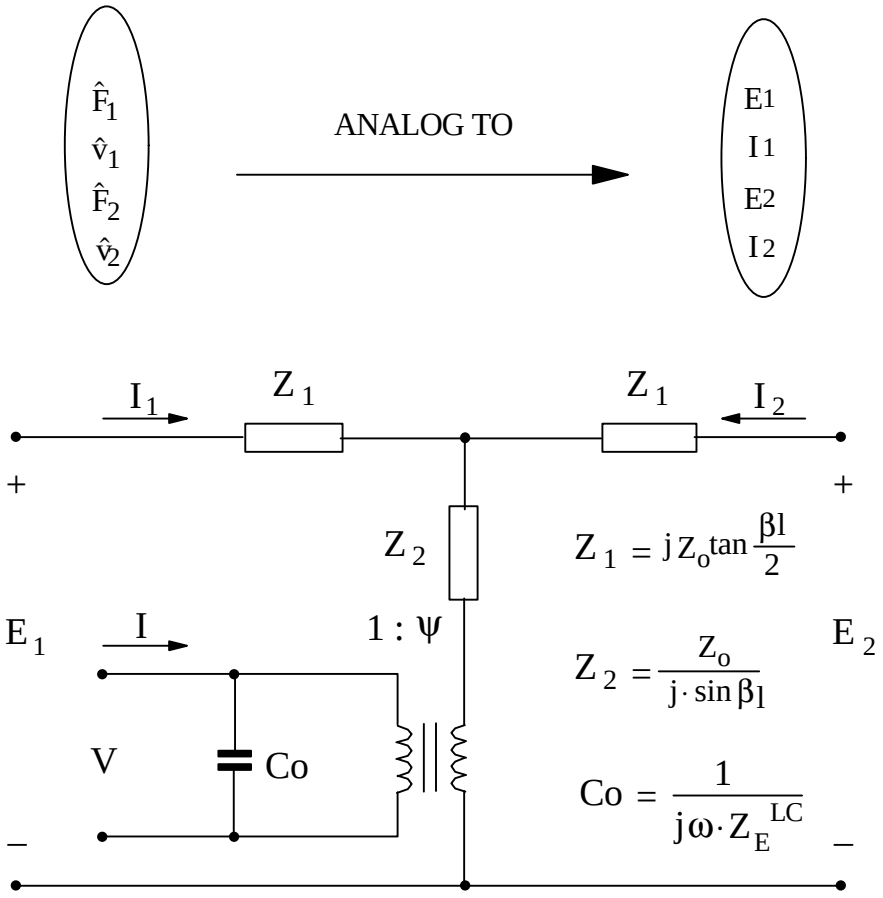

A : surface area = *l* W

$$\psi = W \cdot d_{31} \cdot Y_{11}^{E} \qquad \beta = \frac{\omega}{vsound} \qquad vsound = \sqrt{\frac{1}{\rho \cdot s_{33}^{E}}}$$

$$Z_E^{LC} = \frac{h}{j\,\omega \cdot A \cdot \varepsilon^{T} \cdot (1 - k_{31}^{2})} \qquad Z_o = \sqrt{\rho \cdot Y_{11}^{E}} \cdot h \cdot W$$

Fig. A.3. Basic model for the side-plated bar. If $\psi = 0$, it means that the piezoelectric constant is equal to zero. There is no coupling between electrical and mechanical systems.

$$\hat{F}_1 = \left(\frac{Z_o}{j \cdot \tan \beta l} - \frac{Z_o}{j \cdot \sin \beta l} \right) \cdot \hat{v}_1 + \frac{Z_o}{j \cdot \sin \beta l} \cdot \left(\hat{v}_1 + \hat{v}_2 \right) + \psi \cdot \hat{V}$$
$$= j \cdot Z_o \cdot \tan \frac{\beta l}{2} \cdot \hat{v}_1 + \frac{Z_o}{j \cdot \sin \beta l} \cdot \left(\hat{v}_1 + \hat{v}_2 \right) + \psi \cdot \hat{V} \; ; \qquad \text{(A.35.a)}$$

$$\hat{F}_2 = \left(\frac{Z_o}{j \cdot \tan \beta l} - \frac{Z_o}{j \cdot \sin \beta l} \right) \cdot \hat{v}_2 + \frac{Z_o}{j \cdot \sin \beta l} \cdot \left(\hat{v}_1 + \hat{v}_2 \right) + \psi \cdot \hat{V}$$
$$= j \cdot Z_o \cdot \tan \frac{\beta l}{2} \cdot \hat{v}_2 + \frac{Z_o}{j \cdot \sin \beta l} \cdot \left(\hat{v}_1 + \hat{v}_2 \right) + \psi \cdot \hat{V} \; ; \qquad \text{(A.35.b)}$$

$$\hat{V} = \psi \cdot Z_E{}^{LC} \cdot (\hat{v}_1 + \hat{v}_2) + Z_E{}^{LC} \cdot \hat{I} \; . \qquad \text{(A.35.c)}$$

Figure A.3. shows the basic equivalent circuit for a side-plated piezoceramics, and $\psi = W \cdot d_{31} \cdot Y_{11}{}^{E}$. If $\psi = 0$, it means the piezoelectric constant $d_{31} = 0$, and there is no coupling between the electrical and mechanical systems. This model is good for any mode of operation for the side-plated piezoceramics.

A.2.2 End-Plated Bar

A.2.2.1 Derivation of One-Dimensional Wave Equation

Figure A.1 (b). shows a piezoceramic side-plated bar, and the electrical excitation, E, is generated across electrodes along x_1 or in the longitudinal direction. Stresses along x_2 and x_3 are zero, $T_2 = T_3 = 0$, and this means that the piezoceramics are free to vibrate along x_2 and x_3 directions. The piezoceramic material is considered to be nonconductive and no fling flux; therefore $D_2 = D_3 = 0$. Electrical flux, D_1, and mechanical stress, T_1, are selected to be the independent variables of the linear piezoelectric equations:

$$S_1 = s_{11}{}^{D} \cdot T_1 + g_{11} \cdot D_1$$
$$E_1 = -g_{11} \cdot T_1 + \beta_{11}{}^{T} \cdot D_1 \; , \qquad \text{(A.36)}$$

From Fig. A.1 (a)., a similar derivation in the last section can be obtained from Newton's law, F = m a, to give

$$F = \rho \cdot A \cdot \Delta x_1 \cdot \frac{\partial^2 u_1}{\partial t^2} = \frac{\partial T_1}{\partial x_1} \cdot \Delta x_1 \cdot A \; , \qquad \text{(A.37)}$$

Stress, T_3, can be replaced by Strain, S_3, in (A.36), and the previous equation becomes

$$\rho \cdot A \cdot \Delta x_1 \cdot \frac{\partial^2 u_1}{\partial t^2} = \frac{\partial}{\partial x_1}\left(\frac{1}{s_{11}^{\ D}} S_1 - \frac{g_{11}}{s_{11}^{\ D}} D_1\right) \cdot \Delta x_1 \cdot A \ . \tag{A.38}$$

Since $\frac{\partial}{\partial x_1} D_1 = 0$, the one-dimensional wave equation is

$$\rho \cdot \frac{\partial^2 u_1}{\partial t^2} = \frac{1}{s_{11}^{\ D}} \cdot \frac{\partial^2 u_1}{\partial x_1^{\ 2}} \ . \tag{A.39}$$

If the excitation strain, S, is sinusoidal , $D_1 = D_0\, e^{j\omega t}$, the solution for the wave equation (A.39) is

$$u_1 = (B_1 \sin \beta x_1 + B_2 \cos \beta x_1) \cdot e^{j\omega t} \ , \tag{A.40}$$

where

$$\beta = \frac{\omega}{c} \quad \text{and} \quad c = \sqrt{\frac{1}{\rho \cdot s_{11}^{\ D}}} \tag{A.41}$$

To simplify the analysis, phasor representation is used and has already been introduced in the previous section. The forces at both ends of the end-plated bar are shown in Fig. A.1 (b)., and are equal to

$$\hat{F}_1 = \frac{-\beta \cdot A}{s_{11}^{\ D}} B_1 + \frac{g_{11} \cdot A}{s_{11}^{\ D}} \hat{D}_1 \ ; \tag{A.42}$$

$$\hat{F}_2 = \frac{-\beta \cdot A}{s_{11}^{\ D}} (B_1 \cos \beta l - B_2 \sin \beta l) + \frac{g_{11} \cdot A}{s_{11}^{\ D}} \hat{D}_1 \ . \tag{A.43}$$

2.2.2.2 Basic Model Cell

The electrical properties, voltage and current, are derived from (A.21).

$$\begin{aligned} I &= \frac{\partial}{\partial t} \oint_A D_1 \cdot dA \ ; \\ \hat{I} &= j \cdot \omega \cdot \hat{D}_1 \cdot h \cdot W \ ; \end{aligned} \tag{A.44}$$

$$
\begin{aligned}
\hat{V} &= -\int_{l}^{0} \hat{E}_1 dx_1 \\
&= \int_0^l \left(- g_{11} \cdot \hat{T}_1 + \beta_{11}{}^{E} \cdot \hat{D}_1 \right) \cdot dx_3 \\
&= \frac{- g_{11}}{s_{11}{}^{D}} \cdot \int_0^l \left(\hat{S}_1 - g_{11} \cdot \hat{D}_1 \right) \cdot dx_1 + \beta_{11}{}^{T} \cdot \hat{D}_1 \cdot l \\
&= \frac{- g_{11}}{s_{33}{}^{D}} \cdot \left(\hat{u}_1 \big|_{x_1 = l} - \hat{u}_1 \big|_{x_1 = 0} \right) + l \cdot \left(\beta_{11}{}^{T} + \frac{g^2{}_{11}}{s_{11}{}^{D}} \right) \cdot \hat{D}_1 \\
&= \frac{g_{11}}{j \cdot \omega \cdot s_{11}{}^{D}} \cdot \left(\hat{v}_1 + \hat{v}_2 \right) + Z_E{}^{LC} \cdot \hat{I} \, ,
\end{aligned}
\tag{A.45}
$$

where $Z_E{}^{LC}$ is the clamped impedance and equals

$$
Z_E{}^{LC} = \frac{l}{j \cdot \omega \cdot h \cdot W} \cdot \left(\beta_{11}{}^{T} + \frac{g_{11}{}^{2}}{s_{11}{}^{D}} \right) . \tag{A.46}
$$

Substituting B1 and B2 into (A.42) and (A.43), F_1 and F_2 in phasor representation become

$$
\begin{aligned}
\hat{F}_1 &= \frac{- \beta \cdot A}{s_{11}{}^{D}} \cdot \frac{-1}{j\omega} \left(\frac{\hat{v}_1}{\tan \beta l} + \frac{\hat{v}_2}{\sin \beta l} \right) + \frac{g_{11} \cdot A}{s_{11}{}^{D}} \cdot \frac{\hat{I}}{j \cdot \omega \cdot A} \\
&= \frac{Z_o}{j \cdot \tan \beta l} \cdot \hat{v}_1 + \frac{Z_o}{j \cdot \sin \beta l} \cdot \hat{v}_2 + \frac{g_{11}}{j \cdot \omega \cdot s_{11}{}^{D}} \cdot \hat{I} \, ;
\end{aligned}
\tag{A.47}
$$

$$
\begin{aligned}
\hat{F}_2 &= \frac{- \beta \cdot A}{s_{11}{}^{D}} \left(\left(\frac{-1}{j\omega} \left(\frac{\hat{v}_1}{\tan \beta l} + \frac{\hat{v}_2}{\sin \beta l} \right) \right) \cos \beta l - \frac{\hat{v}_1}{j\omega} \cdot \sin \beta l \right) + \frac{g_{11} \cdot A}{s_{11}{}^{D}} \cdot \hat{D}_1 \\
&= \frac{Z_o}{j \cdot \sin \beta l} \cdot \hat{v}_1 + \frac{Z_o}{j \cdot \tan \beta l} \cdot \hat{v}_2 + \frac{g_{11}}{j \cdot \omega \cdot s_{11}{}^{D}} \cdot \hat{I} \, ;
\end{aligned}
\tag{A.48}
$$

where

$$
\begin{aligned}
Z_o &= \frac{\beta \cdot A}{s_{33}{}^{D} \cdot \omega} \\
&= \sqrt{\rho \cdot s_{33}{}^{D}} \cdot h \cdot W \, .
\end{aligned}
\tag{A.49}
$$

From (A.45) to (A.48), a three port network is built, as shown in Fig. A.2, and the impedances Z_1 to Z_6 equal

$$
\begin{aligned}
Z_1 &= \frac{Z_o}{j\cdot\tan\beta l} - \frac{Z_o}{j\cdot\sin\beta l} - \frac{g_{11}}{j\cdot\omega\cdot {s_{11}}^D};\\
Z_2 &= \frac{Z_o}{j\cdot\sin\beta l};\\
Z_3 &= \frac{g_{11}}{j\cdot\omega\cdot {s_{11}}^D};\\
Z_4 &= \frac{Z_o}{j\cdot\tan\beta l} - \frac{Z_o}{j\cdot\sin\beta l} + \frac{g_{11}}{j\cdot\omega\cdot {s_{11}}^D};\\
Z_5 &= -\frac{g_{11}}{j\cdot\omega\cdot {s_{11}}^D};\\
Z_6 &= {Z_E}^{LC}.
\end{aligned}
\tag{A.50}
$$

Comparing (A.50) to (A.34), let′s assume

$$
\psi\cdot {Z_E}^{LC} = \frac{g_{11}}{j\cdot\omega\cdot {s_{11}}^D}\ . \tag{A.51}
$$

Then, (A.45) to (A.48) can be rearranged, to give

$$
\begin{aligned}
\hat{V} &= \psi\cdot(\hat{v}_1+\hat{v}_2) + {Z_E}^{LC}\cdot\hat{I};\\
\hat{F}_1 &= \left(\frac{Z_o}{j\cdot\tan\beta l} - \frac{Z_o}{j\cdot\sin\beta l}\right)\cdot\hat{v}_1 + \frac{Z_o}{j\cdot\sin\beta l}\cdot\left(\hat{v}_1+\hat{v}_2\right) + \psi\cdot\left(V - \psi\cdot {Z_E}^{LC}\cdot\left(\hat{v}_1+\hat{v}_2\right)\right);\\
\hat{F}_2 &= \left(\frac{Z_o}{j\cdot\tan\beta l} - \frac{Z_o}{j\cdot\sin\beta l}\right)\cdot\hat{v}_2 + \frac{Z_o}{j\cdot\sin\beta l}\cdot\left(\hat{v}_1+\hat{v}_2\right) + \psi\cdot\left(V - \psi\cdot {Z_E}^{LC}\cdot\left(\hat{v}_1+\hat{v}_2\right)\right).
\end{aligned}
\tag{A.52}
$$

Figure A.4. shows the basic equivalent circuit for the end-plated piezoceramics, and

$$
\begin{aligned}
\psi &= \frac{g_{11}}{j\cdot\omega\cdot {s_{11}}^D}\cdot\frac{1}{{Z_E}^{LC}}\\
&= \frac{h\cdot W}{l}\cdot\frac{g_{11}\cdot {Y_1}^D}{{\beta_{11}}^T + {g_{11}}^2\cdot {Y_1}^D};
\end{aligned}
\tag{A.53}
$$

$$V = \psi \cdot (\hat{v}_1 + \hat{v}_2) + Z_E^{LC} \cdot I$$

$$\hat{F}_1 = j Z_o \tan\frac{\beta l}{2} \cdot \hat{v}_1 + \frac{Z_o}{j \cdot \sin\beta l} \cdot (\hat{v}_1 + \hat{v}_2) + \psi \cdot \left(V - \psi \cdot Z_E^{LC} \cdot (\hat{v}_1 + \hat{v}_2)\right)$$

$$\hat{F}_2 = j Z_o \tan\frac{\beta l}{2} \cdot \hat{v}_2 + \frac{Z_o}{j \cdot \sin\beta l} \cdot (\hat{v}_1 + \hat{v}_2) + \psi \cdot \left(V - \psi \cdot Z_E^{LC} \cdot (\hat{v}_1 + \hat{v}_2)\right)$$

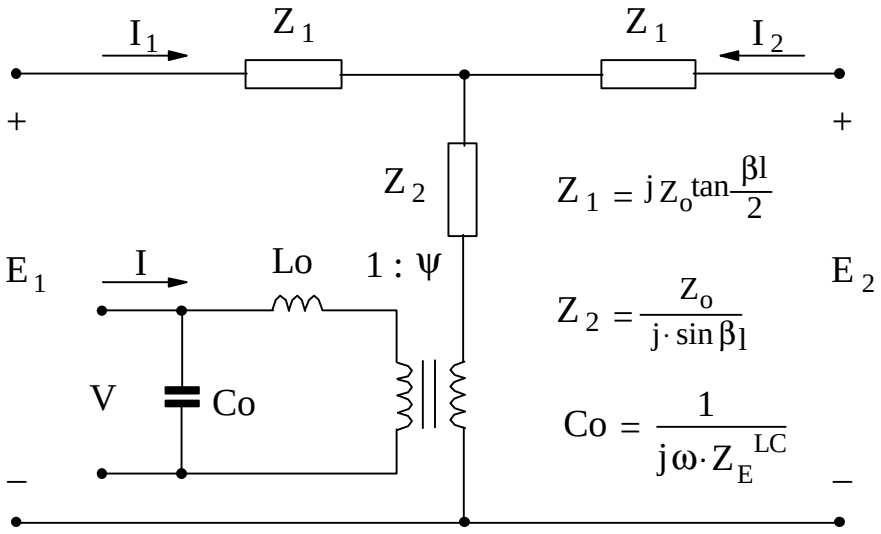

A_C : cross-section area = h W

$$\psi = \frac{g_{11}}{j \cdot \omega \cdot s_{11}^{D}} \cdot \frac{1}{Z_E^{LC}} \qquad Lo = \frac{1}{\omega^2 \, Co}$$

$$Z_E^{LC} = \frac{l}{j \cdot \omega \cdot A_C} \cdot \left(\beta_{11}^{T} + \frac{g_{11}^{2}}{s_{11}^{D}}\right) \qquad Z_o = \sqrt{\rho \cdot Y_{11}^{D}} \cdot A_C$$

Fig. A.4. Basic model for the end-plated bar. An extra equivalent inductance, Lo, is added in the electrical system.

A.2.3 Complete Model

For a longitudinal piezoelectric transformer, the side-plated bar is the input or driver part, and the end-plated bar is the output part. Theoretically, manufacturing these two portions in a piece of piezoceramic constitutes a longitudinal mode PT. However, the electrode for the end-plated bar located in the center of the PT had been placed in different positions for the purposes of manufacturing or insulation. Figure A.5. shows the insulated and noninsulated longitudinal mode PTs. The electrode, near the driver portion of the side-plated part is either shared with one of the electrodes of the driver or appears on the surface of the output portion. These arrangements will affect the performance of the longitudinal mode PT slightly [5].

Some terms related to continuum mechanics are explained first. ″Free at a surface″ means that this surface allows to vibrate freely; in other words, the force on the surface is zero. Physically, this surface is placed without any applied stress. Clamped at a surface indicates that displacement is zero at any point of the surface and the velocity is zero. According to continuum mechanics [46], the velocity is a continuous function of x_1 or x_3, and is dependent on the selected coordinate. The complete equivalent circuit of the longitudinal mode PT is composed of the equivalent circuits of the side-plated bar and the ended-plated bar shown in Fig. A.3. and A.4, respectively. The following assumptions and boundary conditions are very important to constructing the model of the longitudinal PTs from two different model cells.

1. All the variables for the equivalent circuit of the side plated bar are added a prime, x', in superscript to distinguish them from those belonging to the end plated bars, for example: E_1', I_1', V' and I' etc.
2. $-I_2' = I_1$ or $-v_2' = v_1$ at $x_1 = 0$;
3. $E_2' = E_1$ or $F_2' = F_1$;
4. $E_1' = E_2 = 0$ or $F_1' = F_2 = 0$.

The conditions 2 and 3 are essential to combining two different electrical networks together. The last statement is particularly important and illustrates that the ends of the longitudinal-mode PT are free from force. Since $F_1' = F_2 = 0$ is analogous to its electrical counterpart: $E_1' = E_2 = 0$. The mechanical input port in Fig. A.3. for the side-plated bar and the mechanical output port in Fig. A.4. for the end-plated bar are shorted according to the definition from electrical network theory. Figure A.6 (a) shows the dimension of the complete longitudinal mode PT. In x_1 axis, the length of the side-plated bar is from -l′ to the origin. For the new boundary conditions, the equations for boundary velocities in section 2.2.2.1 change to

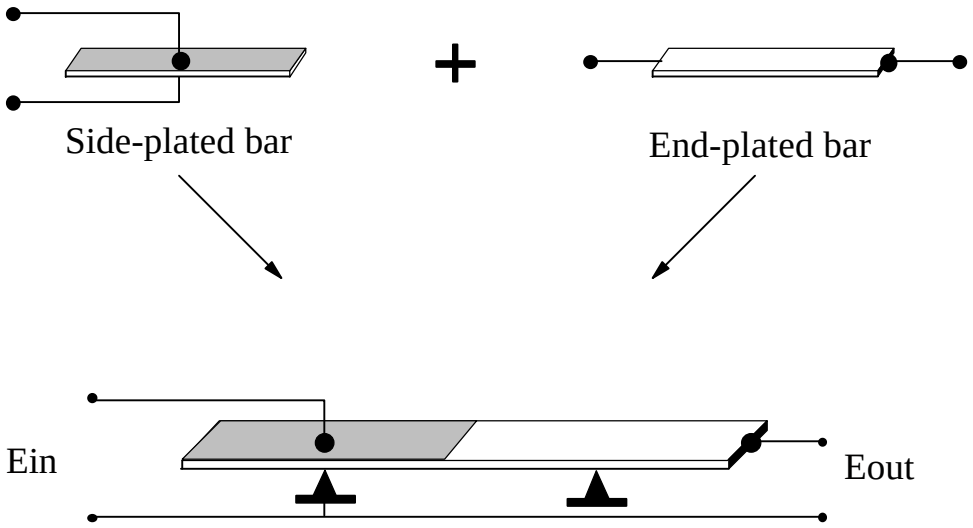

(a) Nonisolated type

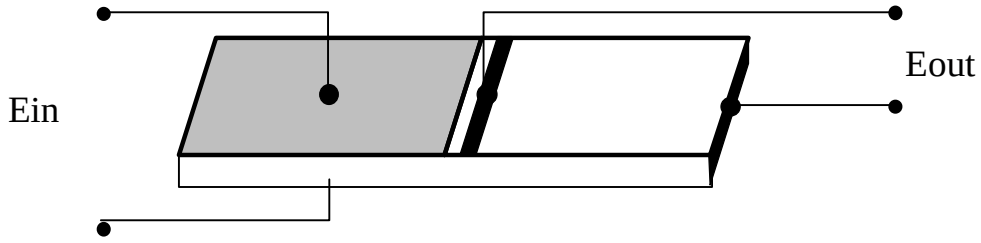

(b) Isolated type

Fig. A.5. Construction of longitudinal PTs. (a) nonisolated type. (b) isolated. The electrode, near the driver portion of the side-plated part is either shared with one of the electrodes of the driver or appears on the surface of the output portion. These arrangements will affect the efficiency of the longitudinal-mode PT slightly. The support points at nodes also affect the efficiency of PTs.

$$v_2' = -\left.\frac{\partial u_1'}{\partial t}\right|_{x_1=0}; \qquad \text{(A. 54)}$$

$$\hat{v}_2' = -j\omega B_2';$$

$$v_1' = \left.\frac{\partial u_1'}{\partial t}\right|_{x_1=-l'}; \qquad \text{(A.55)}$$

$$\hat{v}_1' = j\omega((-B_1' \sin\beta' l' + B_2' \cos\beta' l');$$

$$B_2' = -\frac{\hat{v}_2'}{j\omega}. \qquad \text{(A.56)}$$

The forces at both ends of the side-plated bar equal

$$\hat{F}_2' = -\omega \cdot Z_o' \cdot B_1' + \frac{d_{31}' \cdot A'}{s_{11}^{E'}} \hat{E}_3'; \qquad \text{(A.57)}$$

$$\begin{aligned} \hat{F}_1' &= -\hat{T}_1'\Big|_{x_1=-l'} \cdot A'; \\ &= -\omega \cdot Z_o' \cdot (B_1' \cos\beta' l' - B_2' \sin\beta' l') + \frac{d_{31}' \cdot A'}{s_{11}^{E'}} \hat{E}_3'. \end{aligned} \qquad \text{(A.58)}$$

Because $-v_2' = v_1$, equating (A.54) and (A.17) gives

$$B_2' = B_2. \qquad \text{(A.59)}$$

In order to meet all the boundary conditions required above, mismatching the physical dimensions in the driver and generator parts greatly reduces the complexity of the analysis [4]. This is a special case, looking for the solution of two separated mechanical systems. The mismatching makes it possible to obtain

$$Z_o' = Z_o, \qquad \text{(A.60)}$$

and

$$\beta' l' = \beta l. \qquad \text{(A.61)}$$

From (A.57) and (A.42), condition 3 sets

$$B_1' = B_1. \qquad \text{(A.62)}$$

Since (A.59) and (A.62) hold, it means that the displacement is continuous at the boundary of the driver and receiver parts. Figure A.6 (b). shows the complete model of the longitudinal-mode PT when the ends of the PT are free of force. Its simplified model is shown in Fig. A.6 (c). by introducing Δ-Y impedance transformation. The resultant model is suitable for all frequency ranges. If the frequencies of interested occur at resonance frequencies only, an L-C lumped equivalent circuit is found at every resonance frequency where

$$\beta l = \pi, 2\pi, 3\pi, 4\pi \cdots .$$

Let this PT operate under the full wave mode, it means that the total length of the PT equals a wave length and

$$\beta' l' = \beta l = \pi$$

By using Tylor's series expansion, the impedance of the mechanical branch, shown in Fig. A.7 (a)., is expanded at ω_o.

$$\begin{aligned} f(\omega) &= \frac{Z_o}{j} \cdot \frac{1}{\tan\frac{\beta l}{2}} = \frac{Z_o}{j} \cdot \frac{1}{\tan\frac{\omega \cdot l}{2 \cdot v}} \\ &= f\left(\frac{\pi \cdot v}{l}\right) + f'\left(\frac{\pi \cdot v}{l}\right) \cdot \left(\omega - \frac{\pi \cdot v}{l}\right) + \frac{1}{2} \cdot f'\left(\frac{\pi \cdot v}{l}\right) \cdot \left(\omega - \frac{\pi \cdot v}{l}\right)^2 + \cdots \end{aligned} \tag{A.63}$$

Assume the series resonance frequency is ω_o, and

$$\omega_o = \frac{\pi \cdot v}{l} = \frac{\pi}{l} \cdot \sqrt{\frac{Y_{11}^{E}}{\rho}} \tag{A.64}$$

$$f'(\omega_o) = -\frac{\pi \cdot Z_o}{2 \cdot j \cdot \omega_o} \tag{A.65}$$

Let $\omega = \omega o + \delta$, and substitute it into (A.63) with only the first-order approximation:

$$f(\omega_o + \delta) \approx 0 + f'(\omega_o) \cdot \delta = j \cdot \pi \cdot Z_o \cdot \frac{\delta}{2 \cdot \omega_o} . \tag{A.66}$$

At the same time, the impedance of a series L_m and C_m is

$$f_{LC}(\omega) = j \cdot \sqrt{\frac{L}{C}} \cdot \left(\frac{\omega}{\omega_o} - \frac{\omega_o}{\omega}\right) \approx f_{LC}(\omega_o) + f_{LC}'(\omega_o) \cdot (\omega - \omega_o) \ ; \tag{A.67}$$

$$f_{LC}(\omega + \delta) \approx 0 + f_{LC}'(\omega_o) \cdot \delta = 2 \cdot j \cdot L_m \cdot \delta \quad . \tag{A.68}$$

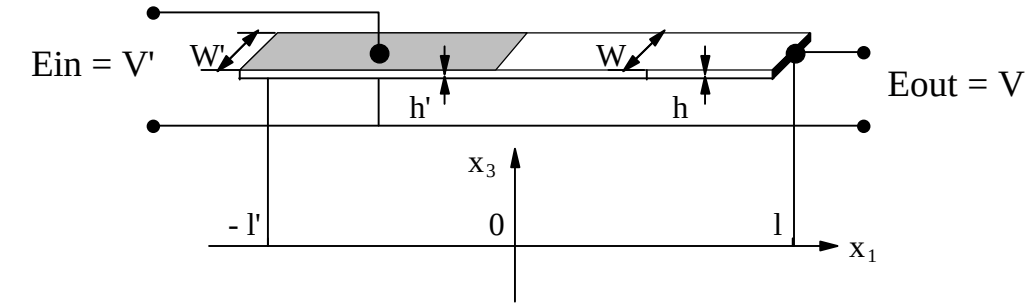

(a)

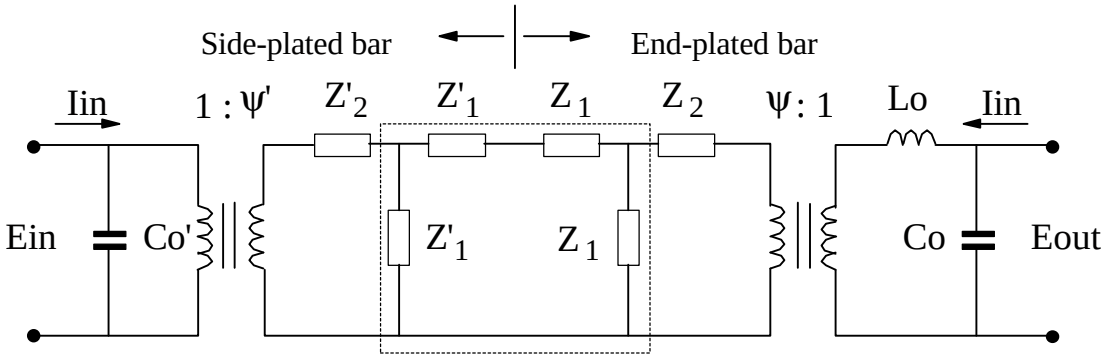

(b)

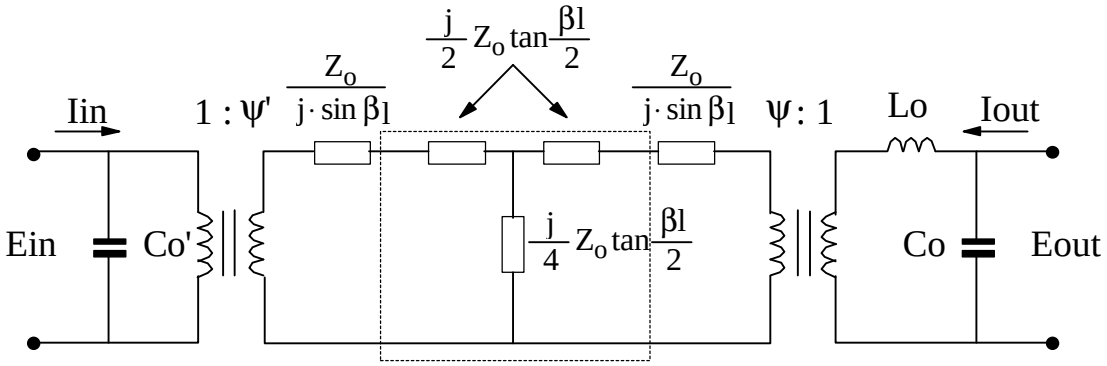

(c)

Fig. A.6. Model and definition of dimensional variables of a longitudinal PT (a) dimensional definition. (b) combined model of the two basic cells. (c) DELTA to Y impedance transformation. In order to meet the boundary conditions of two basic model cells, a number of assumptions and boundary conditions need to be considered.

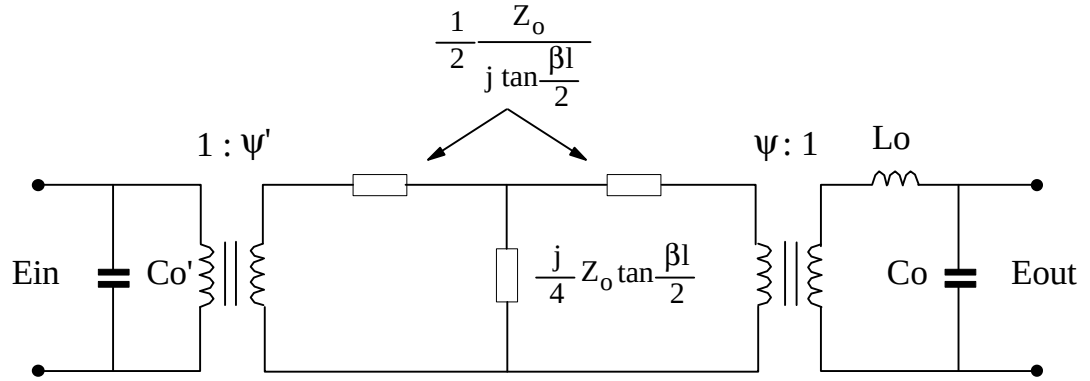

(a)

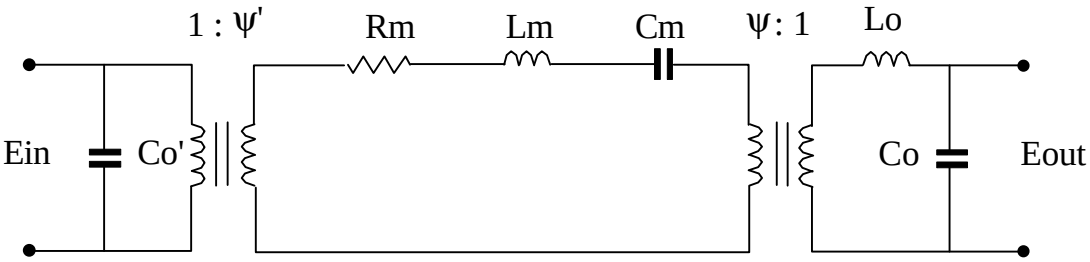

$$L_m = \frac{\pi \cdot Z_o}{4 \cdot \omega_o} = \frac{1}{4}(\rho \cdot \text{volume}) \qquad R_m = \frac{\pi \cdot Z_o}{4 \cdot Q_m} \qquad C_m = \frac{1}{\omega_o^2 \cdot L_m}$$

(b)

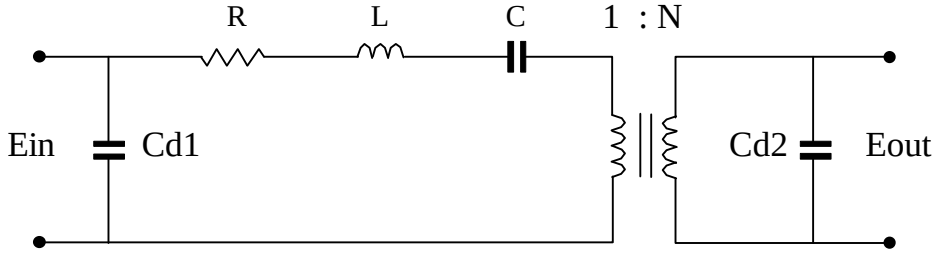

$$R = \frac{\pi \cdot Z_o}{4 \cdot Q_m \cdot \psi'^2} \qquad C = \frac{4\,\psi'^2}{\pi \cdot \omega_o \cdot Z_o} \qquad L = \frac{\pi \cdot Z_o}{4\,\omega_o \cdot \psi'^2} + \frac{\psi^2}{\psi'^2} L_o$$

(c)

Fig. A.7. Lumped model of the longitudinal PT. (a) dimensional definition. (b) combined model of two basic cells. (c) DELTA to Y impedance transformation. In order to meet the boundary conditions of two basic model cells, a number of assumptions and boundary conditions need to be considered.

Equating (A.66) and (A.68), L_m is

$$L_m = \frac{\pi \cdot Z_o}{4\,\omega_o} = \frac{\pi \cdot A \cdot \sqrt{\rho\, Y_{11}^{\ E}}}{4 \cdot \frac{\pi}{l} \cdot \sqrt{\frac{Y_{11}^{\ E}}{\rho}}} = \frac{1}{4}\left(\rho \cdot \text{volume}\right); \tag{A.69}$$

$$C_m = \frac{1}{\omega_o^{\ 2} \cdot L_m} = \frac{4}{\pi \cdot \omega_o \cdot Z_o} = \frac{4 \cdot l}{\pi^2 \cdot W \cdot h \cdot Y_1^{\ D}}; \tag{A.70}$$

$$R_m = \frac{\omega_o \cdot L_m}{Qm}\ . \tag{A.71}$$

The volume in (A.69) represents the volume of the end-plated or side-plated bar only. In other words, the volume here is approximately half of the piezoelectric transformer. The mechanical loss, R_m, is calculated liberally according to the mechanical quality factor, Qm, and is shown in (A.71). The impedance in the center leg of the T-network in Fig. A.7 (a). is opened when the PT operates at its resonance frequencies. From (A.69) to (A.71), the equivalent circuit with lumped components for the PT operating at fs is shown in Fig. A.7 (b). The final equivalent circuit of the longitudinal mode PT is shown in Fig. A.7 (c) by reflecting the mechanical branch to the primary side of the model.

A.3 Model of the Thickness Extensional Mode PT

An 1:1 thickness extensional mode PT is composed of input and output broad plate piezoceramics, as shown in Fig. A.8 (a). If several pieces of piezoceramics are found in the output port and connected in parallel electrically, it is called a multilayer thickness extensional mode PT. When a sinusoidal electrical field is applied to the electrodes of a piezoelectric crystal, the latter will contract and expand along the thickness axis. As the frequencies of the electrical field approach the mechanical resonant frequencies of the piezoelectric crystal, the amplitude of the mechanical vibration within the crystal will become relatively large. Analogously, the induced amplitude of the electrical field will become large when the frequencies of the stress applied to the crystal approach its resonant frequencies. So, it is our objective to operate the PTs around their mechanical resonant frequencies to increase their efficiency. The analytical electromechanical wave motion of the PTs can be described by an electrical equivalent circuit in the neighborhood of mechanical resonant frequencies of the PTs. But it is not accurate enough to use inductor-capacitor networks to represent the mechanical resonance without considering the mechanical and dielectric losses. First, considering the mechanical loss, there are two ways to include the mechanical loss into the equivalent circuit of the PTs. One is to neglect the loss term when the wave equation is solved and then to add this loss to the respective LC networks [2,3], as shown in the previous section. The other method includes mechanical losses of the PTs in the beginning of the analysis, assuming that elastic constants are complex numbers [4]. However, these two

methods will lead to the same equivalent circuits with a mechanical quality constant, Q_m. The latter method will be introduced here because this method provides a general way to incorporate the loss terms directly.

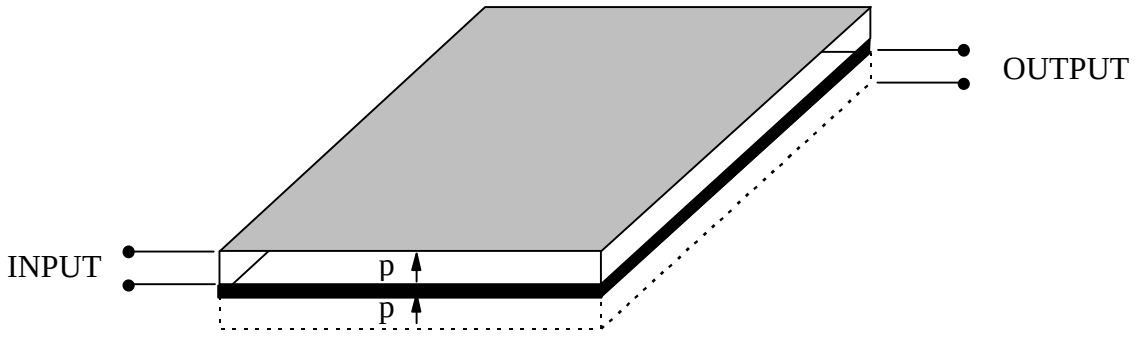

(a)

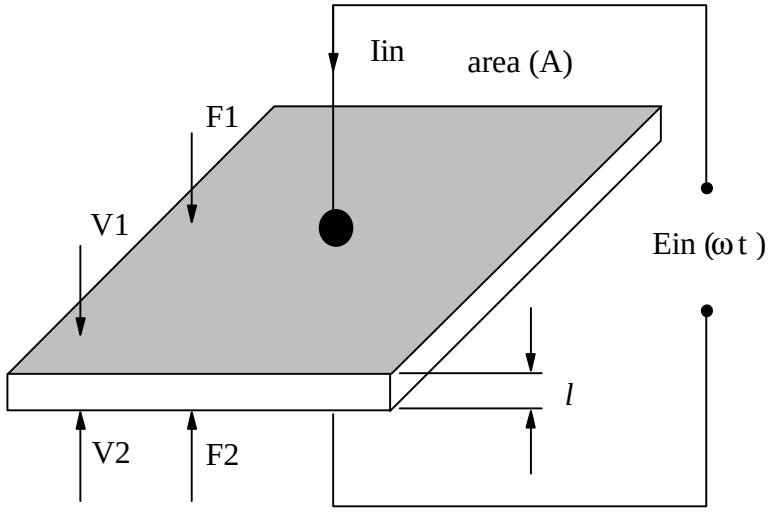

(b)

Fig. A.8. 1:1 broad-plated PT. (a) construction and size. (b) its driver part.

A.3.1 Derivation of One-Dimensional Wave Equation

The analytical solutions of the wave equations with boundary force conditions and the initial conditions can exactly disclose the displacement or wave-like motions inside the PTs. Taking the first derivative of the displacement, the strain is derived and the induced electric field is calculated. Hardly any physical interactions can be explained as well by equations as by electrical networks. Using a powerful network theory, the forces and the velocities, on the mechanical properties, are described as voltages and currents, respectively. The equivalent circuits of individual parts of the PTs can thus be combined into an electrical network having both electrical and mechanical characteristics.

Following the same rules as those applied to the longitudinal PTs, the equivalent circuits for the PTs with the thickness vibration mode are derived in detail to establish a basis for the future investigation of the models of the stacked PTs. To simplify the analysis, an 1:1 broad plate PT [5] is selected for its high symmetry and one-dimensional operation in the thickness axis. If the turns ratios of the PTs are other than 1:1, an ideal transformer can be added. Assuming that the driver and receiver parts are identical so that symmetrical principles can apply to this PT, only one system equation needs to be derived for either the driver part or the receiver part. The following assumptions are made to obtain the electrical equivalent circuit of a 1:1 broad plate PT for the driver part:

1. lateral dimensions exceeding many wavelengths of sound,
2. no appreciable motion, except in the thickness direction,
3. description by a one-dimensional subscript of all stress, strain, electrical field, and current density,
4. loss-free insulation layers,
5. fundamental-mode operation, and
6. free motion in both end surfaces.

So far, there are three types of piezoceramics introduced. The independent variables for the side-plated bar and the end-plated bar are [T,E] and [T,D], respectively. The dependent variables for broad plate piezoceramics are [S,D] because the lateral dimension exceeds length in thickness direction. Therefore, the circumference of the plate is actually clamped; $S_1 = S_2 = 0$, and S3 is chosen as one of the independent variables for electromechanical equations. And electric flux, D_3, is the other independent variable for an insulating piezoceramic without any flux leakage. The resultant one-dimensional piezoelectric equations are

$$\begin{aligned} T_3 &= c_{33}^{\ D} \cdot S_3 - h_{33} \cdot D_3 ; \\ E_3 &= -h_{33} \cdot S_3 + \beta_{33}^{\ S} \cdot D_3 . \end{aligned} \tag{A.72}$$

Figure A.8 (b). shows the driver part of a broad plate PT with thickness extensional mode vibration. The one-dimensional wave equation for a broad-plate piezoceramics is obtained by adopting a similar derivation in the previous section:

$$\rho \cdot \frac{\partial u_3^{\,2}}{\partial t^2} = c^D \cdot \frac{\partial u_3^{\,2}}{\partial x_3^{\,2}} \ . \tag{A.73}$$

Assuming that the electrical excitation is sinusoidal, $D_3 = D_O\, e^{j\omega t}$, and c^D is a real number, the general solution of (A.73) can be expressed as the following equation:

$$u_3 = (B_1 \cdot \sin \beta x_3 + B_2 \cdot \cos \beta x_2) \cdot e^{j\omega t} \ , \tag{A.74}$$

where ω = frequency of the input voltage in rad/sec,

$$\beta = \omega \cdot \sqrt{\frac{\rho}{c^D}} \ , \tag{A.75}$$

$$v_{sound} = \sqrt{\frac{\rho}{c^D}} \text{ = speed of the sound, m/sec .} \tag{A.76}$$

If c^D is a complex number, the solution of the wave equation is a hyperbolic function rather than a sinusoidal representation:

$$c^D = c_1^{\,D} + j \cdot c_2^{\,D}, \tag{A.77}$$

$$u_3 = (B_1 \cdot \sinh \gamma \cdot x_3 + B_2 \cdot \cosh \gamma \cdot x_3) \cdot e^{j\omega t}, \tag{A.78}$$

where

$$\gamma = \alpha + j \cdot \beta = \omega \sqrt{\frac{\rho}{c^D}} \approx \omega \sqrt{\frac{\rho}{c_1^{\,D}}} \cdot \left(j + \frac{1}{2Q_m} \right), \text{ and} \tag{A.79}$$

$$Q_m = \frac{c_1^{\,D}}{c_2^{\,D}}, \text{ mechanical constant.} \tag{A.80}$$

In (A.78), B1 and B2 can be calculated and expressed as a function of velocities, v_1 and v_2.

$$v_1 = \left. \frac{\partial u_3}{\partial t} \right|_{x_1 = 0} ; \tag{A.81}$$
$$\hat{v}_1 = j\omega B_2 \ ;$$

$$v_2 = -\left. \frac{\partial u_3}{\partial t} \right|_{x_1 = l} ; \tag{A.82}$$
$$\hat{v}_2 = -j\omega \left((B_1 \sinh(\alpha + j \cdot \beta) l + B_2 \cos(\alpha + j \cdot \beta) l \right) ;$$

where $\hat{v}_1$ and $\hat{v}_2$ are phasor representations of v_1 and v_2.. From (A.81)-(A.82), B_2 and B_1 are

$$B_2 = \frac{1}{j\omega} \cdot \hat{v}_1 \ ; \tag{A.83}$$

$$\begin{aligned} B_1 &= \frac{1}{-j\omega \cdot \sinh(\alpha + j\cdot\beta)l}\left(\hat{v}_2 + \hat{v}_1 \cdot \cosh(\alpha + j\cdot\beta)l\right) \\ &= \frac{-1}{j\omega}\left(\frac{\hat{v}_1}{\tanh(\alpha + j\cdot\beta)l} + \frac{\hat{v}_2}{\sinh(\alpha + j\cdot\beta)l}\right). \end{aligned} \tag{A.84}$$

A.3.2 Basic Model Cells

The electrical properties, voltage and current, are obtained from (A.21).

$$\hat{I} = j\cdot\omega\cdot\hat{D}_3\cdot h\cdot W \ ; \tag{A.85}$$

$$\begin{aligned} \hat{V} &= -\int_l^0 \hat{E}_3 dx_3 \\ &= \int_0^l \left(-h_{33}\cdot\hat{S}_3 + \beta_{33}{}^D\cdot\hat{D}_3\right)\cdot dx_3 \\ &= -h_{33}\cdot\left(\hat{u}_1\big|_{x_1=l} - \hat{u}_1\big|_{x_1=0}\right) + l\cdot\beta_{33}{}^D\cdot\hat{D}_3 \\ &= \frac{c_{33}{}^D\cdot g_{33}}{j\cdot\omega}\cdot\left(\hat{v}_1 + \hat{v}_2\right) + Z_E{}^{LC}\cdot\hat{I}\,, \end{aligned} \tag{A.86}$$

where $h_{33} = c_{33}{}^D\cdot g_{33}$, and $Z_E{}^{LC}$ is the clamped impedance and equals

$$Z_E{}^{LC} = \frac{l\cdot\beta_{33}{}^D}{j\cdot\omega\cdot h\cdot W}\ . \tag{A.87}$$

Forces are function of velocities, v_1 and v_2, and electrical current, I:

$$\begin{aligned} \hat{F}_1 &= -A\cdot c_{33}{}^D\cdot\gamma\cdot B_1 + A\cdot h_{33}\cdot\hat{D}_3 \\ &= -A\cdot c_{33}{}^D\cdot\gamma\cdot\frac{-1}{j\omega}\left(\frac{\hat{v}_1}{\tanh\gamma l} + \frac{\hat{v}_2}{\sinh\gamma l}\right) + A\cdot h_{33}\cdot\frac{\hat{I}}{j\omega\cdot A} \\ &= Z_o\cdot\left(\frac{\hat{v}_1}{\tanh\gamma l} + \frac{\hat{v}_2}{\sinh\gamma l}\right) + \frac{c_{33}{}^D\cdot g_{33}}{j\omega}\cdot\hat{I}\,; \end{aligned} \tag{A.88}$$

$$\begin{aligned}\hat{F}_2 &= -A \cdot {c_{33}}^D \gamma \cdot (B_1 \cdot \cos \gamma l + B_2 \cdot \sin \gamma l) + A \cdot h_{33} \cdot \hat{D}_3 \\ &= -A \cdot {c_{33}}^D \cdot \gamma \cdot \frac{-1}{j\omega} \cdot \left((\frac{\hat{v}_1}{\tanh \gamma l} + \frac{\hat{v}_2}{\sinh \gamma l}) \cdot \cosh \gamma l - \hat{v}_1 \cdot \sinh \gamma l \right) + \frac{{c_{33}}^D \cdot g_{33}}{j\omega} \cdot \hat{I} \\ &= Z_o \cdot (\frac{\hat{v}_1}{\sinh \gamma l} + \frac{\hat{v}_2}{\tanh \gamma l}) + + \frac{{c_{33}}^D \cdot g_{33}}{j\omega} \cdot \hat{I}\,,\end{aligned} \tag{A.89}$$

where

$$\begin{aligned}Z_o &= \frac{A \cdot {c_{33}}^{D \cdot \gamma}}{j \cdot \omega} \\ &\cong A \cdot \sqrt{{c_1}^D \cdot \rho} \cdot \left(1 + \frac{j}{2 \cdot Q_m} \right).\end{aligned} \tag{A.90}$$

Summarizing (A.86), (A.88), and (A.89), these equations can be rearranged to give

$$\begin{aligned}&\hat{V} = \psi \cdot (\hat{v}_1 + \hat{v}_2) + {Z_E}^{LC} \cdot \hat{I}\,; \\ &\hat{F}_1 = \left(\frac{Z_o}{j \cdot \tanh \gamma l} - \frac{Z_o}{j \cdot \sinh \gamma l} \right) \cdot \hat{v}_1 + \frac{Z_o}{j \cdot \sinh \gamma l} \cdot \left(\hat{v}_1 + \hat{v}_2 \right) + \psi \cdot \left(V - \psi \cdot {Z_E}^{LC} \cdot \left(\hat{v}_1 + \hat{v}_2 \right) \right); \\ &\hat{F}_2 = \left(\frac{Z_o}{j \cdot \tanh \gamma l} - \frac{Z_o}{j \cdot \sinh \gamma l} \right) \cdot \hat{v}_2 + \frac{Z_o}{j \cdot \sinh \gamma l} \cdot \left(\hat{v}_1 + \hat{v}_2 \right) + \psi \cdot \left(V - \psi \cdot {Z_E}^{LC} \cdot \left(\hat{v}_1 + \hat{v}_2 \right) \right).\end{aligned} \tag{A.91}$$

Figure A.9 shows the basic equivalent circuit for a broad plate piezoceramics, and the turns ratio of the PT is

$$\begin{aligned}\psi &= \frac{{c_{33}}^D \cdot g_{33}}{j \cdot \omega} \cdot \frac{1}{{Z_E}^{LC}} \\ &= \frac{h \cdot W}{l} \cdot \frac{{c_{33}}^D \cdot g_{33}}{{\beta_{33}}^D}\,.\end{aligned} \tag{A.92}$$

A.3.3 Boundary Conditions

Figure A.8 (a). shows the construction of a thickness extensional mode PT whose step-down ratio is 1:1. Because the same materials and identical physical dimensions have been used for both driver and receiver parts, there is no mismatch required to have different sizes for them. The boundary conditions are the same as those required for a longitudinal mode PT. The prime system is used again to represent the variables in the driver part:

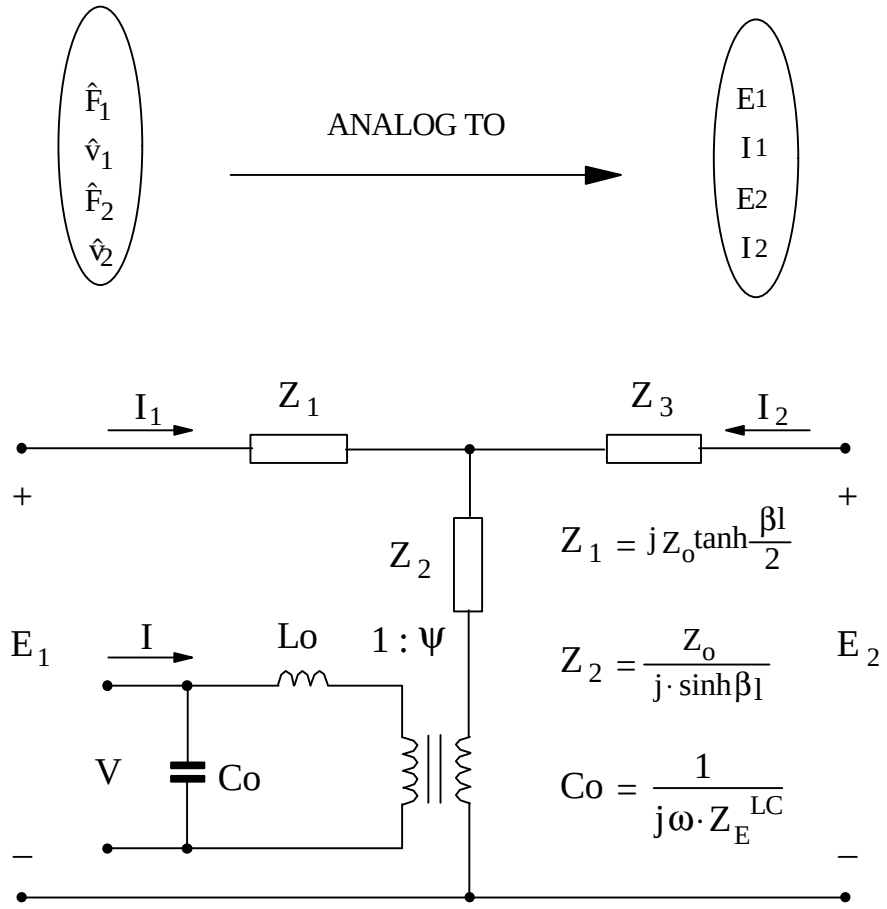

A : surface area = h W

$$Z_E^{LC} = \frac{l \cdot \beta_{33}^S}{j\omega \cdot A} \qquad Co = \frac{1}{j\omega \cdot Z_E^{LC}} = \frac{A\ \varepsilon_{33}^S}{h} \qquad Lo = \frac{1}{\omega^2\ Co}$$

$$Z_o = \frac{A \cdot c_{33}^D \cdot \gamma}{j\ \omega} \qquad \psi = \frac{A}{l} \cdot \frac{c_{33}^D\ g_{33}}{\beta_{33}^D}$$

Fig. A.9. Basic model cell of the broad plate piezoceramic. Because the mechanical loss is included in the model, the sinusoidal functions are replaced by the hyperbolic functions. The difference between this model cell and that of the end-plated bar results from using different independent variables in linear piezoelectric equations.

1. $-I_2' = I_1$ or $-v_2' = v_1$;
2. $E_2' = E_1$ or $F_2' = F_1$;
3. $E_1' = E_2 = 0$ or $F_1' = F_2 = 0$.
4. Assume the presence of supporting points, which are located at the four corners of the bottom surface, will not hinder the vibration in the thickness direction.

A.3.4 Complete Model

Following the similar procedure for developing the complete equivalent circuit of the longitudinal mode PT, Fig. A.10 (a)-(c). shows the model of an 1:1 thickness mode PT. Generally, this is the model which is suitable to a wide range of operating frequencies. However, only the frequencies around the resonant frequency of the PT are of interest. Figure A.11 (a). shows the resultant equivalent circuit in Fig. A.10 (c). By using Tylor's series expansion, the impedance of the mechanical branch in the middle of Fig. A.11 (a). is expanded at ω_o, and is equal to

$$f(\omega) = \frac{Z_o}{\tanh\frac{rl}{2}} \approx \frac{Z_o}{\tanh\frac{\omega\cdot l}{2\cdot v}\cdot\left(1+\frac{j}{2\cdot Qm}\right)} = \frac{Z_o}{\tanh\frac{\beta(\omega_o)}{2}\cdot l} \approx f(\omega_o) + f'(\omega_o)\cdot(\omega-\omega_o) + \frac{1}{2}\cdot f''(\omega_o)\cdot(\omega-\omega_o)^2 + \cdots . \tag{A.93}$$

Assume the series resonance frequency is ω_o and

$$\beta(\omega_o)\cdot l = \pi \ ; \tag{A.94}$$

$$\omega_o = \frac{\pi\cdot v}{l} = \frac{\pi}{l}\cdot\sqrt{\frac{c_1^{\ D}}{\rho}} \ ; \tag{A.95}$$

$$f(\omega_o) \approx Z_o\cdot\frac{e^{\beta l}+1}{e^{\beta l}-1} \approx Z_o\cdot\frac{e^{\frac{\pi}{2\cdot Q_m}}-1}{e^{\frac{\pi}{2\cdot Q_m}}+1} \approx Z_o\cdot\frac{\frac{\pi}{2\cdot Q_m}}{2+\frac{\pi}{2\cdot Q_m}} \approx \frac{\pi}{4\cdot Q_m} \ ; \tag{A.96}$$

$$f'(\omega_o) \approx Z_o\cdot\frac{-2\cdot e^{\beta l}}{\left(e^{\beta l}-1\right)^2}\cdot\frac{\pi}{\omega_o}\cdot\left(j+\frac{1}{2\,Q_m}\right) \approx \frac{2\cdot\pi\cdot Z_o}{\omega_o}\cdot\left(j+\frac{1}{2\,Q_m}\right)\cdot\frac{\left(1+\frac{\pi}{2\,Q_m}\right)}{\left(4+\frac{\pi}{Q_m}\right)} \approx \frac{\pi\cdot Z_o}{2\cdot\omega_o}\cdot j . \tag{A.97}$$

Equations (A.96) and (A.97) can be simplified due to $Q_m >> 200$ for the PTs. Let $\omega = \omega o + \delta$, and substitute it into (A.93) with only first order approximation:

$$f(\omega_o + \delta) \approx f(\omega_o) + f'(\omega_o) \cdot \delta = \frac{\pi \cdot Z_o}{4 \cdot Q_m} + j \cdot \frac{\pi \cdot Z_o}{2 \cdot \omega_o} \cdot \delta \ . \tag{A.98}$$

$$f_{LC}(\omega) = R_m + j \cdot \sqrt{\frac{L_m}{C_m}} \cdot \left(\frac{\omega}{\omega_o} - \frac{\omega_o}{\omega} \right) \approx f_{LC}(\omega_o) + f_{LC}'(\omega_o) \cdot (\omega - \omega_o) \ ; \tag{A.99}$$

$$f_{LC}(\omega_o + \delta) \approx R + f_{LC}'(\omega_o) \cdot \delta = R_m + 2 \cdot j \cdot L_m \cdot \delta \ . \tag{A.100}$$

Equating (A.98) and (A.100), a lumped equivalent circuit is shown in Fig. A.11 (b) and R_m, L_m, and C_m are calculated as follows:

$$R_m = \frac{\pi \cdot Z_o}{4 \cdot Q_m} \ , \tag{A.101}$$

and

$$L_m = \frac{\pi \cdot Z_o}{4 \cdot \omega_o} = \frac{\pi \cdot A \cdot \sqrt{\rho \, Y_1^{\,D}}}{4 \cdot \frac{\pi}{l} \cdot \sqrt{\frac{Y_1^{\,D}}{\rho}}} = \frac{1}{4} (\rho \cdot \text{volume}) \ ; \tag{A.102}$$

$$C_m = \frac{1}{\omega_o^{\,2} \cdot L_m} = \frac{4}{\pi \cdot \omega_o \cdot Z_o} = \frac{4 \cdot l}{\pi^2 \cdot W \cdot h \cdot Y_1^{\,D}} \ , \tag{A.103}$$

where l is only half of the thickness of the 1:1 PT; accordingly, the volume in (A.102) is actually half of the real volume. Figure A.12. shows the final lumped equivalent circuit of the 1:1 PT when the mechanical branch is referred to the primary side of the PT. The calculated values of the equivalent RLC network are

$$R = \frac{\pi \cdot Z_o}{4 \cdot Q_m \cdot \psi^2} \ ; \tag{A.104}$$

$$L = \frac{\pi \cdot Z_o}{4 \cdot \omega_o \cdot \psi^2} + 2 \cdot L_o \ ; \tag{A.105}$$

$$C = \frac{4 \cdot \psi^2}{\pi \cdot \omega_o \cdot Z_o} \ . \tag{A.106}$$

At the same time, the impedance of a series R, L and C is derived from (A.68) by adding an extra R.

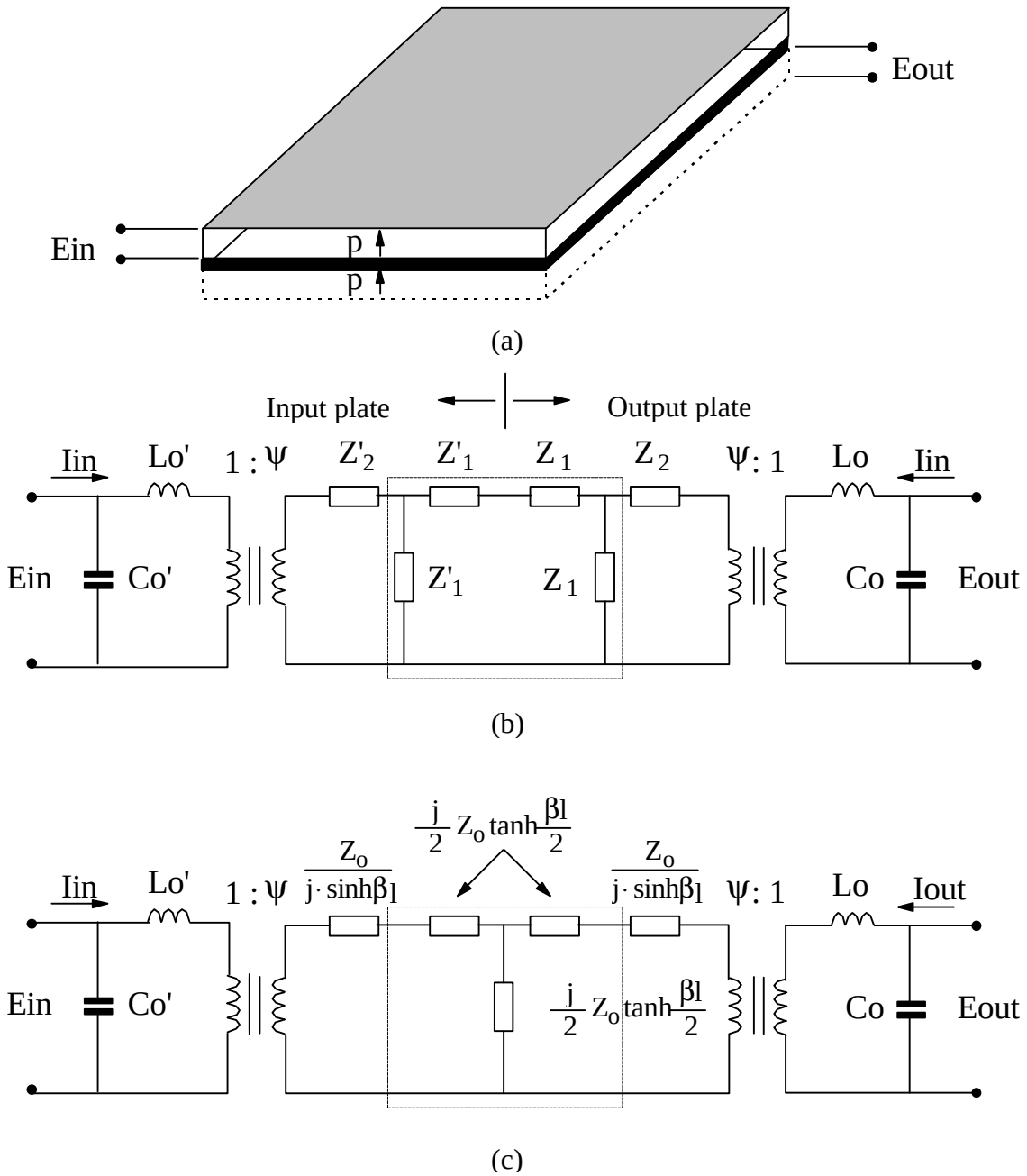

Fig. A.10. Construction of the thickness vibration PT. (a) 1:1 broad PT. (b) combined model of two basic cells. (c) delta-to-Y impedance transformation. Because input and output parts are physically identical, it is easy to get the complete model of this PT.

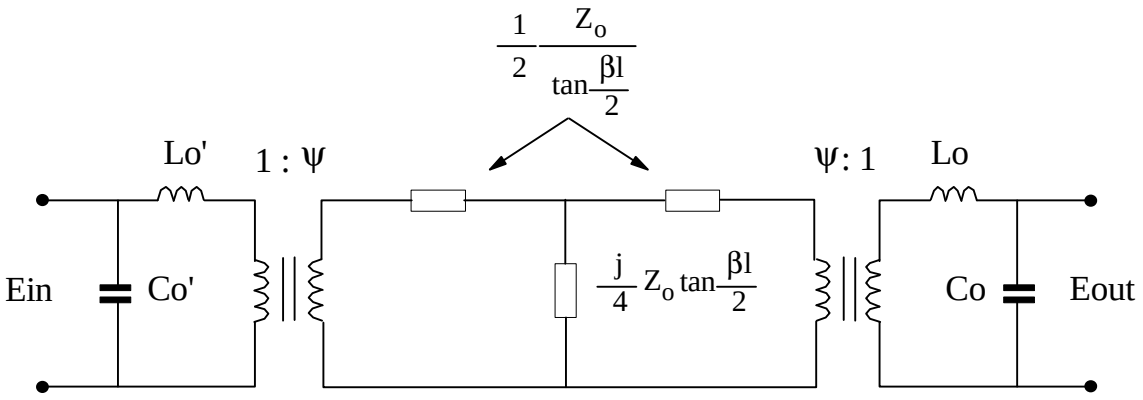

(a)

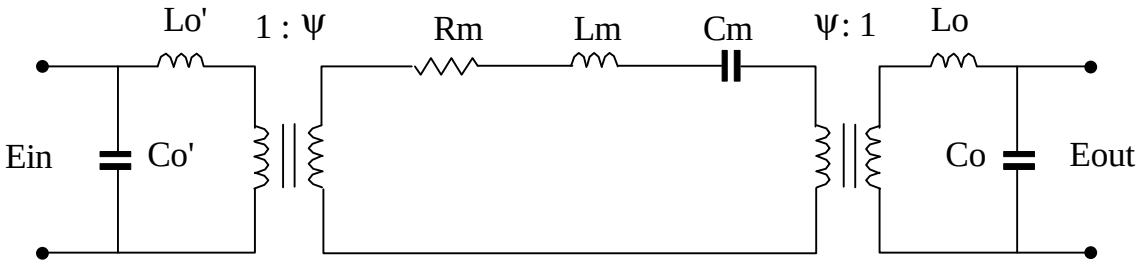

(b)

$$L_m = \frac{\pi \cdot Z_o}{4 \cdot \omega_o} = \frac{1}{4}(\rho \cdot \text{volume}) \qquad R_m = \frac{\pi \cdot Z_o}{4 \cdot Q_m} \qquad C_m = \frac{1}{\omega_o^2 \cdot L_m}$$

Fig. A.11. Lumped model of the thickness vibration PT around fs. The mechanical branch is represented by an Rm-Lm-Cm circuit operating around fs.

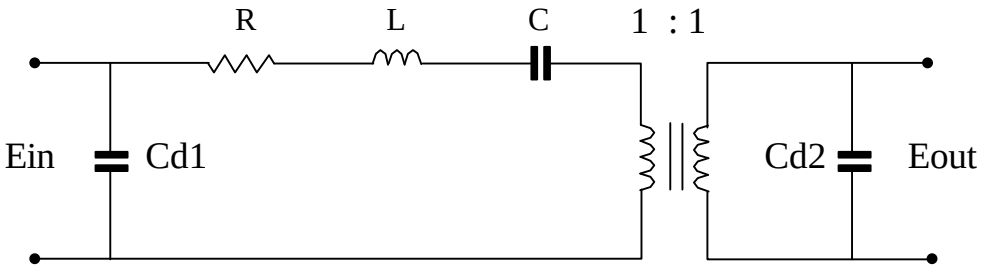

$$R = \frac{\pi \cdot Z_o}{4 \cdot Q_m \cdot \psi^2} \qquad L = \frac{\pi \cdot Z_o}{4 \cdot \omega_o \cdot \psi^2} + 2 \cdot L_o \qquad C = \frac{4 \cdot \psi^2}{\pi \cdot \omega_o \cdot Z_o}$$

Fig. A.12. Final Lumped model of an 1:1 thickness vibration PT around fs.

A.4 Summary and Conclusion

A study of electrical equivalent circuits for the PTs with regard to mechanical vibrations and related mechanical losses gives a better understanding of how the PTs work. The measurement results obtained from either impedance or network analyzer can be successfully used to verify the parameter values of the electrical equivalent circuit calculated from the physical size and material properties of an 1:1 PT. This work suggests that it is possible to design a stacked PT with any desired transformer ratio for different applications by using a simulation tool. In the future, the ANSYS finite-element software program will be used as a tool to verify the design of the PTs.

APPENDIX B : MCAD Program to Calculate the Physical Model of PTs

B.2 Thickness extensional PT (LVPT-11)

Engineering exponential identifier:

$Meg := 1\cdot10^{6}$ $k := 1\cdot10^{3}$ $m := 1\cdot10^{-3}$ $\mu := 1\cdot10^{-6}$ $n := 1\cdot10^{-9}$ $p := 1\cdot10^{-12}$

Pseudo-units to be used for constants and results:

$\varepsilon o := 8.854187\cdot pico$

$V := 1$ $A := 1$ $\Omega := 1$ $H := 1$ $F := 1$ $W := 1$ $J := 1$ $Hz := 1$ $S := 1$

$T := 1$ $Wb := 1$ $K := 1$ $dB := 1$ $N := 1$ $mH := 0.001\cdot H$ $pF := pico\cdot F$

$meter := 1$ $cm := 0.01\cdot meter$ $dm := 10\cdot cm$ $mm := 0.1\cdot cm$ $km := k\cdot meter$

$inch := 2.54\cdot cm$ $ft := 12\cdot inch$ $sec := 1$ $kg := 1$ $g := m\cdot kg$

PT constants:

$kt := 0.51$ $\varepsilon 33s := 211\cdot\left(1 - kt^{2}\right)$ dielectric constant ε33t = 211

$\varepsilon := \varepsilon 33s$ $\varepsilon = 156.119$

$c33d := \dfrac{11.9\cdot10^{10}}{\left(1 - kt^{2}\right)}$ elastic constant c33e=11.9

$c := c33d$ $c = 1.608\cdot10^{11}$ $kp := 0.044$

$\rho := 6900\cdot\dfrac{kg}{meter^{3}}$ density

$g := 32.6\cdot m$ piezoelectric constant

$tan\delta := 0.006$ loss factor

$Qm := 1200$ the mechanical quantity

Physical size of the PT (LVPT-11):

$Aa := 0.0004\cdot meter^{2}$ area of the PT

$la := 3.44\cdot mm$ the total thickness of the PT - insulation

Calculation of natural frequency when rl = π :

$vsound := \sqrt{\frac{c}{\rho}}$ vsound = 4.828 k

$fo := \frac{vsound}{la}$ fo = 1.043e6

$\omega o := fo \cdot 2 \cdot \pi$

Rm Lm Cm for the fundamental mechanical branch:

$Zo := \sqrt{c \cdot \rho} \cdot Aa$ Zo = 1.333e4 Ω

$Rm := \pi \cdot \frac{Zo}{4 \cdot Qm}$ Rm = 8.721 Ω

$Lm := 0.125 \cdot \rho \cdot Aa \cdot la$ Lm = 1.187 mH

$Cm := \frac{2 \cdot la}{\pi^2 \cdot Aa \cdot c}$ Cm = 10.836 pF

$ft := \frac{1}{\sqrt{Lm \cdot Cm}} \cdot \frac{1}{2 \cdot \pi}$ ft = 1.403e6

Value of the Parameters for the final equivalent circuit:

$h := c \cdot g$ h = 5.243e9

$\phi := \frac{Aa \cdot \varepsilon \cdot \varepsilon o \cdot h}{\left(\frac{la}{2}\right)}$ ϕ = 1.685

$\phi 2 := \phi^2$ ϕ2 = 2.841

$Cd1 := \frac{211 \cdot \varepsilon o \cdot Aa}{\left(\frac{la}{2}\right)}$ cd1 = 434.473 pF

$Lo := \frac{1}{\omega o^2 \cdot Cd1}$ Lo = 29.598 μ

$R := \frac{Rm}{\phi 2}$ R = 3.07 Ω

$L := \frac{Lm}{\phi 2} + 2 \cdot Lo$ L = 476.953 μ

$C := \phi 2 \cdot Cm$ C = 30.783 pF

$ff := \frac{1}{2 \cdot \pi \cdot \sqrt{L \cdot C}}$ ff. = 1.313e6

APPENDIX C : Derivation of Resonant And Anti-resonant Frequencies

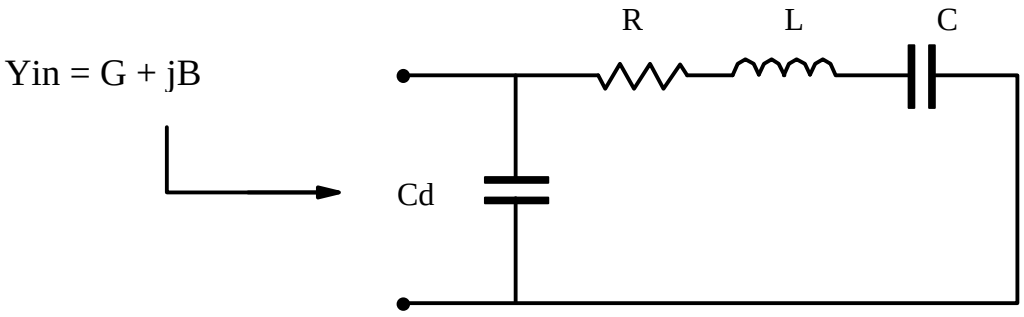

The above figure shows the electrical equivalent circuit of the quartz and its input admittance Yin. The resonant and antiresonant frequencies are represented by ωr and ωa respectively. They are derived by equating the imaginary part of Yin to zero.

$$\mathrm{Yin} = j\omega\,\mathrm{Cd} + \frac{1}{\mathrm{R} + j\omega\,\mathrm{L} + \frac{1}{j\omega\,\mathrm{C}}} = j\omega\,\mathrm{Cd} + \frac{j\omega\,\mathrm{C}}{\left(1 - \omega^2\,\mathrm{L\,C}\right) + j\omega\,\mathrm{R\,C}} \qquad \text{(C.1)}$$

$\mathrm{Im}[\mathrm{Yin}] = 0$, (C.2)

therefore,

$$j\omega\,\mathrm{Cd}\cdot\left(\left(1 - \omega^2\,\mathrm{L\,C}\right)^2 + \left(\omega\,\mathrm{R\,C}\right)^2\right) + j\omega\,\mathrm{C}\cdot\left(1 - \omega^2\,\mathrm{L\,C}\right) = 0 \ ,$$

$$\mathrm{Cd}\cdot\left(\left(1 - \omega^2\,\mathrm{L\,C}\right)^2 + \left(\omega\,\mathrm{R\,C}\right)^2\right) + \mathrm{C}\cdot\left(1 - \omega^2\,\mathrm{L\,C}\right) = 0 \ . \qquad \text{(C.3)}$$

Let $y = \omega^2$,

$$(1 - y\,L\,C)^2 + y \cdot (R\,C)^2 + \frac{C}{Cd} \cdot (1 - y\,L\,C) = 0 \ ; \tag{C.4}$$

$$\begin{aligned} y &= \frac{1}{2L^2C^2}\left(-\left((R\,C)^2 - 2LC - \frac{C}{Cd} L\,C \right) \pm \sqrt{\left((R\,C)^2 - 2LC - \frac{C}{Cd} L\,C \right)^2 - 4L^2C^2\left(\frac{C}{Cd} + 1 \right)} \right) \\ &= \frac{1}{LC}\left(1 + \frac{C}{2Cd} - \frac{R^2C}{2L} \pm \sqrt{\left(\frac{C}{2Cd} \right)^2 + \frac{R^2C}{2L}\left(\frac{R^2C}{2L} - \frac{C}{Cd} - 2 \right)} \right) \end{aligned} \tag{C.5}$$

Let $x = R^2$, the first order Tylor series expansion of y at x = 0 is

$$= y\big|_{x=0} \quad \frac{\partial y}{\partial}\bigg|_{x=} \cdot x \quad . \tag{C.6}$$

$$\big|_{=0} = \frac{1}{LC} \quad , \tag{C.7}$$

where the sign is '-" in (C.5), or

$$y\big|_{\ 0} = \frac{1}{L}\left(1 + \frac{C}{Cd} \right) \ . \tag{C.8}$$

$$\frac{\partial y}{\partial x} = \frac{1}{LC}\left(-\frac{C}{2L} \mp \frac{1}{2}\left(\left(\frac{C}{2Cd} \right)^2 + \frac{R^2C}{2L}\left(\frac{R^2C}{2L} - \frac{C}{Cd} - 2 \right) \right)^{-0.5} \cdot \left(\frac{C}{2L}\left(\frac{R^2C}{2L} - \frac{C}{Cd} - 2 \right) + \frac{R^2C}{2L}\left(\frac{C}{2L} \right) \right) \right)$$

. (C.9)

$$\frac{\partial y}{\partial x}\bigg|_{x=0} = \frac{1}{LC}\left(-\frac{C}{2L} \mp \frac{1}{2}\left(\frac{C}{2Cd} \right)^{-1} \cdot \left(\frac{C}{2L}\left(-\frac{C}{Cd} - 2 \right) \right) \right) .$$

$$\begin{aligned} \frac{\partial y}{\partial x}\bigg|_{x=0} &= \frac{1}{LC}\left(-\frac{C}{2L} - \frac{1}{2}\left(\frac{2Cd}{C} \right) \cdot \left(\frac{C}{2L}\left(-\frac{C}{Cd} - 2 \right) \right) \right) \\ &= \frac{Cd}{L^2C} \end{aligned} \ , \tag{C.10}$$

where the sign is '-"in (C.5), or

$$\left.\frac{\partial y}{\partial x}\right|_{x=0} = \frac{1}{LC}\left(-\frac{C}{2L}+\frac{1}{2}\left(\frac{2Cd}{C}\right)\cdot\left(\frac{C}{2L}\left(-\frac{C}{Cd}-2\right)\right)\right) = \frac{Cd}{L^2C}\left(-\frac{C}{Cd}-1\right) \quad . \tag{C.11}$$

According to (C.6), combining (C.7) and (C.10) makes

$$y = \omega_r{}^2 = \frac{1}{LC}\cdot\left(1+\frac{R^2}{L}\cdot Cd\right) \quad . \tag{C.12}$$

When the sign is '+' in (C.5),

$$y = \omega_a{}^2 = \frac{1}{LC}\cdot\left(1+\frac{C}{Cd1}-\frac{R^2}{L}\cdot(C+Cd)\right) \quad . \tag{C.13}$$

APPENDIX D : MCAD Program to Calculate the Equivalent Circuits of PTs

D.1 Longitudinal PT (HVPT-1)

Engineering exponential identifier:

$Meg := 1\cdot10^{6}$ $k := 1\cdot10^{3}$ $m := 1\cdot10^{-3}$ $\mu := 1\cdot10^{-6}$ $n := 1\cdot10^{-9}$ $p := 1\cdot10^{-12}$

Measurement results for 2nd mode operation:

(a) output is shorted:

$Ct := 848.5\cdot p$ $fs := 67054.25$ $fp := 68597.5$ $Gmax := 0.0146088$

$fr := 67055$ $fa := 68595$ $r := \frac{1}{Gmax}$

(b) input is shorted:

$Ct\phi := 8.75\cdot p$ $fs\phi := 67079.625$ $fp\phi := 73275$ $Gmax2 := 0.0004904$

$fr2 := 67079.875$ $fa2 := 73282.5$

Calculation results for 2nd mode operation:

$keff2 := \frac{fp^2 - fs^2}{fp^2}$ $cd1 := \frac{fs^2}{fp^2}\cdot Ct$ $c := keff2\cdot Ct$ $l := \frac{1}{(2\cdot\pi\cdot fs)^2\cdot c}$

$cd1 = 810.7517\cdot p$ $c = 37.7483\cdot p$ $l = 0.1492$ $keff2 = 0.0445$

$keff\phi := \frac{fp\phi^2 - fs\phi^2}{fp\phi^2}$ $Cd1\phi := \frac{fs\phi^2}{fp\phi^2}\cdot Ct\phi$ $c\phi := keff\phi\cdot Ct\phi$ $l\phi := \frac{1}{(2\cdot\pi\cdot fs\phi)^2\cdot c\phi}$

$cd2 := Cd1\phi$ $c\phi = 1.4171\cdot p$ $l\phi = 3.9725$ $keff\phi = 0.162$

$n := \sqrt{\frac{c}{c\phi}}$ $n1 := \sqrt{\frac{l\phi}{l}}$ $n3 := \sqrt{\frac{Gmax}{Gmax2}}$ $cd2 = 7.3329\cdot p$

$n = 5.1612$ $n1 = 5.1593$ $n3 = 5.458$ $r = 68.4519$

D.2 Thickness extensional PT (LVPT-21)

Pseudo-units to be used for constants and results:

$\varepsilon o := 8.854187 \cdot pico$

$V := 1$ $A := 1$ $\Omega := 1$ $H := 1$ $F := 1$ $W := 1$ $J := 1$ $Hz := 1$ $S := 1$

$T := 1$ $Wb := 1$ $K := 1$ $dB := 1$ $N := 1$ $mH := 0.001 \cdot H$ $pF := pico \cdot F$

$meter := 1$ $cm := 0.01 \cdot meter$ $dm := 10 \cdot cm$ $mm := 0.1 \cdot cm$ $km := k \cdot meter$

$inch := 2.54 \cdot cm$ $ft := 12 \cdot inch$ $sec := 1$ $kg := 1$ $g := m \cdot kg$

Measurement results for 2nd mode operation:

(a) output is shorted:

$Gmx2 := 0.4493 \cdot S$ $\frac{1}{Gmx2} = 2.22568$

$fs21 := 1860.25 \cdot k \cdot Hz$ $\frac{1}{Gmxr2} = 0.62197$

$fr21 := 1860.75 \cdot k \cdot Hz$

$fa21 := 1937.25 \cdot k \cdot Hz$

$Ct21 := 2830 \cdot pico \cdot F$

(b) input is shorted:

$Gmxr2 := 1.6078$

$fs22 := 1860.25 \cdot k \cdot Hz$

$fr22 := 1860.5 \cdot k \cdot Hz$

$fa22 := 1937.25 \cdot k \cdot Hz$

$Ct22 := 10320 \cdot pico \cdot F$

Calculation results for 2nd mode operation:

$Cd1 := \frac{fr21^2}{fa21^2} \cdot Ct21$ $C2 := Ct21 - Cd1$ $L2 := \frac{1}{C2 \cdot (2 \cdot \pi \cdot fs21)^2}$

$Cd2 := \frac{fr22^2}{fa22^2} \cdot Ct22$ $C2n := Ct22 - Cd2$ $L2n := \frac{1}{C2n \cdot (2 \cdot \pi \cdot fs22)^2}$

$fs := \frac{1}{2 \cdot \pi \cdot \sqrt{L2 \cdot C2}}$ $N2 := \sqrt{\frac{L2}{L2n}}$ $N2c := \sqrt{\frac{C2n}{C2}}$ $N2r := \sqrt{\frac{Gmxr2}{Gmx2}}$

$fs = 1860.25\ k$ $N2 = 1.91267$ $N2c = 1.91267$ $N2r = 1.89168$

$Rcd1 := \frac{1}{2 \cdot \pi \cdot fs \cdot Cd1 \cdot 0.006}$ $Rcd1 = 5.461\ k$

$Rcd2 := \frac{1}{2 \cdot \pi \cdot fs \cdot Cd2 \cdot 0.006}$ $Rcd2 = 1.498\ k$

Equivalent circuits of spurious vibrations:

(a) fsm = 1835 kHz

$Gsmax := 0.15455$ $fm45 := 1834000$ $fp45 := 1836000$ $fss := 1835250$

$rsm := \frac{1}{Gsmax}$ $rsm\ 6.4704$

$csm := \frac{1}{2 \cdot \pi \cdot rsm} \cdot \frac{fp45 - fm45}{fp45 \cdot fm45}$ c $sm = 14.610\ pico$

$lsm := \frac{rsm}{2 \cdot \pi} \cdot \frac{1}{fp45 - fm45}$ $lsm = 0.5149\ m$

(b) fsm = 1891 kHz

$Gsmax := 0.072378$ $fm45 := 1890500$ $fp45 := 1894250$

$rsm := \frac{1}{Gsmax}$ rsm = 13.81635

$csm := \frac{1}{2 \cdot \pi \cdot rsm} \cdot \frac{fp45 - fm45}{fp45 \cdot fm45}$ csm = 12.06269 pico

$lsm := \frac{rsm}{2 \cdot \pi} \cdot \frac{1}{fp45 - fm45}$ $lsm = 586.38423 \cdot \mu$ $fs := \sqrt{fp45 \cdot fm45}$

fs = 1892.374 k

(c) fsm = 1943 kHz

$Gsmax := 0.01731$ $fs := 1942250$

$fm45 := 1939500$ $fp45 := 1947000$

$rsm := \frac{1}{Gsmax}$ rsm = 57.77008

$csm := \frac{1}{2 \cdot \pi \cdot rsm} \cdot \frac{fp45 - fm45}{fp45 \cdot fm45}$ csm = 5.47171 pico

$lsm := \frac{rsm}{2 \cdot \pi} \cdot \frac{1}{fp45 - fm45}$ lsm = 1.22592 m

APPENDIX E : MATLAB Program to Calculate the Optimal Load of PTs

% Program list for power flow method for LVPT-21

```
clear

% input section
pt213189                    % measured S-parameters from network analyzer
ii=sqrt(-1);

Rload=9.8;                  % assumed load of the PT
Lload=450e-9;

% lumped model of LVPT-21
fs21=1860250;
R=2.225;
C=219.09e-12;               % C=199.09e-12;
L=1/C/(2*pi*fs21)^2;        % L=36.766e-6;
cd1=2211e-12;
cd2=9518.4e-12;
nc=1.913;
rcd1=5461;
rcd2=1498;

% measurement from spurious vibrations
fs211=1835000;
R4=6.47;
C4=14.6099e-12;
L4=1/C4/(2*pi*fs211)^2;             % L4=586.38e-6
```

```
fs217=1892374;
R7=13.81;
C7=12.06269e-12;
L7=1/C7/(2*pi*fs217)^2;                  %  L7=440.2e-6

fs218=1943246;
R8=57.77;
C8=5.472e-12;
L8=1/C8/(2*pi*fs218)^2;                  %  L8=0.0012

% calculation of the optimal load employing the lumped model
for i= 1:601

im=i+200;
f(I)=sm(im,9);
w=2*pi*f(I);
yload=1/(Rload+ii*w*Lload);              % Load admittance

% directly calculate y11, y12, y21, y22
zs2=R+ii*w*L+1/w/C/ii;
zs4=R4+ii*w*L4+1/w/C4/ii;
zs7=R7+ii*w*L7+1/w/C7/ii;
zs8=R8+ii*w*L8+1/w/C8/ii;
zs=1/(1/zs2+1/zs4+1/zs7+1/zs8);
z11=1/(1/rcd1+ii*w*cd1);
z22=1/(1/rcd2+ii*w*cd2);
y11=1/z11+1/zs;
y12=-nc/zs;
y21=y12;
y22=1/z22+nc*nc/zs;

c=abs(y12*y21)/abs(2*real(y11)*real(y22)-real(y12*y21));      % c: Linvill constant
x=-1/c+sqrt(1-c^2)/c;
lk(i)=1-x*real(y12*y21)/abs(y12*y21);
mk(i)=imag(y12*y21)*x/abs(y12*y21);
cck(i)=c;

kk=-y21/2/real(y22);
phi2=(lk(i)+ii*mk(i))*kk;
sin=y11+phi2*y12;                        % input power
yin(i)=sin;                          % input admittance ( vin =1 )
rin(i)=1/real(sin);
```

```
cin(i)=imag(sin)/2/pi/f(i);
pin(i)=real(sin);                       % input real power
qin(i)=imag(sin);                       % input reactive power
gammal=2*real(y22)/(lk(i)+ii*mk(i))-y22;
yoptk(i)=abs(gammal);                   % calculated optimal load
ayoptk(i)=ANGLE(gammal)/2/pi*360;
zl(i)=real(1/gammal);
ll(i)=imag(1/(gammal)/2/pi/f(i));
zlp(i)=1/real(gammal);
llp(i)=-1/imag(gammal)/2/pi/f(i);
sout=abs(phi2)^2*gammal;                % output power
eff(i)=real(sout)/real(sin);
pout(i)=real(sout);                     % output real power
qout(i)=imag(sout);                     % output reactive power
vgain(i)=abs(y21/(gammal+y22));         % voltage gain under optimal load

y11c=1/z11+1/zs;
y12c=-nc/zs;
y21c=y12c;
y22c=1/z22+nc*nc/zs;

y11k(i)=abs(y11c);
gfk(i)=real(y11c);
bfk(i)=imag(y11c);
angle=atan2(bfk(i),gfk(i));
anglek(i)=angle/2/pi*360;

y22k(i)=abs(y22c);
gbk(i)=real(y22c);
bbk(i)=imag(y22c);

yinldc=y11c-y12c*y21c/(yload+y22c);     % input admittance for yload
pinldc=real(yinldc);
vldc=-y21c/(yload+y22c);
poutldc=abs(vldc)*abs(vldc)*real(yload);

rinldk(i)=1/real(yinldc);
cinldk(i)=imag(yinldc)/w;
yinlk(i)=abs(yinldc);
ayinlk(i)=ANGLE(yinldc)/3.14165*360;
pinldk(i)=pinldc;
poutldk(i)=poutldc;
effldk(i)=poutldc/pinldc;
```

```
vgainldk(i)=abs(vldc);                    % voltage gain under yload

y11c=y11c*50;
y12c=y12c*50;
y21c=y21c*50;
y22c=y22c*50;

ky=1/((1+y11c)*(1+y22c)-y12c*y21c);
s11=ky*((1-y11c)*(1+y22c)+y12c*y21c);
s12=-2*ky*y12c;
s22=ky*((1+y11c)*(1-y22c)+y12c*y21c);
s21=-2*ky*y21c;

s11k(i)=20*log10(abs(s11));
s21k(i)=20*log10(abs(s21));
s22k(i)=20*log10(abs(s22));

% calculation of the optimal load employing two-port parameters
s21f(i)=sm(im,3);
sm(im,1)=10^(sm(im,1)/20);
sm(im,3)=10^(sm(im,3)/20);
sm(im,5)=10^(sm(im,5)/20);
sm(im,7)=10^(sm(im,7)/20);

s11=sm(im,1)*exp(ii*sm(im,2)/180*pi);
s21=sm(im,3)*exp(ii*sm(im,4)/180*pi);
s12=sm(im,5)*exp(ii*sm(im,6)/180*pi);
s22=sm(im,7)*exp(ii*sm(im,8)/180*pi);

s21m(i)=20*log10(abs(s21));
s12m(i)=20*log10(abs(s12));
s11m(i)=20*log10(abs(s11));
s22m(i)=20*log10(abs(s22));

deltas=s11*s22-s12*s21;
k=0.02/(1+s22+s11+deltas);
y11=k*(1+s22-s11-deltas);
y12=-2*k*s12;
y21=-2*k*s21;
y22=k*(1+s11-s22-deltas);

yinld=y11-y12*y21/(yload+y22);
pinld=real(yinld);
```

```
vld=-y21/(yload+y22);
poutld=abs(vld)*abs(vld)*real(yload);

rinldm(i)=1/real(yinld);
cinldm(i)=imag(yinld)/w;
yinlm(i)=abs(yinld);
ayinlm(i)=ANGLE(yinld)/3.14165*360;
pinldm(i)=pinld;
poutldm(i)=poutld;
effldm(i)=poutld/pinld;
vgainldm(i)=abs(vld);

y11m(i)=abs(y11);
gfm(i)=real(y11);
bfm(i)=imag(y11);
angle=atan2(bfm(i),gfm(i));
anglem(i)=angle/2/pi*360;

y22f(i)=abs(y22);
gbm(i)=real(y22);
bbm(i)=imag(y22);

c=abs(y12*y21)/abs(2*real(y11)*real(y22)-real(y12*y21));
x=-1/c+sqrt(1-c^2)/c;
lm(i)=1-x*real(y12*y21)/abs(y12*y21);
mm(i)=imag(y12*y21)*x/abs(y12*y21);
ccm(i)=c;

kk=-y21/2/real(y22);
phi2=(lm(i)+ii*mm(i))*kk;
sin=y11+phi2*y12;
yinm(i)=sin;
rinm(i)=1/real(sin);
cinm(i)=imag(sin)/2/pi/f(i);
pinm(i)=real(sin);
qinm(i)=imag(sin);
gammal=2*real(y22)/(lm(i)+ii*mm(i))-y22;
yoptm(i)=abs(gammal);
ayoptm(i)=ANGLE(gammal)/2/pi*360;
zlm(i)=real(1/gammal);
llm(i)=imag(1/(gammal)/2/pi/f(i));
zlpm(i)=1/real(gammal);
llpm(i)=-1/imag(gammal)/2/pi/f(i);
```

```
sout=abs(phi2)^2*gammal;
effm(i)=real(sout)/real(sin);
poutm(i)=real(sout);
qoutm(i)=imag(sout);
vgainm(i)=abs(y21/(gammal+y22));

y11f(i)=abs(y11);
gfm(i)=real(y11);
bfm(i)=imag(y11);

y22f(i)=abs(y22);
gbm(i)=real(y22);
bbm(i)=imag(y22);

end

figure(1)
subplot(2,2,1), plot(f,s21k,f,s21m,f,s12m)
subplot(2,2,2), plot(f,s11k,f,s11m)
subplot(2,2,3), plot(gfk,bfk,gfm,bfm)
subplot(2,2,4), plot(f,s22k,f,s22m)
pause

figure(2)
subplot(4,2,1), plot(f,zl,f,zlm)
subplot(4,2,2), plot(f,ll,f,llm)
subplot(4,2,3), plot(f,yoptk,f,yoptm)
subplot(4,2,4), plot(f,ayoptk,f,ayoptm)
subplot(4,2,5), plot(f,vgain,f,vgainm)
subplot(4,2,6), plot(f,cin,f,cinm)
subplot(4,2,7), plot(f,eff,f,effm)
subplot(4,2,8), plot(f,pin,f,pinm)
pause

figure(3)
subplot(2,2,1), plot(f,pinldk,f,pinldm)
subplot(2,2,2), plot(f,poutldk,f,poutldm)
subplot(2,2,3), plot(f,effldk,f,effldm)
subplot(2,2,4), plot(f,vgainldk, f,vgainldm)
pause
```

APPENDIX F : MATLAB Program to Calculate the DC Characteristics of SE-QR Amplifiers

% APPENDIX F.1

```
% Flyback single-ended quasi-resonant converters.
% Calculation of normalized gain, voltage stress, and current stress of HVPT-2.
% ZVS operation when Vs1=0 and Ilr<0.

clear

% input section
cwind=1e-9;                    % winding capacitance
eps=1e-3;
ii=sqrt(-1);
effconv=0.95;
nr=6.9;
RLD=[50e3 100e3 200e3 300e3 400e3 500e3]; % load resistance of the PT
Lrr=50e-6;                     % input value for resonant inductor

% lump model of HVPT-2
cd1=810.75e-12;
fs21=67054.25;
C=37.748e-12;
L=1/C/(2*pi*fs21)^2;           % L=0.1492;
R=68.45;
cd2=8.8e-12;                   % cd2=7.33e-12;
nc=1/5.16;                     % step-up ratio of HVPT-2
rcd1=615e3;
rcd2=66e6;
```

```
%  beginning of the program
for ik = 1:21
fs(ik)=65000+(ik-1)*500;                %  step of switching frequency Fs
ws=2*pi*fs(ik);
fn1=ws*sqrt(Lrr*(cd1*(nr)^2+cwind));

%  calculation of the fundamental voltage when qp is very large
[vcrms,vc1st,ilmax,vcmax,vcn,iln,nt] = wavexmer(1e-6,fn1);

    for j = 1:(nt+1);
    wstn(j)=1/fs(ik)/nt*j;
    end

vcrmsn=vcrms;                   %  normalized RMS voltage across S1
vc1stn=vc1st;                   %  normalized fundamental voltage across S1

%  y11, y12, y21, y22
zs2=R+ii*ws*L+1/ws/C/ii;
zs=1/((1/zs2));
z11=1/(1/rcd1+ii*ws*cd1);
z22=1/(1/rcd2+ii*ws*cd2);
y11c=1/z11+1/zs;
y12c=-nc/zs;
y21c=y12c;
y22c=1/z22+nc*nc/zs;

    for i=1:6
    flg=0;
    jb=0;
    Rload=RLD(i);               %  load of the PT
    yload=1/Rload;              %  Load admittance
    zload=1/yload;
    yinldc=y11c-y12c*y21c/(yload+y22c)-1/z11;
    cinldk(i)=imag(yinldc)/ws;

%  calculation of the equivalent Racp
    vldc=-y21c/(yload+y22c);
    vgainldk(i)=abs(vldc);
    vgainco(i)=vc1stn*vgainldk(i)*nr/sqrt(2);
    poutld(i)=vgainco(i)^2/abs(zload);
    racp(i)=(vcrmsn)^2/poutld(i)*effconv;
    racpk(i,ik)=racp(i);
```

```
    ri=racp(i);
    ci(i)=cd1*nr^2+cwind;
    w=sqrt(1/Lrr/ci(i)-1/4/ri^2/ci(i)^2);
    fn2=ws/w;
    fn(i)=fn2;
    adw=1/2/ri/ci(i)/w;
    wodw=sqrt(1+(adw)^2);
    qp(i)=0.5*wodw/adw;

%  calculation of the voltage and current waveforms
    [vcrms,vc1st,ilmax,vcmax,vcn,iln,nt] = wavexmer(adw,fn2);
    vcnrms(i,ik)=vcrms;
    ilnmax(i,ik)=ilmax;
    vcnmax(i,ik)=vcmax;
    vgaincon(i,ik)=vgainco(i);

    figure(1)
    subplot(2,1,1); plot(wstn,vcn); hold on; grid on;
    ylabel('vcn');
    subplot(2,1,2); plot(wstn,iln); hold on; grid on;
    ylabel('iln');

                                        end
end

figure(2);
subplot(2,1,1); mesh(fs,RLD,vcnrms); grid on;
title ('Lrr = 50 uH');
xlabel ('Freqency');
ylabel (' Rload ');
zlabel ('vcn_rms');
view(45,45);
subplot(2,1,2); mesh(fs,RLD,vgaincon); grid on;
title ('Lrr = 50 uH');
xlabel ('Freqency');
ylabel (' Rload ');
zlabel ('vgaincon');
```

% APPENDIX F.2

```
% Function for calculating steady-state voltage and current of the flyback
% single-ended quasi-resonant converter
% Reference to Fig. 4.15 (c)

% Normalized input variables: adw and fn
% fn: ratio between switching frequency fs and resonant frequency
% adw: ratio between 1/(2 racp cin) and resonant frequency, a = 1/(2 racp cin)

% Normalized output variables: vcrms,vc1st,ilmax,vcmax,vcn,iln,nt
% vcrms: RMS voltage across S1
% vc1st: fundamental voltage of S1
% ilmax: peak to peak resonant inductor current
% vcmax: maximum voltage across S1
% vcn: voltage waveform across S1
% iln: current waveform of the resonant inductor Lr
% nt: number of iteration

function [vcrms,vc1st,ilmax,vcmax,vcn,iln,nt] = waveperf(adw,fn);

% input section
niter=200;
eps=1e-3;
ii=sqrt(-1);
wodw=sqrt(1+(adw)^2);          % ratio between wo and w for an input adw
qp=0.5*wodw/adw;               % qp= rin/zo = 0.5 wo/a = 0.5 wodw/adw
flg=0;
jb=0;

% calculation of the steady-state variables

for j=1:niter

    wtoff=pi*(1.005+0.9*j/niter);
    wtoffn(j)=wtoff/2/pi*360;

% calculation of fn under the ZVS condition
    eat=exp(-adw*wtoff); % exponential term caused by the load resistance

% derivation of Io when voltage across S1 is equal to zero for a arbitrary wtoff
```

```
    ion(j)=-(1-cos(wtoff)*eat+adw*sin(wtoff)*eat)/wodw/sin(wtoff)/eat;
    Io=ion(j);                  %  initial current when S1 is turned off

    il1=eat*(wodw*sin(wtoff)+ion(j)*(cos(wtoff)+adw*sin(wtoff)));
    il2=0;
    iln(j)=il1+il2;
    Il=iln(j);                  %  inductor current when Vs1 = 0

    DELTA(j)=abs(Io-Il);
    fsk(j)=2*pi/(DELTA(j)+wodw*wtoff);
    deltaf=fn-fsk(j);
    wtoffk(j)=wtoff;

    if (deltaf <=eps),jb=j,break, end        %  the approximated solution for wtoff
    if (j == niter), jb=j, break, end
    end

fs=fsk(jb);                     %  record of fs, stoptime, and starttime
stoptime=wtoffk(jb);
startime=wtoffk(jb-1);

%  narrow down the region of the solution
for j=1:(niter/2+1)
    if (jb == niter), break, end

    wtoff=startime+(stoptime-startime)*(j-1)/(niter/2);
    wtoffn(j)=wtoff/2/pi*360;

%  calculation of fn under the ZVS condition
    eat=exp(-adw*wtoff);
    ion(j)=-(1-cos(wtoff)*eat+adw*sin(wtoff)*eat)/wodw/sin(wtoff)/eat;
    Io=ion(j);

    il1=eat*(wodw*sin(wtoff)+ion(j)*(cos(wtoff)+adw*sin(wtoff)));
%   il2=1/qp*(1-cos(wtoff)*eat-adw*sin(wtoff)*eat);
    il2=0;
    iln(j)=il1+il2;
    Il=iln(j);

    DELTA(j)=abs(Io-Il);
%   fsk(j)=2*pi/(DELTA(j)/wodw+wtoff);
    fsk(j)=2*pi/(DELTA(j)+wodw*wtoff);
    deltaf=fn-fsk(j);
```

```
            if (deltaf <=eps),jb=j,break,end
    end

%  waveforms for vcn and iln.

nt=400;
deltat=2*pi/nt/fn;

for j=1:(nt+1)
    wotn(j)=j;
    if (jb == niter), vcn(j)=0; iln(j)=0; Io=0; Il=0;
    else

    wst(j)=(j-1)*2*pi/nt;
    wt=wst(j)/fn;
    if flg==0,
    eat=exp(-adw*wt);
    vcn(j)=(1-cos(wt)*eat+adw*sin(wt)*eat)+Io*wodw*sin(wt)*eat;
    il1=eat*(wodw*sin(wt)+Io*(cos(wt)+adw*sin(wt)));
    il2=0;
    iln(j)=il1+il2;

    if ((vcn(j)+eps) < 0),flg=1; end;
    else
    vcn(j)=0;
    iln(j)=iln(j-1)+deltat;
    end
    end

    vcrm(j)=(vcn(j)-1)^2;  %  RMS value of Vs1
end

vcrms=sqrt(sum(vcrm)/(nt+1));
if (vcrms == 1); vcrms=0; end
ilmax=Io-Il;
vcmax=max(vcn);
[Freq, Spec]=spec_st(nt,vcn,wotn,9);     % calculate the harmonics of Vs1 or vcn
vc1st=abs(Spec(2))*2;

return
```

VITA

The author, Chih-yi Lin, was born in Taiwan, Republic of China, on January 25, 1961. He received his B.S. degree in Electrical Engineering in 1982 from Tatung Institute of Technology, Taipei. He received M.S. degree from National Tsing-Hua University in 1984 in Electrical Engineering. After serving in Chinese Army, he joined Chung-San Institute of Science and Technology as a assistant researcher from 1984 to 1990. In 1991, he enrolled in the Electrical Engineering Department, Virginia Polytechnic Institute & State University, as a graduate student and become a member of the Virginia Power Electronics Center to work toward his Ph.D. degree ever since.

His main research interests include modeling, analysis, and design of low-power to high-power as well as low-voltage to high-voltage dc/dc converters.